

**Search for the Higgs Boson
and a study of $e^+e^- \rightarrow ZZ$
using the L3 Detector at LEP**

Serge Likhoded

**Search for the Higgs Boson
and a study of $e^+e^- \rightarrow ZZ$
using the L3 Detector at LEP**

D i s s e r t a t i o n

zur Erlangung des akademischen Grades

d o c t o r r e r u m n a t u r a l i u m

(Dr. rer. nat.)

im Fach Physik

eingereicht an der

**Mathematisch-Naturwissenschaftlichen Fakultät I
der Humboldt-Universität zu Berlin**

von

Diplom-Physiker **Serge Likhoded**
geboren am 18. Juni 1973 in Moskau

**Präsident der Humboldt-Universität zu Berlin
Prof. Dr. J. Mlynek**

**Dekan der Mathematisch-Naturwissenschaftlichen Fakultät I
Prof. Dr. B. Ronacher**

Gutachter: 1. Prof. Dr. T. Hebbeker
 2. Prof. Dr. H. Kolanoski
 3. Prof. Dr. M. Kienzle

Tag der mündlichen Prüfung: 11.12.2002

Zusammenfassung

Die Arbeit beinhaltet die Suche nach dem Higgs Boson, welches vom Standardmodell der elektroschwachen Wechselwirkungen vorhergesagt wird, und die Messung der Z Boson Paarproduktion in Elektron-Positron Annihilationen.

Nach dem Higgs Boson wird in allen experimentell relevanten Endzuständen in Daten gesucht, welche in den Jahren 1999–2000 mit dem L3 Detektor am Speicherring LEP bei Energien bis 209 GeV genommen wurden.

Es wurde kein Signal für die Erzeugung von Higgs Bosonen gefunden. Die beobachteten Kandidaten sind mit den Untergrundereignissen verträglich.

Neue untere Grenzen für die Masse des Higgs Boson wurden auf 95% Vertrauensniveau bestimmt:

$$m_H > 112.0 \text{ GeV}$$

Wird dieses Ergebnis mit den Analysen der anderen LEP Experimente kombiniert, ergibt sich:

$$m_H > 114.1 \text{ GeV}.$$

Die Paarproduktion von Z Bosonen $e^+e^- \rightarrow ZZ$, wird für Schwerpunktsenergien zwischen 200 und 209 GeV analysiert.

Der Wirkungsquerschnitt σ_{ZZ} wird sowohl für alle sichtbaren Z Zerfallsmoden als auch speziell für Z Zerfälle in b-Quarks gemessen.

Das Ergebnis ist für Schwerpunktsenergien von 205 GeV und 207 GeV:

$$\begin{aligned}\sigma_{ZZ}(205.1 \text{ GeV}) &= 0.86_{-0.21}^{+0.23} \pm 0.07 \text{ pb} \quad (\text{SM} : 1.07 \text{ pb}), \\ \sigma_{ZZ}(206.8 \text{ GeV}) &= 1.21_{-0.17}^{+0.19} \pm 0.10 \text{ pb} \quad (\text{SM} : 1.08 \text{ pb}),\end{aligned}$$

Die Messwerte sind in Übereinstimmung mit der Vorhersage im Standard Model (SM).

Für den Prozess $e^+e^- \rightarrow ZZ \rightarrow b\bar{b}X$, $\sigma_{ZZ \rightarrow b\bar{b}X}$ ist das Ergebnis:

$$\sigma_{ZZ \rightarrow b\bar{b}X}(206.2 \text{ GeV}) = 0.23 \pm 0.09 \pm 0.02 \text{ pb}.$$

Auch dieser Wert stimmt mit der Vorhersage des Standardmodells von 0.30 pb sehr gut überein.

Aus der Analyse der Z Paarproduktion werden Grenzen für Eichbosonen-Selbstkopplungen ZZZ und γZZ , welche im Standard Model verboten sind, abgeleitet. Auf 95% Vertrauensniveau ergibt sich:

$$\begin{aligned}-0.42 &\leq f_4^Z \leq 0.41 \\ -0.46 &\leq f_5^Z \leq 1.21\end{aligned}$$

$$\begin{aligned} -0.24 &\leq f_4^\gamma \leq 0.26 \\ -0.48 &\leq f_5^\gamma \leq 0.56 \end{aligned}$$

Für die Bestimmung dieser Grenzen werden auch ältere Daten bei niedrigeren LEP Energien benutzt.

Abstract

The first part of this thesis is devoted to the search for the Higgs boson predicted by the Standard Model (SM). By the introduction of this particle into the theory, the masses of bosons and fermions can be explained. The search is performed in channels characterised by quarks and leptons in the final state. The analysis uses data taken during the years 1999–2000 with the L3 detector at the Large Electron Positron collider LEP.

The observed candidates are consistent with the expectation from Standard Model background processes. Evidence for Higgs boson production is not found. New mass limits were determined superseding previous mass limits established by L3 and other experiments.

A lower mass limit of

$$m_H > 112.0 \text{ GeV}$$

is derived at the 95% confidence level. Combining this result with the limits, obtained by three other LEP experiments, a lower mass limit of

$$m_H > 114.1 \text{ GeV.}$$

was set on the SM Higgs boson.

The second part of this thesis contains results on the pair-production of Z bosons in e^+e^- collisions at LEP at center-of-mass energies between 200 and 209 GeV. The cross section of this process is measured both for all Z decay modes and for final states containing b quarks. The ZZ cross section σ_{ZZ} for the two values of averaged center-of-mass energies, 205 GeV and 207 GeV, is found to be:

$$\begin{aligned}\sigma_{ZZ}(205.1 \text{ GeV}) &= 0.86_{-0.21}^{+0.23} \pm 0.07 \text{ pb (SM : 1.07 pb)}, \\ \sigma_{ZZ}(206.8 \text{ GeV}) &= 1.21_{-0.17}^{+0.19} \pm 0.10 \text{ pb (SM : 1.08 pb)},\end{aligned}$$

in good agreement with the expected cross section in the Standard Model, reported in parentheses.

These analyses can also be interpreted in terms of the NC02 ansatz, which describes the production of two Z bosons by means of the t -channel $e^{(*)}$ exchange:

$$\begin{aligned}\sigma_{ZZ}^{\text{NC02}}(205.1 \text{ GeV}) &= 0.84_{-0.21}^{+0.23} \pm 0.07 \text{ pb (SM : 1.05 pb)}, \\ \sigma_{ZZ}^{\text{NC02}}(206.8 \text{ GeV}) &= 1.20_{-0.17}^{+0.18} \pm 0.10 \text{ pb (SM : 1.07 pb)},\end{aligned}$$

The result for the cross section for $e^+e^- \rightarrow ZZ \rightarrow b\bar{b}X$, $\sigma_{ZZ \rightarrow b\bar{b}X}$ is:

$$\sigma_{ZZ \rightarrow b\bar{b}X}(206.2 \text{ GeV}) = 0.23 \pm 0.09 \pm 0.02 \text{ pb.}$$

in agreement with the Standard Model prediction of 0.30 pb.

Limits on triple couplings between neutral gauge boson, forbidden in the Standard Model, are derived at 95% confidence level:

$$-0.42 \leq f_4^Z \leq 0.41$$

$$-0.46 \leq f_5^Z \leq 1.21$$

$$-0.24 \leq f_4^\gamma \leq 0.26$$

$$-0.48 \leq f_5^\gamma \leq 0.56$$

Those limits include results from the previous analyses at lower center-of-mass energies.

In memory of my grandmother...

Contents

1	Introduction	1
2	The Theory	3
2.1	The Standard Model	3
2.1.1	Gauge Field Theory	3
2.1.2	Lagrangian for Strong, Weak and Electromagnetic Forces	5
2.2	The Higgs Mechanism	7
2.2.1	Abelian Higgs Model	7
2.2.2	Higgs Mechanism in the Standard Model	9
2.2.3	Problems with the Higgs Mechanism	12
2.3	Restrictions on Higgs Boson Masses	13
2.3.1	Theoretical Bounds on the Higgs Boson Mass	13
2.3.2	Limits from Indirect Searches	17
2.3.3	Limits from Direct Searches	18
2.4	Higgs Production at LEP	19
2.4.1	Cross sections	19
2.4.2	Higgs Branching Fractions	21
2.4.3	Standard Model Processes	25
3	The Experiment	29
3.1	The LEP Machine	29
3.2	The L3 Detector	31
3.2.1	The L3 Coordinate System	32
3.2.2	Magnet	33
3.2.3	Silicon Microvertex Detector	34
3.2.4	Central Tracking Chamber	35
3.2.5	Electromagnetic Calorimeter	37
3.2.6	Scintillation Counters	38
3.2.7	Hadronic Calorimeter	38
3.2.8	Muon Spectrometer	40
3.2.9	Luminosity Monitor	41
3.2.10	Trigger	42

4	Data and Monte Carlo Samples	45
4.1	Data Sample	45
4.2	Monte Carlo Samples	45
4.3	Simulation and Reconstruction	46
4.3.1	DURHAM Jet Clustering Algorithm	47
4.3.2	Kinematic Fit	48
4.3.3	The Resolution Functions of Jet Measurement in the L3 Detector	50
4.3.4	B-tagging	59
5	Search for the Standard Model Higgs Boson	65
5.1	Analysis Procedure	65
5.1.1	Preselection	66
5.1.2	Cut Optimization	66
5.1.3	The Final Discriminant	66
5.1.4	Interpretation of Observed Data	67
5.2	The $HZ \rightarrow b\bar{b}q\bar{q}$ channel	67
5.3	The $HZ \rightarrow b\bar{b}\nu\bar{\nu}$ channel	75
5.3.1	Cross-checks	77
5.4	The $HZ \rightarrow b\bar{b}l^+l^-$ and $HZ \rightarrow \tau^+\tau^-q\bar{q}$ channels	78
6	Interpretation of the Results	81
6.1	The Confidence Level	81
6.2	Combining All Search Channels	84
6.3	The Statistical and Systematic Uncertainties	85
6.4	Mass Limit	87
6.5	The LEP-wide combination	88
6.5.1	Contributions from single events	91
6.5.2	Bounds for the Higgs boson mass and coupling	92
7	Measurement of the Cross Section of $e^+e^- \rightarrow ZZ$	95
7.1	Data and Monte Carlo samples	96
7.2	Signal Definition	96
7.3	Analysis Procedure	98
7.3.1	The $ZZ \rightarrow q\bar{q}q'\bar{q}'$ Channel	99
7.3.2	Cut Optimization	105
7.3.3	The $q\bar{q}\nu\bar{\nu}$ Channel	108
7.3.4	The $q\bar{q}l^+l^-$ Channel	109
7.3.5	The $l^+l^-\nu\bar{\nu}$ Channel	110
7.3.6	The $l^+l^-l^+l^-$ Channel	111
7.4	Measurement of the ZZ Cross Section	111
7.5	Study of Systematic Errors	113
7.6	Measurement of the $ZZ \rightarrow b\bar{b}X$ Cross Section	114
7.7	Anomalous Couplings	116
7.8	The L3 Combination	118
7.9	The LEP-wide Combination	118

8	Conclusions	121
8.1	Higgs Searches	121
8.2	ZZ Production	122
8.3	The Phantom of LEP?	122
8.4	Life After LEP	123
A	Beam Spot Size Determination	127
	Bibliography	131
	Acknowledgements	139

Chapter 1

Introduction

The topics that particle physicists study have changed as the understanding became deeper, but the final goal behind this progression has remained the same - the attempt to understand how the universe came into being.

Particle physics tries to answer the questions about the origin of our universe by studying the objects that are regarded as being fundamental and the ways in which they interact.

It started from the simplest blocks of matter - electron and nucleus and have gone further and further in the search for the more fundamental components, which today are regarded as leptons and quarks. Theories have been developed to structure all the knowledge obtained from the experimental observations and to make further predictions for future experiments to investigate.

The contemporary version of elementary particle physics, the so-called “Standard Model”, encompasses the progress that has been made in the past half-century in the understanding of three major interactions mediated by vector bosons - the weak, electromagnetic, and strong, starting from a fundamental principle, which is the requirement to conserve certain physical quantities in space and time.

Despite the enormous success of the Standard Model the exact mechanism by which the masses of the weakly-interacting vector bosons and the fermions are generated remains uncertain. One solution of this crucial aspect of the theory is introducing a scalar Higgs field which manifests itself in one physical particle - the Higgs boson.

The search for the Higgs boson has become the holy grail of all particle accelerators. The discovery of the Higgs boson would complete the Standard Model.

In this thesis, Chapter 2 will introduce the Standard Model of electroweak interactions and, in particular, the Higgs boson. Chapter 3 describes the Large Electron Positron Collider (LEP) at the European Centre for Particle Physics (CERN), Geneva and the L3 detector, which were constructed to measure electroweak interactions up to the centre-of-mass energy of about 200 GeV. Searches for the Standard Model Higgs boson were described in the Chapter 5. The search is performed in several search channels based on four distinct event topologies: $HZ \rightarrow q\bar{q}q\bar{q}$, $HZ \rightarrow q\bar{q}\nu\bar{\nu}$, $HZ \rightarrow q\bar{q}l^+l^-$ ($l = e, \mu, \tau$) and $HZ \rightarrow \tau^+\tau^-q\bar{q}$. With the exception of the $HZ \rightarrow \tau^+\tau^-q\bar{q}$ decay mode, all the analyses are optimised for the $H \rightarrow b\bar{b}$ decay. This mode represents about 80% of the Higgs branching fraction in the mass range of interest. The results from the different

channels are then combined for the final consideration along the results from the three other LEP experiments.

The high energy of the LEP accelerator allowed the study of gauge boson pair production. In the process $e^+e^- \rightarrow W^+W^-$ triple gauge boson couplings, a phenomenon of non-Abelian symmetries, are predicted by the Standard Model. The process $e^+e^- \rightarrow ZZ$, where triple gauge boson couplings are forbidden in the Standard Model, is for the first time accessible at LEP.

The thesis is complemented with a cross section measurement of the process $e^+e^- \rightarrow ZZ$. The pair production of Z boson is tested for the existence of the triple gauge boson couplings, ZZZ and $ZZ\gamma$. The results are in agreement with the Standard Model. Limits on the values of CP conserving and CP violating triple gauge boson couplings are given. As for the search of the SM Higgs boson, the analyses cover all possible decays channels.

Moreover, the ZZ final state is of particular interest as it constitutes an irreducible background for the search of the Standard Model Higgs boson.

The author of this thesis performed an analysis for the search of the Higgs boson in the SM in the four-jet channel using the data of the years 1999 and 2000. Since the results from the year 2000 supersede the ones from 1999 the only first ones are given. The measurement of the ZZ cross section was done for the four-jet topology using the data from 2000. Furthermore, the author has developed the new resolution functions for the error matrix parametrisation which is used in the kinematic fit, based on the study of two-jet events; performed tests and cross-checks for proving the significance of the Higgs boson candidate observed in $H\nu\bar{\nu}$ channel with the highest signal over background ratio .

Chapter 2

The Theory

*An idea is not responsible for
the people who believe in it.*

Theoretical physics is the instrument to structure physical objects and interactions between them, to understand and explain experimental observations in a large scope and to make hypotheses and predictions to be tested by experiments. Each theory can be evaluated by the range of its validity and accuracy in describing experimental facts.

2.1 The Standard Model

The Standard Model [1] describes strong and electroweak interactions starting from a fundamental principle, which is the requirement to conserve certain physical quantities in space and time.

The electroweak Standard Model established by Glashow, Salam and Weinberg [2] is an example of a relativistic gauge field theory. Quantum theory of strong interactions is denoted as Quantum Chromodynamics (QCD) [3] and based on the SU(3) color group.

The electroweak Standard Model is a non-Abelian theory based on the SU(2) \times U(1) group. The generators of the group are the three components of the weak isospin \vec{T} and the hypercharge Y. They are related to the electromagnetic charge in the following way:

$$Q = T_3 + Y. \quad (2.1)$$

Parity violation is introduced by grouping left-handed and right-handed particles in different weak isospin multiplets. Left-handed fermions are grouped in doublets whereas right-handed fermions are singlets. Table 2.1 summarises the fermions of the Standard Model.

2.1.1 Gauge Field Theory

A successful concept in describing the interactions of elementary particles is given by gauge theories. Gauge theories are guided by the idea of symmetry. Requiring the invariance of physical properties under local gauge transformations naturally introduces the

Fermions	Generation			Isospin T_3	Hypercharge Y	EM Charge Q
	1	2	3			
Leptons	$\begin{pmatrix} \nu_e \\ e \end{pmatrix}_L$	$\begin{pmatrix} \nu_\mu \\ \mu \end{pmatrix}_L$	$\begin{pmatrix} \nu_\tau \\ \tau \end{pmatrix}_L$	1/2	-1/2	0
	e_R	μ_R	τ_R	-1/2	-1/2	-1
				0	-1	-1
Quarks	$\begin{pmatrix} u \\ d' \end{pmatrix}_L$	$\begin{pmatrix} c \\ s' \end{pmatrix}_L$	$\begin{pmatrix} t \\ b' \end{pmatrix}_L$	1/2	1/6	2/3
	u_R	c_R	t_R	-1/2	1/6	-1/3
				0	2/3	2/3
	d_R	s_R	b_R	0	-1/3	-1/3

Table 2.1: Multiplet and quantum number assignments for the fermions in the Standard Model. The prime indicates that the weak eigenstates of the quarks are not their mass eigenstates. The quark mixing is described by the Cabibbo-Kobayashi-Maskawa matrix [4]. The indices $L(R)$ denote left(right)-handed fermions.

interaction of fermions (Spin $-\frac{1}{2}$ particles) by the exchange of gauge bosons (Spin -1 particles). Let us briefly discuss some examples of gauge symmetries.

Global Abelian Symmetry U(1)

The simplest example [5] is a global gauge symmetry leading to charge conservation. It is expressed as the invariance of the Lagrangian with respect to transformations of the type:

$$\begin{aligned}\Psi &\rightarrow \Psi' = e^{i\eta e}\Psi, \\ \bar{\Psi} &\rightarrow \bar{\Psi}' = \bar{\Psi}e^{-i\eta e}\end{aligned}$$

where e is the charge of the particle described by the field Ψ and η is an arbitrary number independent of space-time coordinates of the particle. Not only the electric charge, e , but other charges as well (baryonic charge B , leptonic charge L , etc.) may play the part of the above charge. The group of these phase transformations is called U(1).

Various transformations of the group U(1) commute. Such groups are called Abelian. If the parameter η is independent of spatial coordinates and time, the group is called global.

Gauge Transformations

In particle physics, the idea of gauge invariance has been elevated to a requirement for a field theory to be considered viable. In contrast to the previous example, we require now local gauge invariance, which means that η is a function of the space x , and in Quantum Electrodynamics (QED) the Lagrangian, \mathcal{L} , for an electron field (with charge e), $\Psi(x)$ must be invariant under a transformation of the type:

$$\Psi(x) \rightarrow \Psi'(x) = e^{-i\eta(x)e}\Psi(x), \quad (2.2)$$

The Lagrangian:

$$\mathcal{L} = \bar{\Psi}\gamma^\mu iD_\mu\Psi(x) - m\bar{\Psi}\Psi - \frac{1}{4}F_{\mu\nu}F^{\mu\nu}, \quad (2.3)$$

with

$$\begin{aligned} F_{\mu\nu} &= \partial_\nu A_\mu - \partial_\mu A_\nu \quad \text{and} \\ D_\mu &= (\partial_\mu + ieA_\mu), \end{aligned}$$

will stay the same. This is obtained by adding to the differential operator ∂_μ a vector field A_μ , which is identified with the photon. Indeed, the relevant terms transform as:

$$\begin{aligned} \Psi(x) &\rightarrow e^{-i\eta(x)e}\Psi(x) \\ \bar{\Psi}(x) &\rightarrow \bar{\Psi}(x)e^{i\eta(x)e} \\ A_\mu &\rightarrow A_\mu + \partial_\mu\eta(x) \\ D_\mu\Psi(x) &\rightarrow e^{-i\eta(x)e}D_\mu\Psi(x) \\ F_{\mu\nu} &\rightarrow F_{\mu\nu}. \end{aligned} \quad (2.4)$$

It is also clearly seen that the mass term for the photon, $\frac{1}{2}m_\gamma^2 A^\mu A_\mu$, would not leave \mathcal{L} invariant, since

$$A_\mu A^\mu \rightarrow A_\mu A^\mu + 2A_\mu \partial^\mu \eta(x) + \partial_\mu \eta(x) \partial^\mu \eta(x). \quad (2.5)$$

So, if we require the Lagrangian to be gauge invariant, then the photon must remain massless.

2.1.2 Lagrangian for Strong, Weak and Electromagnetic Forces

Now we will try to construct a Lagrangian that incorporates the interactions and properties of all known fundamental particles.

Each of the three generations, listed in Table 2.1, has a color $SU(3)_C$ triplet of quarks, q :

$$q = \begin{pmatrix} q^{\text{red}} \\ q^{\text{green}} \\ q^{\text{blue}} \end{pmatrix}, \quad (2.6)$$

a left-handed $SU(2)_L$ lepton and quark doublets, l_L and q_L^c ,

$$l_L = \begin{pmatrix} \nu \\ e \end{pmatrix}_L \quad \text{and} \quad q_L^c = \begin{pmatrix} u^c \\ d^c \end{pmatrix}_L \quad (2.7)$$

where c stands for *red*, *green*, *blue*, and corresponding right-handed singlets, e_R , u_R^c and d_R^c . The three forces carrying bosons are represented by the hypercharge field, B_μ ; the three component weak field, W_μ^i (where $i = 1, 2, 3$); and the eight component strong color field, c_μ^j (where $j = 1, 2, \dots, 8$).

The product of the three symmetries of the Standard Model, $SU(3)_C \otimes SU(2)_L \otimes U(1)_Y$, requires us to redefine the derivative operator ∂_μ such that we can make gauge invariant interaction terms:

$$D_\mu = \partial_\mu + i\frac{g}{2}\tau^i W_\mu^i + ig'YB_\mu + i\frac{g''}{2}\lambda^j G_\mu^j \quad (2.8)$$

where g, g', g'' and τ^i, Y, λ^j are the coupling constants and generators of the $SU(2)_L, U(1)_Y$ and $SU(3)_C$ gauge groups, respectively. The matrices τ^i and λ^j correspond to the three Pauli spin matrices¹ and the eight Gell-Mann matrices. By definition, if a particle lacks the charge of a given group, then the term corresponding to this group in D_μ disappears. As an example, for the leptons with no color charge the last term in D_μ is zero when D_μ is contracted with a lepton field.

So, this part of the Standard Model Lagrangian which does not contain any scalar field can be expressed in a following way:

$$\begin{aligned}
\mathcal{L} = & - \frac{1}{4} B_{\mu\nu}^i B^{i\mu\nu} - \frac{1}{4} W_{\mu\nu} W^{\mu\nu} & \left\{ \begin{array}{l} \text{W and B} \\ \text{kinetic energy} \\ \text{and self-interaction} \end{array} \right. \\
& - \frac{1}{2} G_{\mu\nu}^i G^{i\mu\nu} & \left\{ \begin{array}{l} \text{gluon kinetic energy} \\ \text{and self-interaction} \end{array} \right. \\
& + \bar{l}_L i \gamma^\mu D_\mu l_L + \bar{q}_L^c i \gamma^\mu D_\mu q_L^c & \left\{ \begin{array}{l} \text{left-handed electro-weak} \\ \text{currents for leptons} \\ \text{and quarks; gluon-quark} \\ \text{interaction} \end{array} \right. \\
& + \bar{e}_R i \gamma^\mu D_\mu e_R + \bar{u}_R^c i \gamma^\mu D_\mu u_R^c + \bar{d}_R^c i \gamma^\mu D_\mu d_R^c & \left\{ \begin{array}{l} \text{right-handed electro-weak} \\ \text{currents for leptons} \\ \text{and quarks; gluon-quark} \\ \text{interaction} \end{array} \right. \quad (2.9)
\end{aligned}$$

where the antisymmetric field tensors, $F_{\mu\nu}^i, G_{\mu\nu}^j$, and $H_{\mu\nu}^k$, are

$$\begin{aligned}
W_{\mu\nu}^i &= \partial_\nu W_\mu^i - \partial_\mu W_\nu^i + g \epsilon^{jki} W_\mu^j W_\nu^k \\
B_{\mu\nu} &= \partial_\nu B_\mu - \partial_\mu B_\nu \\
G_{\mu\nu}^j &= \partial_\nu G_\mu^j - \partial_\mu G_\nu^j + g'' f^{klj} G_\mu^k G_\nu^l
\end{aligned} \quad (2.10)$$

and ϵ^{ijk} is a completely antisymmetric Levi-Cevita symbol and f^{jkl} are the antisymmetric structure constants of $SU(3)$. The terms $g \epsilon^{jki} W_\mu^j W_\nu^k$ and $g'' f^{klj} G_\mu^k G_\nu^l$ predicts self-coupling of gauge bosons which is a feature on non-Abelian gauge groups. There are no terms corresponding to the weak vector boson masses since they would be of the form $m^2 W_\mu W^\mu$ and would not transform into themselves under local $SU(2)_L$ rotations, $e^{-\frac{1}{2} \tau^i \eta^i(x)}$. There are also no fermion mass terms because they would be of the form $-m \bar{\Psi} \Psi$ and would also break the $SU(2)_L$ invariance. Thus all the particles must be massless in order to ensure Equation 2.9 to be gauge invariant. This is in direct conflict with the observations, so we have to introduce the so-called Higgs mechanism, which we describe in detail in the next Section.

¹The non-commuting Pauli spin matrixes have the following form:

$$\tau^1 = \begin{pmatrix} 0 & 1 \\ 1 & 0 \end{pmatrix}, \tau^2 = \begin{pmatrix} 0 & -i \\ i & 0 \end{pmatrix}, \tau^3 = \begin{pmatrix} 1 & 0 \\ 0 & -1 \end{pmatrix}.$$

2.2 The Higgs Mechanism

2.2.1 Abelian Higgs Model

The central question of electroweak theory is: “How keep the Lagrangian \mathcal{L} gauge invariant with massive gauge bosons?” The measured values, $m_W = 80$ GeV and $m_Z = 91$ GeV, are far from zero and cannot be considered as small effects. To see that this is a problem, we consider a U(1) gauge theory with a single gauge field, the photon. The Lagrangian is [6]

$$\mathcal{L} = -\frac{1}{4}F_{\mu\nu}F^{\mu\nu}, \quad (2.11)$$

where

$$F_{\mu\nu} = \partial_\nu A_\mu - \partial_\mu A_\nu. \quad (2.12)$$

As it was discussed in a previous Section, local U(1) gauge invariance requires that the Lagrangian is invariant under the transformation:

$$A_\mu(x) \rightarrow A_\mu(x) - \partial_\mu \eta(x) \quad (2.13)$$

for any η and x . Suppose we now add a mass term for the photon to the Lagrangian,

$$\mathcal{L} = -\frac{1}{4}F_{\mu\nu}F^{\mu\nu} + \frac{1}{2}m^2 A_\mu A^\mu. \quad (2.14)$$

It is easy to see that the mass term violates the local gauge invariance. It is thus the U(1) gauge invariance which requires the photon to be massless.

Now we can extend the model by adding a single complex scalar field with charge $-e$ which couples to the photon. The Lagrangian is now,

$$\mathcal{L} = -\frac{1}{4}F_{\mu\nu}F^{\mu\nu} + |D_\mu \phi|^2 - V(\phi), \quad (2.15)$$

where

$$\begin{aligned} D_\mu &= \partial_\mu - ieA_\mu \\ V(\phi) &= \mu^2 |\phi|^2 + \lambda(|\phi|^2)^2. \end{aligned} \quad (2.16)$$

$V(\phi)$ is the most general renormalizable potential allowed by the U(1) gauge invariance.

This Lagrangian is invariant under global U(1) rotations, $\phi \rightarrow e^{i\theta}\phi$, and also under local gauge transformations:

$$\begin{aligned} A_\mu(x) &\rightarrow A_\mu(x) - \partial_\mu \eta(x) \\ \phi(x) &\rightarrow e^{ie\eta(x)}\phi(x). \end{aligned} \quad (2.17)$$

There are now two possibilities for the theory. If $\mu^2 > 0$ the potential has the shape shown in Figure 2.1. and preserves the symmetries of the Lagrangian. The state of lowest energy is that with $\phi = 0$, the vacuum state. The theory is simply quantum electrodynamics with a massless photon and a charged scalar field ϕ with mass μ .

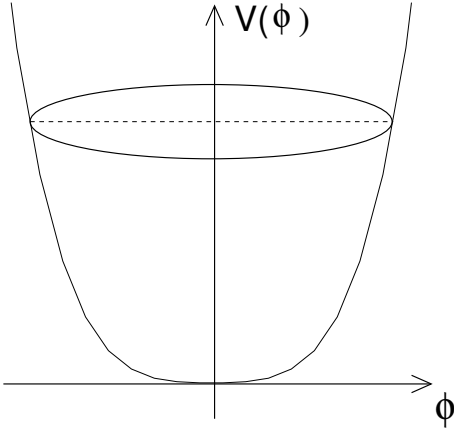


Figure 2.1: Scalar potential with $\mu^2 > 0$.

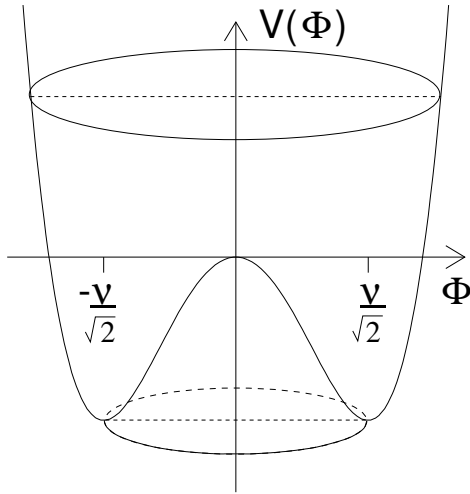


Figure 2.2: Scalar potential with $\mu^2 < 0$.

The alternative scenario is more interesting. In this case $\mu^2 < 0$ and the potential can be written as:

$$V(\phi) = -|\mu^2| |\phi|^2 + \lambda(|\phi|^2)^2, \quad (2.18)$$

which has so-called “Mexican hat” shape shown in Figure 2.2. In this case the minimum energy state is not at $\phi = 0$ but at

$$\langle \phi \rangle = \sqrt{-\frac{\mu^2}{2\lambda}} \equiv \frac{v}{\sqrt{2}}. \quad (2.19)$$

$\langle \phi \rangle$ is called the vacuum expectation value (VEV) of ϕ . Note that the direction in which the vacuum is chosen is arbitrary, but it is conventional to choose it to lie at the real part of ϕ . The VEV then clearly breaks the global U(1) symmetry.

It is convenient to rewrite ϕ as

$$\phi \equiv \frac{1}{\sqrt{2}} e^{i\frac{\chi}{v}} (v + h) \quad (2.20)$$

where χ and h are real fields with VEVs equal zero. If we substitute this expression back into the original Lagrangian, the interactions in terms of the fields with VEVs equal to zero can be found,

$$\begin{aligned} \mathcal{L} = & - \frac{1}{4} F_{\mu\nu} F^{\mu\nu} - ev A_m \partial^\mu \chi + \frac{e^2 v^2}{2} A_\mu A^\mu \\ & + \frac{1}{2} \left(\partial_\mu h \partial^\mu h + 2\mu^2 h^2 \right) + \frac{1}{2} \partial_\mu \chi \partial^\mu \chi \\ & + (\text{h, } \chi \text{ interactions}). \end{aligned} \quad (2.21)$$

This equation describes a theory with a photon of mass $m_A = ev$, a scalar field h with mass-squared $-2\mu^2 > 0$, and a massless scalar field χ . The mixed χ - A coupling is confusing, however. This term can be removed by making a gauge transformation:

$$A'_\mu \equiv A_\mu - \frac{1}{ev} \partial_\mu \chi. \quad (2.22)$$

After performing such gauge transformation the χ field disappears from the theory and we say that it has been “eaten” to give the photon mass. This is called the Higgs mechanism and the χ field is called a Goldstone boson [7]. In the gauge of Equation 2.22 the particle content of the theory is a massive photon and a scalar field h with mass m_H , which we call a Higgs boson.

The Higgs mechanism can be summarised by saying that the spontaneous breaking of a gauge symmetry by a non-zero VEV results in the appearance of a scalar particle, the Higgs boson, a mass term of the vector field A and in the disappearance of a Goldstone boson and its transformation into the longitudinal polarisation component [8] of a massive gauge boson.

2.2.2 Higgs Mechanism in the Standard Model

It is now straightforward to obtain the Weinberg-Salam model of electroweak interactions [2]. The Weinberg-Salam model is an $SU(2)_L \times U(1)_Y$ gauge theory containing three $SU(2)_L$ gauge bosons, $W_\mu^i, i = 1, 2, 3$, and one $U(1)_Y$ gauge boson, B_μ , with kinetic energy terms, given in Eqn. 2.9. Coupled to the gauge fields is a complex scalar $SU(2)$ doublet, Φ ,

$$\Phi = \begin{pmatrix} \phi^+ \\ \phi^0 \end{pmatrix} \quad (2.23)$$

with a scalar potential given by

$$V(\Phi) = \mu^2 |\Phi^\dagger \Phi| + \lambda \left(|\Phi^\dagger \Phi| \right)^2, \quad (2.24)$$

with $\lambda > 0$. This is the most general renormalizable and $SU(2)_L$ invariant potential allowed.

Just as in the Abelian model in the previous section, the state of minimum energy for $\mu^2 < 0$ is not at $\Phi = 0$ and the scalar field has a non-zero VEV. The direction of

the minimum in $SU(2)_L$ space is not determined since the potential depends only on the combination $\Phi^\dagger\Phi$, and we arbitrarily choose

$$\langle \Phi \rangle = \frac{1}{\sqrt{2}} \begin{pmatrix} 0 \\ v \end{pmatrix}. \quad (2.25)$$

With this choice the scalar doublet has $U(1)_Y$ charge, $Y_\Phi = 1$ and the electromagnetic charge, as given in Eqn. 2.1. Therefore,

$$Q \langle \Phi \rangle = 0. \quad (2.26)$$

Electromagnetism, described by a subgroup of

$$SU(2)_L \times U(1)_Y \rightarrow U(1)_{EM}, \quad (2.27)$$

is unbroken by the scalar VEV.

It is now straightforward to see how the Higgs mechanism generates masses for the W and Z gauge bosons in the same fashion as a mass was generated for the photon in the Abelian Higgs model of the previous section. The contribution of the scalar doublet to the Lagrangian is,

$$\mathcal{L}_s = (D^\mu \Phi)^\dagger (D_\mu \Phi) - V(\Phi) \quad (2.28)$$

where

$$D_\mu = \partial_\mu + i\frac{g}{2}\tau \cdot W_\mu + i\frac{g'}{2}B_\mu Y. \quad (2.29)$$

In unitary gauge there are no Goldstone bosons and only the physical Higgs scalar remains in the spectrum after the spontaneous symmetry breaking has occurred. Therefore the scalar doublet in unitary gauge can be written as

$$\langle \Phi' \rangle = \frac{1}{\sqrt{2}} \begin{pmatrix} 0 \\ v + h \end{pmatrix}. \quad (2.30)$$

which gives the contribution to the gauge boson masses from the scalar kinetic energy term of Equation 2.28,

$$\frac{1}{2}(0, v) \left(\frac{1}{2}g\tau \cdot W_\mu + \frac{1}{2}g'B_\mu \right)^2 \begin{pmatrix} 0 \\ v \end{pmatrix}. \quad (2.31)$$

The physical gauge fields are then two charged fields, W^\pm , and two neutral gauge bosons, Z and γ , obtained as:

$$\begin{aligned} W_\mu^\pm &= \frac{1}{\sqrt{2}}(W_\mu^1 \mp iW_\mu^2) \\ Z^\mu &= \frac{-g'B_\mu + gW_\mu^3}{\sqrt{g^2 + g'^2}} \\ A^\mu &= \frac{gB_\mu + g'W_\mu^3}{\sqrt{g^2 + g'^2}}. \end{aligned} \quad (2.32)$$

The gauge bosons obtain masses from the Eqn. 2.31:

$$\begin{aligned} m_W^2 &= \frac{1}{4}g^2v^2 \\ m_Z^2 &= \frac{1}{4}(g^2 + g'^2)v^2 \\ m_A &= 0. \end{aligned} \tag{2.33}$$

Since the massless photon must couple with electromagnetic charge, e , the coupling constants define the weak mixing angle θ_W ,

$$\begin{aligned} e &= g \sin \theta_W \\ e &= g' \cos \theta_W. \end{aligned} \tag{2.34}$$

Again, it is instructive to count the degrees of freedom after the spontaneous symmetry breaking has occurred. We began with a complex scalar $SU(2)_L$ doublet Φ with four degrees of freedom, a massless $SU(2)_L$ gauge field, W_i , with six degrees of freedom and a massless $U(1)_Y$ gauge field, B , with two degrees of freedom, a total of 12. After the spontaneous symmetry breaking there remains a physical real scalar field h with one degree of freedom, massive W and Z fields with nine degrees of freedom, and a massless photon - two degrees of freedom. We say that the scalar degrees of freedom have been “eaten” to give the W^\pm and Z gauge bosons their longitudinal polarisation components.

Fermion Masses

The $SU(2)$ Higgs doublet can also be used to give the fermions mass. The gauge invariant Yukawa coupling to the Higgs boson to the *up* and *down* quarks is:

$$\mathcal{L}_d = -\lambda_d \bar{q}_L \Phi d_R + \text{h.c.}, \tag{2.35}$$

where q_L is $SU(2)_L$ doublet. This gives the effective coupling

$$-\lambda_d \frac{1}{\sqrt{2}} (\bar{u}_L, \bar{d}_L) \begin{pmatrix} 0 \\ v + h \end{pmatrix} d_R + \text{h.c.} \tag{2.36}$$

which can be seen to yield a mass term for the *down* quark if we make the identification:

$$\lambda_d = \frac{m_d \sqrt{2}}{v} \tag{2.37}$$

In order to generate a mass term for the *up* quark we use the fact that $\Phi^c \equiv -i\tau_2 \Phi^*$ is an $SU(2)_L$ doublet and we can write the $SU(2)_L$ invariant coupling

$$\mathcal{L}_u = -\lambda_u \bar{q}_L \Phi^c u_R + \text{h.c.}, \tag{2.38}$$

which generates a mass term for the *up* quark. Similar expressions can be used to generate mass terms for the charged leptons. Since the neutrino has no right-handed partner, it remains massless.

For the multi-family case, the Yukawa couplings, λ_d and λ_u , become $N_F \times N_F$ matrices (where N_F is the number of families). Since the fermion mass matrices and Yukawa matrices are proportional, the interactions of the Higgs boson with the fermion mass eigenstates are flavour diagonal and the Higgs boson does not mediate flavour changing interactions.

Determination of the Vacuum Expectation Value

The parameter v can be estimated from the μ decay, $\mu \rightarrow e\bar{\nu}_e\nu_\mu$, illustrated in Figure 2.3. The interaction strength of the muon decay in the Fermi theory is measured very

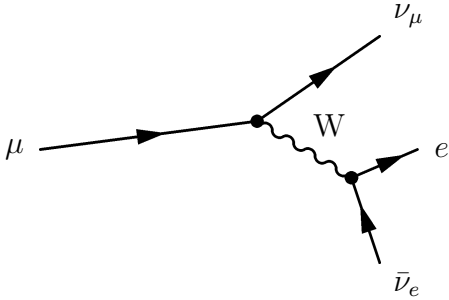


Figure 2.3: The Feynman diagram for the decay of the muon.

accurately to be $G_F = 1.16639 \times 10^{-5} \text{ GeV}^{-2}$ and can be used to determine v . Since the momentum carried by the W boson is of order m_μ it can be neglected in comparison with m_W and we make the identification

$$\frac{G_F}{\sqrt{2}} = \frac{g^2}{8m_W^2} = \frac{1}{2v^2} \quad (2.39)$$

which gives the result

$$v = (\sqrt{2}G_F)^{-1/2} = 246 \text{ GeV}. \quad (2.40)$$

The couplings of the Higgs boson to fermions and gauge bosons are completely determined in terms of coupling constants and fermion masses. The potential of Equation 2.24 had two parameters, μ and λ . We can trade these for:

$$\begin{aligned} v^2 &= -\frac{\mu^2}{2\lambda} \\ m_H^2 &= 2v^2\lambda \end{aligned} \quad (2.41)$$

There are no remaining adjustable parameters and so Higgs production and decay can be computed unambiguously in terms of the Higgs mass alone.

2.2.3 Problems with the Higgs Mechanism

Many theorists firmly believe that the Higgs mechanism cannot be the entire story behind electroweak symmetry breaking. The basic reasons are:

- The Higgs sector of the theory is trivial ($\lambda \rightarrow 0$ as the energy scale $\rightarrow \infty$ unless the Higgs mass is in a very restricted range [8]).
- The Higgs mechanism doesn't explain why $v = 246 \text{ GeV}$.
- The Higgs mechanism doesn't explain why fermions have the masses they do.
- Loop corrections involving the Higgs boson are quadratically divergent and counter-terms must be adjusted order by order in perturbation theory to cancel these divergences. This fine tuning is considered by most theorists to be unnatural.

The most compelling argument against the simplest version of the Standard Model is the quadratically divergent contributions to the Higgs boson mass which arise when loop corrections are computed [8]. At one loop, the quartic self-interactions to the Higgs boson generate a quadratically divergent contribution to the Higgs boson mass which must be cancelled by a mass counterterm. This counterterm must be fine tuned at each order in perturbation theory.

In light of the many objections to the simplest version of the Higgs mechanism several alternatives were considered. One proposal is that the electroweak symmetry be broken dynamically by a mechanism such as technicolor has been widely discussed [9]. Another alternative to the standard model Higgs mechanism is that the Standard Model becomes supersymmetric. The electroweak symmetry is still broken by the Higgs mechanism, but the quadratic divergences in the scalar sector are cancelled automatically because of the expanded particle spectrum of the theory and so the model is no longer considered to be unnatural. In this thesis the phenomenology of the Higgs boson occurring in supersymmetric models will not be discussed. The theoretical underpinning of supersymmetric models has been presented in details by Ramond [10].

2.3 Restrictions on Higgs Boson Masses

In this section restrictions on the mass ranges of the Higgs bosons resulting from general theoretical considerations and precision measurements of electroweak parameters are discussed.

2.3.1 Theoretical Bounds on the Higgs Boson Mass

In this section we discuss some theoretical constraints on the Higgs boson mass. These constraints can often be evaded by postulating the existence of some new physics which enters into the theory at a mass scale above that of current experiments, but below the Planck scale, $M_P = \sqrt{1/G_N} \sim 10^{19}$ GeV where $G_N \sim 10^{-38}$ GeV⁻² is the gravitational constant. Assuming the Standard Model to be valid up to the Planck scale both upper and lower bounds on the Higgs boson mass can be derived.

Triviality

Bounds on the Higgs boson mass have been deduced on the grounds of triviality [11], [12]. The basic argument goes as follows: Consider a pure scalar theory in which the potential is given by

$$V(\Phi) = \mu^2 |\Phi^\dagger \Phi| + \lambda (|\Phi^\dagger \Phi|)^2, \quad (2.42)$$

where the quartic coupling is

$$\lambda = \frac{m_H^2}{2v^2}. \quad (2.43)$$

This is the scalar sector of the Standard Model with no gauge bosons or fermions. The quartic coupling, λ , changes with the effective energy scale Q due to the self interactions

to the scalar field:

$$\frac{d\lambda}{dt} = \frac{3\lambda^2}{4\pi^2} \quad (2.44)$$

where $t \equiv \log(Q^2/Q_0^2)$ and Q_0 is some reference scale (which is often taken to be v in the Standard Model). Equation 2.44 is solved, as:

$$\begin{aligned} \frac{1}{\lambda(Q)} &= \frac{1}{\lambda(Q_0)} - \frac{3}{4\pi^2} \log\left(\frac{Q^2}{Q_0^2}\right) \\ \lambda(Q) &= \frac{\lambda(Q_0)}{\left[1 - \frac{3\lambda(Q_0)}{4\pi^2} \log\left(\frac{Q^2}{Q_0^2}\right)\right]}. \end{aligned} \quad (2.45)$$

Hence if we measure λ at some energy scale, we can predict what it will be at all other energy scales. From the last equation we see that $\lambda(Q)$ blows up as $Q \rightarrow \infty$ with $\lambda(Q_0)$ fixed and positive. This phenomenon is called the Landau pole. Regardless of how small $\lambda(Q_0)$ is, $\lambda(Q)$ will eventually become infinite at some large Q . Alternatively, $\lambda(Q) \rightarrow 0$ as $Q \rightarrow 0$ with $\lambda(Q_0) > 0$. Without the $\lambda\Phi^4$ term of Equation 2.42 the theory becomes a non-interacting theory at low energy, termed a *trivial* theory.

To obtain a bound on the Higgs mass we require the quartic coupling to be finite,

$$\frac{1}{\lambda(\Lambda)} > 0, \quad (2.46)$$

where Λ is some large scale where new physics enters in. Taking the reference scale $Q_0 = v$, and substituting Equation 2.43 gives an approximate upper bound on the Higgs mass,

$$m_H^2 < \frac{8\pi^2 v^2}{3 \cdot \log(\Lambda^2/v^2)}. \quad (2.47)$$

Requiring that there be no new physics below the GUT scale², 10^{16} GeV [8], yields the approximate upper bound on the Higgs boson mass,

$$m_H < 160 \text{ GeV}. \quad (2.48)$$

As the scale Λ becomes smaller, the limit on the Higgs mass becomes progressively weaker and for $\Lambda \sim 3$ TeV, the bound is roughly $m_H < 600$ GeV. This picture is valid only on the level of the one loop evolution equation 2.44. For large λ higher order or non-perturbative corrections to the evolution equation must be included [14].

Everything so far is for a theory with only scalars. The physics changes when we couple the theory to fermions and gauge bosons. Since the Higgs coupling to fermions is proportional to the Higgs boson mass, the most relevant fermion is the top quark. Including the top quark and the gauge bosons, Equation 2.44 becomes [15]:

$$\frac{d\lambda}{dt} = \frac{1}{16\pi^2} \left[12\lambda^2 + 6\lambda \cdot \lambda_t^2 - 3\lambda_t^4 - \frac{3}{2}\lambda(3g^2 + g'^2) + \frac{3}{16}(2g^4 + (g^2 + g'^2)^2) \right], \quad (2.49)$$

²Theoretical calculation and low energy measurements shows that at the energy scale $\sim 10^{14} \div 10^{16}$ the three gauge couplings approach each other, so this scale is considered as the starting point of the Grand Unification Theories (GUT) [13]

where λ_t is the top Yukawa coupling:

$$\lambda_t = \frac{m_t \sqrt{2}}{v} \quad (2.50)$$

and m_t is the mass of the top quark.

For a heavy Higgs boson, $\lambda > g_t, g, g'$, and the dominant contributions to the running of λ are:

$$\frac{d\lambda}{dt} = \frac{\lambda}{16\pi^2} \left[12\lambda + 6\lambda_t^2 - \frac{3}{2}(3g^2 + g'^2) \right]. \quad (2.51)$$

There is a critical value of the quartic coupling λ which depends on the top quark mass,

$$\lambda_c \equiv \frac{1}{8}(3g^2 + g'^2) - \frac{1}{2}\lambda_t^2. \quad (2.52)$$

The evolution of the quartic coupling “stops” when $\lambda = \lambda_c$ [16]. If $m_H > m_H^c \equiv \sqrt{2\lambda_c v}$ then the quartic coupling becomes infinite at some scale and the theory is non-perturbative. If we require that the theory be perturbative (i.e., the Higgs quartic coupling be finite) at all energy scales below some unification scale $\sim 10^{16}$ GeV then an upper bound on the Higgs mass is obtained as a function of the top quark mass. To get a numerical value from the Higgs mass limit, the evolution of the gauge coupling constants and the Higgs Yukawa coupling must also be included. For $m_t = 175$ GeV this bound is $m_H < 170$ GeV [16]. If a Higgs boson were found which is heavier than this bound, it would require that there be some new physics below the unification scale.

Vacuum Stability

A bound on the Higgs mass can also be derived by the requirement that spontaneous symmetry breaking actually occurs [17]; that is,

$$V(v) < V(0). \quad (2.53)$$

This bound is essentially equivalent to the requirement that λ remains positive at all scales Λ (if λ becomes negative, the potential is unbounded from below and has no state of minimum energy). For small λ , Equation 2.49 becomes,

$$\frac{d\lambda}{dt} = \frac{1}{16\pi^2} \left[-3\lambda_t^4 + \frac{3}{16}(2g^4 + (g^2 + g'^2)^2) \right]. \quad (2.54)$$

Solving this and requiring $\lambda(\Lambda) > 0$ gives the bound on the Higgs boson mass,

$$m_H^2 > \frac{v^2}{8\pi^2} \left[-3\lambda_t^4 - \frac{3}{16}(2g^4 + (g^2 + g'^2)^2) \right] \log \left(\frac{\Lambda^2}{v^2} \right). \quad (2.55)$$

A more careful analysis along the same line as above [18] using a 2 loop renormalization group improved effective potential³ and the running of all couplings yields, provided the Standard Model be valid up to scales of order 10^{16} GeV,

$$m_H > (130.5 + 2.1(m_t/\text{GeV} - 174))\text{GeV}. \quad (2.56)$$

³The renormalization group improved effective potential sums all potentially large logarithms, $\log(Q^2/v^2)$

If the standard Model is only valid up to 1 TeV the previous limit transfers to

$$m_H > (71 + .74(m_t/\text{GeV} - 174))\text{GeV}. \quad (2.57)$$

When λ is small (a light Higgs boson) radiative corrections from the top quark and gauge couplings become important and lead to a lower limit on the Higgs boson mass from the requirement of vacuum stability, $\lambda(\Lambda) > 0$. If λ is large (a heavy Higgs boson) then triviality arguments, ($\frac{1}{\lambda(\Lambda)} > 0$), lead to an upper bound on the Higgs mass. The allowed region for the Higgs mass from these considerations as a function of the scale of new physics, Λ is shown in Figure 2.4.

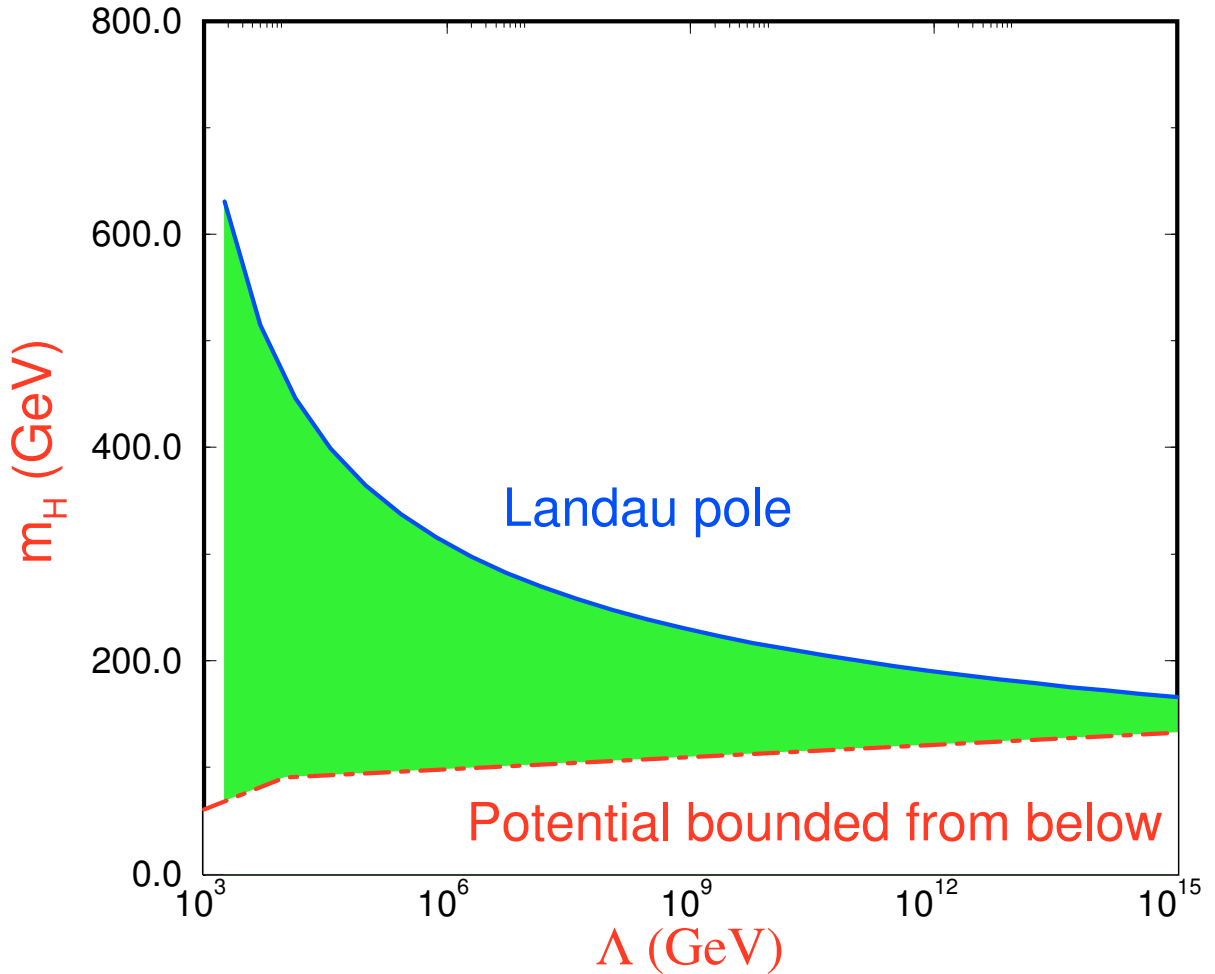


Figure 2.4: Theoretical limits on the Higgs boson mass as function of the energy scale. The allowed region is shaded. The region above the solid line (labelled Landau pole) is forbidden because the quartic coupling becomes infinite. The region below the dot-dash line is forbidden because the quartic coupling is negative, causing the potential to be unbounded from below.

If the Standard Model is valid up to 10^{16} GeV, then the allowed region for the Higgs boson is restricted to be between about 130 GeV and 170 GeV. A Higgs boson with a mass outside this region would be a signal for new physics.

2.3.2 Limits from Indirect Searches

The electroweak precision measurements performed at LEP and elsewhere can be used to estimate the SM Higgs boson mass. This is achieved by fitting the electroweak observables and taking radiative correction into account which describe the exchange of the virtual Higgs bosons as shown in Figure 2.5.

The radiative corrections exhibit a logarithmic dependence on the Higgs boson mass. Many observable quantities that are sensitive to the SM radiative corrections have been measured with high accuracy. The picture that emerges is summarised in Figure 2.5. The error on the fit is currently dominated by the uncertainty on $\alpha(m_Z^2)$ which arises from the uncertainty of the light quark contribution to the photon vacuum polarisation $\Delta_{\text{had}}^{(5)}(m_Z^2)$ [19]:

$$\alpha(m_Z^2) = \frac{\alpha(0)}{1 - \Delta\alpha_\ell(m_Z^2) - \Delta\alpha_{\text{had}}^{(5)}(m_Z^2) - \Delta\alpha_{\text{top}}(m_Z^2)} \quad (2.58)$$

A serious problem for the determination of $\Delta_{\text{had}}^{(5)}(m_Z^2)$ is the low energy contribution of the five light quarks u, d, s, c and b which cannot be reliably calculated using perturbative QCD. In a first approach, this is solved by an integration of the experimentally measured hadronic cross section of e^+e^- data. In a second approach, the cross section of the process $e^+e^- \rightarrow \text{hadrons}$ in non-resonant regions is parametrised using QCD predictions. In the low energy part, additional input from hadronic τ decays is used. If one fits now the

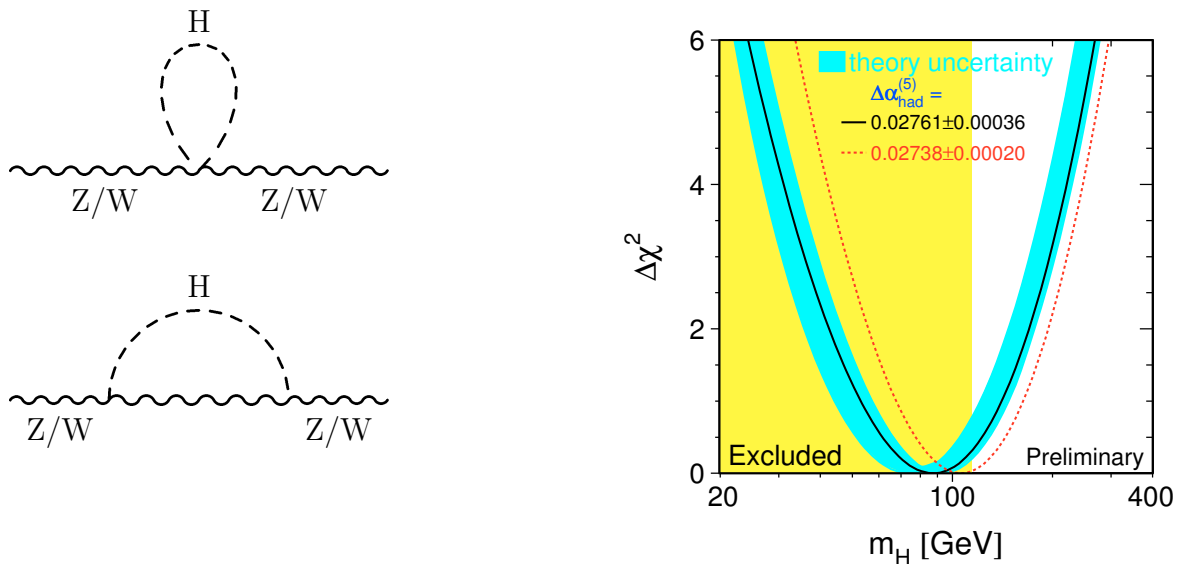


Figure 2.5: The Higgs enters via loop corrections (left) into the electroweak fits. The Higgs mass can be derived by fitting the electroweak observables measured at LEP and at other accelerators(right).

electroweak data measured by the experiments at LEP and by the SLD collaboration [20] combined with the measurements of m_W from UA2 [21], CDF [22] and D0 [23], the top

quark measurements from CDF [24] and D0 [25] and with the measurements of the neutrino-nucleon neutral to charged current ratios from CCFR and NuTeV [26], one obtains [27]:

$$m_H = 88_{-35}^{+53} \text{ GeV}. \quad (2.59)$$

This is graphically illustrated in Figure 2.5. The electroweak data clearly prefer a light Higgs which could be well in the reach of LEP. The one-sided upper limit at 95% confidence level is 196 GeV.

Clearly, despite of all the interesting estimates on the Higgs boson mass made by theorists or indirect mass limits derived from measurements using the Standard Model the direct measurement remains the most convincing step to confirm or to rule out the existence of the Higgs bosons.

2.3.3 Limits from Direct Searches

Before this thesis was started, there was a lower limit on the mass of the Standard Model Higgs boson of 95.2 GeV, which was obtained by the combination of the search results from the 4 LEP experiments [28] up to a centre-of-mass energy of 189⁴ GeV.

This limit is significantly higher than the lower limit on the Higgs boson mass from the theoretical predictions, given by Eqn. 2.57, assuming the SM validity only up to 1 TeV.

⁴The author of this thesis also participated in these data analysis.

2.4 Higgs Production at LEP

Since the Higgs boson coupling to the electron is very small, $\sim m_e/v$, the s-channel production mechanism, $e^+e^- \rightarrow H$, is minute and the dominant Higgs boson production mechanism in e^+e^- annihilations in the energy range of ~ 100 GeV is the associated production with Z, the so-called Higgs-strahlung, $e^+e^- \rightarrow Z^* \rightarrow HZ$, where the electron and the positron annihilate into a virtual Z boson which then emits a Higgs boson, as shown in Figure 2.6

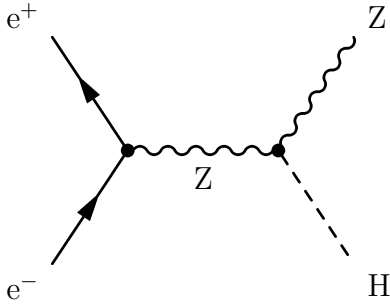


Figure 2.6: Higgs-strahlung: The Higgs Boson is produced together with a Z Boson

With increasing centre-of-mass energy two more diagrams start to contribute a sizable production rate, the WW and the ZZ fusion diagrams in Figure 2.7.

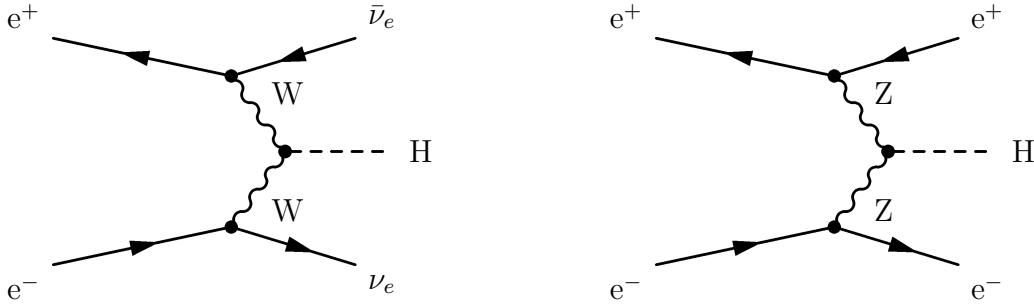


Figure 2.7: WW and ZZ fusion diagrams: They are suppressed by an additional power of the electroweak coupling with respect to the Higgs-strahlung process.

2.4.1 Cross sections

Higgs-strahlung

At LEP, the cross section of the process $e^+e^- \rightarrow HZ$, neglecting the width of the Z, is [29]:

$$\hat{\sigma}(e^+e^- \rightarrow HZ) = \frac{\pi\alpha^2\lambda_{HZ}^{1/2}[\lambda_{HZ} + 12\frac{m_Z^2}{s}][1 + (1 - 4\sin^2\theta_W)^2]}{192s\sin^4\theta_W\cos^4\theta_W(1 - m_Z^2/s)^2} \quad (2.60)$$

where

$$\lambda_{HZ} \equiv \left(1 - \frac{m_H^2 + m_Z^2}{s}\right)^2 - \frac{4m_H^2m_Z^2}{s^2}. \quad (2.61)$$

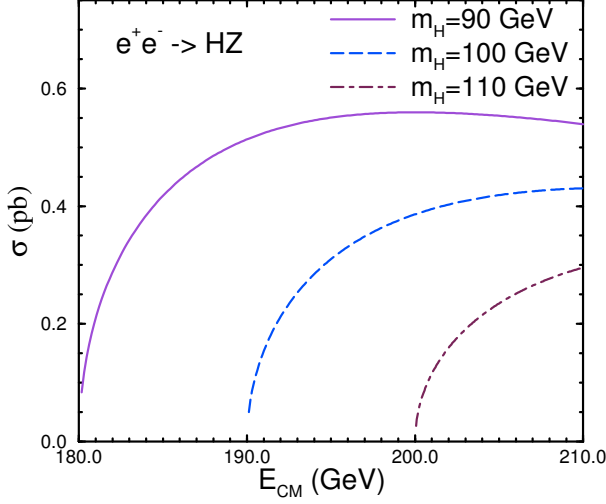


Figure 2.8: Born cross section for $e^+e^- \rightarrow HZ$ as a function of center of mass energy.

The cross section as a function of \sqrt{s} for the different values of the Higgs boson mass is shown in Figure 2.8. It is apparent that the cross section increases rapidly with increasing energy close to the threshold and so the best chance to find the Higgs boson is obtained at the energy just above the production threshold.

The angular distribution of the Higgs boson from the $e^+e^- \rightarrow HZ$ process is:

$$\frac{1}{\sigma} \frac{d\sigma}{d\cos\theta} \sim \lambda_{HZ}^2 \sin^2\theta + \frac{8m_Z^2}{s} \quad (2.62)$$

so that at high energy the distribution approaches

$$\frac{1}{\sigma} \frac{d\sigma}{d\cos\theta} \sim \sin^2\theta. \quad (2.63)$$

Higgs Boson Production from Vector Boson Fusion

At higher energies the W^+W^- and ZZ fusion processes become important:

$$\begin{aligned} e^+e^- &\rightarrow W^+W^- \nu\bar{\nu} \rightarrow H\nu\bar{\nu} \\ e^+e^- &\rightarrow ZZ e^+e^- \rightarrow He^+e^- \end{aligned} \quad (2.64)$$

These production channels give a small contributions to Higgs production at the present LEP energies because of the two W (or Z) boson propagators [30], [31].

The fusion cross sections are found [32] to be:

$$\begin{aligned} \sigma(e^+e^- \rightarrow VV \rightarrow \bar{l}lH) &= \frac{G_F^3 m_V^4}{64\sqrt{2}\pi^3} \int_{\frac{m_H^2}{s}}^1 dx \int_x^1 \frac{dy}{(1+s(y-x)/m_V^2)^2} \\ &\quad \left[(v_e^2 + a_e^2)^2 f(x,y) + 4v_e^2 a_e^2 g(x,y) \right] \end{aligned} \quad (2.65)$$

where

$$f(x,y) = \left(\frac{2x}{y^3} - \frac{1+2x}{y^2} + \frac{2+x}{2y} - \frac{1}{2} \right) \left(\frac{\omega}{1+\omega} - \log(1+\omega) \right)$$

$$\begin{aligned}
& + \frac{x \omega^2(1-y)}{y^2(1+\omega)} \\
g(x,y) &= \left(-\frac{x}{y^2} + \frac{2+x}{2y} - \frac{1}{2} \right) \left(\frac{\omega}{1+\omega} - \log(1+\omega) \right) \\
\omega &\equiv \frac{y(sx - m_H^2)}{m_V^2 x}.
\end{aligned} \tag{2.66}$$

and $v_e = a_e = \sqrt{2}$ for $e^+e^- \rightarrow W^+W^-\nu\bar{\nu} \rightarrow H\nu\bar{\nu}$ and $v_e = -1 + 4\sin^2\theta_W$, $a_e = -1$ for $e^+e^- \rightarrow ZZe^+e^- \rightarrow He^+e^-$. The vector boson fusion cross section as a function of \sqrt{s} are shown in Figure 2.9.

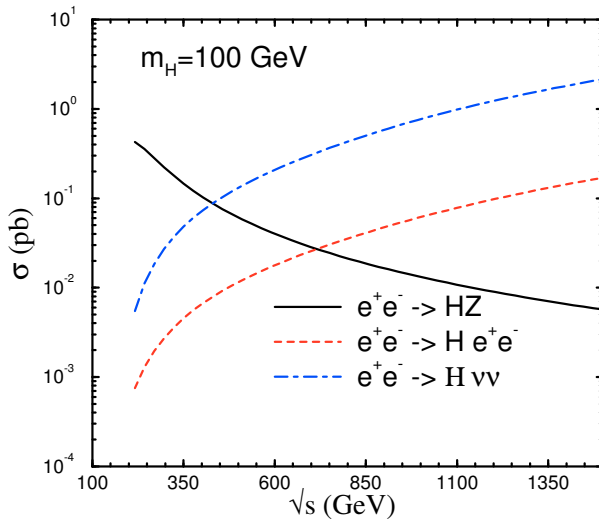


Figure 2.9: Higgs boson production in e^+e^- collisions as a function of center of mass energy for $m_H = 100$ GeV.

The ZZ fusion cross section is an order of magnitude smaller than the W^+W^- fusion process due to the smaller neutral current couplings. At center-of-mass energies covered by LEP the Higgs-strahlung is the dominant Higgs boson production mechanism, but at large \sqrt{s} the cross section for fusion starts to prevail and becomes dominant with the increasing of \sqrt{s} .

The cross section for the Higgs-strahlung and the fusion processes as a function of the Higgs boson mass at $\sqrt{s} = 206.6$ GeV, a typical center-of-mass energy of the last LEP running period, are both shown in Figure 2.10 where the width of the Z is taken into account.

2.4.2 Higgs Branching Fractions

In the Higgs sector, the Standard Model is extremely predictive, with all couplings, decay widths, and production cross sections given in terms of the unknown Higgs boson mass.

Decays to Fermion Pairs

The dominant decays of a Higgs boson with a mass below the W^+W^- threshold are into fermion-antifermion pairs. In the Born approximation, the width into charged lepton

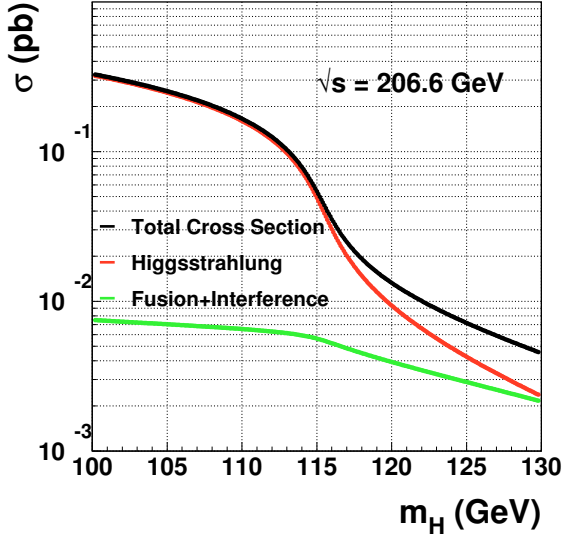


Figure 2.10: Higgs boson production cross section as a function of the Higgs boson mass at $\sqrt{s} = 206.6$ GeV. Interference between fusion and Higgsstrahlung processes was taken into account.

pairs is [8]:

$$\Gamma(H \rightarrow l^+l^-) = \frac{G_F m_l^2}{4\sqrt{2}\pi} m_H \beta_l^3 \quad (2.67)$$

where $\beta_l \equiv \sqrt{1 - 4m_l^2/m_H^2}$ is the velocity of the final state leptons. The Higgs boson decay into quarks is enhanced by the color factor $N_c = 3$ and also receives significant QCD corrections,

$$\Gamma(H \rightarrow q\bar{q}) = \frac{3G_F m_q^2}{4\sqrt{2}\pi} m_H \beta_q^3 \left(1 + \frac{4}{3} \frac{\alpha_s}{\pi} \Delta_H^{\text{QCD}} \right), \quad (2.68)$$

where the QCD correction factor, Δ_H^{QCD} , can be found in Reference [33]. The Higgs boson clearly decays predominantly into the heaviest fermion kinematically allowed.

The branching fractions for the dominant decays to fermion- antifermion pairs are shown in Figure 2.11.

The decrease in the $H \rightarrow f\bar{f}$ branching fractions at $m_H \sim 150$ GeV is due to the turn-on of the W^+W^{*-} decay channel, where W^* denotes a virtual W . For most of the region below the W^+W^- threshold, the Higgs decays almost entirely to $b\bar{b}$ pairs, although it is possible that the decays to $\tau^+\tau^-$ will be useful in the experimental searches.

Decays to Gauge Boson Pairs

The Higgs boson can also decay to gauge boson pairs. At tree level, the decays $H \rightarrow W^+W^-$ and $H \rightarrow ZZ$ are possible, while at one-loop level the decays $H \rightarrow gg, \gamma\gamma$ and $Z\gamma$ occur.

The decay widths of the Higgs boson to physical W^+W^- or ZZ pairs are given by [8]:

$$\Gamma(H \rightarrow W^+W^-) = \frac{G_F m_H^3}{8\pi\sqrt{2}} \sqrt{1 - r_W} \left(1 - r_W + \frac{3}{4} r_W^2 \right)$$

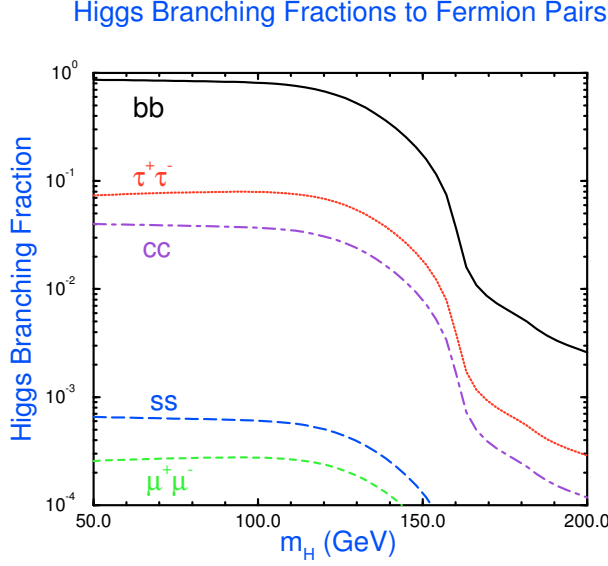


Figure 2.11: Branching fractions of the Standard Model Higgs boson to fermion-antifermion pairs, including QCD radiative corrections.

$$\Gamma(H \rightarrow ZZ) = \frac{G_F m_H^3}{16\pi\sqrt{2}} \sqrt{1 - r_Z} \left(1 - r_Z + \frac{3}{4} r_Z^2\right) \quad (2.69)$$

where $r_V \equiv 4m_V^2/m_H^2$.

Below the W^+W^- and ZZ thresholds, the Higgs boson can also decay to vector boson pairs VV^* , ($V = W^\pm, Z$), with one of the gauge bosons being off-shell. The widths, summed over all available channels for $V^* \rightarrow ff$ are [34]:

$$\begin{aligned} \Gamma(H \rightarrow ZZ^*) &= \frac{g^4 m_H}{2048(1 - s_W)^2 \pi^3} \left(7 - \frac{40}{3} s_W + \frac{160}{9} s_W^2\right) F\left(\frac{m_Z}{m_H}\right) \\ \Gamma(H \rightarrow WW^*) &= \frac{3g^4 m_H}{512\pi^2} F\left(\frac{m_W}{m_H}\right) \end{aligned} \quad (2.70)$$

where $s_W \equiv \sin^2 \theta_W$ and

$$\begin{aligned} F(x) \equiv & - |1 - x^2| \left(\frac{47}{2} x^2 - \frac{13}{2} + \frac{1}{x^2}\right) - 3(1 - 6x^2 + 4x^4) |\ln(x)| \\ & + 3 \frac{1 - 8x^2 + 20x^4}{\sqrt{4x^2 - 1}} \cos^{-1} \left(\frac{3x^2 - 1}{2x^3}\right). \end{aligned} \quad (2.71)$$

These widths can be significant when the Higgs boson mass approaches the real W^+W^- and ZZ thresholds. The WW^* and ZZ^* branching ratios grow rapidly with increasing Higgs mass and above $2m_W$ the branching fraction for $H \rightarrow W^+W^-$ is close to 1. The decay width to ZZ^* is roughly an order of magnitude smaller than the decay width to WW^* due to the smallness of the neutral current couplings as compared to the charged current couplings.

The decay of the Higgs boson to gluons arises through fermion loops [30],

$$\Gamma(H \rightarrow gg) = \frac{G_F \alpha_s^2 m_H^3}{64\sqrt{2}\pi^3} \left| \sum_q F_{1/2}(\tau_q) \right|^2 \quad (2.72)$$

where $\tau_q \equiv 4m_q^2/m_H^2$ and $F_{1/2}(\tau_q)$ is defined to be

$$F_{1/2}(\tau_q) \equiv -2\tau_q [1 + (1 - \tau_q)f(\tau_q)]. \quad (2.73)$$

The function $f(\tau_q)$ is given by

$$f(\tau_q) = \begin{cases} \left[\sin^{-1} \left(\sqrt{1/\tau_q} \right) \right]^2, & \text{if } \tau_q \geq 1 \\ -\frac{1}{4} \left[\log \left(\frac{x_+}{x_-} \right) - i\pi \right]^2, & \text{if } \tau_q < 1, \end{cases} \quad (2.74)$$

with

$$x_{\pm} = 1 \pm \sqrt{1 - \tau_q} \quad (2.75)$$

In the limit in which the quark mass is much less than the Higgs boson mass (the relevant limit for the b quark):

$$F_{1/2} \rightarrow \frac{2m_q^2}{m_H^2} \log^2 \left(\frac{m_q}{m_H} \right). \quad (2.76)$$

A Higgs boson decaying to $b\bar{b}$ loop will therefore be extremely narrow. On the other hand, for a heavy quark, $\tau_q \rightarrow \infty$, and $F_{1/2}(\tau_q)$ approaches a constant:

$$F_{1/2} \rightarrow -\frac{4}{3} \quad (2.77)$$

It is clear that the dominant contribution to the gluonic decay of the Higgs boson is from the top quark loop and from possible new generations of heavy fermions.

For the decay $H \rightarrow \gamma\gamma$ at lowest order, the partial width is [35]:

$$\Gamma(H \rightarrow \gamma\gamma) = \frac{\alpha^2 G_F}{128\sqrt{2}\pi^3} m_H^3 \left| \sum_i N_{ci} Q_i^2 F_i(\tau_i) \right|^2 \quad (2.78)$$

where the sum is over fermions and W^{\pm} bosons with $F_{1/2}(\tau_q)$ given in Equation 2.27 and

$$F_W(\tau_W) = 2 + 3\tau_W [1 + (2 - \tau_W)f(\tau_W)]. \quad (2.79)$$

Here $\tau_W = 4m_W^2/m_H^2$, $N_{ci} = 3$ for quarks and 1 otherwise, and Q_i is the electric charge in units of e . The function $f(\tau_q)$ is given in Equation 2.74. The $H \rightarrow \gamma\gamma$ decay channel probes the possible existence of heavy charged particles. The $H \rightarrow \gamma\gamma$ branching fraction rises with increasing m_H and peaks at around 2×10^{-3} for $m_H \sim 125$ GeV, as shown in Figure 2.12. Above this mass, the WW^* and ZZ^* decay modes are increasing rapidly with increasing Higgs mass and the $\gamma\gamma$ mode becomes further suppressed.

The decay $H \rightarrow Z\gamma$ is not useful phenomenologically, so we will not discuss it here. The complete expression for the branching ratio can be found in Reference [36]. From the Higgs boson decay widths discussed before, at the LEP energy above 200 GeV the range of Higgs boson masses covered is ~ 100 GeV. At these masses only $H \rightarrow b\bar{b}$ and $H \rightarrow \tau^+\tau^-$ decay modes contribute to the search.

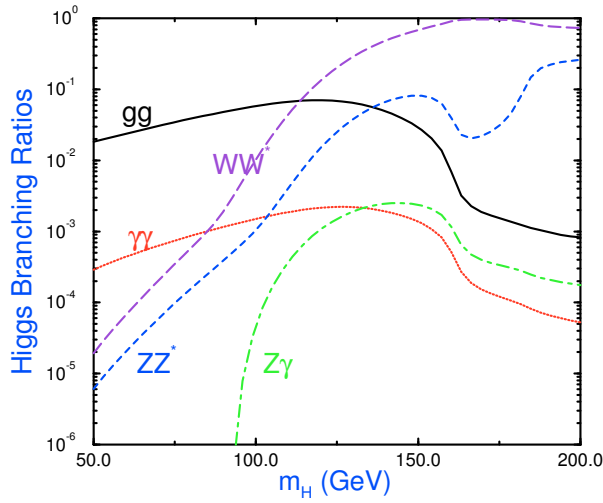


Figure 2.12: Branching fractions of the Standard Model Higgs boson to gauge boson pairs.

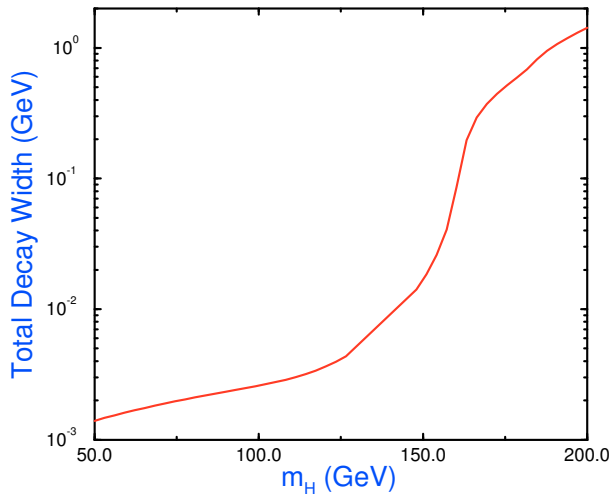


Figure 2.13: Total Higgs boson decay width in the Standard Model, including QCD radiative corrections.

The Total Higgs Boson Width

The total Higgs boson width for a mass less than $m_H \sim 200$ GeV is shown in Figure 2.13. Below around $m_H \sim 150$ GeV, the Higgs boson is quite narrow with $\Gamma_H < 10$ MeV. As the WW^* and ZZ^* channels become accessible, the width increases rapidly with $\Gamma_H \sim 1$ GeV at $m_H \sim 200$ GeV.

2.4.3 Standard Model Processes

Two Photon Interactions

This is the process with the highest cross section in e^+e^- interactions at the present LEP energies. Its cross section as a function of center-of-mass energy, \sqrt{s} , is shown in Figure 2.14. It leads to a four-fermion final state due to the virtual exchange of two photons.

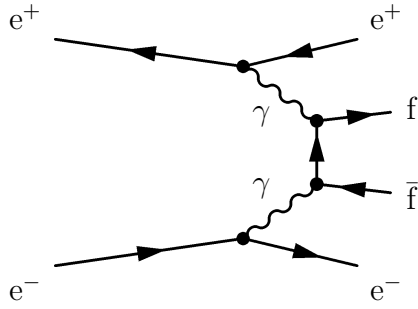


Figure 2.14: Two photon interaction

The electron and positron get slightly scattered in this process losing only a small fraction of their initial energy and very often they vanish undetected through the beam-pipe. The fermion pair which is observed in the detector has therefore a small energy and can be easily separated from the Higgs boson signal. This process has only little impact on the Higgs search.

For the generation of two photon events the program PHOJET [37] was used.

Two Fermion Final States

The process $e^+e^- \rightarrow q\bar{q}(\gamma)$, shown in Figure 2.15, has the second highest cross section. This is a relevant background source. After the annihilation of an electron and a positron

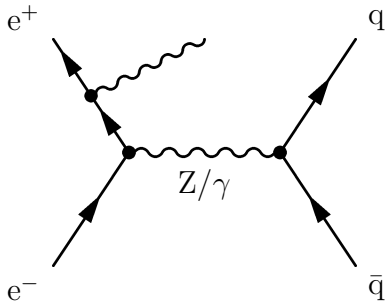


Figure 2.15: The process $e^+e^- \rightarrow q\bar{q}(\gamma)$. In the case of initial state radiation the event is unbalanced if the photon escapes unobserved the detector.

into a virtual Z or γ , a fermion-antifermion pair arise. The most important two-fermion production is the one leading to a quark anti-quark pair in a final state since it has a high cross section of ~ 90 pb at the center-of-mass energies around 200 GeV.

The quark anti-quark pair hadronise and we observe usually two jets in the detector. The radiation of gluons by the quark or anti-quark can lead to additional jets. The jets, originated by gluons, have usually smaller energies and the specific angular distributions which can be used to separate them from the Higgs boson signal.

In the case, where the initial state electron and/or positron radiate photons, it is possible to reduce the effective centre-of-mass energy in such a way that a real Z boson is produced. This is called the **radiative return to the Z**. The photons escape undetected, in most of these cases, down the beam pipe. Therefore, these events are characterised by an energy imbalance where the missing momentum vector points along the beam direction. For the generation of $e^+e^- \rightarrow q\bar{q}(\gamma)$ events the Monte Carlo program KK2f [38] is used. Other final states, corresponding to this process were generated using the PYTHIA [39] program.

W-pair Production

The production of W-pair events is realised in lowest order by three Feynman diagrams, the s-channel γ and Z boson and the t-channel ν_e exchange, as shown in Figure 2.16. The

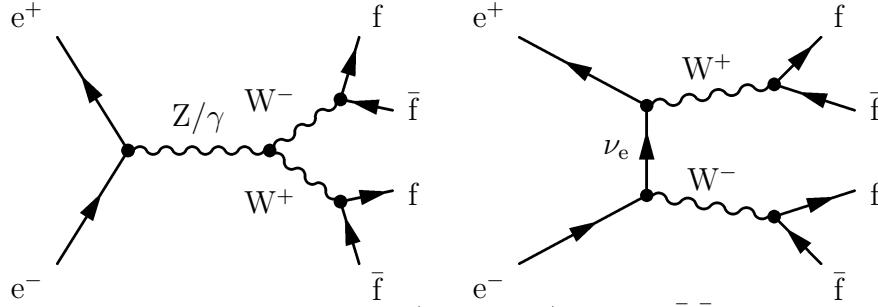


Figure 2.16: The background process $e^+e^- \rightarrow W^+W^- \rightarrow f\bar{f}f\bar{f}$. In lowest order three diagrams contribute to the cross section.

W bosons can decay into a quark-antiquark pair, for example $W^+ \rightarrow u\bar{d}$ or $c\bar{s}$, creating four jets similar to the Higgs boson signal. To separate events from the W-pair decay one can effectively use the detection of B hadrons in the jets originating from the Higgs boson and kinematic variables.

For the generation of the WW background the Monte Carlo generator KORALW [40] was used which takes the three Feynman diagrams presented in Figure 2.16 into account. Contributions from other diagrams are small, which is verified using the four-fermion generator EXCALIBUR [41].

Neutral Current Four Fermion Reactions

Neutral current four-fermion reactions can also be generated using EXCALIBUR. This program is used for the measurement of the resonant ZZ production cross section which will be described in detail in Chapter 7. For the background modelling in the Higgs

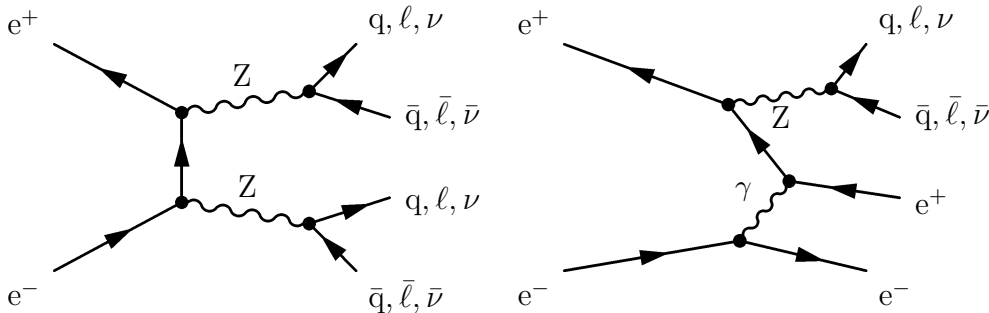


Figure 2.17: Examples for ZZ and Zee production.

search PYTHIA was used taking into account the NC02 approximation⁵ (in the following referred to as ZZ) and single Z production (in the following called Zee). ZZ background is especially severe for the SM Higgs search as it may lead to the same final states as HZ production and is kinematically very similar. It is shown in Figure 2.17).

Figure 2.18 summarises the production cross section for the processes listed above. For the comparison purpose, the SM Higgs boson production cross section for the Higgs boson with a mass of 114 GeV is also shown (dashed line).

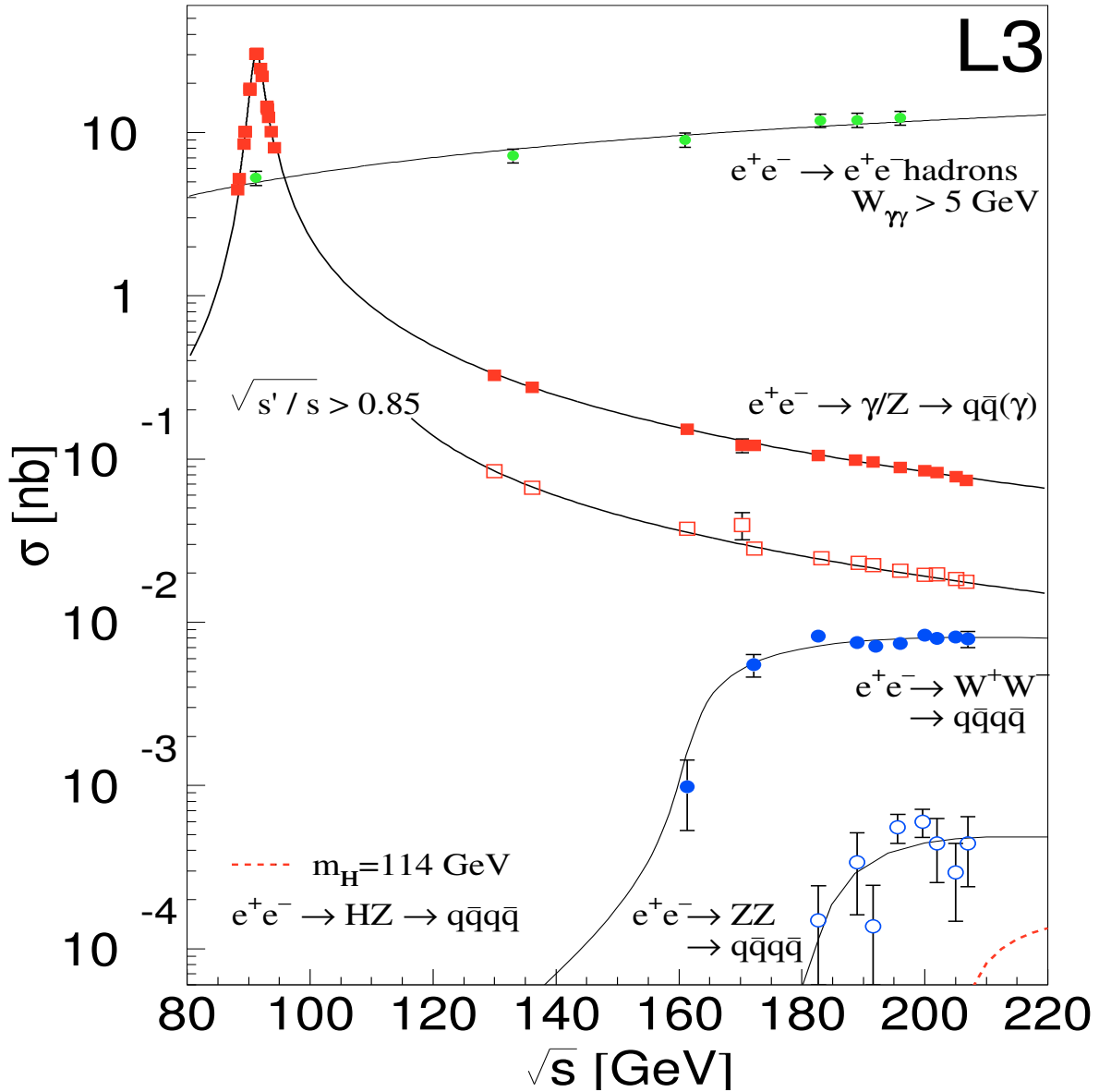


Figure 2.18: Cross section for the background processes from the Standard Model.

⁵At the lowest order, Z pair-production proceeds via two t -channel Feynman diagrams with an internal electron leg (right diagram in Figure 2.17). Considering the Z decays into fermions, this process is conventionally denoted as NC02, from the acronym of the neutral-current production mechanism of the four-fermions and the number of diagrams.

Chapter 3

The Experiment

3.1 The LEP Machine

The design of the CERN Large Electron Positron collider [42, 43], LEP, started in 1976 and by 1978 the aim was to build an e^+e^- machine with a cost-optimised energy of about 90 GeV/beam and luminosity $\mathcal{L} \simeq 10^{31} \text{cm}^{-2} \text{s}^{-1}$. The energies of the machine supposed to be extended by exploiting radio-frequency (RF) cavities to a theoretical maximum of about 130 GeV/beam.

The main physics goal was to test the Standard Model and possibly go beyond it by making precision measurements at the Z peak. It was also foreseen to do searches for new particles, like Higgs bosons or SUSY particles.

The accelerator was constructed inside a closed loop tunnel with a circumference of about 27 km at a mean depth of 100 meters. The schematic view of LEP is shown in Figure 3.1. The circumference was chosen to optimise the energy of the collider and the investment and running costs. Crucial considerations were the synchrotron radiation energy losses and the cost of the tunnel construction. With a circumference of 27 km the energy needed to replenish the energy loss due to synchrotron radiation is reduced to a manageable 220 MeV per turn at $\sqrt{s} = 90$ GeV.

The collider consists of eight bending sections, each 2840 m in length, and eight 490 m straight sections. The bending sections contain the 3304 dipole magnets which steer the beams around the ring. Four of the eight straight section house the large detectors ALEPH [44], DELPHI [45], L3 [46–56] and OPAL [57], as shown in Figure 3.1.

Two of the straight sections contain radio-frequency cavities which are used to accelerate the beams from injection energy to collision energy and to compensate synchrotron radiation losses. On either side of each detector, there are super-conducting quadrupole magnets which compress the beams for increased luminosity.

The LEP ring is actually the last component of a five-step acceleration process that begins with a pair of 200 MeV and 600 MeV linear accelerators (LINACS), as depicted in Figure 3.2. These LINACS provide the initial beam particles - electrons and positrons which are then injected into the Electron-Positron Accumulator ring (EPA). The EPA collects these particles into bunches and transfers them into the Proton Synchrotron (PS), which has been modified to accelerate the electron and positron beams from 600 MeV to 3.5 GeV. Similarly, the Super Proton Synchrotron (SPS) has been altered

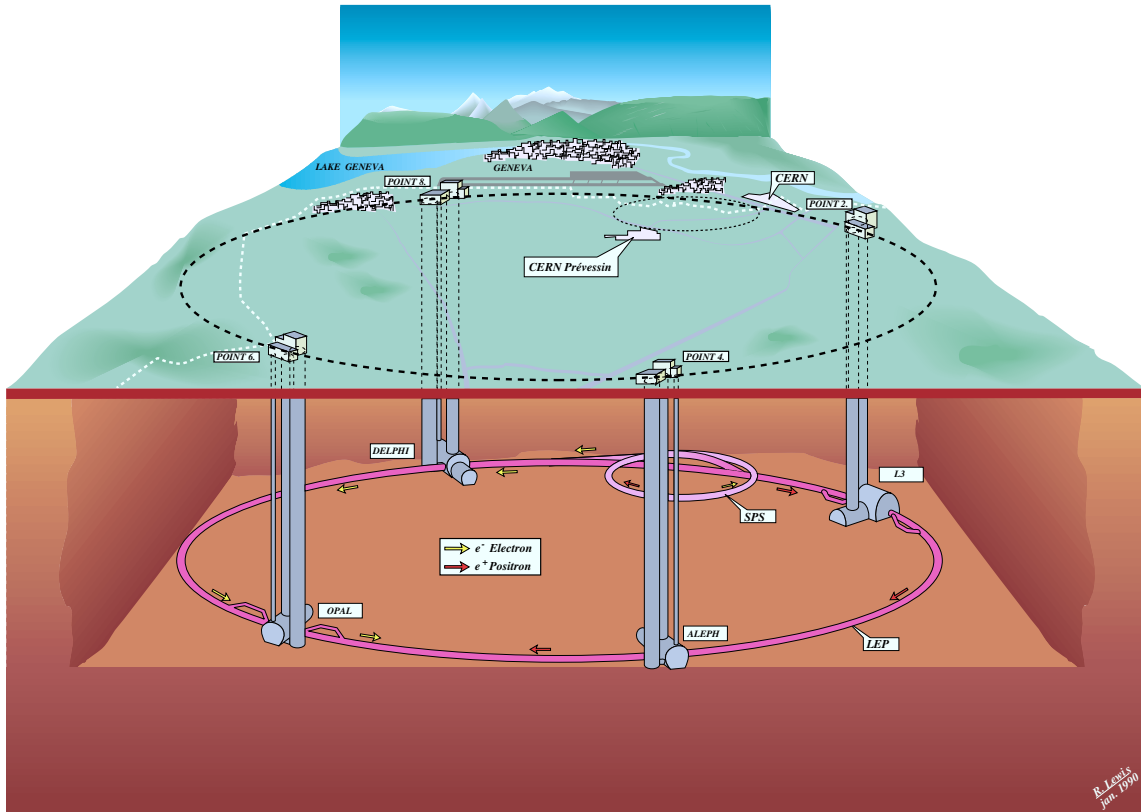


Figure 3.1: The LEP storage ring showing the four interaction points with the ALEPH, DELPHI, L3 and OPAL experiments.

to enable it to receive these 3.5 GeV beams, accelerate them to 20 GeV and inject them into LEP. Once the 20 GeV beams have been extracted from the SPS, they are accelerated to the working beam energy by a system of 128 RF copper cavities. The rotation frequency of the ($\approx 10^{12}$) stored particles is 11 kHz. Thus, in a typical 12 hour running period, each particle will have circulated through the vacuum chamber about 500 million times. This necessitates a very low pressure in the beam-pipe – about 10^{-9} Torr during operation with beam – in order to minimise losses to beam-gas collisions.

Two different acceleration schemes were used. In the first, electrons and positrons were arranged in 2×4 bunches along the LEP ring. The distance between two bunches, *i.e.* the time difference between two potential collisions was 22 μs . In the second scheme, the so-called bunch train regime, the bunches were replaced by trains of up to 4 smaller bunchlets, which have had a distance of 250 ns in time. Therefore, collisions may occur more frequently than in the first scheme. For operation of LEP at the Z peak, the bunch train scheme leads to an increase in luminosity. For running at higher energies, there are usually only 4 bunches used. The total current at high energies amounts 5 to 6 mA at the beginning of the fill.

In the first phase, 1989–1995, LEP was running at a center-of-mass energy close

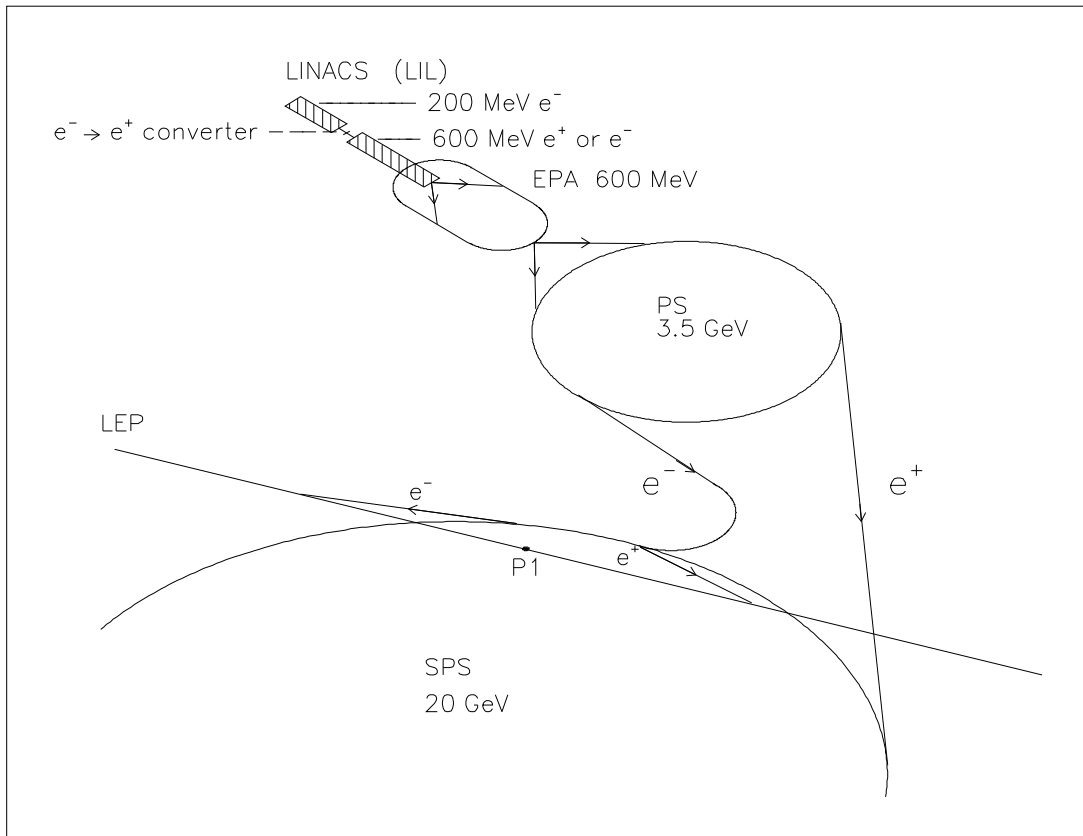


Figure 3.2: Overview of the LEP injector system.

to the mass of the neutral gauge boson Z . The data collected were used for precise measurements of Standard Model parameters on the Z resonance as well as for the search for new particles.

Starting from autumn 1995 the copper cavities were replaced by superconducting ones and the center-of-mass energy was continuously increased. In 1996 a center-of-mass energy above the threshold of W^\pm -pair production was reached allowing the precise determination of important parameters such as mass, coupling and branching fractions of the W^\pm bosons. Next opens the Z boson pair production channel, $e^+e^- \rightarrow ZZ$, and LEP entered new energy domain for the search of the Higgs Boson, expected in the Standard Model and new particles, representing the new physics.

3.2 The L3 Detector

The L3 detector, shown at Figure 3.3, is a general purpose detector with special emphasis on the precise energy measurement of photons, electrons and muons along with the good overall energy resolution and nearly hermetic solid angle coverage (99% of 4π).

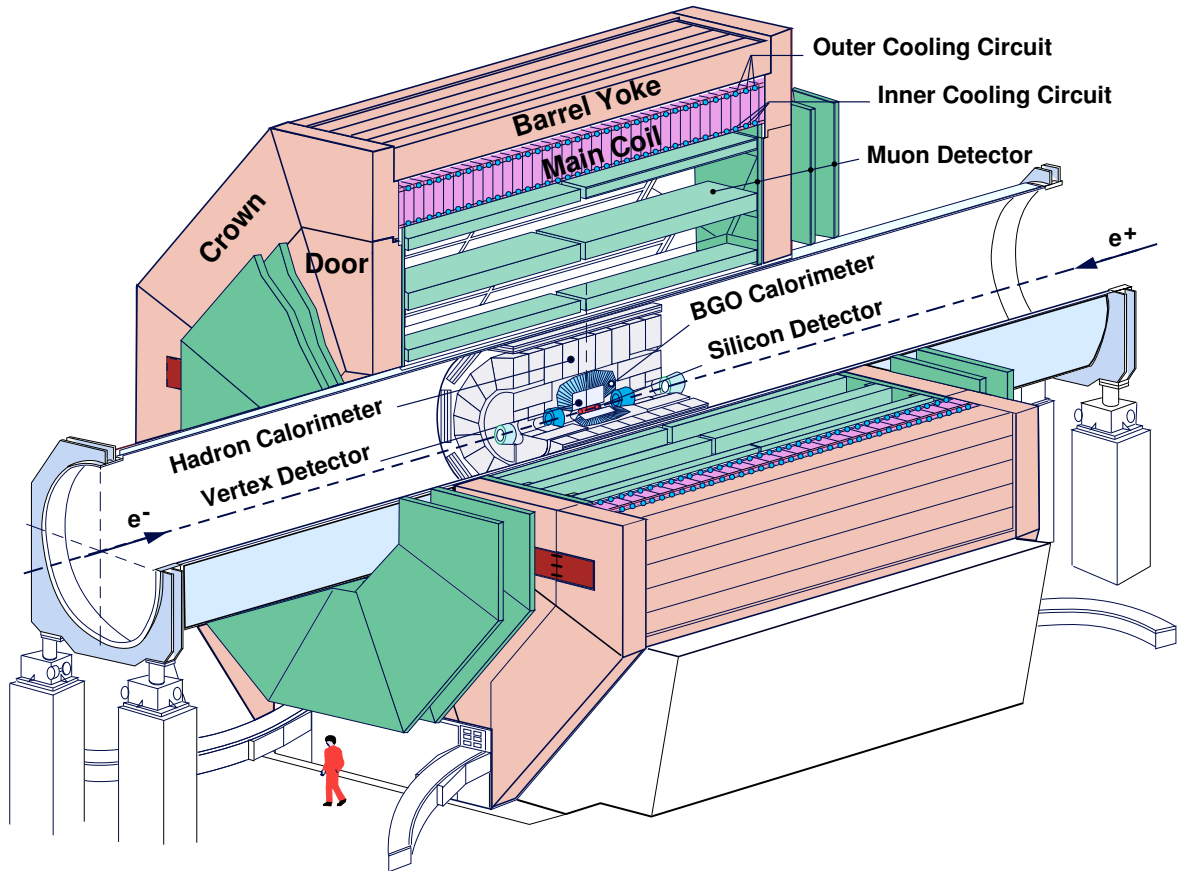


Figure 3.3: Perspective view of the L3 detector.

It is the largest of the four detectors at LEP (14 m long by 16 m wide) and made up of several complementary sub-detectors arranged in a radial layers surrounding the interaction point. The entire detector is enclosed within a 7800 ton, 0.5 T solenoidal magnet that allows for muon track curvature measurements over a long track length. The inner sub-detectors are contained within a 32 m long, 4.45 m diameter steel tube which both supports the detector and preserves its overall alignment relative to the beam. The arrangement of these sub-detectors within the support tube is shown in Figure 3.4. The following sections provide a brief description of the magnet and each detector component, working outwards from the beam pipe to the muon chambers.

3.2.1 The L3 Coordinate System

The L3 coordinate system, as used consistently throughout this thesis, is centered at the collision point with the z -axis aligned along the direction of the electron beam. The other two axes form a right-handed coordinate system with the y -axis directed vertically upwards and the x -axis pointing horizontally towards the center of the LEP ring. Polar angles are always measured from the z -axis ($\theta = 0^\circ$) while azimuthal angles are always measured from the positive x -axis ($\phi = 0^\circ$) in the direction of the positive y -axis.

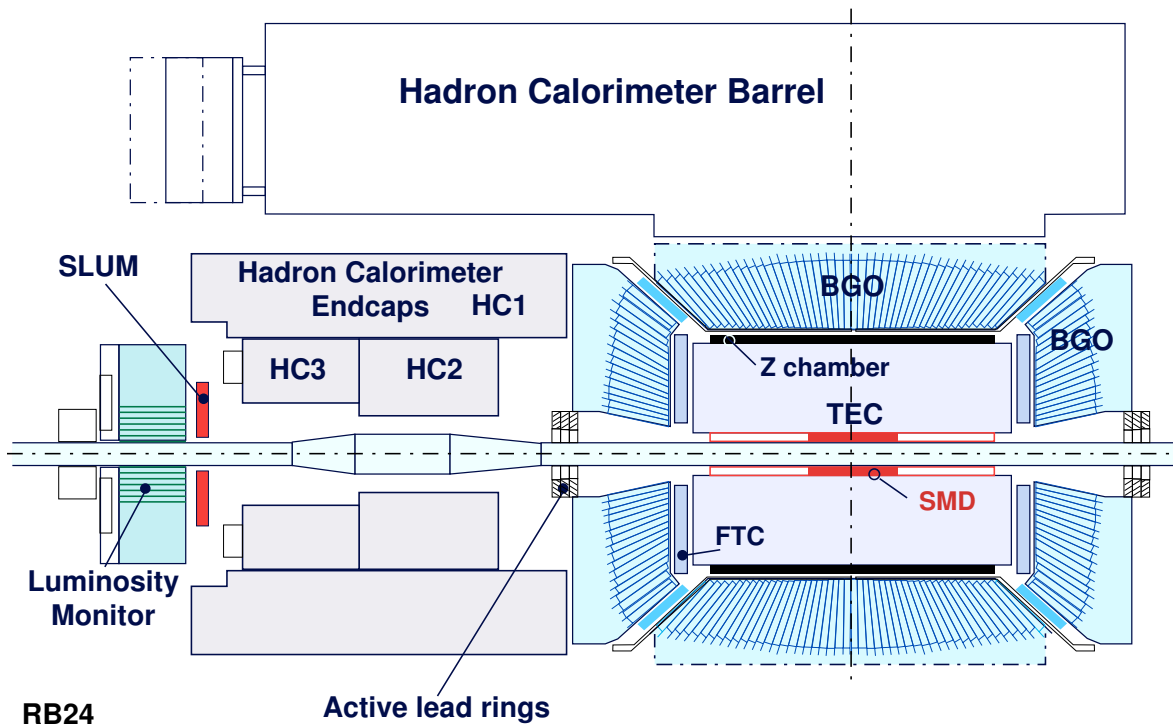


Figure 3.4: Left side of the inner sub-detectors within the L3 support tube. Electron - positron beams collision occurs within the beam pipe at the intersection of the dot-dashed lines.

3.2.2 Magnet

The L3 magnet is the largest conventional electromagnet ever built. Octagonal in shape, it consists of a coil of 1100 ton of aluminium plates arranged into 28 40-ton packages which are bolted together. The total length of the coil is 11.90 m with a 5.93 m inner radius. The flux return yoke is made of soft iron with 0.5% carbon content. 1100 tons of steel form the self-supporting structure of the poles, providing the rigid support and reference frame for the 5600 tons of iron that makes up the flux return in the poles and the barrel. Additionally, each pole includes two 340 ton half-doors which allow access to the muon chambers. A water-cooled thermal shield is located inside the coil to protect the detectors.

With 30 kA of current in the coil, the longitudinal magnetic field in the central region of the detector is 0.5 T. The field inside the support tube has been mapped out using a system of Hall probes, while the field in the outer region is measured by groups of magnetoresistors mounted on the muon chambers. Five NMR probes are also used to monitor the absolute value of the field. Since 1994, the magnet doors are equipped with copper coils and magnetised as part of the forward-backward muon system.

3.2.3 Silicon Microvertex Detector

The Silicon Microvertex Detector (SMD) [52], shown in Figure 3.5 is the innermost sub-

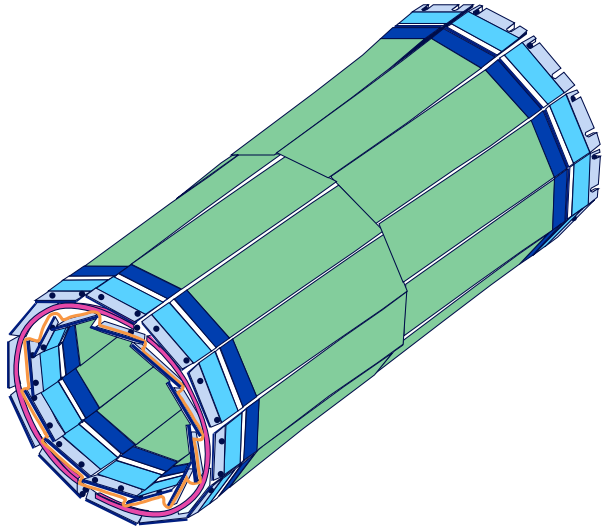


Figure 3.5: Perspective view of the Silicon Microvertex Detector. Overlap regions between the inner ladders are clearly seen.

detector of L3, located right outside of the LEP beam-pipe. Installed in 1993, it was designed to enhance the accuracy of track coordinate measurements of the L3 detector near the collision point.

The length of the SMD is 30 cm which yields a polar angle coverage of $22^\circ \leq \theta \leq 158^\circ$. SMD consists of two radial layers of silicon sensors arranged into ladders located 6 cm and 8 cm away from the z -axis. Adjacent inner ladders have a small (about 10%) overlap region, and outer ladders are positioned inside the support structure with their readout strips tilted 2° with respect to the inner ones. Each of the layers has 12 ladders, which are made up of two electrically independent half-ladders. The half-ladder consist of two silicon sensors. Each of the sensors is 70 mm long, 40 mm wide and made from 300 μm thick high purity n-type silicon. On one side (junction side) of the sensors there are implantation strips every 25 μm with a readout pitch of 50 μm . They run parallel to a beam axis and allow therefore the determination of the r - ϕ coordinate. On the other side the implantation strips are arranged perpendicular to the junction side strips with a pitch of 50 μm . The readout pitch is 200 μm for $0.53 \leq |\cos \theta| \leq 0.93$ and 150 μm for $|\cos \theta| \leq 0.53$. These strips are used for the z measurement. The outer surface of each ladder provides measurements in the r - ϕ plane with an intrinsic accuracy of 7.5 μm while the inner surfaces measure the z -coordinate with an intrinsic accuracy of 14.3 μm [58].

The SMD is a potentially valuable tool for measuring displaced vertices associated with short-lived B hadrons containing b quarks improving the performance of the b-tagging, as described in Section 4.3.4.

To monitor possible displacements of the SMD with respect to the TEC, a Capacitive Displacement Monitoring System (CDMS) and a Laser System were installed in the detector.

3.2.4 Central Tracking Chamber

The central track detector measures charged particles trajectories along their first half-meter of flight through L3. The multicomponent detector consists of a time-expansion chamber (TEC) which provides tracking in $r - \phi$, surrounded by the Z-chamber which measures the track z -coordinate as shown in Figure 3.6 and a forward tracking chamber (FTC) in the end-cap region.

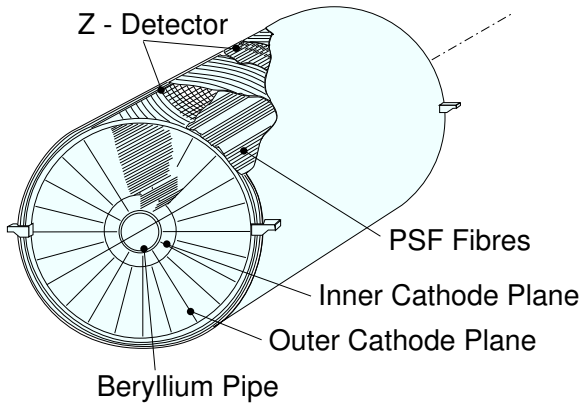


Figure 3.6: Perspective view of the Central Tracking Detector.

The main goal of the Central Tracking Detector is to measure the momentum of the charged particles and together with the Silicon Detector to identify the primary and the second vertices. It also determines the impact point of the charged particles on other detectors and determines at trigger level the number of reconstructed tracks originating from the interaction point.

Time Expansion Chamber

The heart of the Central Tracking Chamber - the Time Expansion Chamber (TEC) [46] - is located between the SMD and Z-chamber. Due to size constraints imposed by the electromagnetic calorimeter, the TEC has only a modest lever arm of 31.7 cm. This necessitates excellent spatial resolution in order to achieve the design goal of charge identification for 50 GeV particles at 95% confidence level. A drift chamber design which follows the time expansion principle was therefore chosen. The chamber is subdivided in azimuthal sector. A homogeneous low-field region, covering most of each sector, is combined with a high-field region near the anode plane in the center of each sector. The slow drift velocity in the low-field region yields good timing resolution while secondary ionization in the high-field region creates an avalanche resulting in a large signal. The electric field lines are perpendicular to the anode plane. The time difference of this signal to the beam crossing determines the distance to the ionization produced by the charged particle in the chamber gas.

A low diffusion gas mixture of 80% CO_2 and 20% iC_4H_{10} at 1.2 bar (drift velocity $\simeq 6 \mu\text{m/ns}$) is used. The chamber is divided into a 12 sector inner chamber and a 24 sector outer chamber, as depicted in the left drawing of Figure 3.7:

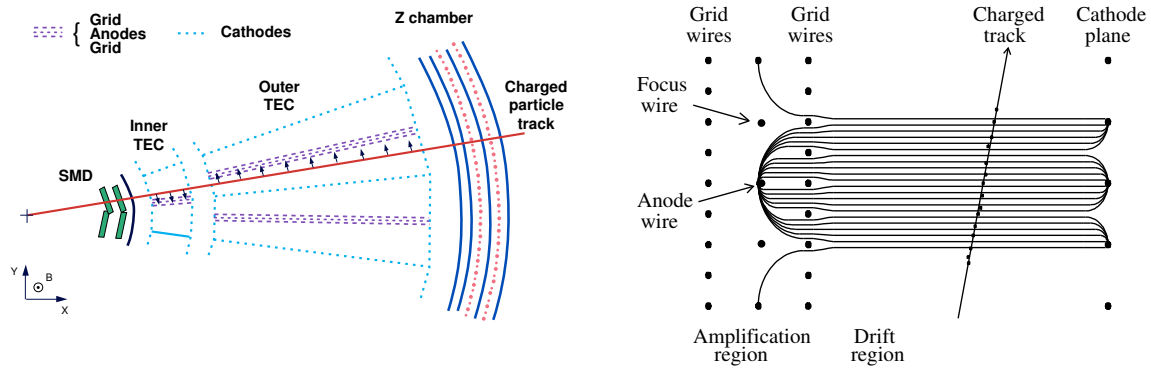


Figure 3.7: Left: r - ϕ view of the central tracker consisting of SMD, TEC and the Z detector. Right: drift field in the TEC.

The electric field forces the electrons to drift toward the anode wire plane arranged radially at the center of each sector. The right drawing of Figure 3.7 shows the arrangement of the wires in one 30° slice of the detector, along with some details of the electric field configuration. Flash Analog to Digital Converters (FADC) are used to sample the anode pulses in order to achieve a $\approx 50 \mu\text{m}$ average single wire spatial resolution.

The inner TEC sectors have 8 anode wires while the outer sectors have 54, giving a maximum of 62 coordinate measurements, or so-called hits, along the track in the transverse plane. Left-right track ambiguities are resolved by matching inner and outer sectors. Given the known magnetic field, a particle's charge and transverse momentum can be determined by fitting a circular arc to these hits. Two of the wires in each inner sector and nine in each outer sector are read out in charge division mode. The signals at both ends of a wire are compared to supply information on the z -coordinate of the track with a resolution of about 2 cm.

Z Chamber

More accurate z -coordinate information is obtained from the Z chamber [50] which consist of two cylindrical multi-wire proportional chambers that cover the outer cylinder of the TEC. All the particles with the polar angle between 42° and 138° will pass through this chamber. This detector operates in with a gas mixture of 80% argon, 16% CO_2 and 4% CH_4 . Signals are read out by cathode strips aligned at $\pm 69^\circ$ and 90° with respect to the z -axis, giving a measured z -coordinate resolution of $320 \mu\text{m}$ and a double track resolution of 7 mm. Z chamber is also used for bunch-tagging.

The Forward Tracking Chambers

The forward tracking chambers [46] extend the coverage given by the Z chamber down to $\theta = 9.5^\circ$ on either side. Installed in early 1991, the FTC provides extra coordinate

measurements in the $x - -y$ plane at a fixed value of z . These chambers operate in drift mode with a gas mixture of 61.5% argon and 38.5% ethane. The anode wires are inclined by 5° and 95° with respect to the x -axis, measuring the x and y coordinates of an isolated track to an accuracy of $150 \mu\text{m}$.

3.2.5 Electromagnetic Calorimeter

The Electromagnetic Calorimeter (ECAL) [47] is designed for the measurement of photons and electrons with superior energy and spatial resolution over the energy range from $\simeq 100 \text{ MeV}$ to 100 GeV . It consists of about 11,000 bismuth germanate ($\text{Bi}_4\text{Ge}_3\text{O}_{12}$ or BGO) crystals arranged in a pointing geometry and grouped into two half barrels and two end-caps surrounding the central tracking chamber, as shown in Figure 3.4. BGO is an especially useful material for electromagnetic calorimetry, forming a dense, clear lattice that serves both as a showering material and a scintillating medium. It has a density of 7.13 g/cm^3 and a radiation length of 1.12 cm , making it an excellent choice for high-precision measurements in a compact environment. Indeed, the 21.4 radiation length thickness of the BGO barrel crystals provides nearly complete absorption of most electromagnetic showers. In addition, the favourable light yield ($\simeq 2800\gamma/\text{MeV}$) and peak emission wavelength of 480 nm make photodiode feasible. Each crystal has two 1.5 cm^2 photodiodes glued to its rear face and is coated with a 40 to $50 \mu\text{m}$ thick layer of highly reflective paint in order to obtain uniform light collection efficiency.

Each crystal is 24 cm long and shaped like a truncated pyramid with the front and back faces measuring approximately $2 \times 2 \text{ cm}^2$ and $3 \times 3 \text{ cm}^2$, respectively, as it shown in Figure 3.8:

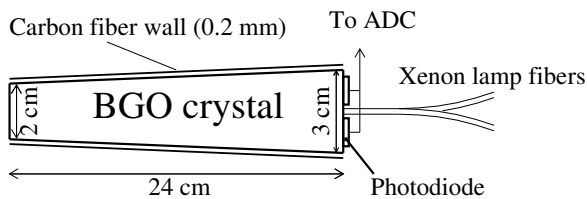


Figure 3.8: A BGO crystal. The front face of $2 \times 2 \text{ cm}^2$ points to the interaction point. The scintillation light is collected by two photodiodes on the rear face.

They are arranged within a carbon fiber composite support structure with $200\mu\text{m}$ thick cell walls and a 10 mm thick cylindrical stepped inner tube attached to a weight-bearing conical funnel on both ends. The area where two half barrels join is additionally reinforced by a $500\mu\text{m}$ thick steel membrane.

Charge-sensitive amplifiers, mounted directly behind each crystal, enhance and shape the photodiode signals before feeding into analog-to-digital converter (ADC). The temperature is monitored by 1792 sensors placed on front and back crystal faces. In addition, crystal transparency is measured by a xenon light system which injects pulses into the

back of each crystal via a network of optical fibres. The energy resolution is 5 % at 100 MeV and less than 2 % at energies larger than 1 GeV [59].

The 7,680 crystals making up the barrel cover the polar angular range $42^\circ < \theta < 138^\circ$ while the 1,527 crystals in each end-cap cover the regions $9.9^\circ < \theta(180^\circ - \theta) < 36.8^\circ$. The gap in polar angular coverage is the result of a 12.8 cm displacement of the end-cap along the z -axis from the original design position in order to accommodate the spatial requirements of the central track detector. It is filled with the lead-scintillating fibre calorimeters (SPACAL) [53], which consists of 24 modules (bricks) containing a lead structure filled with scintillating fibres. The scintillation light is collected by phototriodes glued on the rear site of the bricks. The resolution of the SPACAL is 15% at 45 GeV.

3.2.6 Scintillation Counters

The scintillator system [55] consists of 30 single plastic counters forming a barrel and 2×16 pad counters in the end-caps. They are located between the electromagnetic and the hadron calorimeter to provide time of flight information. The time resolution is about 800 ps in the barrel and 1.9 ns in the end-caps. The scintillation counters therefore allow the discrimination of cosmic muons which pass near the interaction vertex. If LEP operates in the bunch train mode they are used to tag the bunchlet.

3.2.7 Hadronic Calorimeter

The hadron calorimeter (HCAL) [48] surrounds the electromagnetic calorimeter and works in combination with it to measure the energy of hadrons using the total absorption technique. although hadrons generally lose some part of their energy in the electromagnetic calorimeter, they deposit the greater part of it via nuclear interactions in the uranium and brass plate absorbers that made up the HCAL. These interactions result in low-energy particle showers that are detected by the proportional wire chambers interleaved with the absorber.

The hadron calorimeter consist of a barrel, subtending the polar angular range of $35^\circ < \theta < 145^\circ$ and two end-caps, which extend the angular coverage to a range of $5.5^\circ < \theta < 174.5^\circ$, as shown in Figure 3.9: The hadron calorimeter covers 99% of the 4π

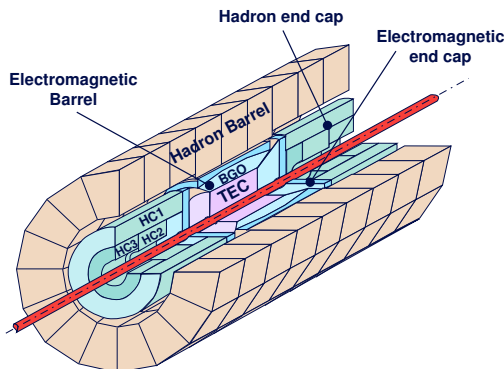


Figure 3.9: Perspective view of the Hadron Calorimeter.

solid angle.

The 216 ton HCAL barrel is composed of 144 modules arranged in 9 rings of 16 modules each. The longitudinal cross-section of the HCAL is illustrated in Figure 3.10: 5 mm thick absorber plates, made of depleted uranium, are interleaved with 5.6 mm

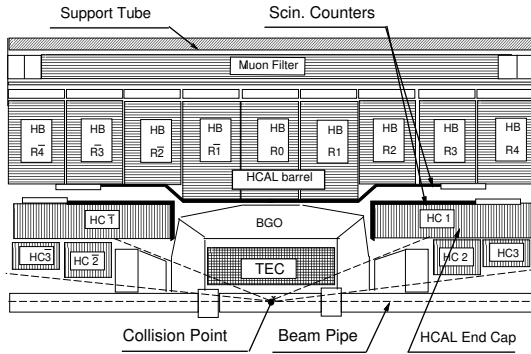


Figure 3.10: Side view of the Hadron Calorimeter.

thick proportional wire chambers to make up a module. The three inner rings are made up of modules, containing 60 layers, while the other six rings are built of modules with 53 layers each. A particle originating from the primary vertex will traverse 3.5 – 5.5 nuclear interaction lengths (free path between collisions) as it passes through the HCAL barrel.

The wire chambers operate in a proportional mode and are filled with a gas mixture of 80% argon and 20% CO_2 , providing a gain of $\approx 10^4$ at 1.6 kV. Each chamber layer is oriented with its wires perpendicular to the previous layer in $\theta - \phi$ plane. The barrel contains 7968 proportional chambers with 370,000 wires.

The two HCAL end-caps are formed of six modules each, with these modules being grouped into one outer (HC1) and two inner (HC2, HC3) rings. The construction of the endcap modules is similar to that of the barrel. The HC1, HC2 and HC3 rings contain 77, 27 and 23 layers, respectively. In contrast to the barrel modules, these layers are oriented in the $x - y$ plane with alternating stereo layers rotated by an angle of 22.5° . The thickness of the absorber plates increases in the outer layers of each module to optimise the absorption power for the available space with minimal loss of resolution. In case of end-caps a particle from the interaction point will pass through $6 \div 7$ nuclear interaction lengths. The hadron jet energy resolution of the calorimeter is $(55/\sqrt{E}+8)\%$, where E is measured in GeV. The direction of the jet axis can be measured with a resolution of about 1.5° .

Muon Filter

The muon filter, mounted on the inside wall of the support tube, suppresses the flow of secondary particles produced in the hadron calorimeter and serves to guarantee that hadrons do not enter the muon chambers. It consists of 6 layers of 1 cm thick brass absorber plates followed by an additional 5 layers of 1.5 cm thick plates. It adds 1.05 absorption lengths to the hadronic calorimeter.

3.2.8 Muon Spectrometer

The Muon Spectrometer [49, 56] is installed in the region between the support tube and the magnet, covering the polar angular range of $36^\circ < \theta < 144^\circ$. It is protected from the magnet coil by an active thermal shield and consists of two octagonal ferris wheels attached to the support tube, as depicted in Figure 3.11. The sixteen independent

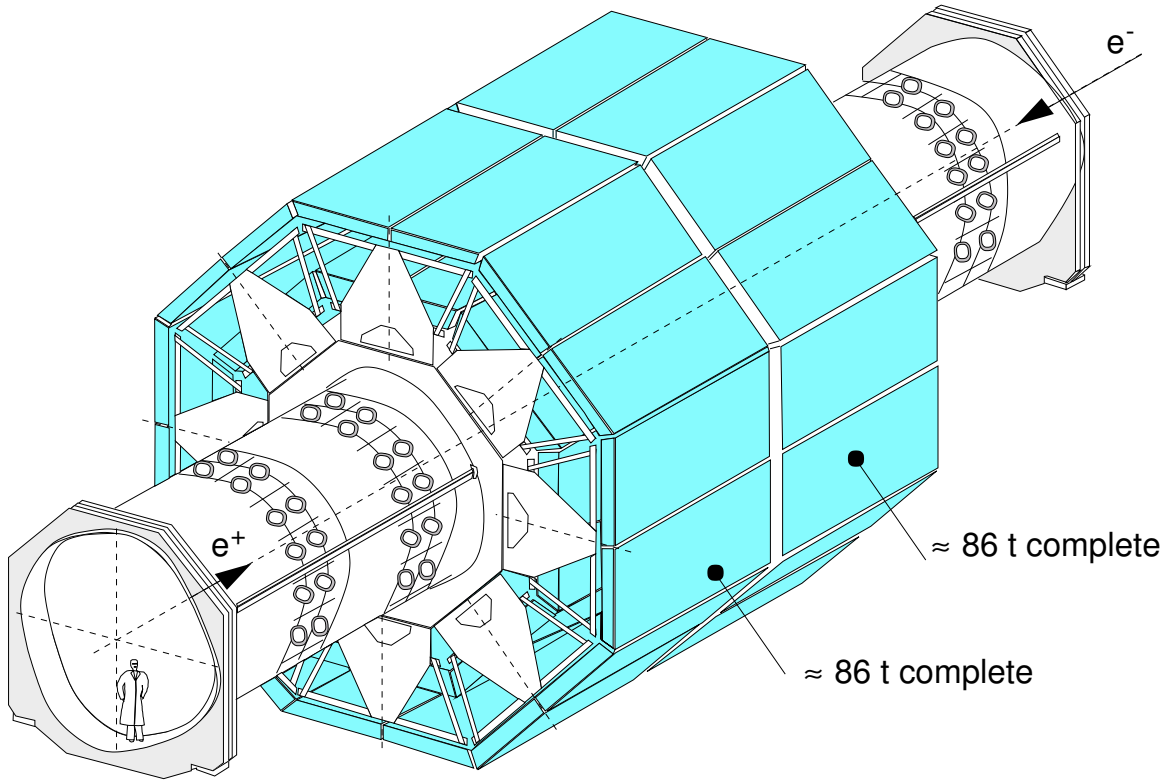


Figure 3.11: Perspective view of the Muon Spectrometer.

octants (8 per 86 ton wheel) form the muon spectrometer. Each octant contains 3 detector layers: the outer layer (MO) resides just inside the coil, the inner (MI) layer is located just outside the support tube and the central (MM) layer lies in between. Five precision “P” drift chambers (2 each per MO and MM and 1 per MI) and 6 “Z”-chambers (4 each per MO and 2 per MI) make up each octant.

The “P”-chambers are designed to give a highly accurate measurement of track coordinates in the bending plane. Each chamber contains about 3,000 wires, 320 of which are sense wires, in a gas mixture of 61.5% argon and 38.5% methane, giving a drift velocity of $50 \mu\text{m}/\text{ns}$. The sense wires are grouped to give either 16 or 24 coordinate measurements per cell, as it shown in Figure 3.12, each with a resolution of $110 \mu\text{m}$ to $250 \mu\text{m}$ depending on the distance from the sense wire.

The “Z”-chamber comprise two drift cell layers with a half-cell relative offset that

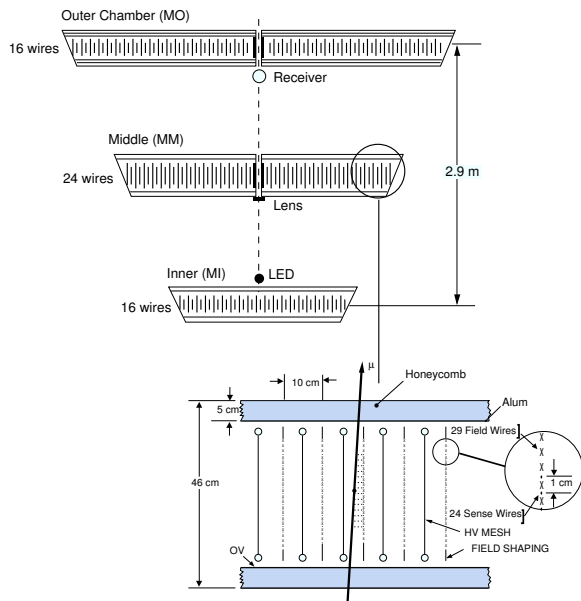


Figure 3.12: One muon detector octant demonstrating details of the five “P”-chambers. The 6 “Z”-chambers make up the top and the bottom covers of the MI and MO chambers. The MM chambers are enclosed by a thin, aluminium honeycomb, adding only 0.9% radiation length and a resultant multiple scattering induced sagitta error of less than $30 \mu\text{m}$ at 50 GeV.

allows resolution of left-right ambiguities. The gas mixture of 91.5% argon and 8.5% methane provides an average drift velocity of $30 \mu\text{m/s}$ and the single wire z -coordinate resolution is $\sim 500 \mu\text{m}$.

Using the muon chamber coordinate measurements in conjunction with the measured magnetic field, the momentum resolution has been measured to $\sigma(E_{beam}/p_{\mu}) = 2.5\%$ at 45 GeV.

In 1994, the angular coverage of the muon spectrometer was extended to the angular region of $22^{\circ} < \theta < 158^{\circ}$ by inclusion of the forward-backward muon chambers. These drift chambers consists of 3 additional layers, one mounted inside and two - outside of each of the magnet doors. Each layer comprises 16 chambers with 4 sense wires per cell giving an average spatial resolution of $200 \mu\text{m}$. The gas mixture is the same as in the “P”-chambers. In the extended angular region from 22° to 36° , the momentum resolution is $\sigma(p_T)/p_T \sim 20\%$ and is limited by multiple scattering in the one meter thick magnet doors.

3.2.9 Luminosity Monitor

A precise knowledge of the luminosity is very important for the main part of the measurements made at LEP. The luminosity is determined with high precision by measuring the rate of low angle Bhabha scattering, $e^+e^- \rightarrow e^+e^-(\gamma)$. This well-understood in the framework of QED process is strongly peaked at low angles and serves as a virtually background free reference for luminosity determination [60]. The luminosity monitor [54] measures Bhabha events using two cylindrically symmetric BGO arrays combined with a tracking system for accurate impact point position measurement. In 1993, the original wire chamber trackers were replaced by more accurate silicon detector, denoted by SLUM in Figure 3.4.

The two luminosity monitors are symmetrically located 2650 mm downstream of the interaction point on either side. Each finely segmented calorimeter contains 304 BGO

crystals, all 26 cm long, covering the polar angle range of $24.93 < \theta(\pi - \theta) < 69.94$ mrad. The crystals are grouped in 8 rings, all of which are aligned to the z -axis. The energy resolution of these BGO arrays has been measured at better than 2% at 45 GeV.

Each silicon detector consists of two layers measuring radial coordinates and one layer measuring ϕ coordinates. These three layers are made up of 16 partially overlapping wafers and total of 4096 readout strips. With this configuration, the luminosity is currently known to an accuracy of 0.2%, with most of the error coming from the theoretical uncertainty in the Bhabha cross section.

3.2.10 Trigger

The L3 trigger system performs a rapid analysis of the response of the various subdetectors at each bunch crossing in order to record interesting physics events. About 100 ms is required to fully digitise all L3 subdetector signals and write an event to disk or tape. The goal is to minimise the dead time that results from writing information from bunch crossings with no detected particles, or from background events caused by beam-gas, beam-wall interactions, synchrotron radiation or detector noise. The trigger system is divided into three levels of increasing complexity. Each of the three levels applies several selection criteria.

Level-1 Trigger

The Level-1 trigger takes individual information from the subdetectors and based on five separate triggers: track information from the TEC (inner and outer TEC triggers), energy deposits in the calorimeters (energy trigger), scintillator hits (scintillator trigger), energy deposits in the luminosity monitor (luminosity trigger) and tracks in the muon chamber (muon trigger). A positive result from any of the five causes the fine digitisation to commence for analysis by the subsequent levels. Level-1 produces a typical trigger rate of less than 8 Hz.

Calorimeter Trigger is designed to select events which deposit energy in the electromagnetic or hadronic calorimeters. The input consist of the analog sums of groups of BGO crystals, grouped into $32 \phi \times 16 \theta$ blocks and hadron calorimeter towers, grouped into 16×11 blocks for layers of less than ~ 1 absorption length and 16×13 blocks for deeper layers. An event is accepted if the BGO energy exceeds 25 GeV in the barrel and endcaps, or 8 GeV in the barrel only, or the total calorimetric energy exceeds 25 GeV in the barrel and endcaps or 15 GeV in the barrel alone. The cluster threshold is 6 GeV, or 2.5 GeV for clusters in spatial coincidence with a track from the TEC trigger. The main source of background for this trigger is electronic noise. The trigger rate is typically $1 \div 2$ Hz.

Scintillator Trigger is used in level-1 to trigger on high multiplicity events. Events with at least 5 hits spread over 90° are selected. This trigger is practically background free and the trigger rate is typically 0.1 Hz.

Muon Trigger selects events with at least one penetrating charged particle. An event is selected if hits in the muon chambers can be formed into a track with transverse momentum greater than 1 GeV. At least 2 P-layers and 3 Z-layers are required. Cosmic

muons are rejected by requiring one good scintillator hit within 15 ns of the beam crossing. A 1 Hz trigger rate is typical.

Luminosity Trigger processes signals in the same way as the calorimeter trigger. An event is selected if any of the following criteria are met: two back-to-back depositions with ≥ 15 GeV, total energy on one side ≥ 25 GeV and on the other ≥ 5 GeV, or total energy on either side ≥ 30 GeV. For the normal beam conditions the typical trigger rate is 1.5 Hz.

TEC Trigger selects events with charged tracks. Tracks are required to have a transverse momentum of more than 150 MeV, and an event is selected if at least two tracks are found with acolinearity less than 60° . The TEC trigger rate is generally around 1 Hz, but during bad beam conditions it can increase by several Hz.

Level-2 Trigger

The level-2 trigger attempts to reject background events, passed through the level-1. At this level, more time can be spent analysing an event without incurring additional dead-time and signals from different subdetectors can be correlated. Level-2 is effective removing calorimeter triggers due to electronic noise, and TEC triggers due to beam-gas and beam-wall interactions. Events that produce more than one level-1 trigger are not rejected by level-2. After level-2 the trigger rate is typically less than 6 Hz.

Level-3 Trigger

This trigger performs a more detailed analysis of events that pass the previous two levels. Results of the fine digitisation are used, so more precise thresholds can be set for the calorimetry, further reducing electronic noise. Muon triggers are required to fall within more stringent 10 ns scintillator coincidence, reducing background from the cosmic muons. Tracks selected by the TEC trigger are correlated with at least 100 MeV of energy deposition in the calorimeters and are checked for quality and for a common vertex. Events that produce more than one level-1 triggers are not rejected by level-3. Overall trigger rate after the level-3 is generally around 3 Hz.

All events passing the trigger level-3 decision are written to disk being then input for the off-line reconstruction program. Furthermore, the raw data are copied to a tape to ensure the possibility of a rerun of the reconstruction.

Chapter 4

Data and Monte Carlo Samples

4.1 Data Sample

This dissertation uses data, collected with the L3 detector during the year 2000 at several center-of-mass energies.

Data from the year 1999 were also analysed to search for SM Higgs boson production, but the results from the year 2000 supersede these results, so they are not quoted in this thesis. However, several systematic studies of general importance were done with the data sample from year 1999. For Z pair production studies only data from the year 2000 were used. A detailed discussion about these data and Monte Carlo can be found in the Chapter 7.

The data from the year 2000 are grouped into seven samples corresponding to effective center-of-mass energies of 202.8, 203.8, 205.1, 206.3, 206.6, 208.0 and 208.6 GeV. Table 4.1 summarises the integrated luminosities corresponding to these samples:

\sqrt{s} (GeV)	202.8	203.8	205.1	206.3	206.6	208.0	208.6
$\int \mathcal{L}$ (pb^{-1})	2.7	7.6	68.1	66.9	63.7	8.2	0.1

Table 4.1: The effective center-of-mass energies and corresponding integrated luminosities.

4.2 Monte Carlo Samples

The Higgs boson production cross sections and branching fractions are calculated using the HZHA generator [61]. Efficiencies are determined on Monte Carlo samples of Higgs events, generated using PYTHIA [39]. As it has been shown in the Section 2.4, the Higgs production cross sections and efficiencies depend on \sqrt{s} . Samples of Higgs events have been simulated at each center-of-mass energy shown in Table 4.1. Higgs events are simulated with the mass of the Higgs boson between 100 and 120 GeV, in steps of 1 GeV. For each Higgs boson mass and each search channel, between 2000 and 10000 events were generated, depending on the search channel.

The estimates of the Standard Model background, as discussed in Section 2.4.3, rely on the following Monte Carlo programs: KK2f [38] for $e^+e^- \rightarrow q\bar{q}(\gamma)$. KORALW [40] for $e^+e^- \rightarrow W^+W^-$, PHOJET [37] for two-photon processes ($e^+e^- \rightarrow e^+e^-q\bar{q}$) and EXCALIBUR [41] for other four-fermion final states. The number of simulated events for the dominant backgrounds is at least 100 times the number of collected data events for such processes to minimise statistical fluctuations.

4.3 Simulation and Reconstruction

The process of simulation can be separated on the several steps. The first step is the generation of the events, where the physics processes are modelled using Monte Carlo events generators. As the output, we have an event with a number of particles with their energy-momentum vectors.

The next step is the simulation of the detector response on these particles, using the GEANT [62] and GHEISHA [63] programs which take into account the effects of multiple scattering, energy loss and showering in the detector as well as the interaction with the magnetic field. At the end of the simulation, the events are available in the same format as the real data recorded in the detector. This is the digitised information of the response for the individual sub-detectors.

The final step is when simulated and real data events are then reconstructed using the same reconstruction code which combines the individual sub-detector information, such as wire hits or crystal amplitudes into tracks and energy clusters. For the simulated events, time-dependent imperfections of the detector, such as dead wires or crystals are taken into account in order to make the simulation as realistic as possible.

The evolution of hadronic final states as e.g. Figure 2.15 can be subdivided into four different phases; beginning from the production of the quarks to the formation of stable particles, which will be detected by the experimental apparatus. These phases correspond to different time and length scales [64]. At the stage of the electroweak phase, which corresponds to 10^{-19} m, a quark anti-quark pair(s) and a number photons are produced.

In the next, perturbative QCD, phase (10^{-17} m) gluon radiation may proceed. The momentum transfer between the quarks and gluons is rather large corresponding to small interaction distances and relatively small values of the strong coupling constant, α_s . This perturbative phase of QCD stops when the momentum transfer becomes too small ($\sim \text{GeV}$) and thus the coupling constant is too large to allow further perturbative steps. The resulting particles from this phase are quarks and gluons and are called final state partons.

The process to build colourless hadrons from quarks, called *hadronisation* or *fragmentation*, starts at the non-perturbative QCD phase (10^{-15} m). Since there is no theory which describes this phase completely models have to be introduced. The models are characterised by many parameters, which are not based on an underlying consistent theory but which are mostly empirically motivated [65].

During the particle decay phase ($> 10^{-15}$ m) unstable hadrons decay forming in most cases mesons which are then registered by the detector. Many of these decays are well un-

derstood from measurements in low-energy experiments. But in case of heavy-flavoured hadrons still some uncertainties remain due to the fact that not all decay modes have been measured with high precision. Several models for the fragmentation process have been proposed in the last years: independent *jet* models [66], *string* fragmentation models [67, 68] and *cluster* fragmentation models [69–72].

The string model has been implemented in the Monte Carlo JETSET [73] and has become the model commonly used to describe e^+e^- annihilations to hadrons in recent years. String models are based on the idea that, if the primary quarks move apart, a *color flux tube* (string) stretches between them. As soon as the potential energy is high enough to build a $q\bar{q}$ pair, the string tears into two parts. The quarks and antiquarks from adjacent breaking can then form mesons. Although well founded on the QCD, the model still contains many parameters controlling transverse and longitudinal momentum, baryon production, etc. However, energy and momentum are conserved at each step in the string fragmentation. Baryon production is included by the production of diquark pairs at some of the string breaks.

The final hadrons are usually contained in a small cone in space which follows the direction of the original parton. These bundles of particles are called jets.

The energy of a hadron entering the calorimeter, E , can be expressed as a function of the energy deposited in the electromagnetic and hadronic calorimeters [74]. This function is usually a linear sum:

$$E = A \cdot E_{\text{elm}} + B \cdot E_{\text{had}}, \quad (4.1)$$

where the weighting factors A and B have to be determined experimentally.

The estimation of the energy of a particle from the energy deposited in the calorimeters goes in the following way. First, raw signals in the calorimeter are grouped into clusters consisting of energy depositions in neighbouring cells. Then calibration factors, denoted as G -factors, are used to transform these raw signal into the energy of cluster. Thus, the energy of a cluster can be expressed in a following way:

$$E^c = \sum_i G_i E_i^c, \quad (4.2)$$

with the sum running over the detector regions where the cluster has deposited its energy. These regions are defined to take into account the non-homogenous structure and imperfections of the detector. The momenta of the muon tracks as measured in the muon chambers or tracks momenta measured in TEC is optionally included. The G -factors are determined using data sample of $e^+e^- \rightarrow$ hadrons and comparing the detector response with center-of-mass energy.

4.3.1 DURHAM Jet Clustering Algorithm

The DURHAM algorithm [75] is a method of clustering deposits of energy in the detector into larger units, called jets. It uses all possible energy measurements of a given object (momenta of the tracks measured using the Central Tracking Chamber and SMD, clusters of calorimetric energy or momentum measurements from the muon chambers).

Individual objects, or clusters of energy, are joined into a pseudo-particle by the requirement to all objects to have a value of the parameter

$$Y_{ij} = 2 \frac{\min(E_i^2, E_j^2)}{E_{\text{vis}}^2} (1 - \cos\theta_{ij}) \quad (4.3)$$

to be below some predefined cutoff value Y_{cut} . Here E_i and E_j are the energies of particles, θ_{ij} is the opening angle between them and E_{vis} is the total visible energy in the event. In this way, the DURHAM scheme merges pairs of objects until the smallest Y_{ij} at the current iteration exceeds some predefined cutoff value Y_{cut} .

For example, for the four-jet final states the value of Y_{cut} where the configuration of the pseudo-particles changes from three jets to four jets is called Y_{34}^D . It is this parameter of the DURHAM algorithm, that is used to define the four-jets nature of the event in the analysis. In the analyses with the final states containing two-jets the value of Y_{cut} where the configuration changes from two jets to three, Y_{23}^D , is used.

4.3.2 Kinematic Fit

The purpose of the kinematic fit is to improve the di-jet mass resolution by utilising the four constraints from momentum and energy conservation.

For the hadronic jets the measurements of the energy and the angles are obtained from the application of the clustering algorithm. Since it is expected that the jet mass will be proportional to the jet energy, the number of free parameters for the jets is restricted to three. The parameters are chosen to be the energy and the polar and azimuthal angles ϕ and θ of the jet. Thus in an 4-jet event we have twelve measured parameters. They are not independent and must obey energy and momentum conservation:

$$\begin{aligned} \sum_{i=1}^4 E_i &= \sqrt{s} \\ \sum_{i=1}^4 \vec{p}_i &= 0 \end{aligned} \quad (4.4)$$

where E_i is the energy of the jets, and \vec{p}_i is their momentum. The jet parameters are varied to minimise a χ^2 function defined in the following way:

$$\chi^2 = (\vec{V} - \vec{V}_0)^T \hat{W}^{-1} (\vec{V} - \vec{V}_0), \quad (4.5)$$

where \vec{V} is the vector of varied quantities, \vec{V}_0 is the vector build from their measured values and \hat{W} is the global error matrix. It is assumed to be diagonal, meaning that the measurement of the jet parameters are uncorrelated. The error parametrisation is discussed in detail in the next Section.

A fit performed with these 4 constraints we denote 4C fit hereafter. Again, different final states require different constraints. The improvement of the di-jet mass resolution on the example of the reconstructed Higgs boson mass with the Higgs boson hypothesis of 110 GeV at $\sqrt{s} = 207$ GeV is shown in Figure 4.1 As we can see from this figure, the 4C fit improved the Higgs boson mass resolution by a factor of about 2.

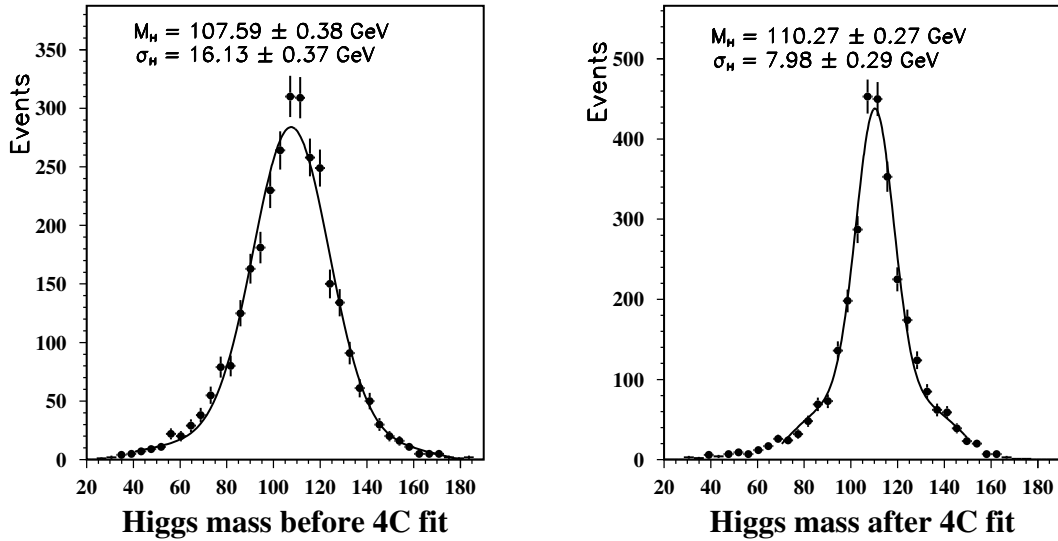


Figure 4.1: Example for the Higgs boson mass resolution improvement after implementing 4C fit to the reconstructed four-jet final state. The distribution of the invariant mass of the two jets coming from the Higgs boson before 4C fit (left) and after 4C fit (right). A Monte Carlo sample with a Higgs boson mass of 110 GeV is used at $\sqrt{s} = 207$ GeV.

Depending on the specific analysis there will be additional constraints and the implementation of the fit may differ. In four-jet events there are six ways we can select a jet pair and three ways we can combine them into two di-jets. In general, there is no way to determine which of these partitions is correct. Therefore, we must take into account all the allowed partitions and choose the di-jet pairing which has the smallest χ^2 tested with a certain assumption.

The 4-jet analysis at high energy e^+e^- collisions can be associated with the following approaches:

- **One unknown and one known mass**, as in HZ search. There are six ways to select which two jets correspond to the Z. We therefore have to make six fits and choose the fit with the smallest χ^2 , given the additional constraint that requires the reconstructed di-jet mass equals the known Z mass.
- **Two unknown, but equal masses**, as in H^+H^- searches but also in W^+W^- and ZZ final states. We have one additional constraint in this case that the two di-jet masses are equal. Then we need to perform three permutation, one for each di-jet partition, and choose either the fit with smallest χ^2 , or accept all partitions which have an acceptable χ^2 , lower than some threshold value χ_{tr}^2 , chosen for each particular case.
- **Two unknown masses**, as in hA searches. In this case we have only the 4C fit - four constraints from momentum and energy conservation. We make one fit

and use the reconstructed jets to calculate the invariant masses of all six possible di-jets. In an hA search all three pairs of di-jet masses must be used.

To remove the background from the W^+W^- and ZZ events in the HZ search we also make fits to the events with two additional constraints from the two known masses. If one of these fits has a small χ^2 the event will probably be a background event.

4.3.3 The Resolution Functions of Jet Measurement in the L3 Detector

Here a detailed study of the jet resolutions [76] of the L3 detector as functions of the energy, the polar and azimuthal angles of the jets is presented using Monte Carlo events fully simulated in the detector. The dependencies of the resolutions are parametrised in two dimensions and then used in the constrained kinematic fit, discussed in the previous section. The results obtained in variables essential for the boson pair production and, especially, for the Higgs boson search are compared to the ones from the standard resolution functions. For example, the mass of the two jets assigned to the Higgs is considered.

Resolutions

The resolutions of the jet energy E , the jet polar angle Θ and the azimuthal angle ϕ follow in the ideal case Gaussian distributions characterised by a width σ_i , where i denotes E , Θ or ϕ .

To obtain σ_i , a fit with a Gaussian is performed to the distributions of the differences of angles, $\Delta\Theta$ and $\Delta\phi$, and jet energies, ΔE , defined as:

$$\begin{aligned}\Delta\Theta &= \Theta^{gen} - \Theta^{rec} \\ \Delta\phi &= \phi^{gen} - \phi^{rec} \\ \Delta E &= \frac{E^{gen} - E^{rec}}{E^{gen}}\end{aligned}\tag{4.6}$$

where the quantity with the superscript ‘‘gen’’ refers to the generated partons and the quantity with ‘‘rec’’ refers to the reconstructed jet parameters.

Two examples for such distributions of the polar angle difference, $\Delta\Theta$, and the energy difference, ΔE , are shown in Figure 4.2. Distribution for the azimuthal angle difference, $\Delta\phi$, looks very similar to the polar angle difference distribution. Since the $\Delta\Theta$ distribution is only poorly described by a single Gaussian a superposition of two Gaussian is used. A narrow one describes the bulk of the distribution and a wide one covers the tails. In average the fraction of events in the narrow Gaussian is about 80%. The width of the narrow Gaussian is taken as the resolution. The distributions of the energy resolution 4.6 are fitted as a superposition of a single Gaussian and a polynomial of second order to account for the tails.

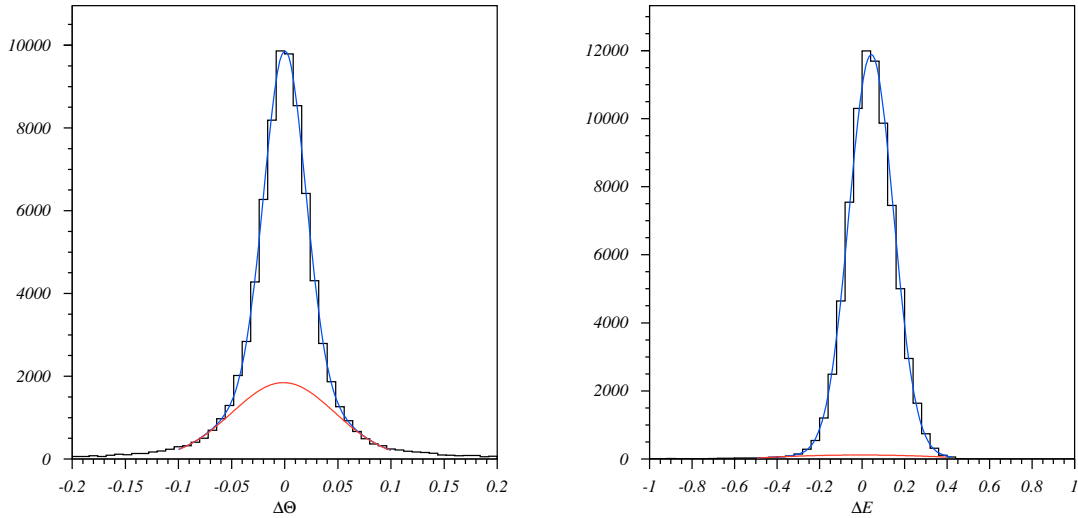


Figure 4.2: Example for a fit to the resolution of the polar angle with the two Gaussian approach (left) and of the energy with a Gaussian and a polynomial of the second order (right).

Monte Carlo samples

For the resolution studies event samples of the following processes are used:

$$\begin{aligned} e^+e^- &\rightarrow Z^*/\gamma^* \rightarrow q\bar{q}(\gamma) \\ e^+e^- &\rightarrow W^+W^- \rightarrow q\bar{q}\nu \end{aligned}$$

The events are generated using the PYTHIA and KORALW programs, and passed through the full L3 detector simulation. The total numbers of events are $\simeq 2.5 \cdot 10^6$ for $e^+e^- \rightarrow q\bar{q}(\gamma)$ and $\simeq 1.5 \cdot 10^6$ for $e^+e^- \rightarrow W^+W^-$ in the centre-of-mass energy range between 192 and 208 GeV.

Event Selection

The signature of the events used in this analysis is two well separated jets with or without an isolated lepton. For events of $e^+e^- \rightarrow q\bar{q}(\gamma)$ the energy deposited in the detector, E_{vis} , must be about the centre-of-mass energy, \sqrt{s} . The effective annihilation energy, $\sqrt{s'}$ must be near \sqrt{s} , and the jets must be almost back-to-back. In events of $e^+e^- \rightarrow W^+W^-$ with one W decaying leptonically some energy is lost due to the neutrino. The invariant mass of the two jets must be consistent with the W mass. Events with a topology different from two-jet are further suppressed by the requirement of small values of Y_{23}^D , where Y_{23}^D is the jet resolution parameter for which an event goes from two-jet to three-jet topology using the DURHAM clustering algorithm described in Section 4.3.1.

The cuts applied for the selection of each channel are listed in Table 4.2.

In addition, to ensure clean di-jet samples, only two high energy partons are allowed on generator level. Furthermore, W decays into τ lepton are not accepted.

Variable	Cut value for $q\bar{q}$	Cut value for W^+W^-
E_{vis}/\sqrt{s}	> 0.82	–
Aplanarity	> 2.8 rad	> 0.5
Acolinearity	> 2.8 rad	> 0.5
Y_{23}	< 0.025	< 0.035
S'/S	> 0.91	–
di-jet mass	–	$\in [60.0:100.0]$

Table 4.2: Selection cuts for $e^+e^- \rightarrow q\bar{q}(\gamma)$ and $e^+e^- \rightarrow W^+W^-$ channels.

Using these two processes allows to cover the range of jet energies between $\simeq 20$ GeV (lowest from $e^+e^- \rightarrow W^+W^-$) up to $\sqrt{s}/2$ (highest from $e^+e^- \rightarrow q\bar{q}(\gamma)$). This is illustrated in Figure 4.3, where the parton energy for $e^+e^- \rightarrow q\bar{q}(\gamma)$ and $e^+e^- \rightarrow W^+W^-$

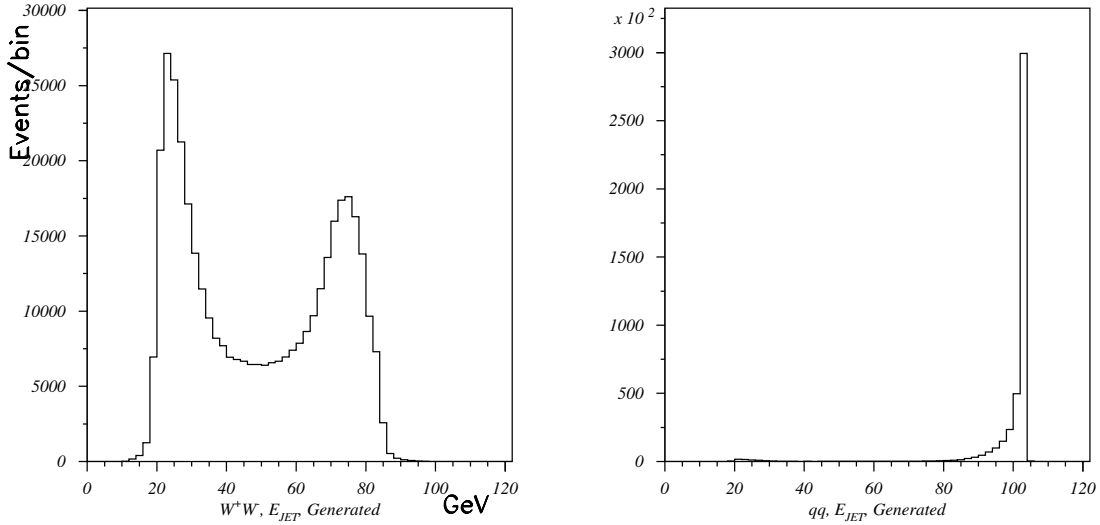


Figure 4.3: Parton energy distribution for W^+W^- (left) and $q\bar{q}$ (right) final states.

events is distributed.

Angular and Energy Dependence of the Resolutions

The energy resolution of the L3 sub-detectors depends on the energy, with different functional form for each sub-detector. Hence we expect also an energy dependence of the resolutions for the jet measurements on the energy. The structure of the L3 detector, shown in Figure 4.4, is not homogeneous in Θ . Hence, a dependence on the polar angle Θ is also expected.

First, the polar angle Θ is subdivided in slices, as shown in Figure 4.4. For each

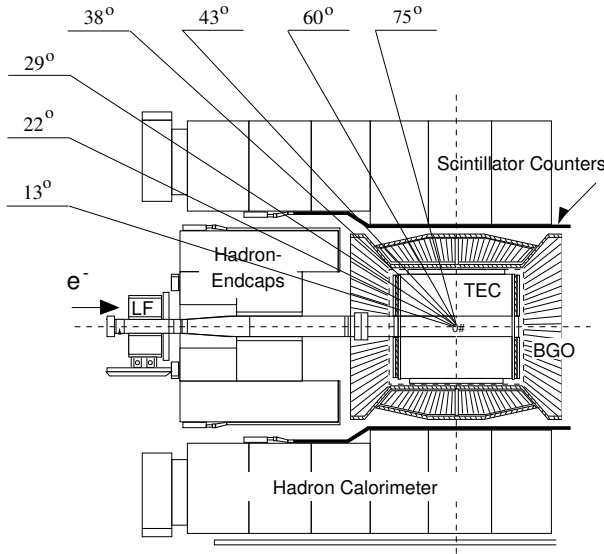


Figure 4.4: The layout of L3 detector and the slices in Θ .

slice the quantities defined in Equations 4.6 are distributed and fitted. The width of the Gaussians, σ_i , where i is Θ , ϕ or E , is then displayed as function of Θ .

Figure 4.5 shows σ_Θ , σ_ϕ and σ_E as function of Θ using events from $e^+e^- \rightarrow q\bar{q}(\gamma)$. Smoothly varying dependences are found. The last plot in this Figure, d), shows σ_Θ as a function of Θ as obtained from the $e^+e^- \rightarrow q\bar{q}(\gamma)$ and $e^+e^- \rightarrow W^+W^-$ samples separately. The dependences show the same shape but the function for $e^+e^- \rightarrow W^+W^-$ is shifted to larger values, pointing to a dependence of the Θ resolution on the jet energy. This is clearly seen in Figure 4.6, where the energy dependence of σ_Θ , σ_ϕ and σ_E is displayed. The distributions of Figures 4.5 and 4.6 are fitted with parametrisations $R_x(\Theta)$ and $R_x(E)$, with $x = \Theta, \phi, E$, which hereafter are called the resolution functions.

Comparison with Control Data

A comparison of the dependence of the energy resolution on Θ between data and Monte Carlo is done using a clean event sample of $e^+e^- \rightarrow q\bar{q}(\gamma)$ events from the year 2000 data taking. The quantity $\Delta E = \frac{\sqrt{s} - E_{jet}}{\frac{\sqrt{s}}{2}}$ is distributed for slices in Θ as defined in Figure 4.4. Each distribution is fitted with a Gaussian. The dependence of the width, σ_E , on the polar angle Θ is shown in Figure 4.7. The distributions from data and Monte Carlo events agree well within the statistical uncertainties.

A comparison of the angular resolution is less straightforward. The resolution in ϕ is expected to effect the shape of the aplanarity distribution. The acolinearity distribution may be affected by both the ϕ and Θ resolutions. A comparison of the aplanarity and acolinearity distributions for di-jet events from data and Monte Carlo is shown in Figure 4.8.

The agreement is very good, giving confidence that the resolution functions derived from Monte Carlo describe the detector response.

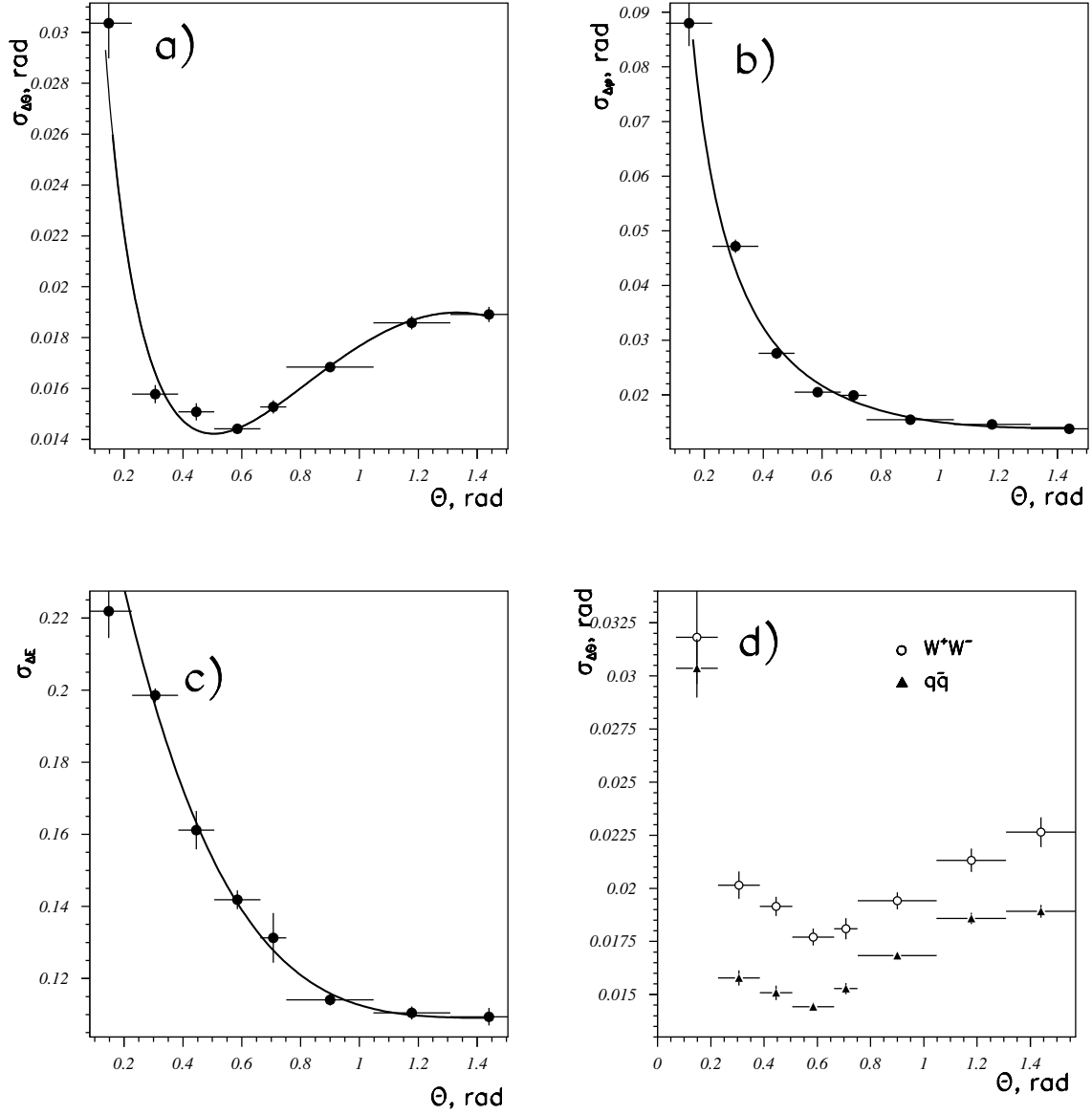


Figure 4.5: The dependence of the resolutions in a) Θ , b) ϕ and c) E on the polar angle Θ using $e^+e^- \rightarrow q\bar{q}(\gamma)$ events. d) shows the dependence of the resolution in Θ as function of Θ for $e^+e^- \rightarrow q\bar{q}(\gamma)$ and $e^+e^- \rightarrow W^+W^-$ separately.

Two dimensional Parametrisation

In order to obtain a proper description of the jet resolution as function of the energy and the polar angle, two dimensional parametrisations are constructed. These new resolution functions, denoted as $R_{\Theta}(\Theta, E)$, $R_{\phi}(\Theta, E)$ and $R_E(\Theta, E)$ are defined as:

$$R_x(\Theta, E) = N_x \cdot R_x(\Theta) \cdot R_x(E)$$

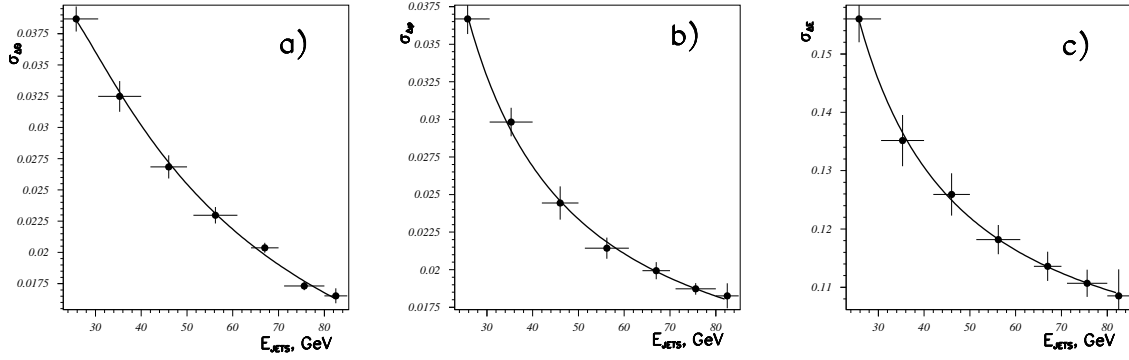


Figure 4.6: The a) Θ , b) ϕ and c) E resolutions as functions of the jet energy.

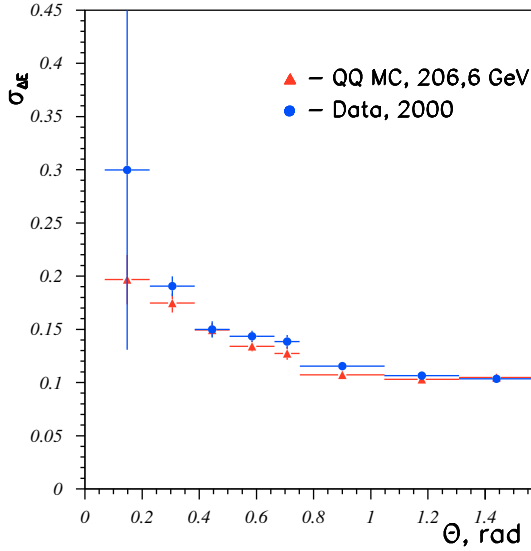


Figure 4.7: The energy resolution as a function of the polar angle Θ for data and Monte Carlo.

where x denotes Θ , ϕ or E and N_x is a normalisation factor. To obtain this factor a two-dimensional fit is performed. This procedure consists of two steps. First, a “grid” of a 6x6 matrix of the distributions defined in Equation 4.6 with six bins in energy and six bins in Θ is created. Each distribution is then fitted as described in the one-dimensional case. The values obtained for the width in each field of the grid, $\sigma_x^{grid}(\Theta, E)$ and its error, $\delta\sigma_x^{grid}(\Theta, E)$, are then used to minimise the quantity

$$\chi^2 = \sum_{i,j} \frac{(N_x \cdot R_x(\Theta_i) \cdot R_x(E_j) - \sigma_x^{grid}(i, j))^2}{\delta\sigma_x^{grid}(i, j)^2}$$

by varying the normalisation factor N_x . Bin-center corrections were taken into account.

The two-dimensional resolution functions obtained in this way are shown in Figure 4.9. Their parametrisation in terms of Θ and E reads:

$$R_{\Theta}(\Theta, E) = 51.726 \cdot \left(\frac{1.3664}{\sqrt{1.0 + E^2}} - \frac{10.861}{1.0 + E^2} - 0.0022766 \right) \times$$

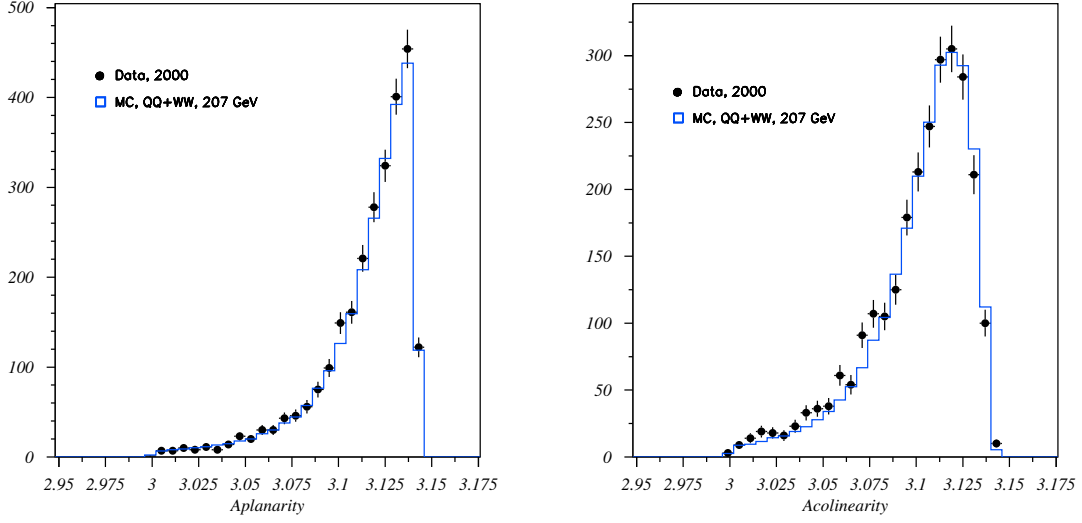


Figure 4.8: Aplanarity and acolinearity between two jets for data and Monte Carlo.

$$\left(\frac{0.22386}{\Theta_{fl}^{0.1}} + 0.0655 \cdot \Theta_{fl} - 0.016299 \cdot \Theta_{fl}^2 - 0.24935 \right) \quad (4.7)$$

$$R_\phi(\Theta, E) = 46.509 \cdot \left(\frac{0.74759}{\sqrt{1.0 + E^2}} - \frac{0.484}{1.0 + E^2} + 0.0094398 \right) \times \left(\frac{0.018577}{\Theta_{fl}} + 0.0095581 \cdot \Theta_{fl} - 0.0095483 \right) \quad (4.8)$$

$$R_E(\Theta, E) = 8.547 \cdot \left(\frac{0.14971}{\sqrt{1.0 + E^2}} + \frac{35.5}{1.0 + E^2} + 0.11176 \right) \times \left(0.033657 \cdot \left(\Theta - \frac{\pi}{2} \right)^4 + 0.1091 \right) \quad (4.9)$$

where $\Theta_{fl} = \Theta$ if $\Theta \leq \frac{\pi}{2}$ and $\Theta_{fl} = \pi - \Theta$ if $\Theta > \frac{\pi}{2}$.

Application to the analysis

The parametrisation of the resolution functions is applied in the L3 software which performs the constrained kinematic fit. With the properly constructed error matrix in the fitting routine we expect to improve the quality of the fits. A sample of Monte Carlo events of the process $e^+e^- \rightarrow ZH$ with $M_H = 110$ GeV is used. After a loose 4-jet selection the events are subject of two kinematic fits (see Section 4.3.2) imposing energy and momentum conservation and, as a fifth constraint, forcing the two di-jet masses to be equal (first fit) and the invariant mass of the two jets assigned to the Z decay to the mass of the Z (second fit).

A first check, whether the errors of the jet measurement are properly described, is the shape of the χ^2 probability, $P(\chi^2)$, distribution of the fits, which is expected to be flat. In

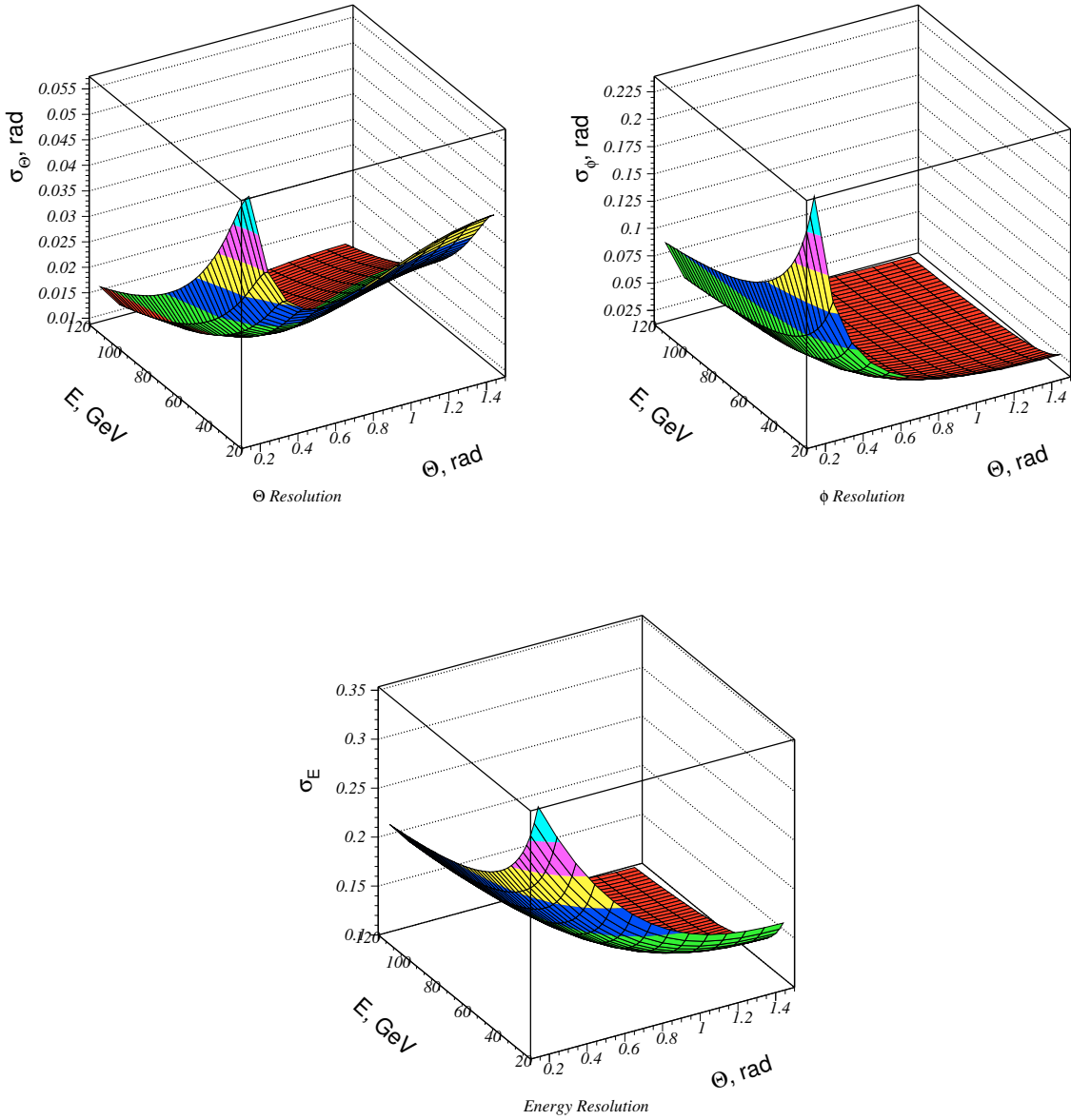


Figure 4.9: Two-dimensional resolution function parametrization for Θ , ϕ and E .

Figure 4.10 can be seen that the $P(\chi^2)$ distribution obtained with the implementation of the new parametrization has a less steep slope than the $P(\chi^2)$ distribution obtained from the old L3 standard fitting software which is also shown in Figure 4.10. Moreover the fraction of events in the bin near $P(\chi^2) = 0$ become less with the new parametrization. This enhancement near zero is expected due to the tails in the resolutions not described by a single Gaussian but also from wrong jet combinations.

The distributions of the invariant mass obtained in the first and second fit is shown in Figure 4.11.

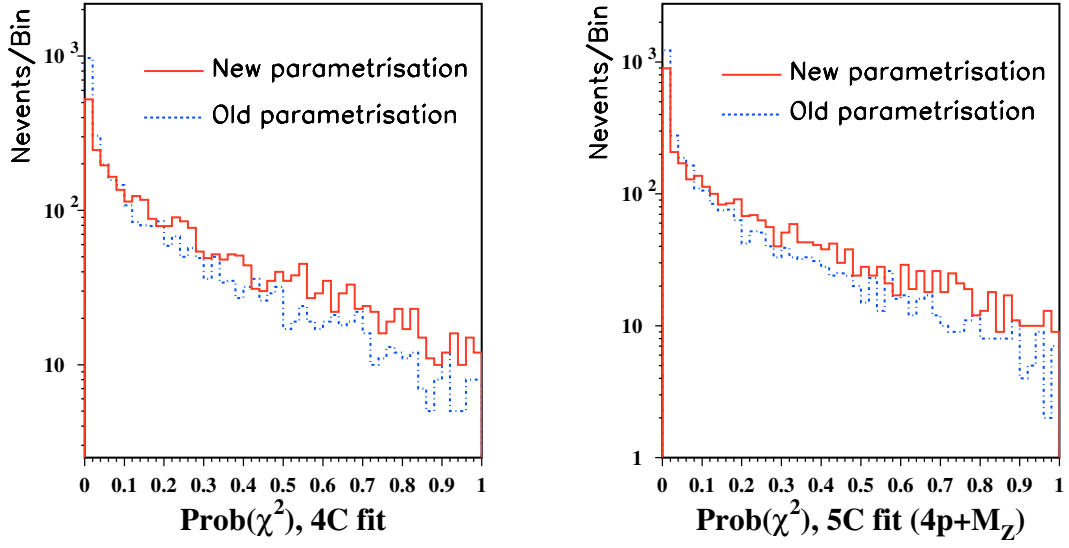


Figure 4.10: Probability of 4C (energy and momentum conservation) fit χ^2 and 5C (4C + additional constraint on the Z boson mass) χ^2 using events of $e^+e^- \rightarrow ZH$. The center-of-mass energy is 206.6 GeV and the mass of the Higgs boson, $M_H=110$ GeV.

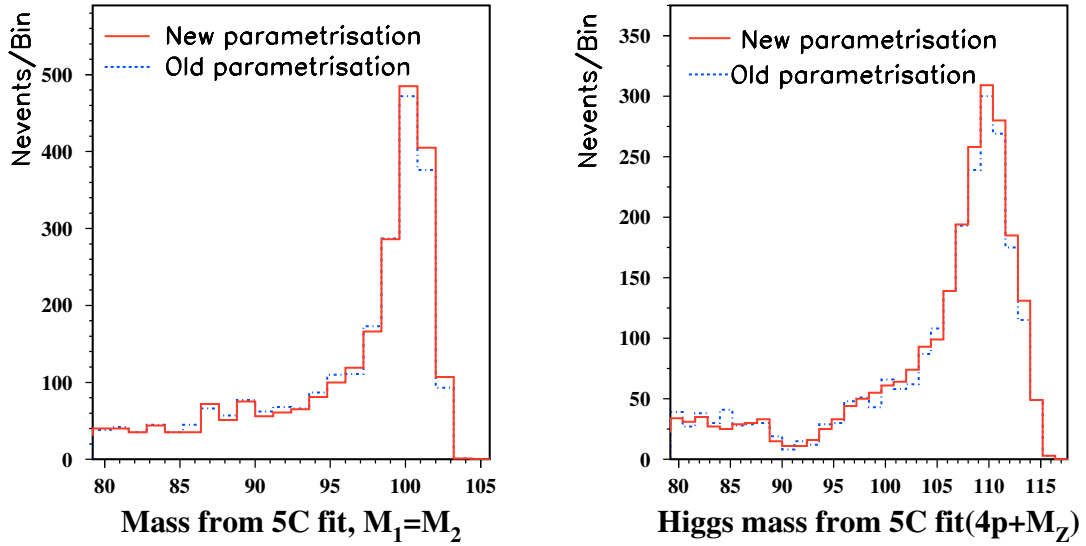


Figure 4.11: Mass for the 5C fit imposing equal mass constraint and Higgs mass after 5C fit with the constraint on the invariant mass of two jets assigned to the Z to be equal to mass of the Z boson using events of $e^+e^- \rightarrow ZH$. The center-of-mass energy is 206.6 GeV and the mass of the Higgs boson, $M_H=110$ GeV.

The same distributions are also shown using the standard software. For both mass

distributions the new parametrisation of the resolution functions enhances the fraction of events in the peak region by $3 \div 5\%$.

4.3.4 B-tagging

Equation 2.68 shows that the Higgs boson decays predominantly into the heaviest fermion kinematically allowed. For the Higgs boson mass range covered by LEP the heaviest fermion is the b-quark (see Figure 2.11). Therefore, one of the most important analysis steps in the search for Higgs boson is the tagging of b-quarks.

Hadrons containing the b-quark have relatively longer lifetime than many hadrons containing c or light quarks. Typical lifetimes and decay lengths of the b hadrons and other particles that can contaminate the sample of b-tags are shown in Table 4.3. At LEP

Particle	Lifetime (ps)	Typical boost $\gamma\beta$ $\sqrt{s} = 91.2 \text{ GeV}$	Decay length $\gamma\beta c\tau$ (mm) $\sqrt{S}=91.2 \text{ GeV}$
B^\pm	1.65 ± 0.04	6	3.0
B^0	1.56 ± 0.04	6	2.8
B_s^0	1.54 ± 0.07	6	2.8
<i>b baryon</i>	1.22 ± 0.05	5.5	2.0
b hadron	1.564 ± 0.014	6	2.8
D^\pm	1.057 ± 0.015	12	3.8
D^0	0.415 ± 0.004	12	1.5
D_s^\pm	0.467 ± 0.017	11.5	1.6
Λ_c^\pm	0.206 ± 0.012	10	0.6
τ lepton	0.291 ± 0.02	25.5	2.2
K_s^0	89.27 ± 0.09	6	160
Λ^0	263 ± 2	2.5	197

Table 4.3: Lifetimes and decay lengths of b hadrons and other particles. The calculation of the typical boosts assumes that the average energy carried away by the hadron is $\langle x_E = E_{hadron}/E_{beam} \rangle \simeq 0.7$ for the b hadrons, ~ 0.5 for the c hadrons and ~ 0.07 for the light flavored hadrons [77]. The row in boldface shows the typical decay lengths to which an inclusive b-tag, such as the one used in the Higgs searches, would be sensitive.

energies this corresponds to the decay length of a few millimetres which is a resolvable distance thanks to the TEC and especially, to the SMD sub-detectors. The b-tagging primarily relies on the decay length information of tracks produced in the collisions. It can be seen from the Table 4.3 that with the typical decay length of 1 mm c-hadrons represents the main source of background for b-tagging. On the other hand, the b-hadrons are characterised by smaller boosts, $\gamma\beta$, in comparison with hadrons composed of c quarks. Typical value of the boost for the B^0 at $\sqrt{s} = 91.2 \text{ GeV}$ is 6, when for

the D^0 this value is 12. Smaller boosts and larger masses of b-hadrons will result in a larger angles between the direction of the b-hadron flight and momentum vectors of the decay products. Other hadrons are either very short lived, decaying practically at the production vertex, or have enough long lifetime to pass through the detector before they decay. Exceptions are K_s and Λ hadrons, with the lifetimes of $\tau(K_s) = 89.3$ ps and $\tau(\Lambda) = 263$ ps and on average decay at distances of about 150 – 200 mm from the production point. Identified K_s 's and Λ 's are removed from the list of tracks used in the b-tagging procedure.

The detailed description of the L3 b-tagging technique can be found in References [77, 78]. In this thesis the main principle is highlighted. The first step of the procedure is the e^+e^- interaction primary vertex reconstruction. The primary vertex reconstruction starts from the average of 200 e^+e^- collisions or fill vertex which is a measure of the position of the LEP beam spot. The procedure of the beam spot size calculation and the primary vertex coordinates determination is discussed in details in Appendix A. In the plane perpendicular to the beam direction (i.e., the $x - y$ plane) the beam spot is of elliptic shape¹, and the primary vertex is constrained to the beam spot envelope. The beam spot position along the beam direction (z - axis), however, is large, $\sigma_z \simeq 7$ mm, compared to the attainable resolution from the tracking information alone and therefore is not used in the constraint. The next step after the the primary vertex reconstruction is the determination of the track decay length along the axis of the jet to which it belongs. The distance between the primary vertex and the crossing point of the track and the jet axes defines the decay length for the track. This distance is projected onto $r - \phi$ and $s - z$, where the $s - z$ plane is defined as the dimension orthogonal to the $r - \phi$ plane where the projected helical trajectory of a track in the solenoidal magnetic field traces out a straight line. The decay lengths in two planes, $L_{r\phi}$ and L_{sz} , are calculated as illustrated in Figure 4.12. These are signed quantities: the decay length is positive if the track crosses the jet axis in the supposed direction of flight; conversely, the decay length is negative if the crossing takes place in the propagated opposite direction of the jet. Using decay lengths in two planes $L_{r\phi}$ and L_{sz} and their error matrix, the weighted average decay length, L , is formed. The decay length significance, $S = L/\sigma_L$, are constructed for different categories of tracks depending on the availability of SMD and Z-chamber information. Figure 4.13 shows the significance S distribution for the category of tracks with both SMD hits (two space points) in data taken at center-of-mass energy $\sqrt{s} = 91$ GeV. The negative side of the distribution is due to finite resolution of the detector. While for the light quarks the decay length significance distribution is symmetric with respect to zero, the c quarks distribution has a shift asymmetry to positive values and the b quarks give rise for the clear excess at the positive side of the distribution.

In the final step of b-tagging, the decay length information for the tracks is combined to form variables characterising the b-quark content of a jet, a hemisphere and a whole event. The combination uses the probability $P(S)$ that a given track with decay length significance S has originated from the primary vertex. In order to have a function describing this probability, the left side of the significance distribution is used, as it cor-

¹The elliptic shape of the beam spot is due to the combine effect of focusing and synchrotron radiation, which induces a spread of the beam particles momenta.

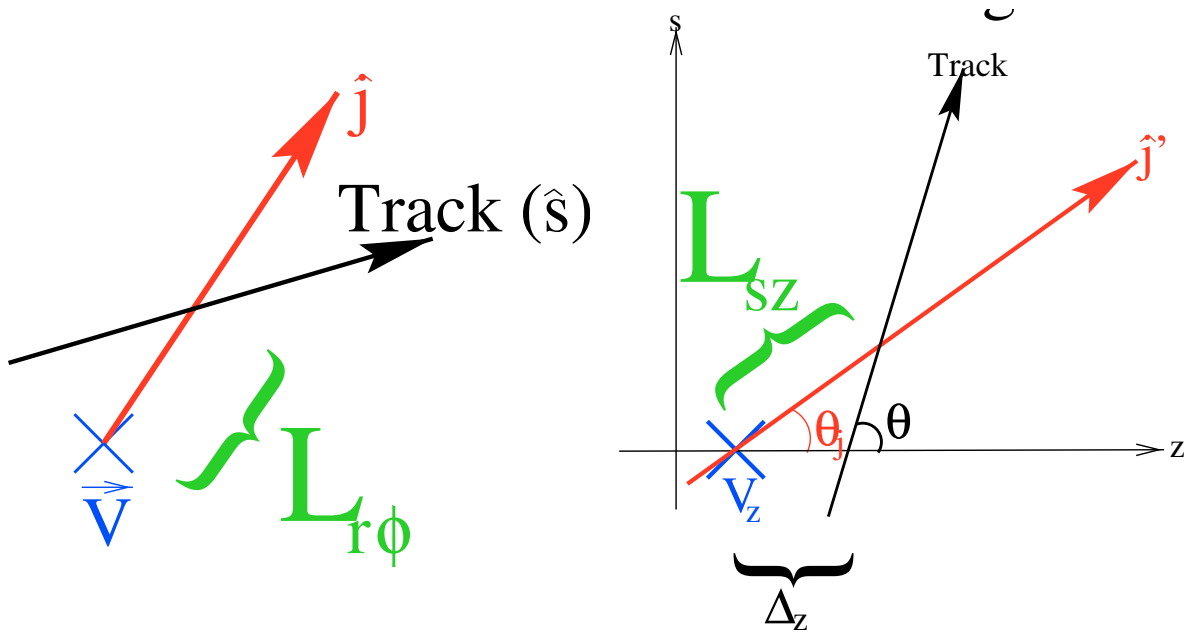


Figure 4.12: The definition of the tagging variable in the $r - \phi$ plane, $L_{r\phi}$ (left) and in $s - z$ plane, L_{sz} , (right).

responds to the sample of zero lifetime tracks. These probability functions are different for different categories of tracks. Values of $P_i(S)$, $i = 1, n_{track}$ for all tracks in the event are combined into P_{events} variable. Events with clear lifetime information have values of P_{events} close to zero. The event b-tagging variable is related to P_{events} , as:

$$D_{Btag} = -\log(P_{events}). \quad (4.10)$$

The distribution of the discriminant D_{Btag} for hadronic events in 1999 data at $\sqrt{s} = 91$ GeV and Monte Carlo for b-, c- and light quarks are shown in Figure 4.14. This Figure also illustrates the discriminating power of this variable in terms of tagging efficiency and purity.

To further improve the b-tag performance, a neural network [80] is used. It exploits in addition to the discriminant above, which is the most powerful variable, information about possibly reconstructed secondary vertices and their track multiplicity, the invariant masses at the primary and secondary vertices, momenta of inclusive leptons and jet shape variables, such as the jet velocity and the sphericity [81]. The neural network output spectrum for calibration data taken at the Z peak in 1999 can be seen in Figure 4.15.

The tracking and b-tagging performances are tuned using 4 pb^{-1} of calibration data collected at $\sqrt{s} \sim m_Z$.

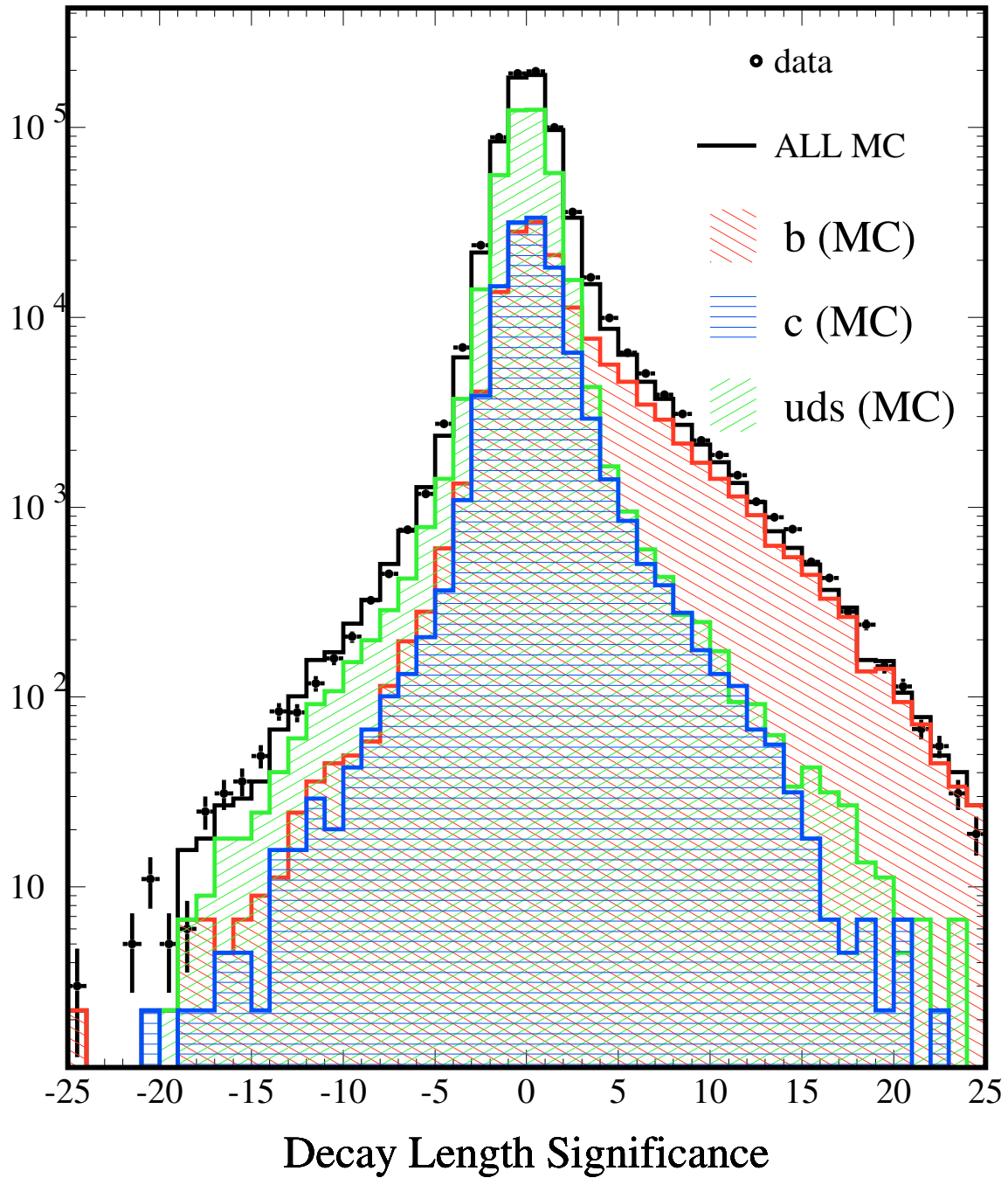


Figure 4.13: Decay length significance for tracks with all SMD hits.

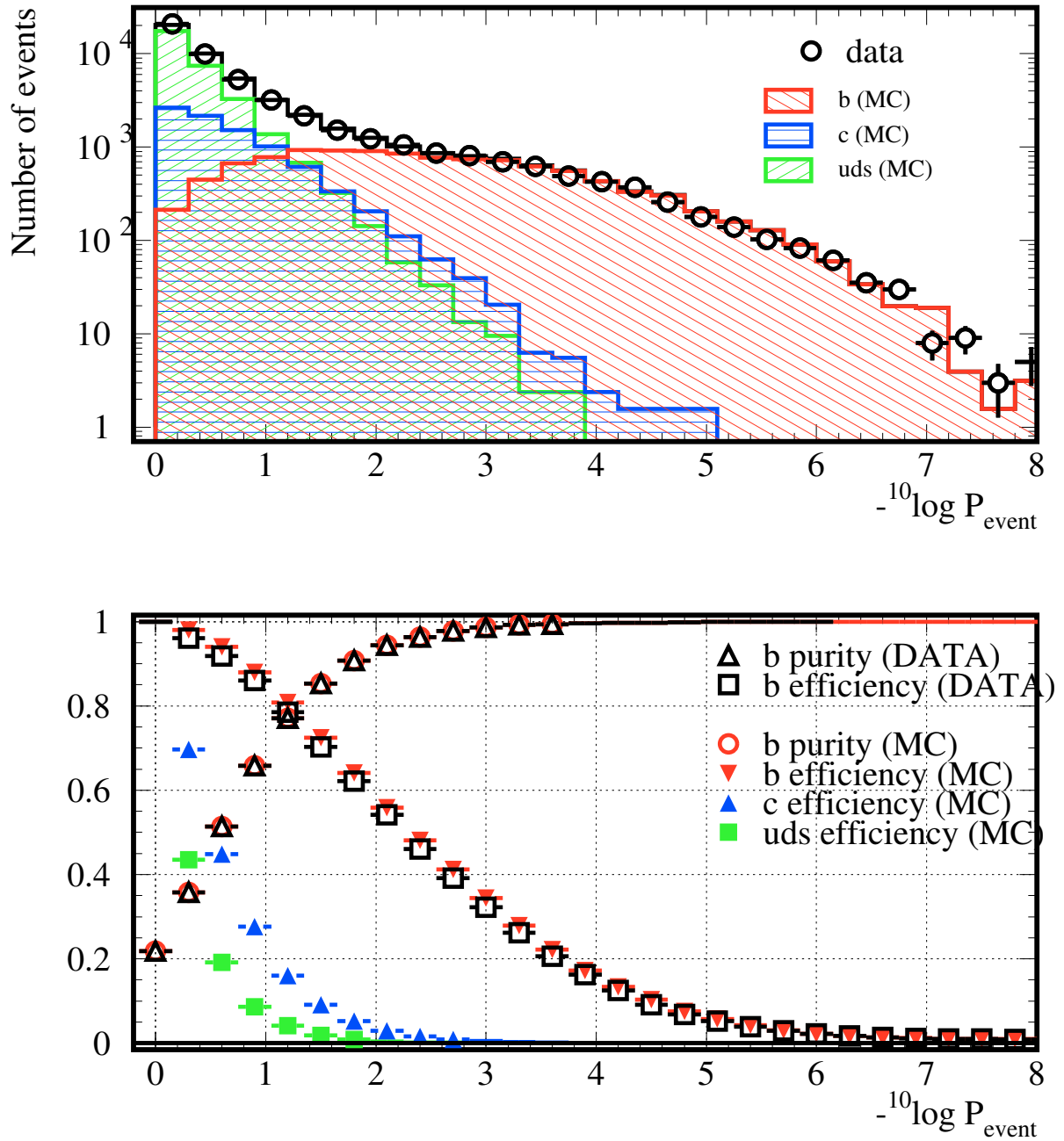


Figure 4.14: Event *b*-tagging discriminant distribution (upper plot) and tagging efficiency and purity as a function of cut on $-\log(P_{event})$ (lower plot) in 1999 Z-peak data and MC.

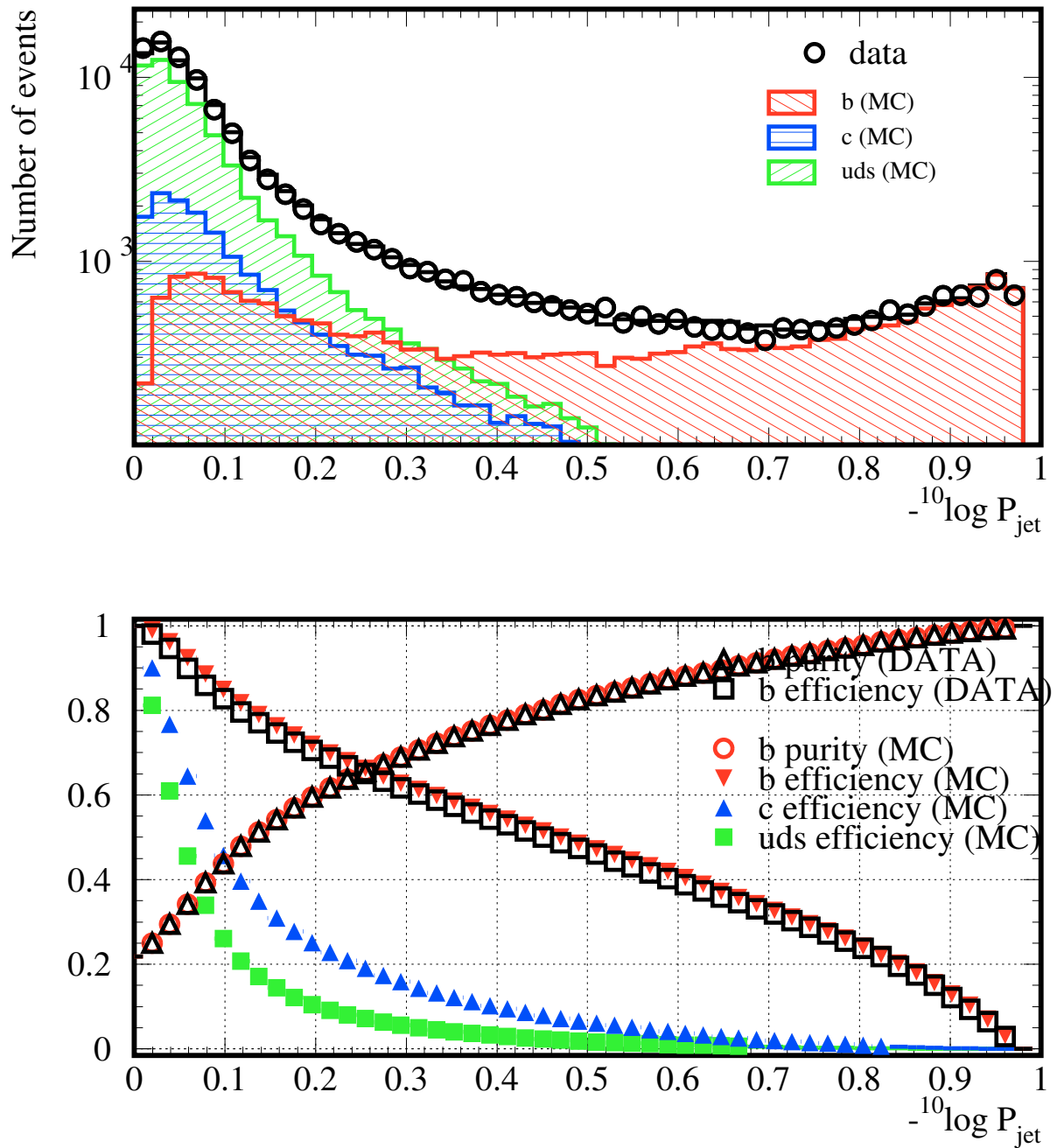


Figure 4.15: The output of the neural network jet tag (upper plot) and corresponding efficiency and purity (lower plot) in 1999 Z peak data and Monte Carlo [79].

Chapter 5

Search for the Standard Model Higgs Boson

In chapter 2 the production and the decay of the Standard Model Higgs boson at highest LEP energies was discussed in detail. In this thesis the following channels are investigated:

- $HZ \rightarrow b\bar{b}q\bar{q}$
- $HZ \rightarrow b\bar{b}\nu\bar{\nu}$
- $HZ \rightarrow b\bar{b}l^+l^-$ and $HZ \rightarrow \tau^+\tau^-q\bar{q}$.

The first channel is studied by the author of this thesis. For the second channel the various cross checks of the analysis using control data, are also done by the author. The principal analysis of the second channel and the other channels, covered by my colleagues from the Higgs Working Group [82] are presented here for sake of completeness. For each of these channels a dedicated selection has been performed putting emphasis on the particular signature of the given final state. With the exception of the $HZ \rightarrow \tau^+\tau^-q\bar{q}$ decay mode, all the analyses are optimised for the $H \rightarrow b\bar{b}$ decay. The general analysis procedure and special analysis techniques are described below.

5.1 Analysis Procedure

All the search channels are analysed in three stages. First, a high multiplicity hadronic event preselection is applied to reduce the large background from two-photon processes, while preserving most of the Higgs boson signal. In a second stage, a kinematic fit is performed which takes into account energy and momentum conservation as well as the constraint that the jet or lepton pair arising from a Z decay has an invariant mass equal to mass of the Z boson, m_Z .

At the next step, topological and kinematical variables together with b-tag variables are used either to construct an event likelihood or fed into a neural network depending on the search channel, to further discriminate between signal and background events. A

b-tag variable is calculated for each hadronic jet, as described in Section 4.3.4. The event b-tag variable is then obtained as a combination of the b-tag variable for each hadronic jet. The b-tagging performance for the high-energy data is verified with samples of $e^+e^- \rightarrow q\bar{q}(\gamma)$ events [83]. The efficiency for tagging light flavoured hadrons is verified with $W^+W^- \rightarrow q\bar{q}l\bar{\nu}$ events.

The last part of the analysis is the construction of a final discriminant for each topology, is described in the Section 5.1.3. It is built from a combination of the event likelihood, or the neural network output, with the reconstructed Higgs boson mass, obtained from the kinematic fit. For each Higgs boson mass hypothesis, the final discriminant is computed for the data and for the expected background and signal. The distributions of the final discriminants are then used to calculate a quantity evaluating the compatibility of the data with the signal, as described in the Chapter 6.

5.1.1 Preselection

The basic goal of this step is to get rid of obvious background events, significantly reducing further processing time. Cuts are placed on a set of variables to suppress background events which are very dissimilar from the signal. Although this is technically the simplest step, it removes the majority of background events and maintains a very high signal efficiency for a broad range of possible signals. The set of variables and cut values used in the preselection stage differs for each search channel and will be discussed in detail further, for each channel separately.

5.1.2 Cut Optimization

In contrast to the preselection step, where the cuts were chosen “by hand”, this step meant to simultaneously remove some “human bias” and to choose the optimal set of cuts that gives the best performance of the analysis. A set of variables, in general different from the preselection variables, are chosen which have some distinguishing power between signal and the background events remaining after the first round of cuts. All the cuts on these variables are independently varied by a computer program that uses MINUIT [84] to reach the minimum of the minimisation function, discussed below. When this function is estimated to be near its minimum value, the cut values are noted.

5.1.3 The Final Discriminant

In this step of the analysis, after the selection, the most discriminating variable is used to evaluate the existence of a signal. In some channels the most discriminating variable after the applied selection is used as the final discriminant, in some channels several most discriminating variables are combined to form the final discriminant. For example, in the $\tau^+\tau^-q\bar{q}$ channel, the mass of the tau pair, calculated by constraining the invariant mass of the two other jets to m_Z , is used as the final discriminant. In four-jet analysis the final discriminant is constructed as combination of several variables using a binned likelihood technique [85]: for each event class $j = (WW, q\bar{q}(\gamma), ZZ, HZ)$, probability density functions $f_j(x_i)$ are derived from Monte Carlo, where x_i denotes a certain

variable, which has discriminating power between the signal class and the background classes. The probability of an event to belong to the event class j , based solely on the value of the variable x_i , is then defined as

$$p^j(x_i) = \frac{f_j(x_i)}{\sum_k f_k(x_i)}. \quad (5.1)$$

where k runs over all classes.

Finally, the individual probabilities are combined into a likelihood. The likelihood that an event belongs to the signal class F_{HZ} is given by the following equation:

$$F_{\text{HZ}} = \frac{\prod_i p^{\text{HZ}}(x_i)}{\sum_k \prod_i p^k(x_i)}, \quad (5.2)$$

where k runs over all event classes and i over all variables considered. The denominator in Equation 5.2 ensures that the value of F_{HZ} lies between zero and one. By including the mass information, this final discriminant becomes mass dependent and needs to be recalculated for every Higgs mass hypothesis that is made.

5.1.4 Interpretation of Observed Data

At this stage we have a final discriminating variable and we know its performance on Monte Carlo. Here we apply the same optimised cuts and build the same final variable for the collected data. In Chapter 6 we define a confidence level that represents the consistency between the actual data and a signal in the presence of background. This is done over the range of possible Higgs boson masses, which represents our “scan” over the data.

5.2 The $\text{HZ} \rightarrow b\bar{b}q\bar{q}$ channel

The $\text{H}q\bar{q}$ analysis aims to select events with four jets, two of which contain b hadrons, while the other two must be consistent with the decay of Z boson. Background from the Standard Model processes, as we discussed in Section 2.4.3, comes mainly from $q\bar{q}$ final states with hard gluon radiation, W^+W^- and ZZ events, especially those where one of the Z bosons decays into b quarks.

First, a high multiplicity hadronic preselection is applied, requiring at least 15 tracks and 50 calorimetric clusters. The energy deposited in the detector, so-called visible energy E_{vis} , must be greater than 70% and not exceed 125 % of the center-of-mass energy.

Leptonic decays of the bosons from gauge boson pair production are suppressed by the requirement on the energy of an isolated electron or muon to be less than 40 GeV. Additionally, events with an isolated photon of more than 20 GeV energy are rejected. However, it will only work if the photon came into detector, rather than down the beam line.

In case where a photon is emitted down the beam pipe, or when a neutrino is produced, there will be less energy left in the detector. Momenta of clusters are defined considering each of the energy clusters in the detector as a vector with its total energy

as its magnitude and having the same direction as the cluster's location relative to the interaction point. If all the energy is captured in the detector, the energy vectors should sum to zero. If they do not, one may consider the missing energy vector to be the vector which needs to be added to make the energy vector sum zero.

The parallel energy imbalance is the component of the missing energy vector along the beamline, and hence cutting on this variable eliminates much of the radiative return to the Z events with photons escaping in the beam pipe. We require this quantity to be less than 20 %. The perpendicular energy imbalance, as the component of the missing energy vector perpendicular to the beam-line, points to the presence of energetic neutrinos in the event. We are interested only in the four-jet final state of $Hq\bar{q}$, so we cut out these and other events containing neutrino, requiring the energy imbalance perpendicular to beam direction be less than 25 %.

Remaining 2-jet events are further suppressed by rejecting events with $Y_{34}^D < 0.002$, where Y_{34}^D is the jet resolution parameter for which an event goes from four-jet to three-jet topology using the DURHAM algorithm. The Y_{34}^D parameter can be considered as a measure of how well the charge tracks and calorimetric clusters are divided into four jets. The $Hq\bar{q}$ events are much cleaner four jet events than, for instance, $q\bar{q}$ events, which can have two large jets and two small ones due to the gluon radiation.

Additionally, a measure of the angular uniformity of the energy distribution, the sphericity, defined as follows:

$$S' = \left(\frac{4}{\pi} \cdot \frac{(\sum_i p_{T,i})_{\min}}{\sum_i |\vec{p}_i|} \right)^2 \quad (5.3)$$

where \vec{p}_i is the momentum of the i th detected particle and $p_{T,i}$ the transverse momentum with respect to the direction which minimises $\sum_i p_{T,i}$, is required to be greater than 0.07. Events from $e^+e^- \rightarrow q\bar{q}$ are usually two-jet events, so the sphericity for these events is lower than for signal events.

Background originating from two-photon interactions is further suppressed by the requirement on the cosine of polar angle of event thrust vector, $|\cos \Theta_T|$ ¹, not to exceed value of 0.95.

Events passing the preselection are then forced into four-jet topology using the DURHAM clustering algorithm and a kinematic fit imposing energy-momentum conservation is performed. The numbers of expected background events and selected data events are given in Table 5.1.

After the preselection the most discriminating variables are combined into one discriminant which is then used to select events into the final sample. This discriminant, L_{HZ} , is constructed using the binned likelihood technique, introduced in Section 5.1.3. Two kinds of variables are used to calculate L_{HZ} . These are first topological and kinematic event characteristics, presented in Figures 5.1 - 5.2:

¹The *Thrust* T of an event is:

$$T = \frac{(\sum_i p_{\parallel,i})_{\max}}{\sum_i |\vec{p}_i|} \quad (5.4)$$

where \vec{p}_i is the momentum of the i th detected particle and $p_{\parallel,i}$ the parallel component momentum with respect to the direction which maximises $\sum_i p_{\parallel,i}$. This direction is called *Thrust axis*.

Data set (GeV)	204	205	206	207	208	209
WW	32.9	298.1	287.0	273.7	34.7	0.42
$q\bar{q}$	12.9	112.2	110.5	102.7	13.2	0.16
ZZ	3.1	28.3	27.3	26.2	1.1	0.01
Total background	48.9	438.6	424.8	402.7	49.0	0.6
Data	60	422	454	419	49	0

Table 5.1: Expected number of background events and the number of selected data events after the preselection. Signal selection efficiency is about 90 % for Higgs boson masses greater than 95 GeV.

number of tracks, N_{TRK} : at the present LEP energies the mass difference between Higgs boson and the gauge bosons Z and W has several observable consequences. First, a larger mass particle will produce more charged particles as it decays, since it has more energy to produce the particles from. Thus, the average number of charged tracks should be higher for HZ than for ZZ or W^+W^- ;

maximal jet triplet boost, $\gamma_{\text{triple}}^{\text{max}}$: the maximum three-jet boost obtained from the four possibilities to construct a different one-jet against three-jet constellation in a four-jet event [86]. For any boson pair production $\gamma_{\text{triple}}^{\text{max}}$ is small as the third jet comes from the oppositely flying boson and the overall three-jet system is slowed down. However for the case of QCD where significant fraction of three-jets come from the same quark leg this is not so small. Thus $\gamma_{\text{triple}}^{\text{max}}$ can be used effectively for reducing QCD background;

logarithm of jet resolution parameter, $\ln Y_{34}^{\text{D}}$: this variable still has a discriminating power after being used at the preselection level;

event b-tag : HZ sample according to our selection should always contain at least one $b\bar{b}$ pair, so we expect event b-tag to be higher for the signal events. Of the weak isospin doublets, the W boson is far too light to decay to $t\bar{b}$. Its hadronic decays are thus limited to $c\bar{s}$ and $u\bar{d}$ ². On the other hand, the Z decays to $b\bar{b}$ roughly 15% of the time [79]. Thus, 28% of ZZ events should contain at least one b.

maximal jet energy difference, ΔE^{max} : Four jet events with gluon radiation, $e^+e^- \rightarrow q\bar{q}gg$ tend to have a higher maximum jet energy than real HZ events, because the gluons will carry off only a small fraction of the total energy, leaving most of energy in the quark jets. Real four-jet events should divide the center-of-mass energy more evenly into four bits. On the other hand, HZ events should have a higher minimum jet energy than $q\bar{q}gg$ events, since the weakest jet in $q\bar{q}gg$ is usually due to a gluon and probably contains less than 10% of the full center-of-mass energy. This makes maximal jet energy difference much smaller for HZ events than for $q\bar{q}gg$ events;

²It is theoretically possible to produce b quarks from quark-mixing effects in W decays, but this effect is negligible.

the sum of the largest and the second largest di-jet boosts among three possible combinations, γ_{L2L3} [86]: this variable is also very useful to control QCD background;

event sphericity, S , defined as:

$$S = \frac{3}{2} \frac{(\sum_i p_{T,i}^2)_{\min}}{\sum_i |\vec{p}_i|^2} \quad (5.5)$$

where \vec{p}_i is the momentum of the i th detected particle. $p_{T,i}$ is the transverse momentum with respect to the direction which minimizes the sum of the squares of the transverse momenta $p_{T,i}$. The *sphericity* is close to 0 for “back-to-back” events and close to 1 for events where the particle momenta are distributed uniformly over the whole solid angle.

Second, the *dijet masses* and the *cosine of the production polar angle* assuming the production of a pair of bosons, $\cos \Theta_{2B}$, are exploited. For the scalar Higgs boson production this distribution is uniform, while for the vector bosons it is different. This set of variables mainly controls the gauge boson pair production.

Four jets can be combined to three different dijet pairings. The invariant masses of both dijet systems are compared with the expectation from the ZZ and W^+W^- final states allowing to identify background from these channels. After the 4C fit for each of three possible dijet pairings a compatibility with the hypothesis of gauge boson pair production is tested by considering the following quantities:

$$\begin{aligned} \chi_{WW}^2 &= (\Sigma_i - 2m_W)^2 / \sigma_{\Sigma_{ZZ}}^2 + \Delta_i^2 / \sigma_{\Delta_{ZZ}}^2, \\ \chi_{ZZ}^2 &= (\Sigma_i - 2m_Z)^2 / \sigma_{\Sigma_{WW}}^2 + \Delta_i^2 / \sigma_{\Delta_{WW}}^2 \end{aligned} \quad (5.6)$$

where Σ_i and Δ_i are di-jet mass sum and di-jet mass difference of the i^{th} pairing. The quantities $\sigma_{\Sigma_{ZZ,WW}}$ and $\sigma_{\Delta_{ZZ,WW}}$ are the di-jet mass sum and di-jet mass difference resolutions. These resolutions are estimated from Monte Carlo [83] and found to be 4.1 and 10.0 GeV for ZZ events and 4.0 and 6.0 GeV for W^+W^- events, respectively. They are also found to be independent on \sqrt{s} in the range considered in this thesis. The χ^2 probability, $P_{2B}(\chi^2)$, is then calculated and the jet combination with the best $P_{2B}(\chi^2)$ for either ZZ or W^+W^- hypothesis is chosen. The distribution of the $P_{2B}(\chi^2)$ is shown in Figure 5.2. For this di-jet pairing the polar production angle, Θ_{2B} , is reconstructed. Figure 5.3 displays the cosine of polar production angle of the boson.

At the next step, a 5C kinematic fit imposing energy and momentum conservation and the requirement of equal di-jet masses is performed with all 3 possible permutations of di-jet combinations.

The combination with the best χ^2 is taken and the invariant mass, M_{5C} , determined. After this fit, most of the W^+W^- background peaks at the W boson mass, around 80.41 GeV [79], the background from the Z pair production peaks close to the Z mass, m_Z , 91.187 GeV [79], while the HZ events are mostly located at $\sqrt{s}/2$, being nicely separated from background events, as can be seen in Figure 5.3.

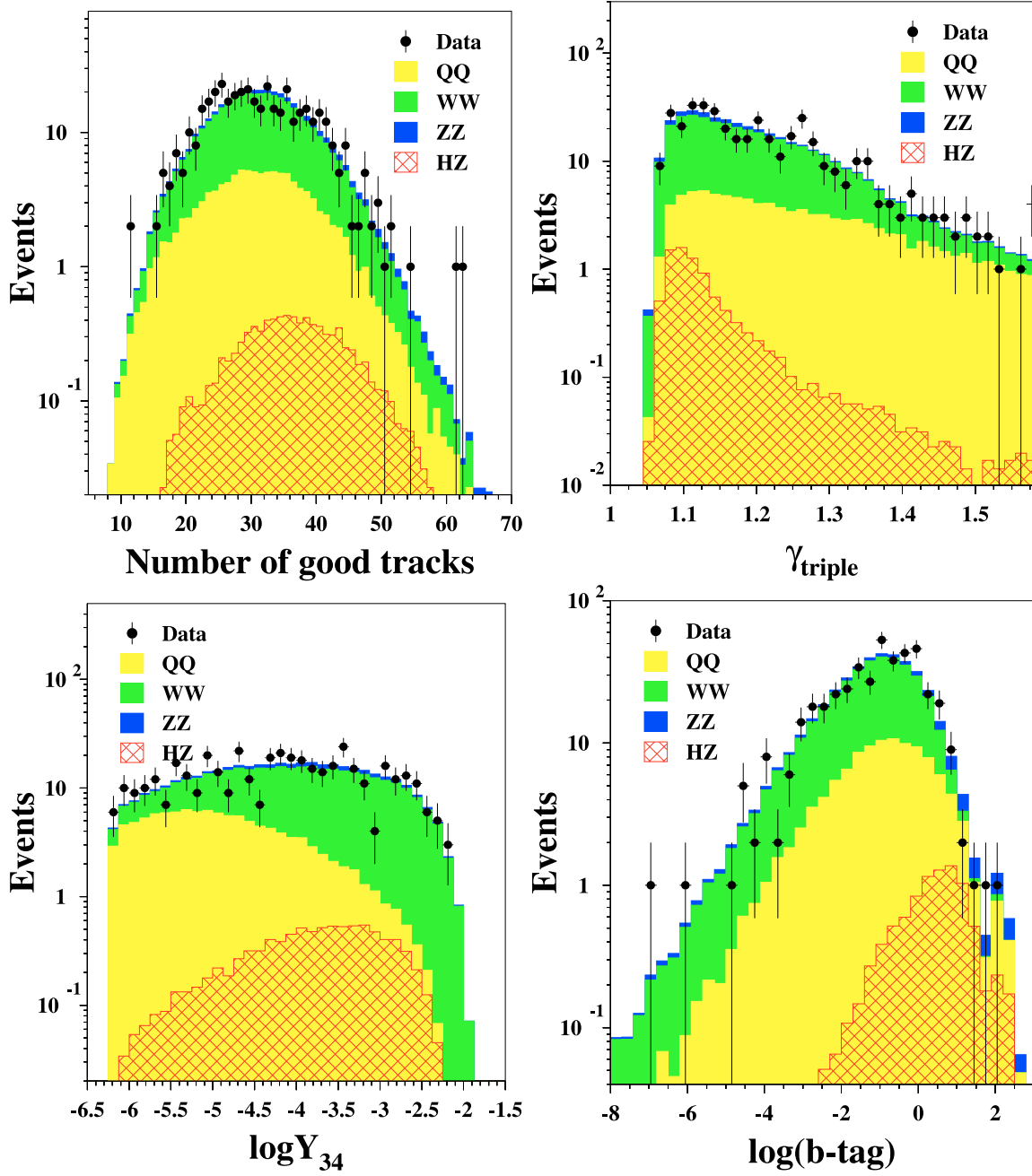


Figure 5.1: Distributions from the $\sqrt{s} = 207$ GeV data and the Higgs boson mass hypothesis of $m_{\text{H}}=110$ GeV, used for the selection likelihood construction: number of good tracks (top left), maximal jet triple boost, γ_{triple} (top right), the logarithm of jet resolution parameter, Y_{34} (bottom left) and the logarithm of the event b-tag (bottom right).

In addition, the compatibility of each event with the probed Higgs boson mass hypothesis is tested by considering the following quantity:

$$\chi_{\text{HZ}}^2 = (\Sigma_i - (m_{\text{H}} + m_{\text{Z}}))^2 / \sigma_{\Sigma_{\text{HZ}}}^2 + (\Delta_i - |m_{\text{H}} - m_{\text{Z}}|)^2 / \sigma_{\Delta_{\text{HZ}}}^2. \quad (5.7)$$

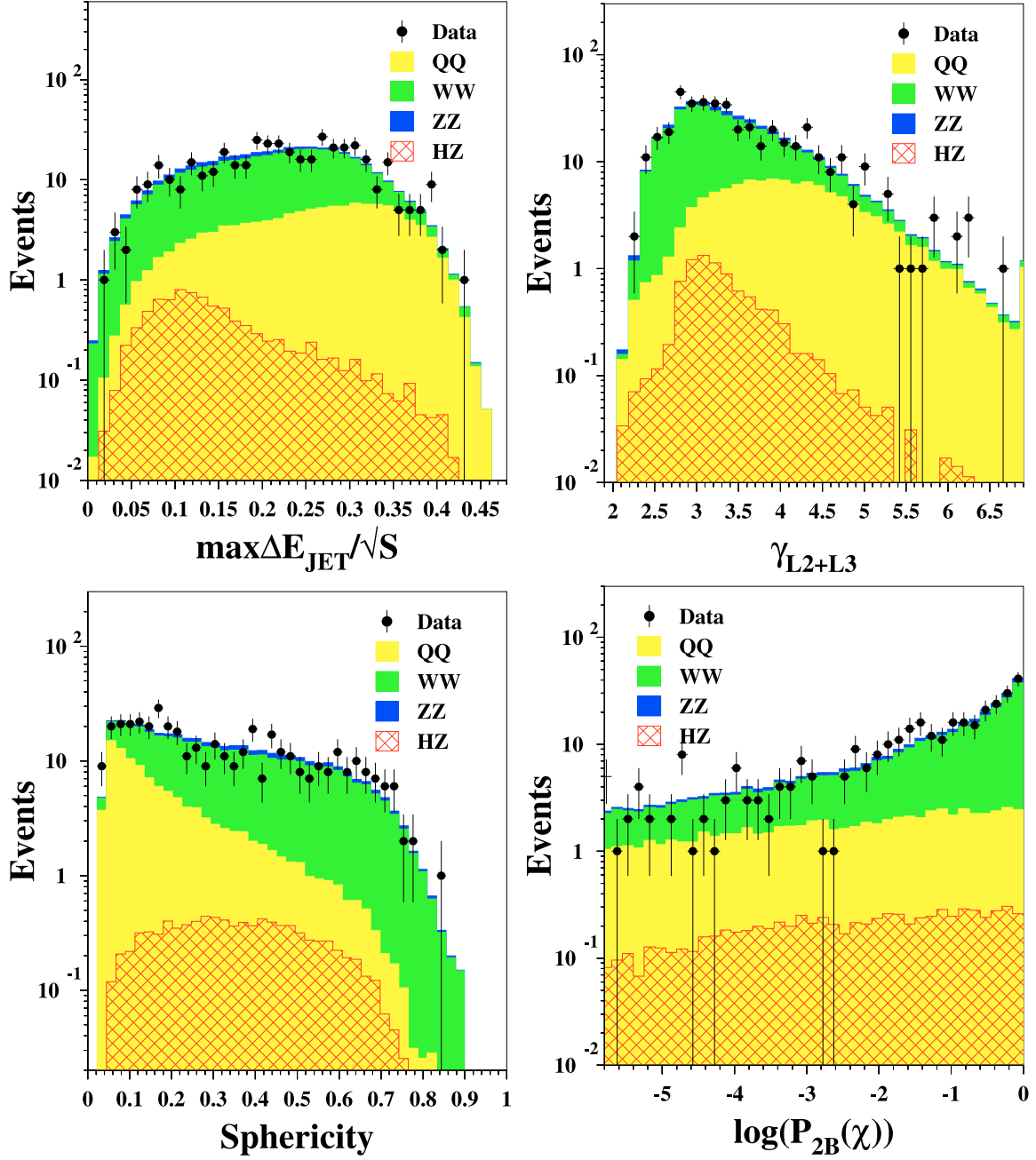


Figure 5.2: Distributions from the $\sqrt{s} = 207$ GeV data and the Higgs boson mass hypothesis of $m_H = 110$ GeV, used for the selection likelihood construction: maximal jet energy difference (top left), the sum of the largest and the second largest di-jet boosts (top right), the event sphericity (bottom left). The bottom right distribution corresponds to the logarithm of $P_{2B}(\chi^2)$ for gauge boson pair production and used for the final discriminant construction.

The resolutions $\sigma_{\Sigma_{HZ}}$ and $\sigma_{\Delta_{HZ}}$ are determined from Monte Carlo as functions of the mass of the Higgs boson for each center-of-mass energy [83]. The typical values for these resolutions at $\sqrt{s} = 207$ GeV and the Higgs boson mass hypothesis of 110 GeV are: $\simeq 3$

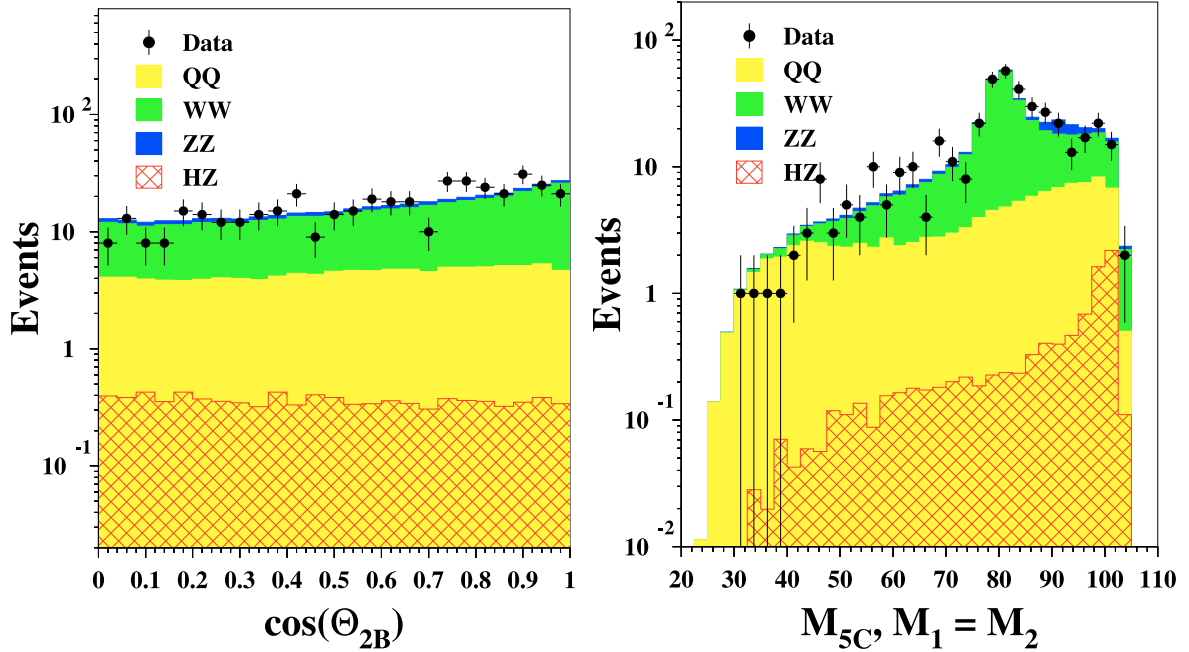


Figure 5.3: Distributions from the $\sqrt{s} = 207$ GeV data and the Higgs boson mass hypothesis of $m_H = 110$ GeV, used to construct the Final Discriminant: Cosine of polar production angle of the boson (left) and the mass from the 5C fit imposing energy and momentum conservation with the additional constraint on the equal di-jet masses (right).

for $\sigma_{\Sigma_{\text{HZ}}}$ and $\simeq 16$ for $\sigma_{\Delta_{\text{HZ}}}$. The jet pairing with the best χ^2 is chosen.

The distributions of the variables used to construct L_{HZ} , shown in Figures 5.1 - 5.3, nicely demonstrate the discriminating power, as difference in the shapes of the signal and the background samples.

Events are selected into the the final sample if the value of L_{HZ} is greater than a certain threshold, which is optimised for each center-of-mass energy and each Higgs boson mass hypothesis. After the cut, the selection likelihood L_{HZ} still has the discriminating power and can be used further for the construction of the final discriminant.

From these events now the final discriminant, FD_{HZ} , is constructed. At the first step the events are classified into three categories depending on the ranking of the values of b tags of the two jets assigned to the Higgs boson. The first category contains events where none of these jets has the highest b-tag value. The second category is composed of events where one of these jets has the highest b tag value. The third category contains events where the two jets assigned to the Higgs boson have the highest b tag values.

The quantity $\log(P(\chi_{\text{HZ}}^2))$, the b-tags of the individual jets and the event category characteristic are combined to FD_{HZ} using the likelihood technique. The distributions of these variables are shown in Figure 5.4.

Since the Higgs boson mass hypothesis enters the Equation 5.7, the final discriminant, FD_{HZ} , becomes mass dependent and must be recalculated for each Higgs boson mass hypothesis. As an example, the final discriminant distribution for a Higgs boson mass

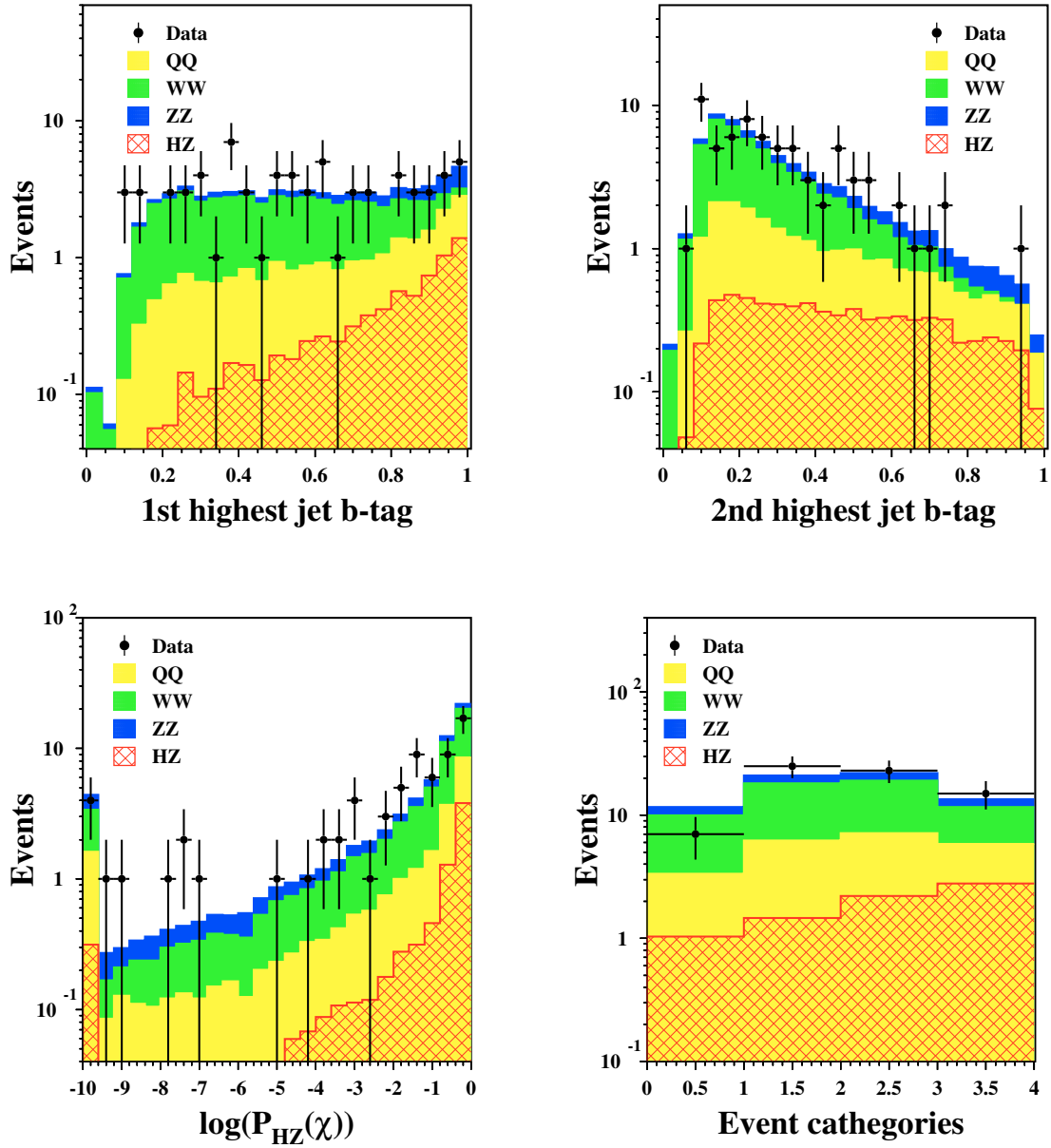


Figure 5.4: Distributions from the $\sqrt{s} = 207$ GeV data, used for the Final Discriminant construction: first highest jet btag (top left), second highest jet btag (top right), the logarithm of $\log(P(\chi^2_{HZ}))$ for a Higgs mass hypothesis of 110 GeV (bottom left) and event categories using the jet assigning to the Higgs (see text) (bottom right).

hypothesis of 110 GeV at $\sqrt{s} = 207$ GeV is shown in Figure 5.5.

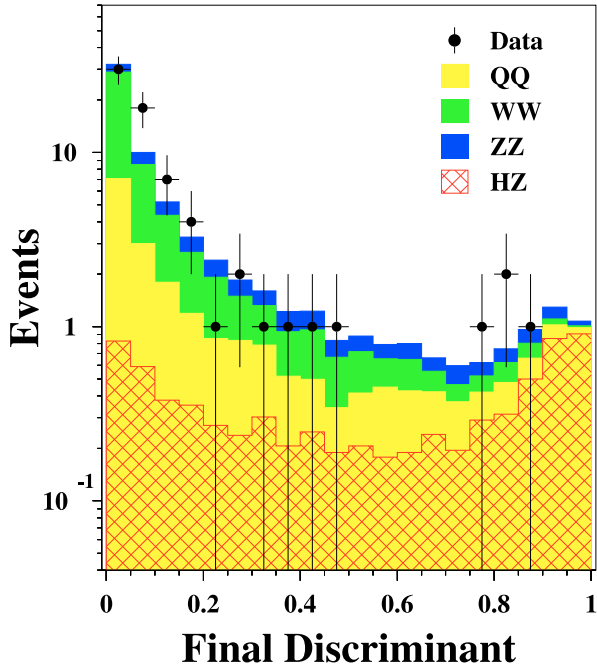


Figure 5.5: Final discriminant distribution for the events selected as $q\bar{q}q\bar{q}$ final states for the Higgs boson mass hypothesis of 110 GeV from the 207 GeV data set.

5.3 The $HZ \rightarrow b\bar{b}\nu\bar{\nu}$ channel

The $HZ \rightarrow b\bar{b}\nu\bar{\nu}$ search [82] is based on the selection of events with two jets containing b hadrons, with large missing energy and with missing mass consistent with m_Z . In the first step of the analysis, high multiplicity hadronic events are selected and forced into two jets using the DURHAM algorithm. The di-jet invariant mass must exceed 40 GeV. These requirements reduce contributions from two-photon interactions, while retaining a significant fraction of hadronic events from $e^+e^- \rightarrow q\bar{q}(\gamma)$ and W -pair production. These backgrounds are then reduced by requiring the visible mass to be less than 140 GeV and the mass recoiling against the hadronic system to lie between 50 GeV and 130 GeV.

Events from $e^+e^- \rightarrow q\bar{q}(\gamma)$ are further suppressed by requiring the longitudinal missing energy to be less than $0.6\sqrt{s}$ and the missing momentum vector to be at least 16° away from the beam axis. The energy in the forward luminosity calorimeter is required to be below 20 GeV. The acolinearity is required to be smaller than 65° . The distribution of the event b -tag after the above cuts is shown in Figure 5.6. A loose cut requiring the event b -tag to be larger than 0.5 is then applied, without further significant loss of signal efficiency. After this set of cuts, there are 123 events in data, while 130 are expected from the background processes with 4.3 and 1.3 events expected for $m_H = 110$ GeV and $m_H = 115$ GeV, respectively.

A kinematic fit imposing four-momentum conservation and requiring the missing mass to be consistent with m_Z is performed to compute the reconstructed Higgs boson mass from the two jets. The distributions of the reconstructed Higgs mass and the missing mass are depicted in Figure 5.7: Then a mass independent neural network [87] is used for the $HZ \rightarrow b\bar{b}\nu\bar{\nu}$ analysis, similar to one described in detail in the References [88] and [89]. The output of the neural network is then combined with the reconstructed Higgs mass to build the final discriminant. In the $HZ \rightarrow b\bar{b}\nu\bar{\nu}$ analysis the final discriminant is called

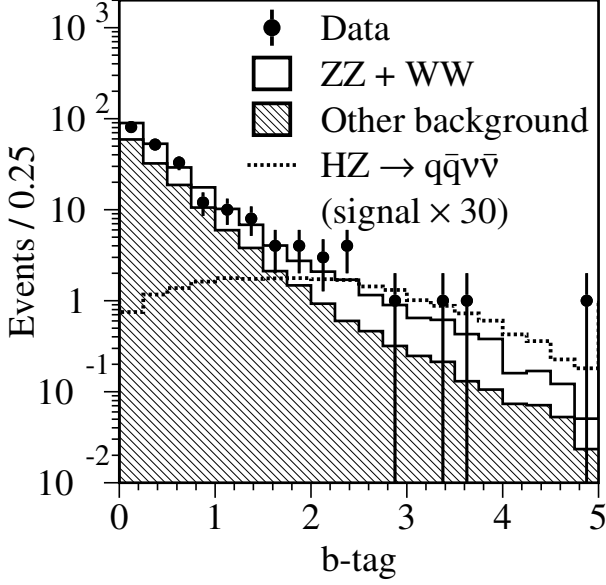


Figure 5.6: The b -tag distribution for the events selected in the $HZ \rightarrow b\bar{b}\nu\bar{\nu}$ search channel. The points represent the data collected as $\sqrt{s} > 206$ GeV [82].

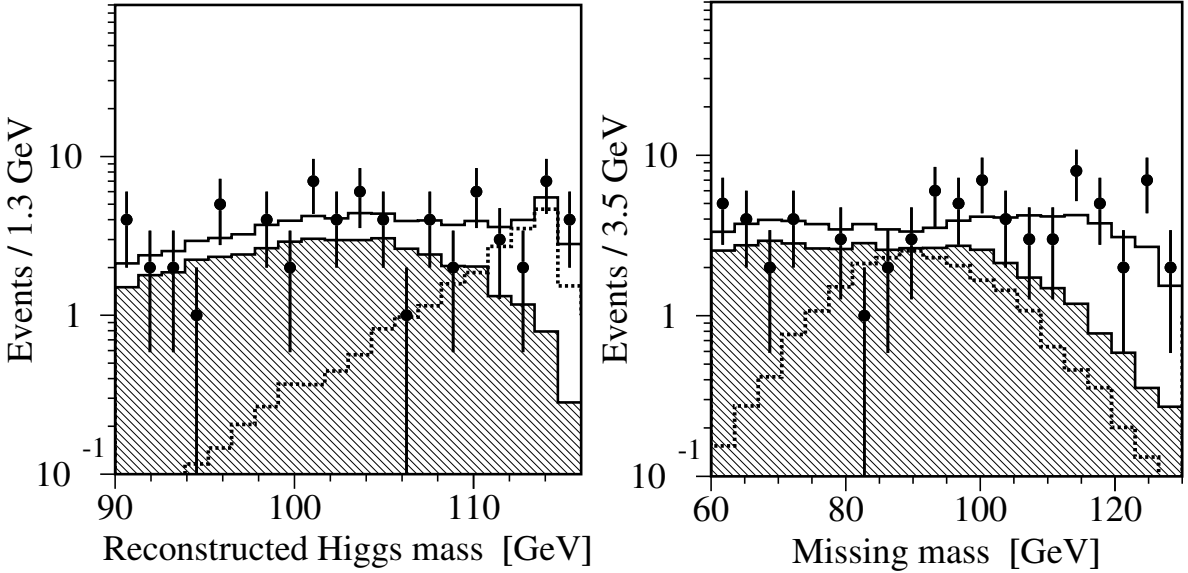


Figure 5.7: Distributions of the reconstructed Higgs mass after applying the 1C kinematic fit (left) and the missing mass, reconstructed from the measured quantities (right). The points represent the data collected as $\sqrt{s} > 206$ GeV. The open and hatched histograms are the expected backgrounds. The dashed line is the expected Higgs boson signal with $m_H = 115$ GeV, scaled by a factor of 30 [82].

Purity, defined in the following way:

$$\begin{aligned}
 Purity &= \frac{P_{S_{i,j}}}{P_{S_{i,j}} + P_{b_{i,j}}}; \\
 P_{S_{i,j}} &= P_{S_i} \times P_{S_j} \times \sigma_s, \\
 P_{b_{i,j}} &= P_{b_i} \times P_{b_j} \times \sigma_b, \\
 P_{b_i} &= P_{q\bar{q}_i} + P_{WW_i} + P_{ZZ_i} + \text{etc.}
 \end{aligned} \tag{5.8}$$

where i and j stands for the variables to be included into the final discriminant construction, $P_{S_{i,j}}$ and $P_{b_{i,j}}$ are the probabilities of an event to belong to the signal or to the background hypothesis, respectively. σ_s and σ_b are the cross sections for the signal events and for the corresponding background hypothesis. The probability of event to belong to the background P_{b_i} is a composition of probabilities, obtained from the comparison with the different background classes. Distributions of the neural network output and the final discriminant are shown in Figure 5.8 compared to the expectation from the

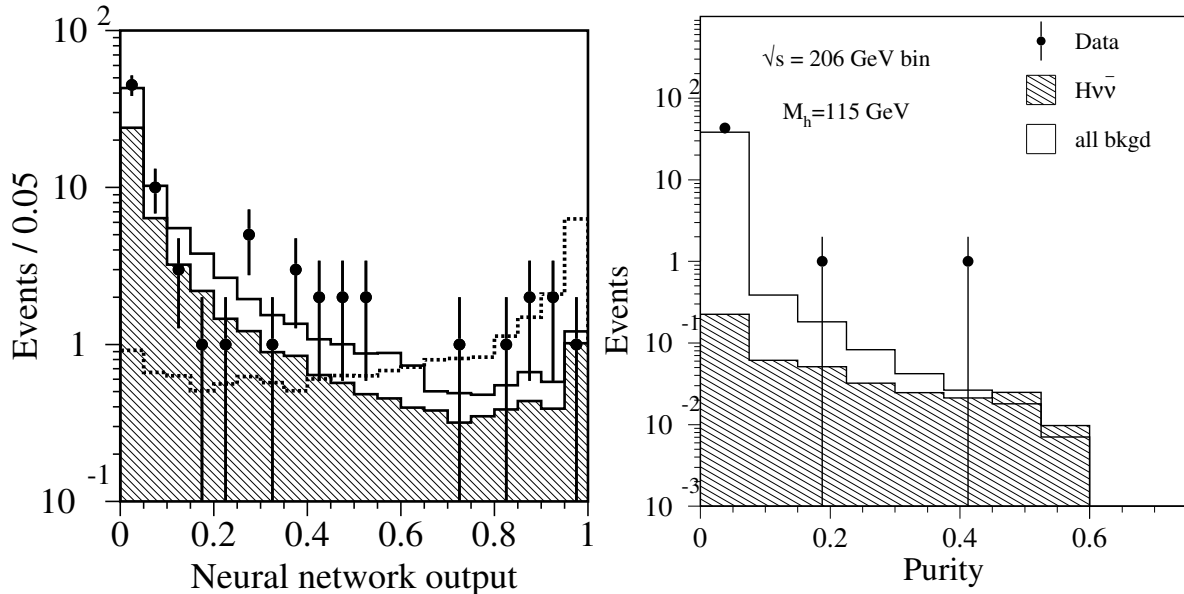


Figure 5.8: Distributions of the neural network output (left), where the points represent the data collected as $\sqrt{s} > 206$ GeV. The open and hatched histograms are the expected backgrounds. The dashed line is the expected Higgs boson signal with $m_H = 115$ GeV, scaled by a factor of 30. The final discriminant for the same data (right) [82].

Standard Model processes. General agreement between data and the expected contribution from Standard Model background is observed in all the distributions. At the final discriminant plot the most significant $H\nu\bar{\nu}$ candidate is seen at the right, signal-like, side of the Purity distribution. The signal over background ratio is 0.7 for the Higgs boson mass hypothesis of 115 GeV.

5.3.1 Cross-checks

The most significant candidate in $e^+e^- \rightarrow HZ \rightarrow b\bar{b}\nu\bar{\nu}$ channel was recorded by the L3 detector on the 16th of October 2000. This event was found after the ALEPH collaboration had reported about an excess of Higgs candidates in the four-jet final state. For the first time in the history of the SM Higgs searches at LEP an event with such a high signal over background ratio was found in the channel different from the four-jet one. That is why this event become a subject of particular interest not only in the LEP community. The region where this $H\nu\bar{\nu}$ event is measured, $\cos\theta_{thrust} = 0.77$, corresponds to the gap region between the barrel and end-cap calorimeters, filled with

the lead-scintillating fibre calorimeters (SPACAL), as shown in Figures 3.4 and 4.3. The event is shown in Figure 5.9 in the $y - z$ projection.

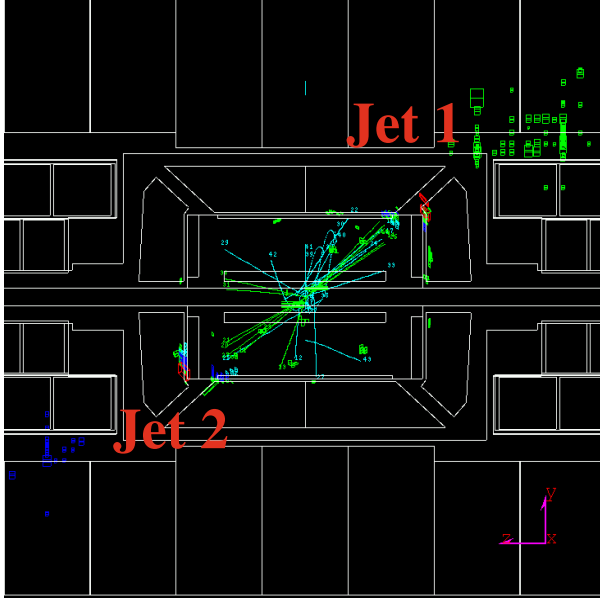


Figure 5.9: The $e^{+}e^{-} \rightarrow HZ \rightarrow b\bar{b}\nu\bar{\nu}$ event candidate.

In order to be sure that this event is not faked by a detector imperfectness several variables were studied and compared between data and Monte Carlo samples. The jet energy measurement in this region of the L3 detector has been extensively studied and checked. A selection of the two-jet events, similar to the one, discussed in the Chapter 4.3.3 and modified to fulfill the major criteria of $H\nu\bar{\nu}$ selection has been performed and several control distributions were then constructed for the data, collected in year 2000, versus the SM prediction. The main point of interest were the energy resolution and the angular distributions of the two jets in the presence of the large missing momentum. Figure 5.10 shows the jets energy distribution in the SPACAL region of the L3 detector and the absolute value of the cosine of the jet polar angle θ . The resolution of the jet energy measurement were studied in the particular regions of the detector, where the main cone of the jets are located. The resolution for data and Monte Carlo events is shown in Figure 4.7.

All these distributions demonstrate a good agreement between data and Monte Carlo, showing no anomaly for this particular region of the L3 detector. This verifies that in the transition between the barrel and end-cap calorimeters, the jet energy measurement is understood and reliable, supporting the weight assignment used in the estimation of the Higgs boson signal.

5.4 The $HZ \rightarrow b\bar{b}l^{+}l^{-}$ and $HZ \rightarrow \tau^{+}\tau^{-}q\bar{q}$ channels

The signatures for the $H\mu^{+}\mu^{-}$ and $H\tau^{+}\tau^{-}$ processes are a pair of high energy electrons or muons with an invariant mass compatible with m_Z and two hadronic jets with b quark content. In $H\tau^{+}\tau^{-}$ events the tau pair invariant mass must be also compatible with m_Z . For these events, the mass resolution is worse than in the other $Hl^{+}l^{-}$ channels due

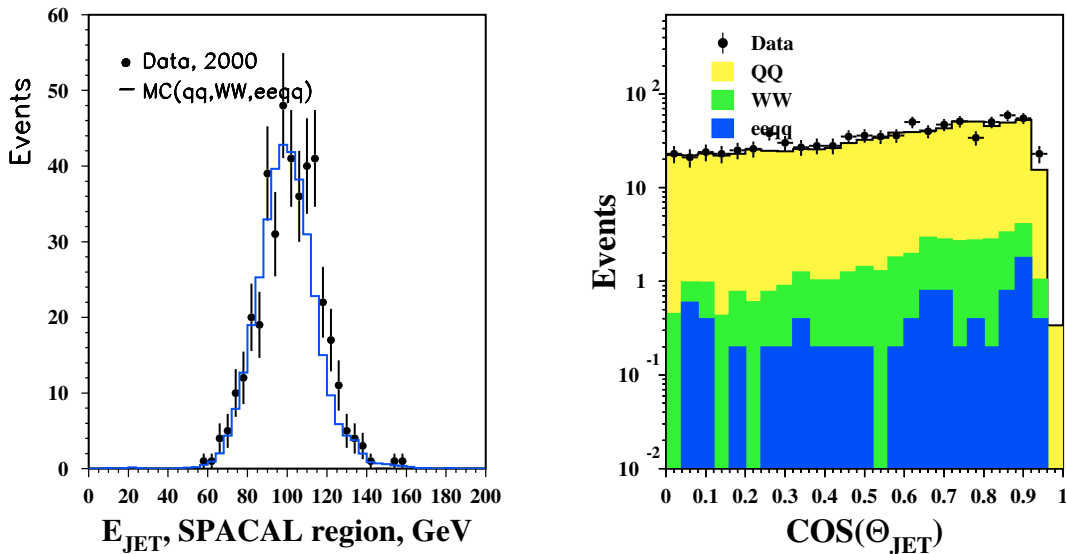


Figure 5.10: The jets energy distribution in the SPACAL region of the L3 detector and the absolute value of the cosine of the jet polar angle θ .

to the missing neutrinos from the τ decays. Events with the Higgs decaying into tau leptons, $\tau^+\tau^-q\bar{q}$, have similar signature to the $H\tau^+\tau^-$ events, with the difference that the hadronic jet mass must be compatible with m_Z and that the b-tag content of the event is reduced.

The analysis [82] requires high multiplicity events. In the $H\tau^+\tau^-$ and $H\mu^+\mu^-$ analyses two well identified electrons or muons are also required. In the tau analyses, tau leptons are identified either by their decay into electrons or muons, or as an isolated low-multiplicity jet with one or three tracks and unit charge. The identified leptons must have a large opening angle and must be well isolated from the hadronic jets.

For all Hl^+l^- selections, the invariant mass of the leptons after a kinematic fit imposing four-momentum conservation must be consistent with m_Z within a mass range depending on the mass resolution. In the $\tau^+\tau^-q\bar{q}$ selection the mass of the two hadronic jets after kinematic fit must be consistent with m_Z .

After Hl^+l^- selection, 18 events are observed with 16.7 expected from the background process and 1.7 or 0.32 signal events expected for $m_H = 110$ GeV or 115 GeV, respectively. After the $\tau^+\tau^-q\bar{q}$ selection, 8 events are observed with 7.8 expected from background and 0.66 or 0.15 signal events expected for $m_H = 110$ GeV or 115 GeV, respectively. The distributions of the di-lepton mass and the reconstructed Higgs mass in the $H\tau^+\tau^-$ and $H\mu^+\mu^-$ channels are shown in Figure 5.11. The distributions of the reconstructed Higgs mass in the $H\tau^+\tau^-$ and $\tau^+\tau^-q\bar{q}$ channels are shown in Figure 5.12

In the Hl^+l^- selection, the di-jet mass after the fit is combined with the b-tag values of the two jets, to form the final discriminant. For the $\tau^+\tau^-q\bar{q}$ selection, the mass of the tau pair, calculated by constraining the invariant mass of the two other jets to m_Z , is used as the final discriminant.

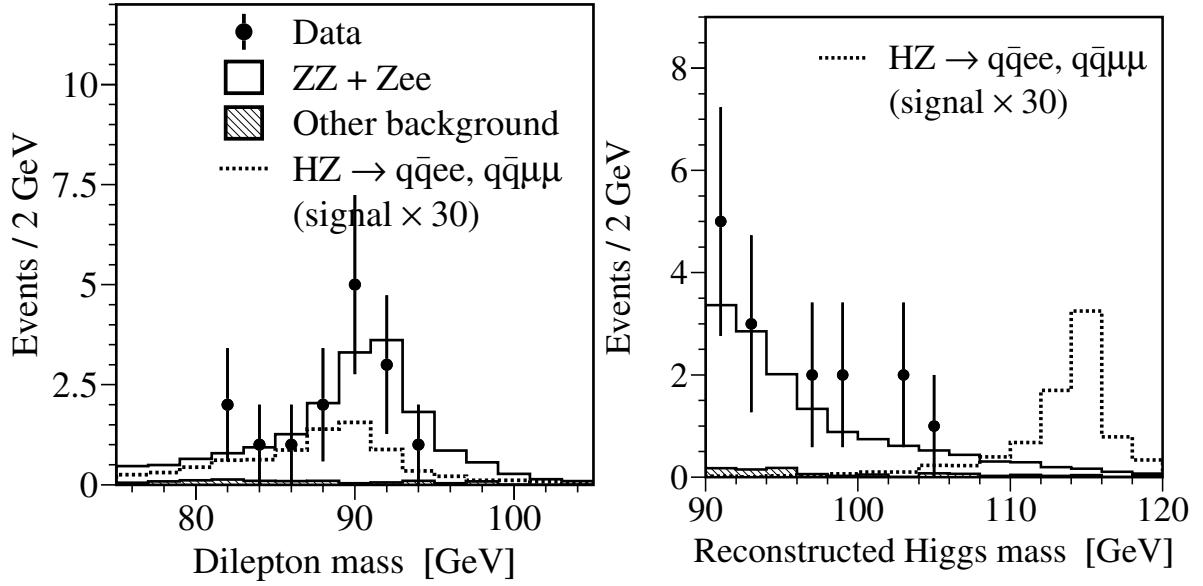


Figure 5.11: Distributions of the di-lepton mass (left) and the reconstructed Higgs mass in the $H\mu^+\mu^-$ and $H\mu^+\mu^-$ channels. The points are data and the open and hatched histograms are expected backgrounds. The dashed line is the expected Higgs signal with $m_H = 115$ GeV, scaled by a factor of 30 [82].

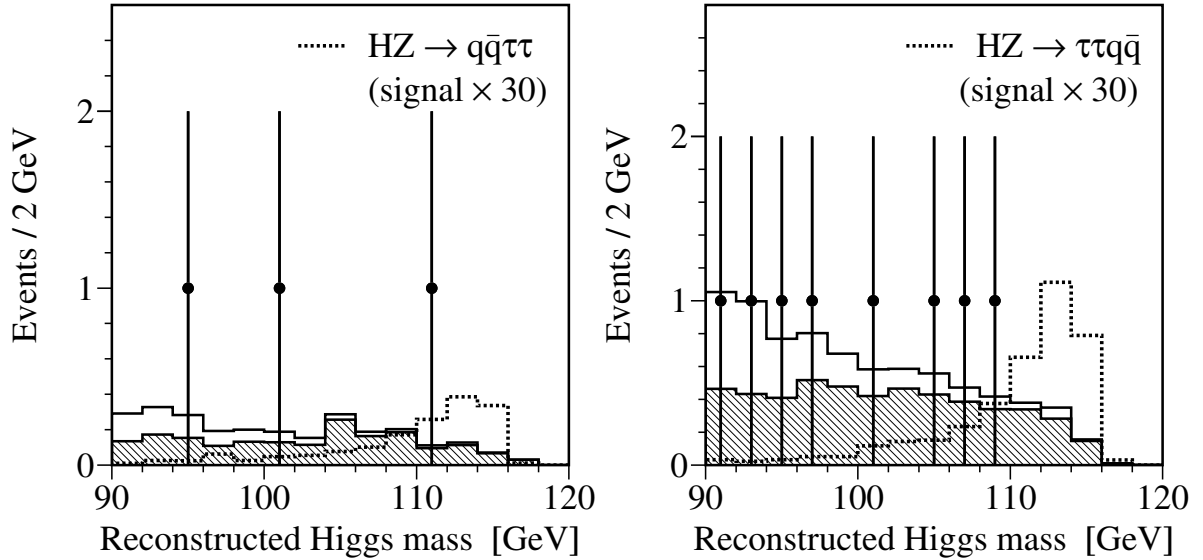


Figure 5.12: Distributions of the reconstructed Higgs mass in the $H\tau^+\tau^-$ (left) and $\tau^+\tau^-q\bar{q}$ (right) channels. The points are data and the open and hatched histograms are expected backgrounds. The dashed line is the expected Higgs signal with $m_H = 115$ GeV, scaled by a factor of 30 [82].

Chapter 6

Interpretation of the Results

In the previous chapter the analyses and the results of the searches for the Standard Model Higgs boson were presented. No hint of a signal was found. In this chapter the results of the individual search channels are combined. As the expected signal is quite small, a possible deviation from the background expectation may only become apparent in the combination of all channels.

6.1 The Confidence Level

The method described in Ref. [90,91] is employed to calculate the confidence level that the signal is absent, allows also to evaluate the presence of a signal. The procedure is described in the following.

First, a binned likelihood based on Poisson statistics is constructed, using the final discriminants distributions for the individual search channels at the different center-of-mass energies discussed above:

$$\mathcal{L}(s + b) = \prod_{k=1}^l \prod_{j=1}^{n_k} \prod_{i=1}^{m_{kj}} \frac{e^{-(s_{ijk}+b_{ijk})} (s_{ijk} + b_{ijk})^{N_{ijk}}}{N_{ijk}!}. \quad (6.1)$$

Here, $k = 1..l$ runs over all investigated centre-of-mass energies, $j = 1..n_k$ over the search channels and $i = 1..m_{kj}$ over the bins of the distribution of a given channel j at the center-of-mass energy k . The variables s_{ijk} , b_{ijk} and N_{ijk} represent the expected signal¹, the expected background and the number of observed candidates for the individual analyses, respectively. The total number of expected signal events, s , is given by:

$$s = \sum_{k=1}^l \sum_{j=1}^{n_k} \sum_{i=1}^{m_{kj}} s_{ijk}. \quad (6.2)$$

The background and signal expectations, b_{ijk} and s_{ijk} , are fixed to their Monte Carlo predictions. Then we consider two hypotheses: the *background-only* hypothesis, which

¹At this point, we take advantage of the fact that the Standard Model predicts the signal cross section as a function of the Higgs boson mass.

assumes no Higgs boson to be present in the mass range investigated, and the *signal+background* hypothesis, where a Higgs boson is assumed to be produced.

A global quantity, $-2\ln Q$, allowing to classify the experimental result between the *background*-like and *signal + background*-like situations is then constructed in a following way:

$$-2 \ln Q = -2 \ln \frac{\mathcal{L}(s + b)}{\mathcal{L}(b)} \quad (6.3)$$

which can be written as:

$$-2 \ln Q = 2 \left(S - \sum_{i=1}^N n_i \ln \left(1 + \frac{s_i}{b_i} \right) \right) \quad (6.4)$$

where now i stands for the i -th bin of the final discriminant of each search channel and each center-of-mass energy, n_i , s_i and b_i are the number of observed events, of expected signal and of expected background, respectively. N is the total number of observed events, S corresponds to the total number of signal events expected.

To set the scale for $-2\ln Q$, a large number of Monte Carlo experiments is generated, separately for the *background-only* and *signal+background* hypotheses, and separately for each m_H . The test-statistics, derived in the following way takes into account experimental details such as detection efficiencies, signal-to-background ratios, resolution functions, and provides a single value for a given model hypothesis (e.g., the test-mass m_H in the Standard Model). The resulting distributions of $-2\ln Q(m_H)$ are normalised to become a probability density functions, and integrated to form the confidence levels $CL_b(m_H)$ and $CL_{s+b}(m_H)$. The integration starts in both cases from the *background*-like end and runs up to the experimental result $-2\ln Q_{observed}$; thus $CL_b(m_H)$ and $CL_{s+b}(m_H)$ express the probabilities that the outcome of an experiment is more *background*-like or less *signal+background*-like, respectively, than the outcome obtained from data. The calculation of confidence levels is illustrated in Figure 6.1.

When performing a search with small expected signal rates, it may happen that the observed number of candidates is far below the expected background level. In such cases the limit may extend beyond the range of sensitivity of the search. To prevent *a priori* such unphysical, but formally valid, results from occurring, we consider the ratio:

$$CL_s = \frac{CL_{s+b}}{CL_b} \quad (6.5)$$

as a conservative approximation to the signal confidence obtained in the absence of background. The 95% CL lower limit for the SM Higgs boson mass is defined here as the lowest value of the test mass m_H which yields $CL_s(m_H) = 0.05$.

The quantity $1 - CL_b$ is an indicator for a possible signal: a SM Higgs boson with true mass m_0 would produce a pronounced drop in this quantity for $m_H \approx m_0$. Values of $1 - CL_b < 5.7 \times 10^{-7}$ ($1 - CL_b < 2.7 \times 10^{-3}$) would indicate a 5σ (3σ) discovery. Background fluctuations may also produce such a drop, allowing for some m_H a “discovery” beneath the expected experimental sensitivity. In analogy to the definition of CL_s , an additional quantity:

$$(1 - CL_b)' = \frac{1 - CL_b}{1 - CL_{s+b}} \quad (6.6)$$

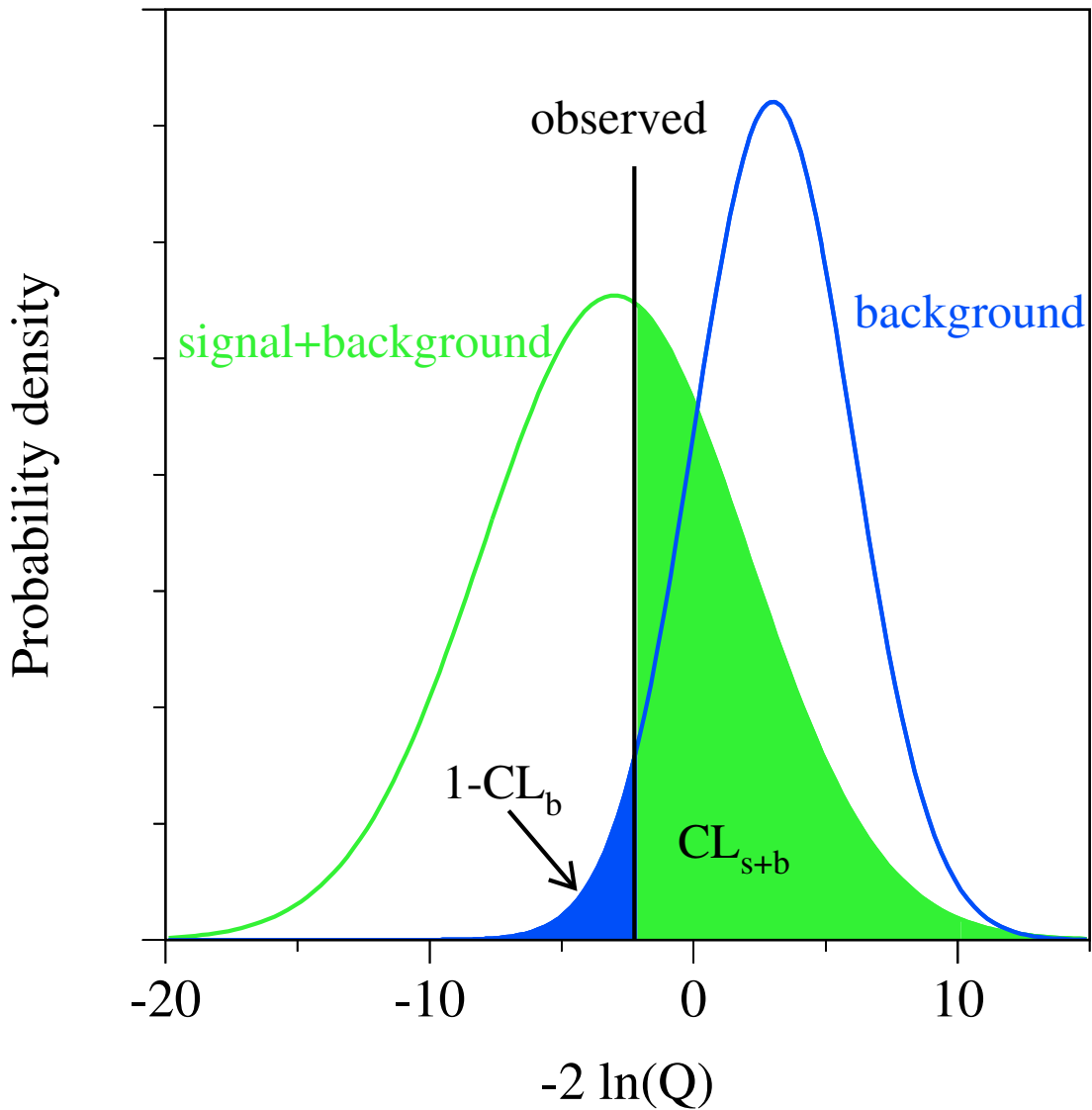


Figure 6.1: An example of the probability distributions for the test statistic $-2\ln Q$ for background-only and signal+background gedanken experiments. This defines the confidences CL_b , CL_{s+b} and CL_s .

is defined to incorporate information about signal sensitivity into the discovery estimator.

The above test-statistic makes the most efficient use of the information available in a search result in a manner similar to the way the concept of maximum likelihood gives the most efficient estimators of parameters in a measurement.

If values of $-2\ln Q_{observed}$ (and thus the integration bounds) are obtained by substituting data with the Monte Carlo simulations of the real experiment, the average expected confidence levels $\langle 1 - CL_b \rangle$ and $\langle CL_s \rangle$ are obtained. Of particular interest are $\langle 1 - CL_b \rangle$ from simulated *signal + background* experiments and $\langle CL_s \rangle$ from simulated *background-only* experiments, since these indicate the expected ranges

of sensitivity of the available data set for discovery and exclusion, respectively.

6.2 Combining All Search Channels

After the selection described in the previous Chapter, only events in bins of the final discriminant with $s/b > 0.05$ are retained. The number of selected events in all the search channels are shown in Table 6.2 for the data, the background and the Higgs signal for

$\sqrt{s} = 203 - 209$ GeV	Mass hypothesis					
	$m_H = 110$ GeV			$m_H = 115$ GeV		
Selection	N_D	N_B	N_S	N_D	N_B	N_S
Hq \bar{q}	49	51.5	11.7	12	9.4	1.8
H $\nu\bar{\nu}$	13	10.7	3.3	5	3.3	0.66
H e^+e^-	0	0.66	0.58	0	0.38	0.14
H $\mu^+\mu^-$	0	0.38	0.45	0	0.26	0.11
H $\tau^+\tau^-$	0	0.53	0.19	1	0.14	0.03
$\tau^+\tau^-q\bar{q}$	3	2.3	0.51	0	0.84	0.15
Total	65	66.1	16.7	18	14.3	2.9

Table 6.1: The number of observed candidates (N_D), expected background (N_B) and expected signal (N_S) events for the data collected by L3 in the year 2000, after a cut on the final discriminant corresponding to a signal-to-background ratio greater than 0.05. This cut is also used to calculate the confidence levels.

two Higgs boson mass hypotheses: $m_H = 110$ GeV and $m_H = 115$ GeV. The number of signal events includes cross-efficiencies from other channels, fusion processes and charm and gluonic Higgs decays.

Figure 6.2 shows the observed $-2\ln Q$ compared to the expectation for the “background-only” and the “signal-background” hypothesis, as a function of the Higgs boson mass, m_H , for each of the search channels. An observed value of $-2\ln Q$ larger than the median² expected value for the background indicates a deficit of events with respect to the expected background while an observed $-2\ln Q$ value below the median expected background value indicates an excess. Good agreement between the observation and the expected background is observed in most channels within one standard deviation from the background expectation. A slight excess of events above one standard deviation from the background is observed in the H $\nu\bar{\nu}$ search channel for m_H above 100 GeV. The observed and expected log-likelihood ratio $-2\ln Q$ for all channels combined as a function of m_H is shown in Figure 6.3.

The most significant candidate for $m_H = 115$ GeV is a H $\nu\bar{\nu}$ event. It has a reconstructed Higgs boson mass of 115 GeV and it was recorded at $\sqrt{s}=206.4$ GeV. The kinematic properties of this event were described in detail in Reference [92].

²median is the “middle” of the probability distribution, when half of the probability lies above and half lies below this value.

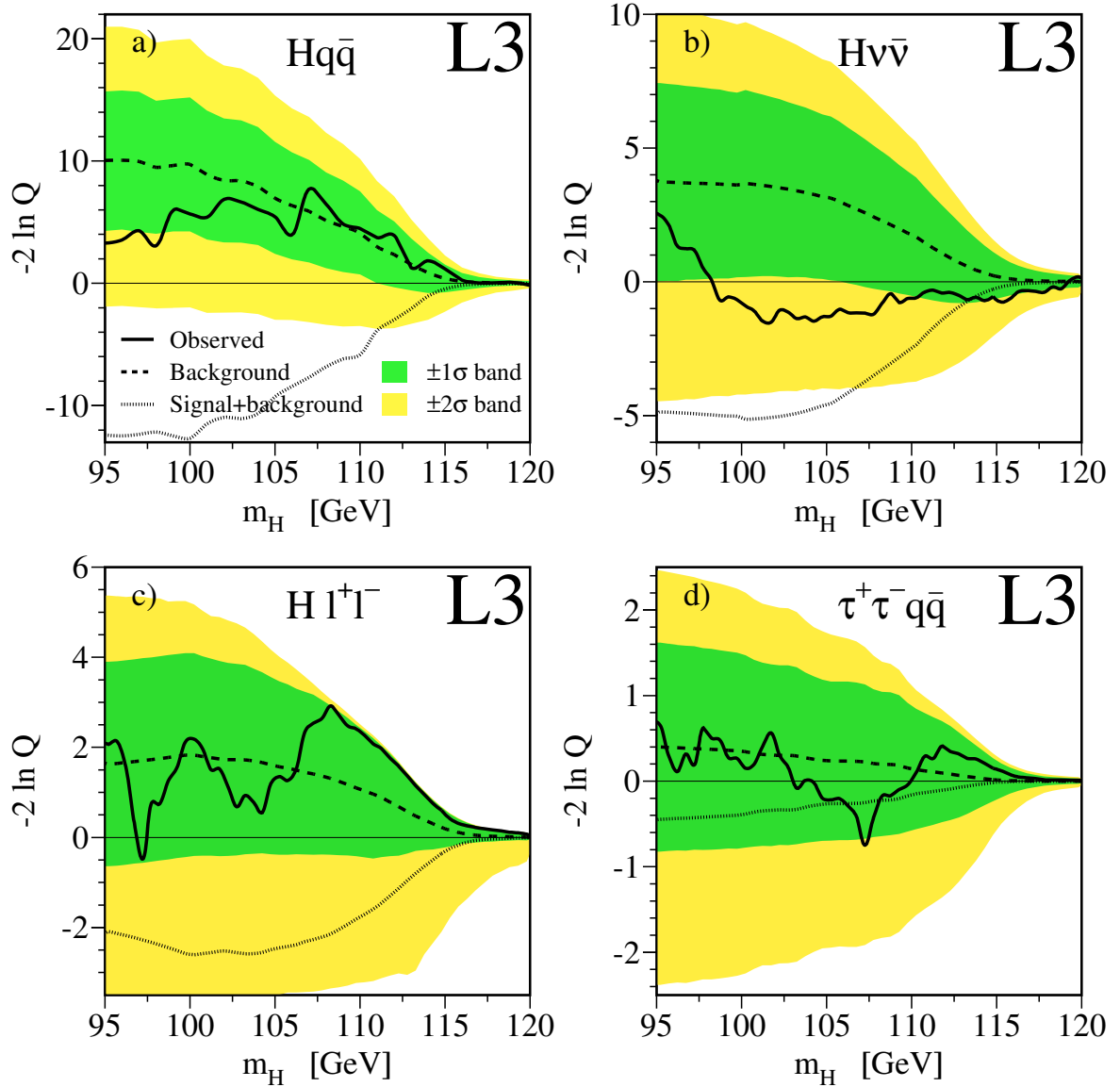


Figure 6.2: The log-likelihood ratio, $-2\ln Q$, as a function of the Higgs mass hypothesis, m_H , for the search channels a) $Hq\bar{q}$, b) $H\nu\bar{\nu}$ [82], c) Hl^+l^- [82] and d) $\tau^+\tau^-q\bar{q}$ [82]. The solid line shows the observed $-2\ln Q$. The dashed line shows the expected median value of $-2\ln Q$ for the “background-only” hypothesis. The dark and the light shaded bands show the 68% and 95% probability intervals centered on the background expected median value. The dotted line is the median expected value for the “signal+background” hypothesis.

6.3 The Statistical and Systematic Uncertainties

The statistical and systematic uncertainties on the signal and background expectations are included in the calculations of the combined confidence levels. Statistical uncertainties on the background and signal predictions, arising from the finite number of generated Monte Carlo events, are evaluated to be up to 8% for the background and 4%

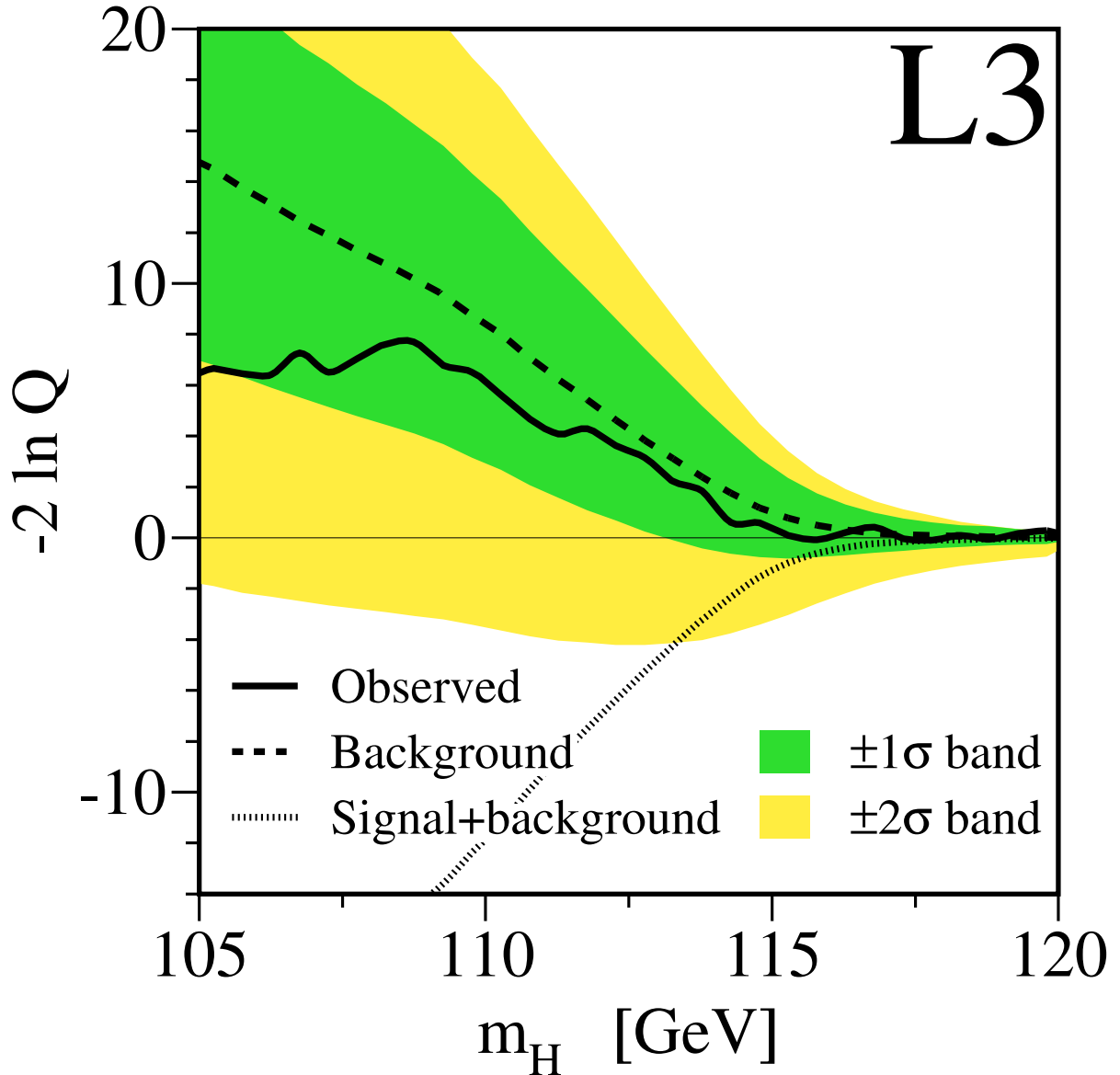


Figure 6.3: The log-likelihood ratio, $-2\ln Q$, as a function of the Higgs boson mass hypothesis, m_H , for all the search channels combined. The solid line shows the observed $-2\ln Q$. The dashed line shows the expected median value of $-2\ln Q$ for the “background-only” hypothesis. The dark and light shaded bands show the 68% and 95% probability intervals centered on the background expected median value. The dotted line is the median expected value for the “signal+background” hypothesis [82].

for the signal. The systematic uncertainties are derived using a similar procedure to the one adopted in previous Standard Model Higgs searches [93]. The following sources of systematic errors are considered:

Energy Scale: A global energy shift of $\pm 2\%$ corresponding to the maximal error in the calibration method [94] was applied leading to the uncertainty on the number of

background events from 3% to 10% above and beyond the HZ kinematic threshold. The uncertainty on the number of signal events varies from 2% to 3% above and beyond the HZ kinematic threshold.

Background Normalisation: Following the suggestion of the LEP ZZ working group, the following uncertainties on the background cross section are assumed: 2% on WW and 5% on $q\bar{q}\gamma$, ZZ and Zee.

Simulation of Selection Variables: The systematic effects potentially originating from event selection variables are estimated with the event reweighting method [95]. For each variable a weight depending on the value of the variable is introduced to bring the simulated distribution in agreement with distribution observed in data. The corrections to the estimated background and signal are then determined and added in quadrature for all variables. This results into an uncertainty on the number of background events between 1% and 10% and on the number of signal events between 2% and 5% above and beyond the HZ kinematic threshold.

Luminosity Error: The relative uncertainty in the luminosity measurement is 0.3%.

Theoretical Signal Uncertainty: Theoretical error on the Higgs boson production cross section due to uncertainties in m_t and α_s [96], amounts to $\approx 0.1\%$. Theoretical error on the Higgs boson decay branching fractions constitutes 1% [97].

B-tag Related Systematics: The systematic effect due to b-tagging is studied using independent reference samples as described in Section 4.3.4. Good agreement between data and Monte Carlo is found in the spectrum of the jet b-tag variable and the related systematic error is estimated to be negligible.

Overall Systematic Uncertainty: Assuming that systematic errors from different sources are uncorrelated total systematic uncertainties are estimated to range from 6% to 15% on the number of background events and from 3% to 6% on the number of signal events above and beyond the HZ kinematic threshold.

The statistical uncertainty is uncorrelated from bin to bin in the final discriminant distributions and has little effect on the confidence level. Bins of the final discriminant distributions with a s/b ratio below 0.05 are not considered in the calculation of the confidence levels, as they degrade the search sensitivity once systematic uncertainties are included in the calculation.

6.4 Mass Limit

The confidence level for the “background-only” hypothesis $1 - CL_b$ and the confidence level for the signal hypothesis CL_s as a function of m_H are shown in Figure 6.4. The results of the L3 Standard Model Higgs boson searches at lower center-of-mass energies [93, 98] are included in the calculation of these confidence levels. Values of m_H below 107 GeV are excluded in the Standard Model with a confidence level greater than 99.5%.

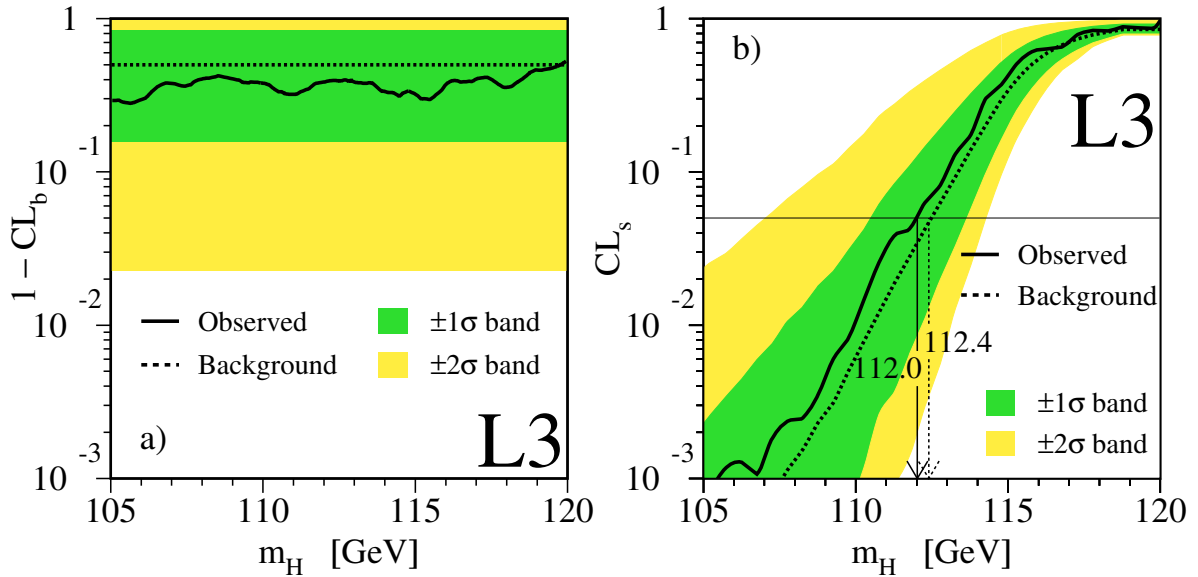


Figure 6.4: a) The background confidence level $1 - \text{CL}_b$ and b) the signal confidence level, CL_s , as a function of the Higgs boson mass hypothesis, m_H , for all the search channels combined. The data collected at $189 \leq \sqrt{s} \leq 202$ GeV [98] are also included in the combination. The solid line shows the observed value. The dashed line shows the median expected value in a large number of simulated “background-only” experiments. The dark and light shaded bands show the expected 68% and 95% probability intervals centered on the background expected median value. The observed lower limit on the Higgs boson mass is set at 112.0 GeV, with an expected median value of 112.4 GeV, at the 95% confidence level [82].

The observed lower limit³ on m_H is 112.0 GeV at the 95% confidence level, for an expected lower limit of 112.4 GeV. This value improves upon and supersedes previously published limit [98]. For $m_H = 112.0$ GeV, where CL_s is 5%, the background probability $1 - \text{CL}_b$ is 40%. For $m_H = 115$ GeV, the background probability is 32%. The previously published background probability estimates [98] are consistent with the final result presented here, given in the size of the uncertainties affecting the signal and background estimate in the vicinity of the kinematic limit.

6.5 The LEP-wide combination

The combination of the results from the four LEP experiments [99] has been done in the same way as described above. Figure 6.5 shows the quantity $-2 \ln Q$ as a function of the test-mass for the present combination of LEP data. The expected curves and their spreads are obtained by replacing the observed data configuration by a large number of simulated event configurations.

³This limit was obtained using the published version of four-jet analysis. The observed lower limit on the Higgs boson mass m_H for the combination, made with the analysis performed by the author and described in this thesis is 112.3 GeV.

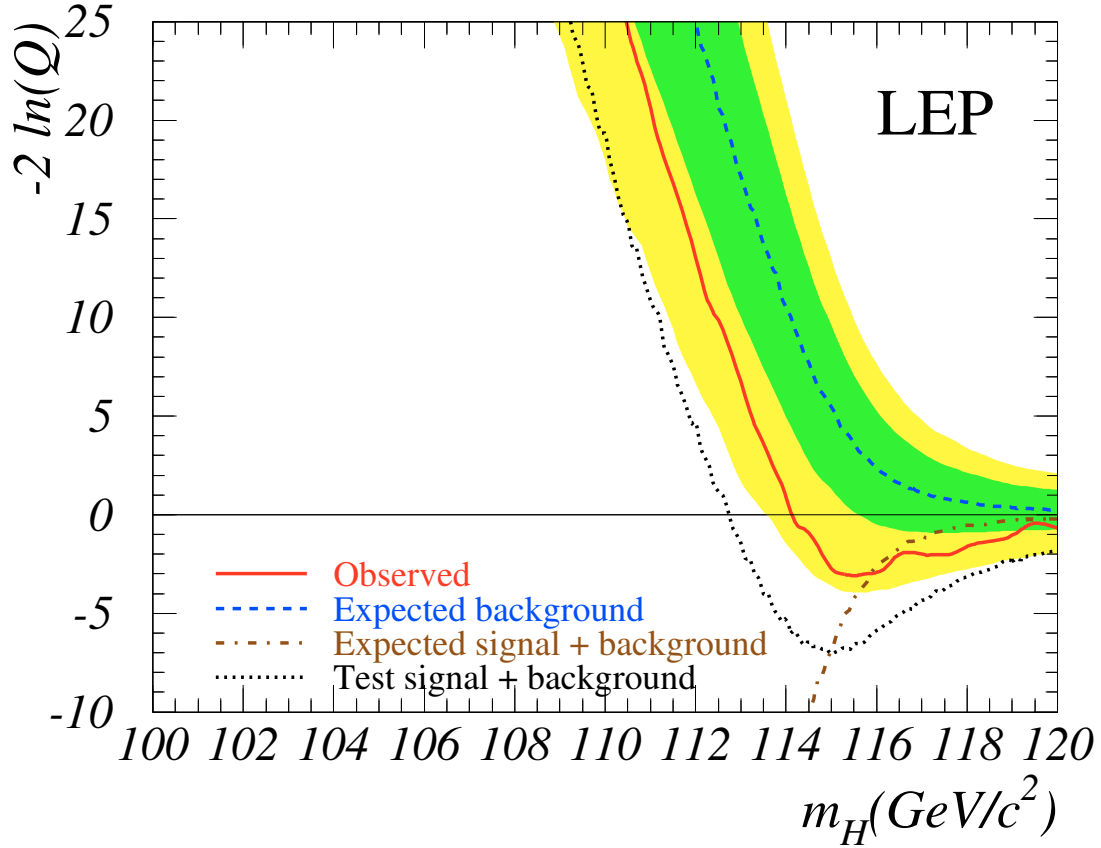


Figure 6.5: Observed and expected behaviour of the likelihood ratio $-2\ln Q$ as a function of the test-mass m_H , obtained by combining the data of all four experiments. The solid line represents the observation; the dashed/dash-dotted lines show the median background(signal+background) expectations. The dark(light) shaded bands around the background expectation represent the $\pm 1(\pm 2)$ standard deviation spread of the background expectation obtained from a large number of background experiments. The dotted line is the result of a test where the signal from a 115 GeV Higgs boson has been added to the background and propagated through the likelihood ratio calculation [99].

There is a minimum in the observed $-2\ln Q$ at $m_H = 115.6$ GeV (maximum of the likelihood ratio Q) indicating a deviation from the background hypothesis. The minimum coincides with the signal+background expectation for the same test-mass. The value of $-2\ln Q$ at $m_H = 115.6$ GeV is -2.88 .

Another feature in Figure 6.5 is a persistent tail in the observation towards lower test-masses where the observed curve stays away from the prediction for background. This is interpreted as being due to a large extent to the experimental resolution. A test has been performed where the signal expected from a 115 GeV Higgs boson was injected in the background simulation and propagated through the likelihood ratio calculation at each m_H value. Although the resulting curve (dotted line) reproduces the main feature

of the observed tail⁴, a local excess of events due to statistical fluctuations can also contribute to the tail [100].

In Figure 6.6 the likelihood test is applied to subsets of the data, from individual

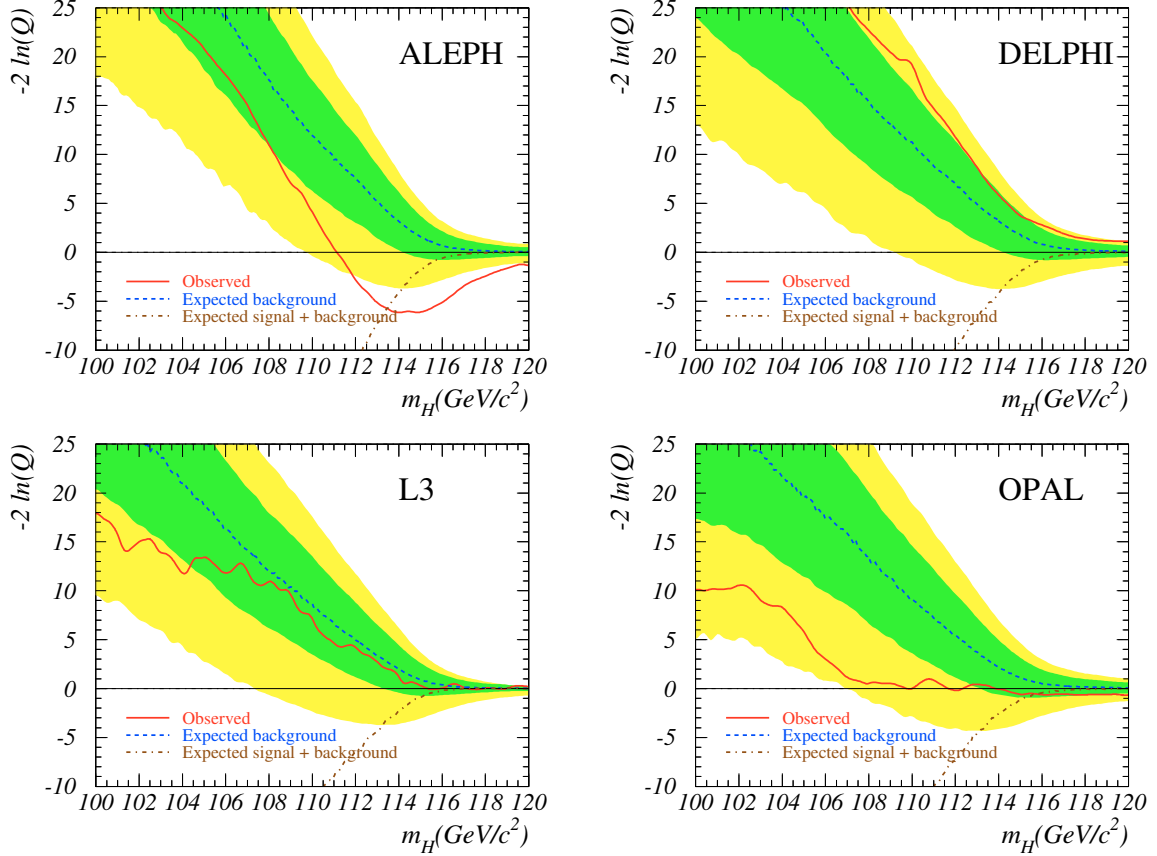


Figure 6.6: Observed and expected behaviour of the test statistic ($-2 \ln Q$) as a function of the test-mass m_H obtained when the combination procedure is applied to the data sets from single experiments [99] (see Figure 6.5 for the notations).

experiments and final-state topologies. In the vicinity of $m_H = 115$ GeV, the signal-like behaviour only originates from the ALEPH data and is concentrated in the four-jet final state. One should note that none of the four experiments, taken separately, have the statistical power to distinguish between the background and the signal+background hypotheses at the level of two standard deviations for a test mass of 115 GeV (see the intersection of the signal+background curve with the lower edge of the light-shaded bands). Among the final-state topologies, only the LEP combined four-jet channel is sufficiently powerful to do so.

⁴For a Higgs mass of 115.6 GeV, the outcome would follow closely the dotted curve, slightly displaced, so that its minimum coincides with the signal+background expectation (dash-dotted curve) at $m_H = 115.6$ GeV.

6.5.1 Contributions from single events

The likelihood ratio $-2 \ln Q$ is built up from individual event weights $\ln(1 + s/b)$. The 20 candidates with the highest weights at $m_H = 115$ GeV are listed in Table 6.2. Some of these candidates are discussed in detail in Ref's [101], [92], [93], [102] and [103]. For

	Expt	E_{cm}	Decay channel	m_H^{rec} (GeV)	$\ln(1 + s/b)$ @115 GeV
1	Aleph	206.7	$Hq\bar{q}$	114.3	1.73
2	Aleph	206.7	$Hq\bar{q}$	112.9	1.21
3	Aleph	206.5	$Hq\bar{q}$	110.0	0.64
4	L3	206.4	$H\nu\bar{\nu}$	115.0	0.53
5	Opal	206.6	$Hq\bar{q}$	110.7	0.53
6	Delphi	206.7	$Hq\bar{q}$	114.3	0.49
7	Aleph	205.0	Lept	118.1	0.47
8	Aleph	208.1	Tau	115.4	0.41
9	Aleph	206.5	$Hq\bar{q}$	114.5	0.40
10	Opal	205.4	$Hq\bar{q}$	112.6	0.40
11	Delphi	206.7	$Hq\bar{q}$	97.2	0.36
12	L3	206.4	$Hq\bar{q}$	108.3	0.31
13	Aleph	206.5	$Hq\bar{q}$	114.4	0.27
14	Aleph	207.6	$Hq\bar{q}$	103.0	0.26
15	Opal	205.4	$H\nu\bar{\nu}$	104.0	0.25
16	Aleph	206.5	$Hq\bar{q}$	110.2	0.22
17	L3	206.4	$H\nu\bar{\nu}$	110.1	0.21
18	Opal	206.4	$H\nu\bar{\nu}$	112.1	0.20
19	Delphi	206.7	$Hq\bar{q}$	110.1	0.20
20	L3	206.4	$H\nu\bar{\nu}$	110.1	0.18

Table 6.2: Properties of the 20 candidates contributing with the highest weight $\ln(1 + s/b)$ to $-2 \ln Q$ at $m_H = 115$ GeV. The experiment, center-of-mass energy, decay channel, the reconstructed mass and the weight at $m_H = 115$ GeV are listed. This list is obtained requiring $s/b > 0.2$ or $\ln(1 + s/b) > 0.18$ at $m_H = 115$ GeV. The corresponding expected signal and background rates are 8.8 and 16.5 events, respectively [99].

the events of each experiment with the highest weight at $m_H = 115$ GeV, the evolution of $\ln(1 + s/b)$ with test-mass is shown in Figure 6.7. Due to the experimental resolution, candidate events with a given reconstructed mass are seen to have sizeable weights for a range of test-masses, with the maximum weight being for test-masses close to the reconstructed mass.

The distribution of event weights for the test-mass fixed at $m_H = 115.6$ GeV is shown in the upper part of Figure 6.8 ($\log_{10} s/b$ is plotted for better visibility). For the purpose of this figure, a cut at $s/b > 0.01$ has been applied. The upper right plot shows the integrals of these distributions, starting from high values of s/b . The data prefer slightly the signal+background hypothesis over the background hypothesis although the separa-

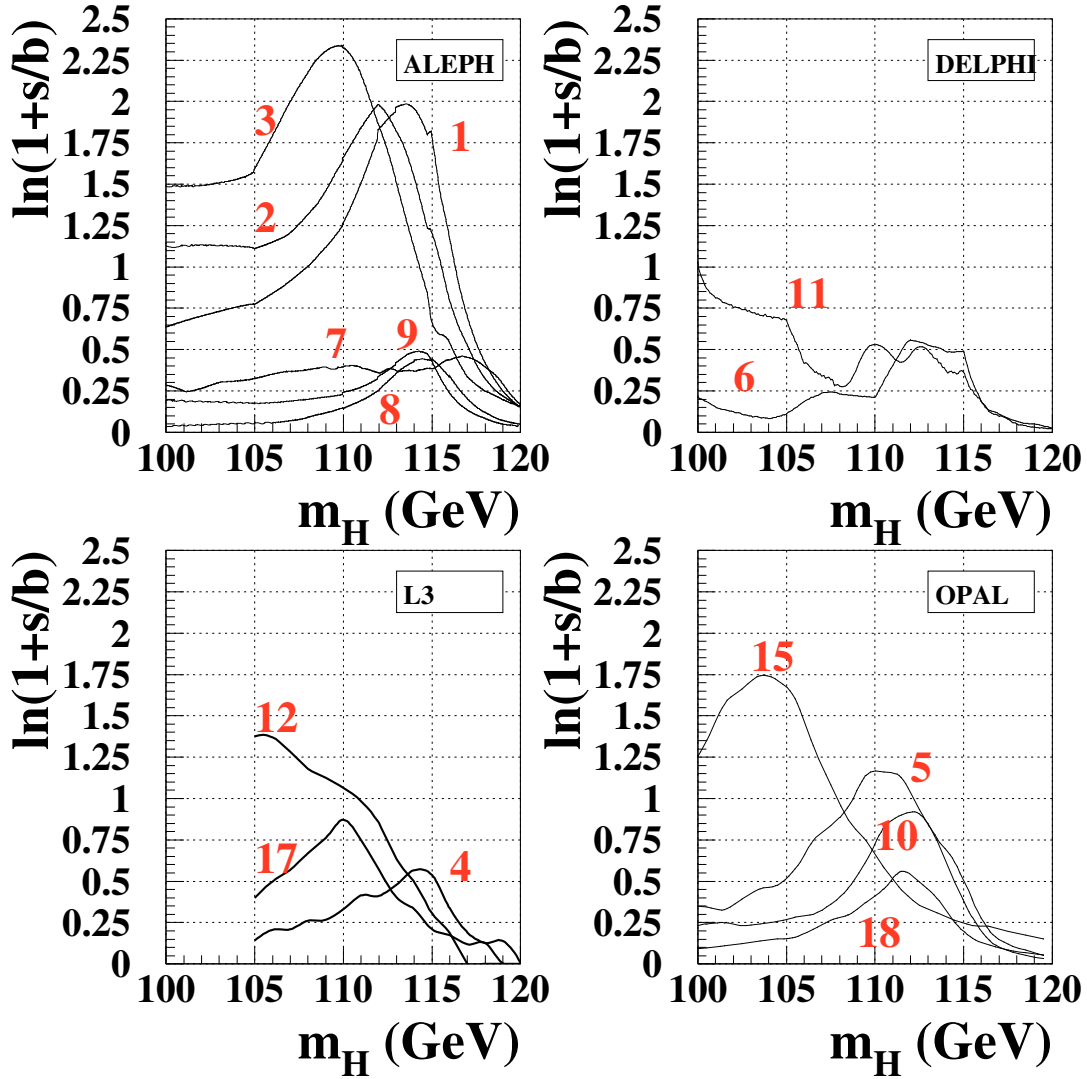


Figure 6.7: Evolution of the event weight $\ln(1+s/b)$ with test-mass m_H , for the events with the largest contributions to $-2\ln Q$ at $m_H = 115$ GeV. The labels correspond to the numbering in the first column of Table 6.2 [99].

tion is weak. The two plots in the lower part show the corresponding distributions for a test-mass chosen arbitrarily at $m_H = 110$ GeV. The data show clear preference for the background hypothesis in this case.

6.5.2 Bounds for the Higgs boson mass and coupling

The ratio CL_s as a function of the test-mass, shown in Figure 6.9, is used to derive a lower bound for the SM Higgs boson mass [104]. The test-mass corresponding to $CL_s = 0.05$

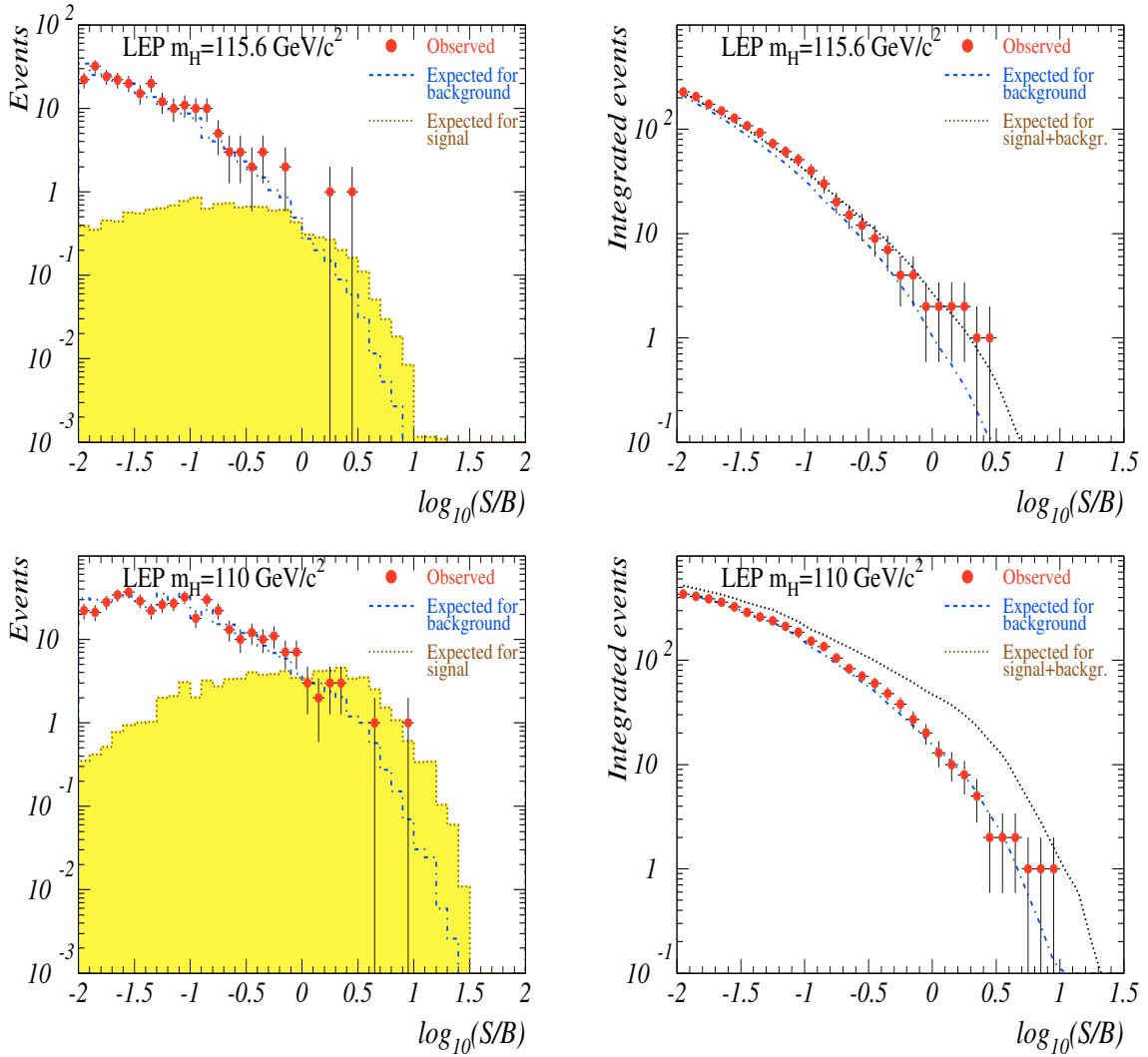


Figure 6.8: Left hand side: expected and observed distributions of $\log_{10}s/b$ for a test-mass of $m_H = 115.6 \text{ GeV}$ (upper part) and 110 GeV (lower part). White/shaded histograms: expected distributions for the background/signal; points with error bars are data. Right hand side: the integrals, from right to left, of the distributions shown in the plots on the left hand side. Dash-dotted/dotted lines: expected for background/signal+background [99].

defines the lower bound at the 95% confidence level. The expected and observed lower bounds obtained for the SM Higgs boson mass are listed in Table 6.3. The current lower bound from LEP is 114.1 GeV at the 95% confidence level. There is an excess which can be interpreted as production of a Standard Model Higgs boson with a mass higher than the quoted limit. It is concentrated mainly in the data sets with centre-of-mass energies higher than 206 GeV . The likelihood test designates 115.6 GeV as the preferred mass. The probability for a fluctuation of the Standard Model background is 3.4%. This effect is mainly driven by the ALEPH data and the four-jet final state.

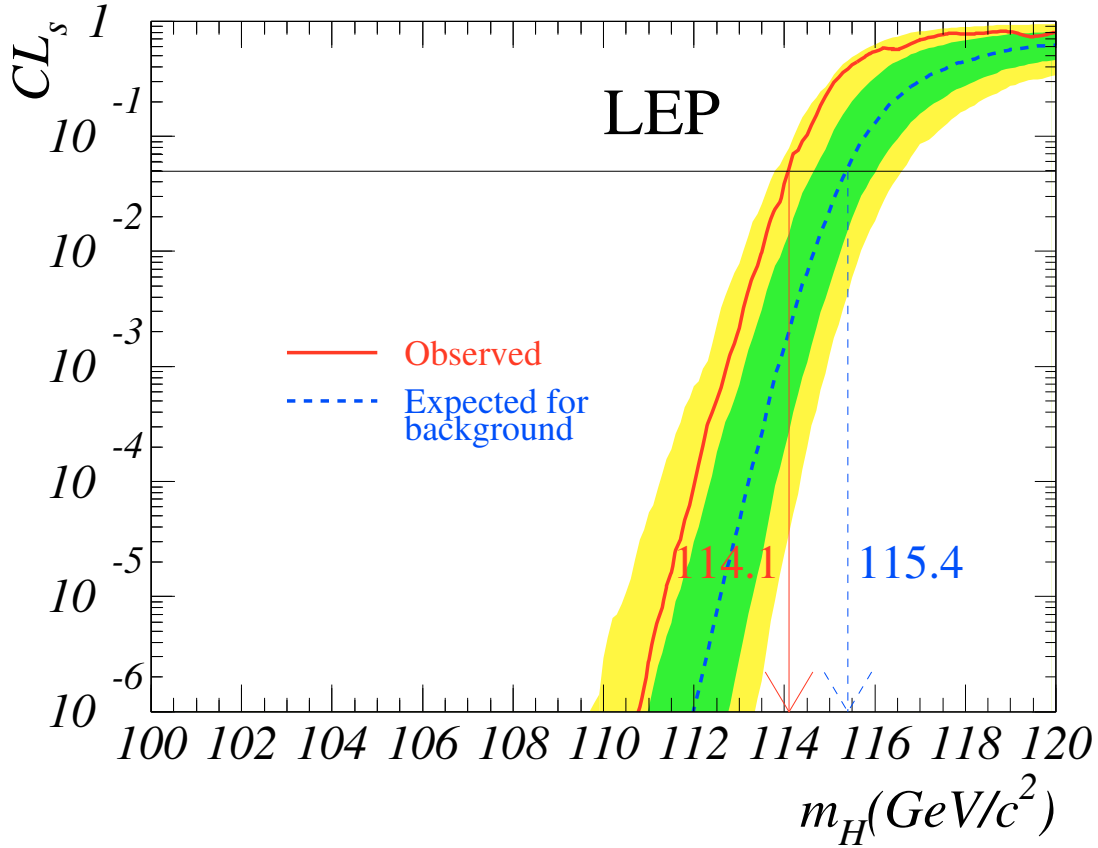


Figure 6.9: Confidence level CL_s for the signal+background hypothesis. Solid line: observation; dashed line: median background expectation. The dark/light shaded bands around the median expected line correspond to the $\pm 1/\pm 2$ standard deviation spreads from a large number of background experiments [99].

	Expected limit (GeV)	Observed limit (GeV)
ALEPH	114.2	111.5
DELPHI	113.5	114.3
L3	112.4	112.0
OPAL	112.6	109.4
LEP	115.4	114.1

Table 6.3: Expected (median) and observed 95% CL lower bounds on the SM Higgs boson mass, for the individual experiments and for all LEP data combined [99].

Chapter 7

Measurement of the Cross Section of $e^+e^- \rightarrow ZZ$

Resonant ZZ production is an important process to be studied at LEP as it offers a further test of the Standard Model of the electroweak interactions in the neutral gauge boson sector at energies never attained before. Measurements of the cross section differing from the expectations of the SM could signal the existence of new physics. In the Standard Model a pair of Z bosons can be produced via exchange of a virtual electron in the t-channel, as depicted in Figure 7.2 (conversion). Contributions from triple neutral gauge boson couplings are forbidden in the SM. A measurement of these couplings different from zero would indicate new physics phenomena. Therefore, a search for anomalous triple neutral gauge boson couplings is performed.

The most general ZZV vertex ($V = Z$ or γ , where the V subscript corresponds to an anomalous coupling ZZV) for on-shell Z's, shown in Figure 7.1 is given by [105]:

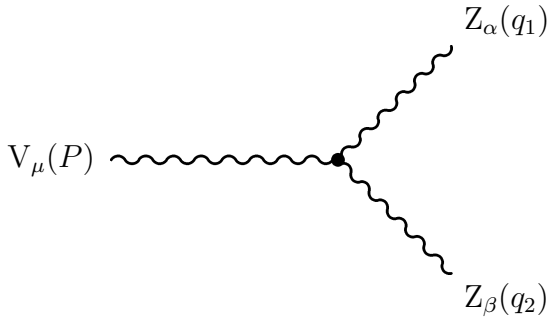


Figure 7.1: The most general Feynman graph for the anomalous ZZV vertex.

$$\Gamma_{ZZV}^{\alpha\beta\mu}(q_1, q_2, P) = \frac{s - m_V^2}{m_Z^2} \left[i f_4^{ZZV} (P^\alpha g^{\mu\beta} + P^\beta g^{\mu\alpha}) + i f_5^{ZZV} \epsilon^{\mu\alpha\beta\rho} (q_1 - q_2)_\rho \right]. \quad (7.1)$$

The vertex function vanishes at $s = m_V^2$ because of gauge invariance for $V=\gamma$, and Bose symmetry for $V = Z$. The interactions come from dimension-six operators. CP invariance forbids a non-zero f_4^{ZZV} and parity conservation requires $f_5^{ZZV} = 0$. If at least one of the final Z bosons are off-shell, five other couplings are possible. They are, however, proportional to $q^2 - m_Z^2$. Assuming on-shell production of a pair of Z bosons, only four couplings f^{Vi} may be different from zero. At tree level these couplings are zero in the Standard Model.

Furthermore, resonant ZZ production constitute an irreducible background for the search of the Standard Model Higgs boson.

The experimental investigation of the Z pair-production is made difficult by its rather low cross section in comparison with competing two- and four-fermion processes. Apart from W pair production, the most severe backgrounds comes from QCD processes.

The measurement of the cross section for the particular case of Z pair-production and decay into at least one b quark pair is also performed.

7.1 Data and Monte Carlo samples

The data were collected in the year 2000 by the L3 detector at LEP at the centre-of-mass energies of 200, 202, 204, 205, 206, 207, 208 and 209 GeV, and amount to an integrated luminosity of 217 pb^{-1} . For this analysis data at the center-of-mass energies less than 205.5 GeV and greater than 205.5 GeV are put together and denoted as 205 GeV and 207 GeV data, respectively, hereafter. The corresponding integrated luminosities are: 78 pb^{-1} at 205 GeV and 139 pb^{-1} at 207 GeV.

The EXCALIBUR [41] Monte Carlo is used to generate events belonging to both the signal and the background neutral-current four-fermion processes.

Background from fermion-pair production is modelled using KK2f [38] for $e^+e^- \rightarrow q\bar{q}(\gamma)$, KORALZ 4.02 [106] for $e^+e^- \rightarrow \mu^+\mu^-(\gamma)$ and $e^+e^- \rightarrow \tau^+\tau^-(\gamma)$ and BHWIDE [107] for $e^+e^- \rightarrow e^+e^-(\gamma)$. Background from charged-current four-fermion processes is generated with EXCALIBUR for $e\nu_e q\bar{q}'$ and $l^+\nu_l l^-\bar{\nu}_l$ with $l = e, \mu, \tau$ and KORALW 1.21 [40] for on-shell W pair-production. Contributions from two photon processes are modelled by PHOJET [37] for $e^+e^- \rightarrow e^+e^-q\bar{q}$ and DIAG36 [108] for $e^+e^- \rightarrow e^+e^-l^+l^-$.

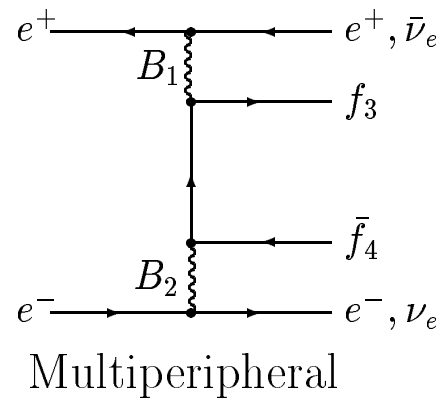
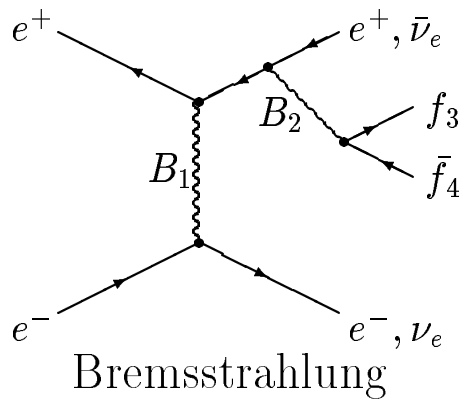
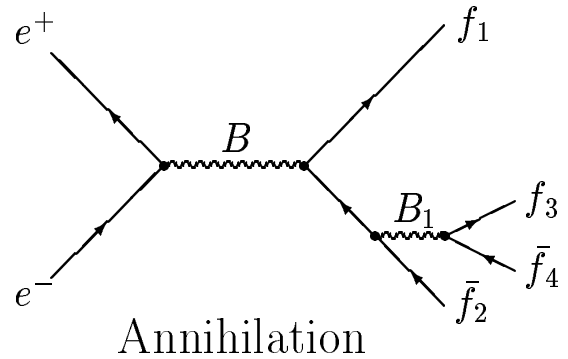
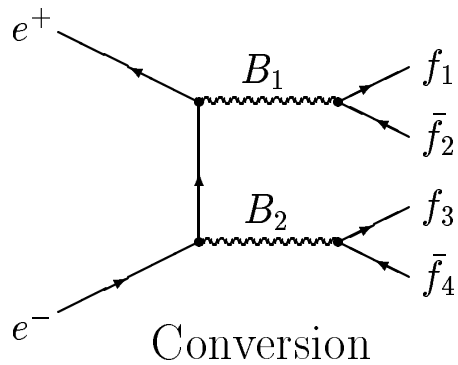
The L3 detector response is simulated using the GEANT program [62], which takes into account the effects of energy loss, multiple scattering and showering in the detector. Time dependent detector inefficiencies, as monitored during data taking period, are reproduced in simulations.

7.2 Signal Definition

Other neutral and charged current reactions can also result in a four fermion final state not distinguishable from $ZZ \rightarrow f\bar{f}f'\bar{f}'$, the signal definition needs therefore some explanation. The ZZ signal is defined using $e^+e^- \rightarrow f\bar{f}f'\bar{f}'$ events generated with the EXCALIBUR Monte Carlo event generator which takes all possible interference diagrams between initial and final state fermions from the several production mechanisms, as depicted in Figure 7.2, into account. Phase space cuts on the generator level are applied to define the region where both Z bosons are produced on-shell. The masses of the generated fermion pairs with the same flavour in the final state, $M(f_i\bar{f}_i)$ and $M(f_j\bar{f}_j)$, are required to be in the range between 70 and 105 GeV as shown in Figure 7.3 [109].

In the final states with four fermions of the same flavour, it is required that, at least for one of the two possible fermion pair combinations this requirement on the invariant mass of the fermion pair is fulfilled. The final states $u\bar{u}d\bar{d}$ and $c\bar{c}s\bar{s}$ can also result from

Abelian Classes



Nonabelian Classes

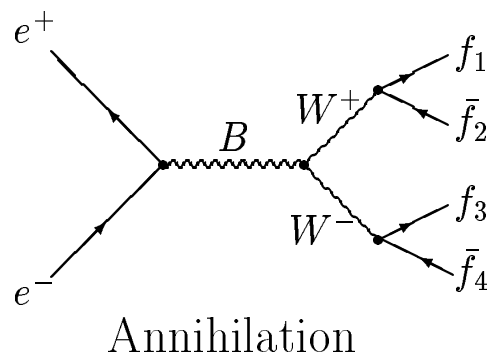
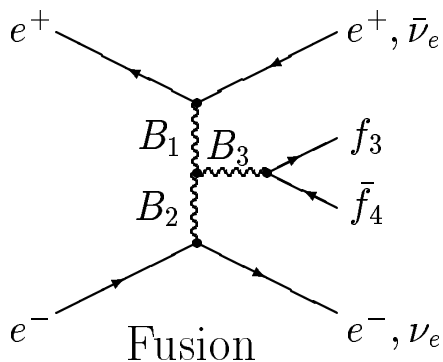


Figure 7.2: Topologies Feynman diagrams for the $e^+e^- \rightarrow f\bar{f}f'\bar{f}'$ process. The curly lines represent any allowed gauge boson ($B = \gamma, Z^0, B_1, B_2, B_3 = Z^0, \gamma, W^\pm$).

the process $e^+e^- \rightarrow W^+W^-$. To minimise the contribution of such events the masses of the fermion pairs susceptible to come from W decay are required to be either smaller

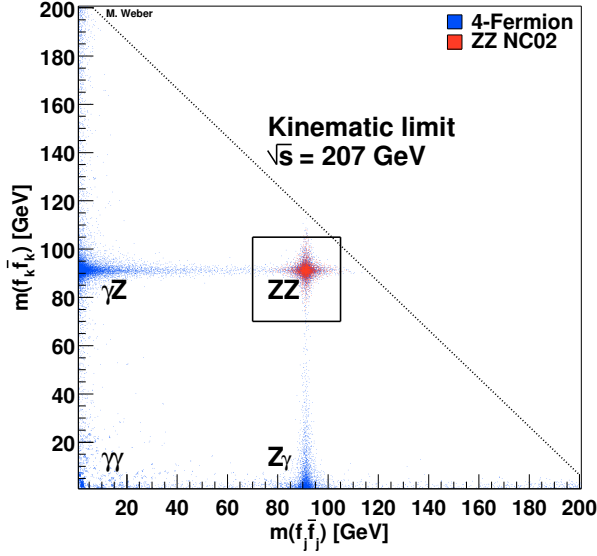


Figure 7.3: Requirement on the masses of the generated fermion pairs with the same flavour in the final state.

than 75 GeV or larger than 85 GeV, as demonstrated in Figure 7.4 [109].

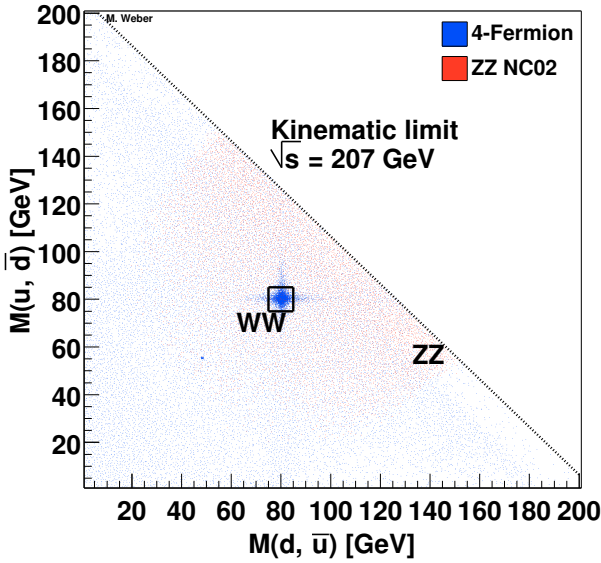


Figure 7.4: Requirement on the masses of the generated fermion pairs to minimise the contribution of W pair production.

Events with electrons in the final state are rejected if $|\cos \theta_e| > 0.95$, where θ_e is the electron polar angle. With these generator cuts the resulting cross sections for the ZZ signal for 207 GeV center-of-mass energy are given in Table 7.1.

Events which did not fulfil the signal definition criteria are considered as background and denoted as non- ZZ background hereafter.

7.3 Analysis Procedure

All visible final states of the Z pair decay are investigated with criteria similar to the Higgs boson analysis, described in detail in Chapter 5, but modified to follow the different

$ZZ \rightarrow$	$\sigma(pb)$	$ZZ \rightarrow$	$\sigma(pb)$	$ZZ \rightarrow$	$\sigma(pb)$	$ZZ \rightarrow$	$\sigma(pb)$
$u\bar{u}u\bar{u}$	0.01845	$u\bar{u}d\bar{d}$	0.03448	$u\bar{u}c\bar{c}$	0.03084	$\sum q_i\bar{q}_i q_j\bar{q}_j$	0.51702
$u\bar{u}s\bar{s}$	0.03901	$u\bar{u}b\bar{b}$	0.03901	$d\bar{d}d\bar{d}$	0.02553		
$d\bar{d}c\bar{c}$	0.03901	$d\bar{d}s\bar{s}$	0.04923	$d\bar{d}b\bar{b}$	0.04923		
$c\bar{c}c\bar{c}$	0.01845	$c\bar{c}s\bar{s}$	0.03448	$c\bar{c}b\bar{b}$	0.03901		
$s\bar{s}s\bar{s}$	0.02553	$s\bar{s}b\bar{b}$	0.04923	$b\bar{b}b\bar{b}$	0.02553		
$u\bar{u}\nu_e\bar{\nu}_e$	0.01792	$u\bar{u}\nu_\mu\bar{\nu}_\mu$	0.01687	$u\bar{u}\nu_\tau\bar{\nu}_\tau$	0.01687		
$d\bar{d}\nu_e\bar{\nu}_e$	0.02264	$d\bar{d}\nu_\mu\bar{\nu}_\mu$	0.02133	$d\bar{d}\nu_\tau\bar{\nu}_\tau$	0.02133		
$c\bar{c}\nu_e\bar{\nu}_e$	0.01792	$c\bar{c}\nu_\mu\bar{\nu}_\mu$	0.01687	$c\bar{c}\nu_\tau\bar{\nu}_\tau$	0.01687		
$s\bar{s}\nu_e\bar{\nu}_e$	0.02264	$s\bar{s}\nu_\mu\bar{\nu}_\mu$	0.02133	$s\bar{s}\nu_\tau\bar{\nu}_\tau$	0.02133		
$b\bar{b}\nu_e\bar{\nu}_e$	0.02264	$b\bar{b}\nu_\mu\bar{\nu}_\mu$	0.02133	$b\bar{b}\nu_\tau\bar{\nu}_\tau$	0.02133		
$u\bar{u}e^+e^-$	0.00979	$u\bar{u}\mu^+\mu^-$	0.00900	$u\bar{u}\tau^+\tau^-$	0.00900	$\sum q_i\bar{q}_i l_j^+ l_j^-$	0.15995
$d\bar{d}e^+e^-$	0.01207	$d\bar{d}\mu^+\mu^-$	0.01136	$d\bar{d}\tau^+\tau^-$	0.01136		
$c\bar{c}e^+e^-$	0.00979	$c\bar{c}\mu^+\mu^-$	0.00900	$c\bar{c}\tau^+\tau^-$	0.00900		
$s\bar{s}e^+e^-$	0.01207	$s\bar{s}\mu^+\mu^-$	0.01136	$s\bar{s}\tau^+\tau^-$	0.01136		
$b\bar{b}e^+e^-$	0.01207	$b\bar{b}\mu^+\mu^-$	0.01136	$b\bar{b}\tau^+\tau^-$	0.01136		
$e^+e^-\nu_e\bar{\nu}_e$	0.00497	$e^+e^-\nu_\mu\bar{\nu}_\mu$	0.00521	$e^+e^-\nu_\tau\bar{\nu}_\tau$	0.00521		
$\mu^+\mu^-\nu_e\bar{\nu}_e$	0.00521	$\mu^+\mu^-\nu_\mu\bar{\nu}_\mu$	0.00430	$\mu^+\mu^-\nu_\tau\bar{\nu}_\tau$	0.00492		
$\tau^+\tau^-\nu_e\bar{\nu}_e$	0.00521	$\tau^+\tau^-\nu_\mu\bar{\nu}_\mu$	0.00492	$\tau^+\tau^-\nu_\tau\bar{\nu}_\tau$	0.00430		
$e^+e^-e^+e^-$	0.00251	$e^+e^-\mu^+\mu^-$	0.00316	$e^+e^-\tau^+\tau^-$	0.00316	$\sum l_i^+ l_i^- l_j^+ l_j^-$	0.01543
$\mu^+\mu^-\mu^+\mu^-$	0.00199	$\mu^+\mu^-\tau^+\tau^-$	0.00262	$\tau^+\tau^-\tau^+\tau^-$	0.00199		

Table 7.1: Cross sections calculated with EXCALIBUR for the ZZ signal at 206.80 GeV center-of-mass energy. Total cross section is 1.079 pb. $\alpha_s = 0.119$ is included for the vertex correction, but not for QCD background.

characteristics of the signal topology, which manifests *e.g.* in a larger boost of the Z bosons since the Higgs boson is expected to be heavier. All selections are based on the identification of two fermion pairs each with a mass close to the Z boson mass. The fully hadronic channel is studied by the author of this thesis and the other channels covered by my colleagues from the ZZ Working Group [110] are presented here for sake of completeness.

7.3.1 The $ZZ \rightarrow q\bar{q}q'\bar{q}'$ Channel

The selection of $e^+e^- \rightarrow ZZ \rightarrow q\bar{q}q'\bar{q}'$ [111] has to cope with the large QCD and W pair production backgrounds. As for HZ final state, there are four-jet background processes with larger cross section, like $e^+e^- \rightarrow W^+W^-$ or $e^+e^- \rightarrow q\bar{q}gg$. First, to retain the majority of boson pair production events and remove a large fraction of background events arising from radiative return to Z , events from two photon processes, Ze^+e^- and W and Z leptonic and semi-leptonic decays, a preselection of high-multiplicity hadronic events with large visible energy and small missing energy is applied. At least 20 good tracks and 50 calorimetric clusters are required. The visible energy must not exceed 135%

and be greater than 75% of the centre-of-mass energy. Events must be well balanced, so the energy imbalance perpendicular to the beam direction must be less than 20% and the energy imbalance parallel to the beam energy must not exceed 26% of the visible energy. No identified electron or muon with an energy above 40 GeV in the event is required to suppress W pair production with one of the bosons decaying leptonically. In addition, events with an isolated photon of more than 25 GeV energy are rejected. The events passing this preselection are forced to four jets using the DURHAM algorithm [75] and then a constrained fit imposing four-momentum conservation is performed to improve the di-jet mass resolution.

The ZZ events from the signal MC selected and the contribution from $e^+e^- \rightarrow W^+W^-$ and $e^+e^- \rightarrow q\bar{q}(\gamma)$ Monte Carlo simulations along with the number of events selected in data are given in Table 7.2.

data set (GeV)	205	207
ZZ	33.5	61.2
<i>non</i> – ZZ	5.1	11.7
W^+W^-	389.6	646.8
$q\bar{q}(\gamma)$	127.9	277.0
Total background	522.5	935.5
Total expected	556.0	996.7
Data	550	1047

Table 7.2: Expected number of signal and background events and the number of selected data events after preselection. Signal efficiencies are larger than 80% for each of the data sets.

After the preselection the four jets are combined to three different di-jet pairings. For each of the three di-jet pairing the compatibility with the the hypothesis of Z pair production is tested by considering the quantity:

$$\chi_{ZZ}^2 = (\Sigma_i - 2m_Z)^2 / \sigma_{\Sigma_{zz}}^2 + \Delta_i^2 / \sigma_{\Delta_{zz}}^2,$$

where Σ_i and Δ_i are di-jet mass sum and di-jet mass difference of the i^{th} pairing and the quantities $\sigma_{\Sigma_{zz}}$ and $\sigma_{\Delta_{zz}}$ are the di-jet mass sum and di-jet mass difference resolutions, estimated from Monte Carlo. The pairing with the smallest value of χ_{ZZ}^2 is chosen. For this pairing the sum of the invariant masses of the di-jet systems $\Sigma_{M_{JJ}^{Z1}, M_{JJ}^{Z2}}$ is shown in Figure 7.5. Only events with $\Sigma_{M_{JJ}^{Z1}, M_{JJ}^{Z2}}$ above 165 GeV are accepted to suppress a large part of the W -pair production.

At the next step the invariant masses of the di-jet systems are compared to the expectation from the W^+W^- final states allowing to identify background from this channel. The quantity χ_{WW}^2 is constructed in a same way as χ_{ZZ}^2 but with respect to the W boson mass. The corresponding $\Sigma_{M_{JJ}^{W1}, M_{JJ}^{W2}}$ is calculated.

The most discriminating variables are combined into one discriminant using the binned likelihood technique [85]. Eleven variables are used to calculate the likelihood L_{ZZ} (description of the most of the variables can be found in the Higgs searches section, in Chapter 5):

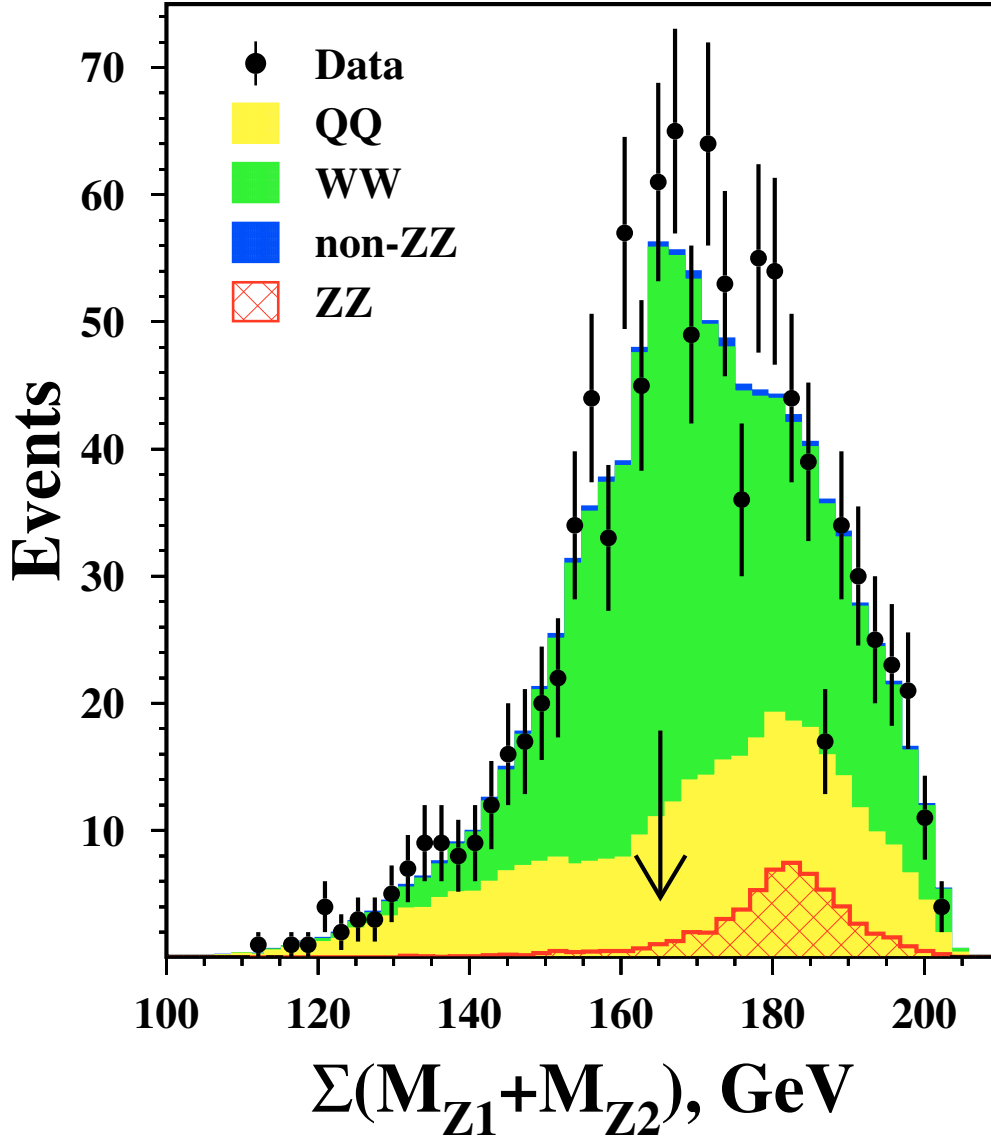


Figure 7.5: The sum of the invariant masses of the di-jet systems $\Sigma_{M_{JJ}^{Z1}, M_{JJ}^{Z2}}$.

- event sphericity, S ,
- maximal jet triplet boost, γ_{triple} ,
- maximal jet energy, $E_{\text{jet}}^{\text{max}}$,
- maximal jet boost, γ_{L1} ,

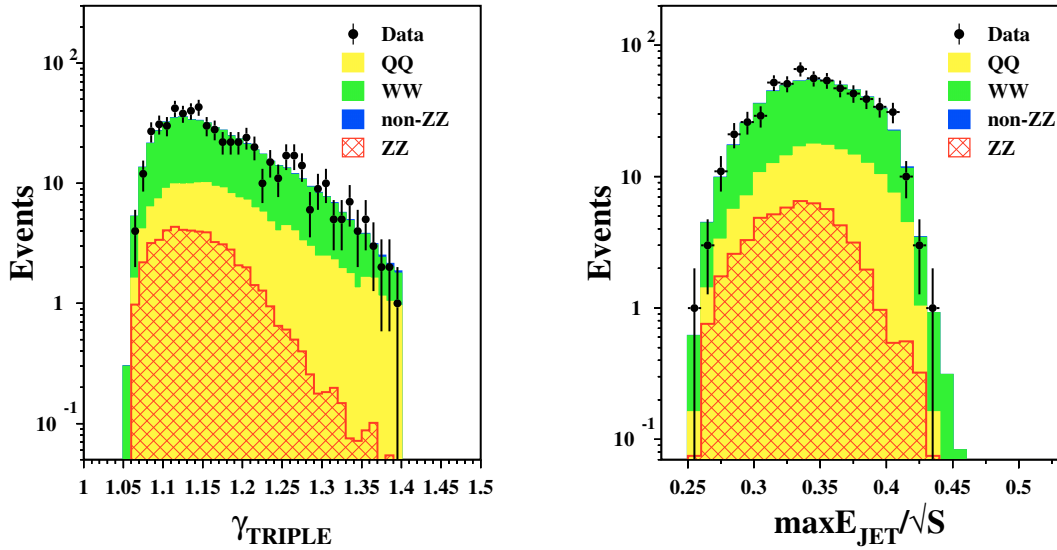


Figure 7.6: Distributions of variables used to construct the signal likelihood L_{ZZ} : triple jet boost γ_{triple} (left); maximal jet energy normalised to center-of-mass energy (right).

- maximal jet energy difference between any two jets, ΔE_{jet}^{max} ,
- opening angle between most and least energetic jets, Θ_{minmax} ,
- Mass from the 5C fit with $M_1 = M_2$, M_{eq}^{5C} ,
- Cosine of polar angle of the event thrust vector, $\cos \Theta_T$
- logarithm of the jet resolution parameter, Y_{34}^D ,
- χ_{ZZ}^2 ,
- χ_{WW}^2

The distribution of the M_{eq}^{5C} , $\log Y_{34}$, γ_{triple} , $-\log \text{Prob} \chi_{ZZ}^2$, E_{jet}^{max} , $\cos \Theta_T$ for the events selected as $ZZ \rightarrow q\bar{q}q'\bar{q}'$ for the 207 GeV energy bin compared to the expectation for the Standard Model processes, are shown in Figure 7.6 and Figure 7.7.

As it has been discussed in detail in Chapter 5.1.3, for the construction of this discriminant each process is considered as the separate event class k (k runs over ZZ , $non-ZZ$, W^+W^- and $q\bar{q}(\gamma)$ final states). For each of variables x_i which has discriminating power between the signal and the background a probability density function $f^k(x_i)$ is derived from Monte Carlo. Then the probability of an event to belong to the event class k , based solely on the value of the variable x_i , is calculated. Finally, the individual probabilities are combined into a likelihood. The likelihood L_{ZZ} for both 205 GeV and 207 GeV energy bins is shown in Figure 7.8.

Events are selected into the final sample if the value of L_{ZZ} exceeds a certain threshold which is optimised to minimise the expected error on the cross section ratio, $X = \frac{\sigma_{obs}}{\sigma_{SM}}$.

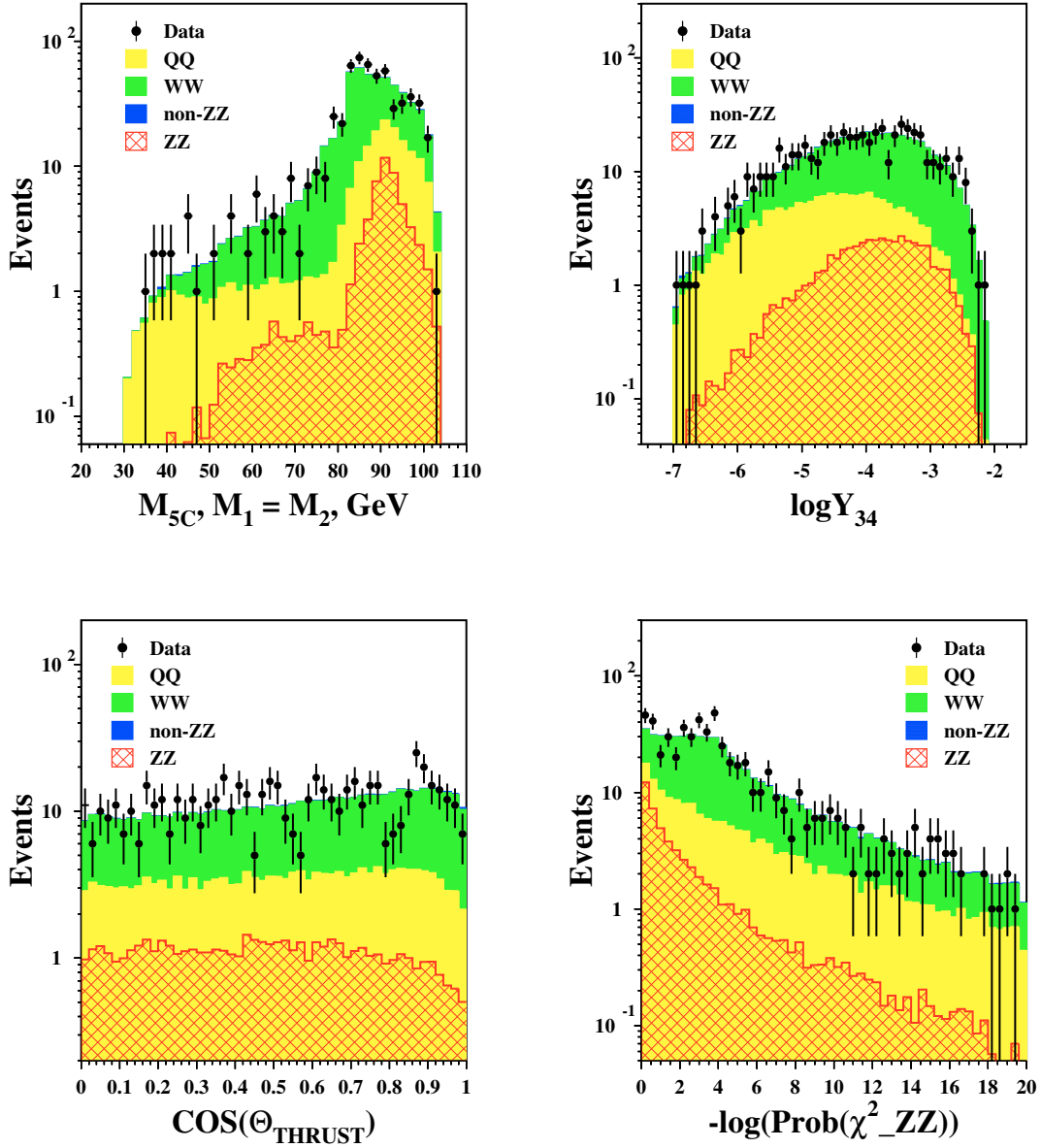


Figure 7.7: Distributions of variables used to construct the signal likelihood L_{ZZ} : mass from 5C fit (upper-left); logarithm of Y_{34} parameter (upper-right); Cosine of polar angle of event thrust vector, $\cos\Theta_T$ (lower-left); Logarithm of probability of χ^2_{ZZ} (lower-right).

The cut optimization procedure will be discussed later, after introducing the final discriminant construction.

The ZZ candidates selected and the contribution from $e^+e^- \rightarrow W^+W^-$ and $e^+e^- \rightarrow q\bar{q}(\gamma)$ Monte Carlo simulations along with the number of events selected in data are given in Table 7.3.

From these events the final discriminant is constructed in two steps. In the first step event characteristics without a b-tag information are used yielding a flavour blind

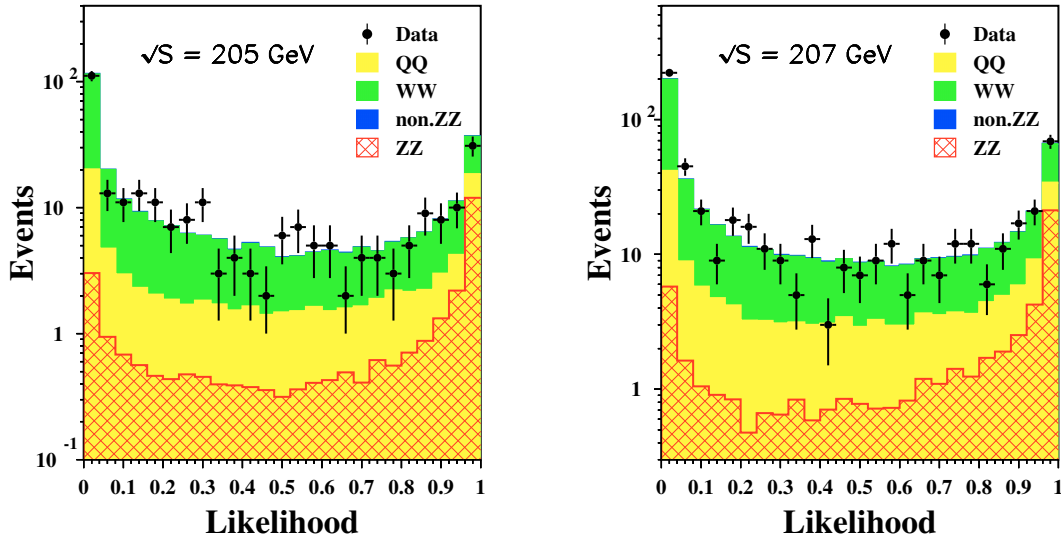


Figure 7.8: The Likelihood L_{ZZ} distribution for the signal and different background sources for the 205 GeV energy bin (left) and for 207 GeV energy bin (right).

measurement. The logarithm of the selection likelihood after applying the cut, $\log(L_{ZZ})$, $\Sigma_{M_{J_1}^{Z_1}, M_{J_2}^{Z_2}}$, the logarithm of jet resolution parameter, Y_{34}^{JADE} , and the event thrust are combined into the final discriminant for the flavour-blind approach. In the second step the two highest jet b tags in the event were added to the set of variables to form the final discriminant for the b-sensitive measurement. Distributions of some of the variables used to construct the final discriminants are shown as an example in Figure 7.9.

The final discriminants for 205 GeV and 207 GeV energy bins in the flavour-blind measurement are shown in the Figure 7.10. Figure 7.11 shows the final discriminant distributions for the b-sensitive case.

data set (GeV)	205	207
ZZ	25.0	46.7
$non - ZZ$	1.36	2.9
W^+W^-	105.4	184.7
$q\bar{q}(\gamma)$	36.23	72.3
Total background	143.0	259.9
Total expected	168.0	306.6
Data	165	301

Table 7.3: Expected number of signal and background events and the number of selected data events after the final selection. Signal efficiencies are above 60% for each of the data sets.

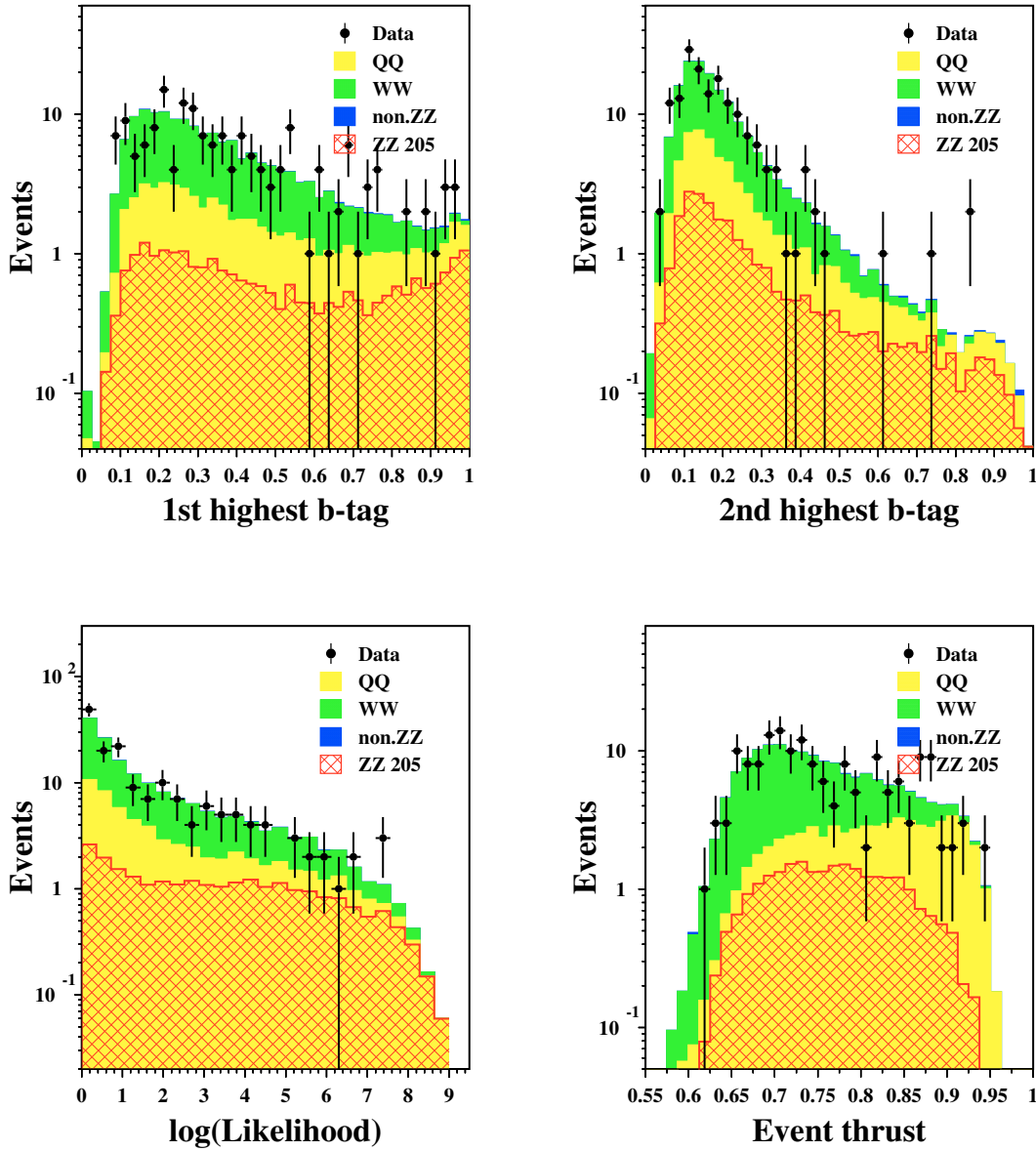


Figure 7.9: Distributions of variables used to construct the signal likelihood L_{ZZ} : 1st highest b -tag in the event (upper-left); 2nd highest b -tag in the event (upper-right); The logarithm of the selection likelihood after applying the cut, $\log(L_{ZZ})$ (lower-left); The event thrust (lower-right).

7.3.2 Cut Optimization

The cut optimisation procedure aims to maximise the performance of the analysis. The measure of the performance is the expected error on the cross section. Hence a procedure is invented to obtain the cut value on L_{ZZ} which result in the minimum of the expected error. For each final discriminant one million “gedanken experiments” have been per-

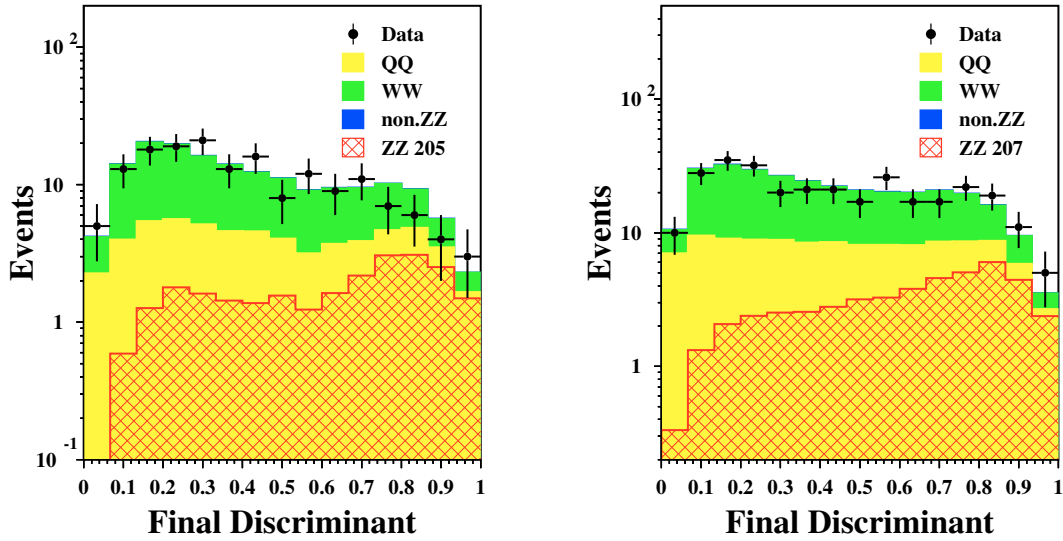


Figure 7.10: The final discriminant distribution for the data, signal and different background sources for the 205 GeV energy bin (left) and for 207 GeV energy bin (right) in the flavour-blind measurement.

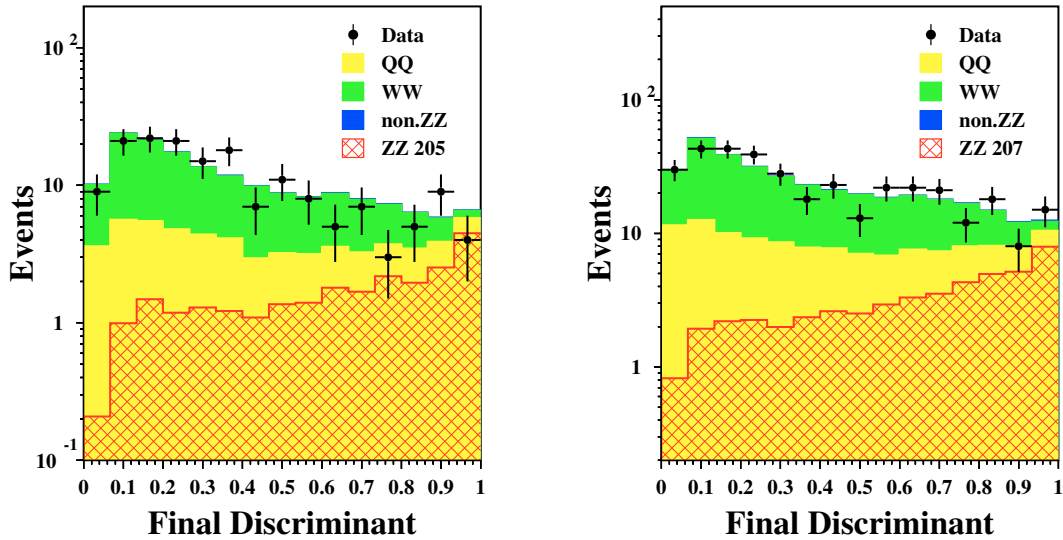


Figure 7.11: The final discriminant distribution for the data, signal and different background sources for the 205 GeV energy bin (left) and for 207 GeV energy bin (right) in the b -sensitive measurement including two highest jet b -tags.

formed, simulating the data content in each bin according to a Poissonian distribution given by the Standard Model signal and background expectations. In each experiment the value of cross section ratio X was calculated using the binned log-likelihood fit de-

scribed below. Figure 7.12 shows the distribution of the cross section ratio, X . A central

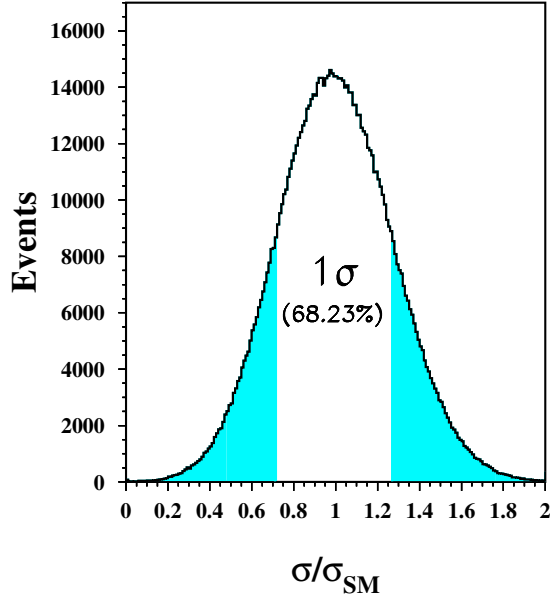


Figure 7.12: Distribution of the fitted cross section ratio imposing one million Poisson trials for each bin in the Final Discriminant. The central confidence interval with 68.23% confidence level is illustrated.

confidence interval of 68.23% is then calculated and upper and the lower bounds were taken as the expected error.

The value of the expected error on the cross section as the function of the cut on the selection likelihood is shown in Figure 7.13. The minimum of the total expected error

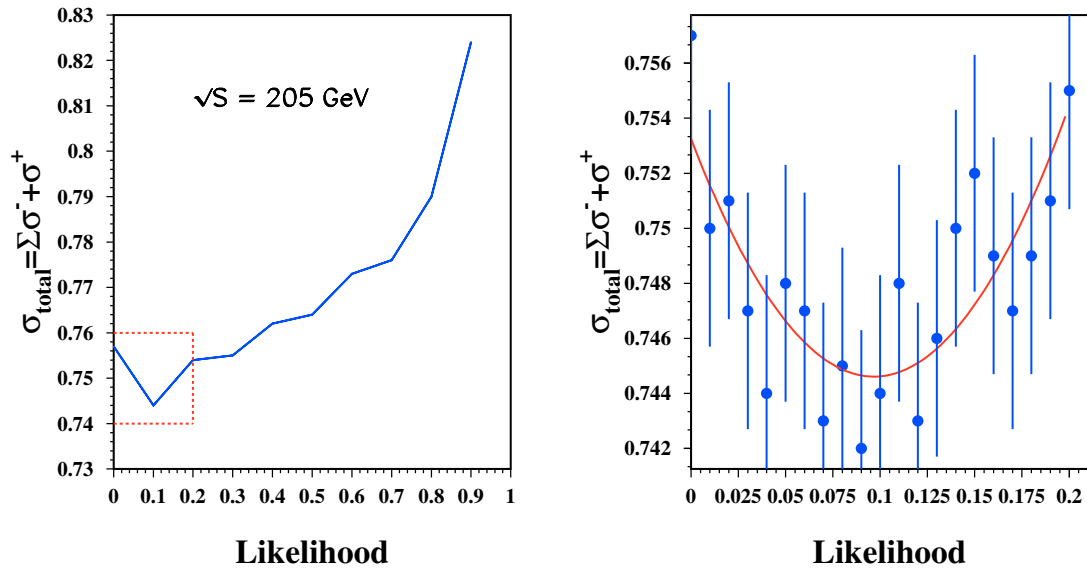


Figure 7.13: The total expected error on the cross section as the function of the cut value on the L_{ZZ} for the 205 GeV energy bin (left) and its zoomed area (right).

is clearly seen and the value of the cut on L_{ZZ} is fixed to the one, corresponding to this minimum.

7.3.3 The $q\bar{q}\nu\bar{\nu}$ Channel

High multiplicity hadronic events with more than three charged tracks and at least 15 calorimetric energy clusters are selected. The event invariant mass must exceed 50 GeV. These cuts reduce contributions from purely leptonic two-fermion final states, as well as two-photon interactions, while keeping a significant fraction of hadronic events from $q\bar{q}(\gamma)$ and W -pair production. These latter contributions are further reduced by requiring the visible mass to be less than 130 GeV and the mass recoiling against the hadronic system to exceed 50 GeV.

In addition, the transverse momentum is required to be greater than 5 GeV and the longitudinal momentum to be smaller than 40% of the visible energy. The energy deposition in the forward calorimeters must not exceed 10 GeV and the missing momentum vector must be at least 16° away from the beam axis. No electrons, muons or photons with energies above 20 GeV are allowed in the event and the energy in a 25° azimuthal sector around the missing energy direction, E_{25} , is required to be smaller than 30 GeV.

A total of 56.2 events satisfy the selection criteria with 25.4 and 30.8 events expected from the signal and background Monte Carlo simulations respectively. The dominating background is due to charged-current four-fermion processes. To separate further the ZZ signal from the remaining background a neural network is constructed. The inputs to the neural network include event shape variables, the sum of invariant and missing masses, the mass of two jets and the total missing momentum and E_{25} . The use of the neural network increases the signal fraction in the selected sample to approximately 60% for large neural network output values, as demonstrated in Figure 7.14. The efficiency

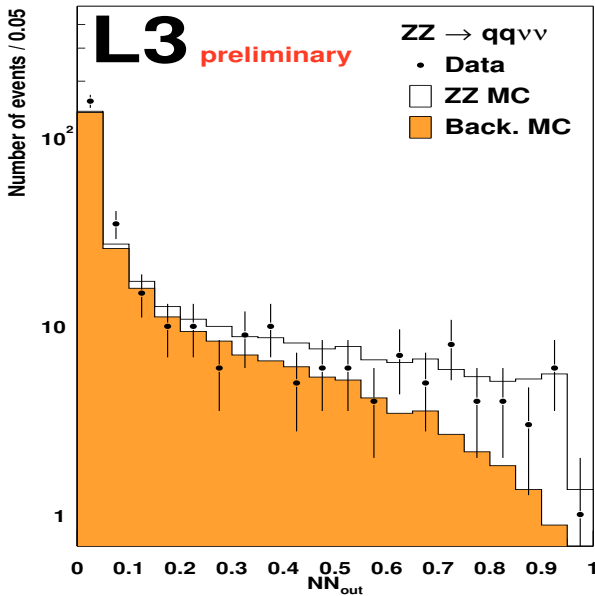


Figure 7.14: Distribution of the Neural Network output for data, Monte Carlo signal and background events in the $q\bar{q}\nu\bar{\nu}$ final state [112].

and the yield of this selection are reported in Table 7.4 for a cut at 0.5, while the full spectrum is used for the cross section determination.

Selection	Data	Signal MC	Background MC	Efficiency
$q\bar{q}q\bar{q}$	466	71.7	402.9	62%
$q\bar{q}\nu\bar{\nu}$	48	25.4	30.8	49%
$q\bar{q}l^+l^-$	31	18.4	6.4	55%
$l^+l^-\nu\bar{\nu}$	6	2.0	1.7	22%
$l^+l^-l^+l^-$	2	1.3	1.3	41%

Table 7.4: Data, signal and background Monte Carlo events selected by each analysis and their efficiencies. The numbers include data from all the center-of-mass energies collected by L3 in the year 2000. The numbers for the $q\bar{q}\nu\bar{\nu}$ final state are given for the neural network outputs larger than 0.5.

7.3.4 The $q\bar{q}l^+l^-$ Channel

A dedicated selection is performed¹ for each of the final states $q\bar{q}e^+e^-$, $q\bar{q}\mu^+\mu^-$ and $q\bar{q}\tau^+\tau^-$ after the application of a common preselection. This requires at least five charged tracks, 15 calorimetric clusters and a visible energy of more than $0.4\sqrt{s}$ together with two leptons of the same flavour.

Electrons are identified from energy depositions in the electromagnetic calorimeter whose shower shape is compatible with those initiated by an electron or a photon. At least one electron must have a matched track. Muons are reconstructed from tracks in the muon spectrometer pointing to the interaction vertex. Energy depositions in the calorimeters consistent with a minimum ionising particle (MIP) which have an associated track are also accepted as the second muon candidate. For the $q\bar{q}\tau^+\tau^-$ channel both a particle-based and a jet-based selection are performed. In the first, tau leptons are identified via their decay into isolated electrons or muons, or as an isolated low-multiplicity jet with one or three tracks and unit charge. In the jet-based selection, the event is forced into four-jets using the DURHAM algorithm. Two of the jets must each have less than four tracks. These jets are considered as tau candidates, but at least one of them must coincide with a tau candidate defined in the particle-based selection.

In the electron and the muon channels both the lepton and the jet pair must have an opening angle of at least 120° , tightened to 130° for taus. The invariant mass of the jet-jet and the lepton-lepton system after performing the kinematic fit, which imposes energy and momentum conservation, must be within 70 GeV and 120 GeV. The events are then subject to the DURHAM algorithm requiring $\log Y_{34}$ to be greater than -6.0 for the electron and tau channels and -6.5 for the muon one. Furthermore, the visible energy in the lepton channel must be at least $0.8\sqrt{s}$ and between $0.6\sqrt{s}$ and $0.9\sqrt{s}$ for the jet-based selection.

Additional requirements are applied in the tau selection to reduce the radiative $q\bar{q}(\gamma)$ background rejecting events containing a photon of energy larger than 30 GeV. Semi-leptonic WW events are rejected by requiring the transverse missing momentum to be lower than 40 GeV in events with no identified electron or muon with energy larger than 40 GeV.

¹Analysis of this channel is done by other members of the L3 ZZ working group.

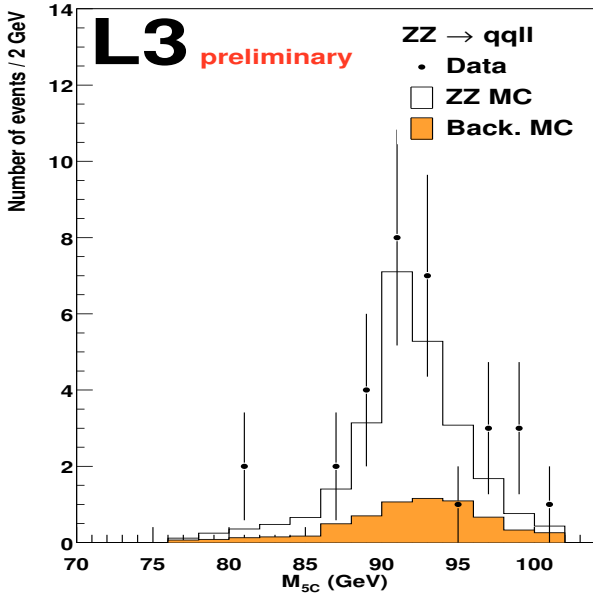


Figure 7.15: Distribution of the invariant mass M_{5C} after a kinematic fit of the lepton and jet pair for the $q\bar{q}l^{+}l^{-}$ selected events [112].

The kinematic fit is repeated on events that pass at least one of the four selection described above with the extra constraint of equal invariant masses for the jet-jet and lepton-lepton systems. The distribution of the invariant mass arising from the fit, M_{5C} , is shown in Figure 7.15. Table 7.4 summarises the yield of this selection.

7.3.5 The $l^{+}l^{-}\nu\bar{\nu}$ Channel

The selection for $ZZ \rightarrow l^{+}l^{-}\nu\bar{\nu}$ is optimised for electron and muon pairs identified as in the previous section and characterised by an invariant mass, M_{ll} , between 85 GeV and 95 GeV. The requirement on the associated track for electrons is dropped and MIPs are not considered.

In the electron channel only events with a visible energy between 75 GeV and 98 GeV are selected; this requirement is loosened to the range 65 GeV – 140 GeV for muons. The opening angle of the two electrons must be below 160° and from 143° to 172° for the two muons. In order to reduce the background from radiative Bhabha scattering and purely leptonic decays of W pairs, the recoil mass to the electron pair is required to be less than 95 GeV. The background from other resonant and non-resonant four-fermion processes is reduced by performing a kinematic fit imposing the Z mass to the visible pair of leptons and recalculating their four-momenta. The recoil mass, M_{rec} , after the fit is required to be less than 98 GeV for electrons and in excess of 84 GeV but not larger than 98 GeV for muons. The transverse momentum has to lie in the range from 4 GeV to 29 GeV.

The spectrum of the sum of M_{ll} and M_{rec} , peaking around twice the Z boson mass is used as a final variable and shown in Figure 7.16. Table 7.4 lists the efficiencies and the yield of the selection. No contribution in the $\tau^{+}\tau^{-}\nu\bar{\nu}$ signal channel is expected.

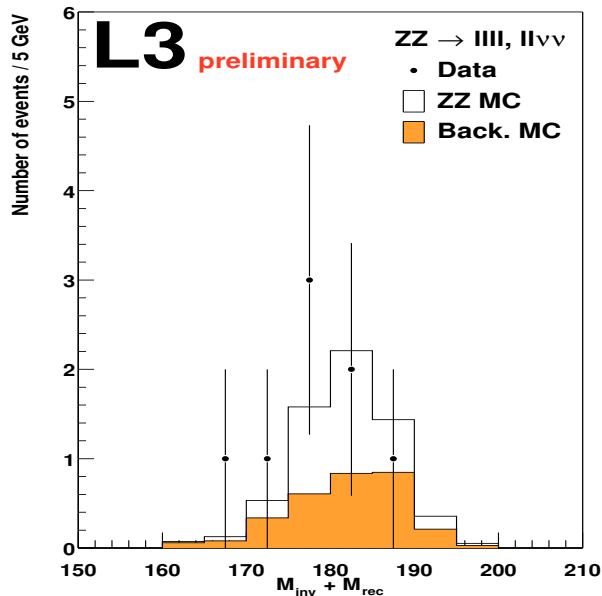


Figure 7.16: Sum of the invariant and recoil masses for the $l^+l^-\nu\bar{\nu}$ and $l^+l^-l^+l^-$ selected events [112].

7.3.6 The $l^+l^-l^+l^-$ Channel

This selection is based on events with at least four loosely identified leptons of a minimum energy of 3 GeV and the subsequent study of just one pair of them.

First a low multiplicity event preselection is applied, requiring at least two tracks but less than 15 calorimetric clusters, with a total visible energy between $0.2\sqrt{s}$ and $1.3\sqrt{s}$. Electrons and muons are identified as described in Section 7.3.4. Low angle electromagnetic showers ($|\cos\theta| > 0.95$) without a matching track are also considered and accepted as electrons. Tau candidates are identified as low multiplicity hadronic jets with either one or three tracks in a cone of 10° half opening angle. To reject hadronic jets, the energy between 10° and 30° around the tau direction must not exceed half of the energy in a cone of 10° half opening angle. To increase the selection efficiency, MIPs are also accepted.

If there are more than four lepton candidates, the four most consistent with energy and momentum conservation are chosen. Events are then required to have at least one electron, muon, tau or muon-MIP pair. Low angle electrons are not considered in this procedure. If more than one such pair is possible, the one with the invariant mass, M_{ll} , closest to the Z boson mass is chosen.

Both M_{ll} and the recoil mass, M_{rec} , to this selected lepton pair are required to lie between 70 GeV and 105 GeV. The data and Monte Carlo distributions for $M_{ll} + M_{rec}$ are shown in Figure 7.16. The performances of this analysis are summarised in Table 7.4.

7.4 Measurement of the ZZ Cross Section

The cross section of the Z pair-production is determined using a binned maximum likelihood fit to the most significant variables described above as the final variable for each final state. In this fit the ratio X of the measured cross section to the Standard Model one has been determined from the minimum of the logarithm of the likelihood. This

quantity can be written as:

$$P(X|N_j, b_j, s_j) = -\log \prod_j^{n_{\text{bins}}} \frac{e^{-(Xs_j + b_j)} (Xs_j + b_j)^{N_j}}{N_j!},$$

where j runs over the n_{bins} of the final discriminants used in the fit. In the above formula s_j, b_j and N_j are, respectively, the Standard Model signal and background expectations and the data contents in the j -th bin.

The change of one half of this logarithm of the likelihood with respect to the minimum represents the statistical error on X as it shown in Figure 7.17.

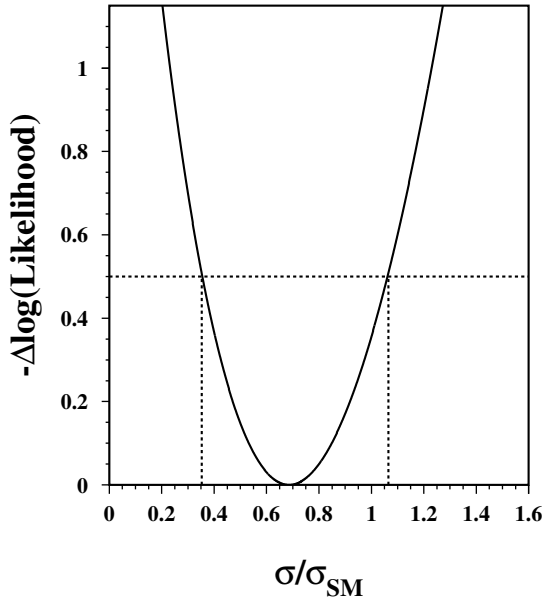


Figure 7.17: Difference to the minimum of the likelihood, whose change of one half with respect to the minimum represents the statistical error. This distribution obtained from the binned maximum likelihood fit of the final discriminant from 205 GeV energy bin in the frame of flavour-extended approach for the $q\bar{q}q\bar{q}$ final state.

The measured values of the ZZ cross section in the individual final states are listed in Table 7.5.

Data set	Cross section (pb)	$q\bar{q}q\bar{q}$	$q\bar{q}\nu\bar{\nu}$	$q\bar{q}l^+l^-$	$l^+l^-\nu\bar{\nu}$	$l^+l^-l^+l^-$
205 GeV	Measured	$0.35^{+0.18}_{-0.17}$	$0.10^{+0.10}_{-0.08}$	$0.11^{+0.06}_{-0.05}$	$0.15^{+0.12}_{-0.06}$	$0.00^{+0.08}_{-0.00}$
	Expected	0.511	0.295	0.158	0.044	0.015
207 GeV	Measured	$0.53^{+0.14}_{-0.14}$	$0.28^{+0.08}_{-0.07}$	$0.18^{+0.06}_{-0.05}$	$0.06^{+0.07}_{-0.05}$	$0.03^{+0.03}_{-0.02}$
	Expected	0.517	0.299	0.159	0.044	0.015

Table 7.5: Result of the individual cross section fits compared to the SM expectations

Assuming the Standard Model predictions for the relative weights of different channels, the ZZ cross section, σ_{ZZ} , for the two energy points is found to be:

$$\begin{aligned} \sigma_{ZZ}(205.1\text{GeV}) &= 0.86^{+0.23}_{-0.21} \pm 0.07 \text{ pb} \quad (SM : 1.07\text{pb}), \\ \sigma_{ZZ}(206.8\text{GeV}) &= 1.21^{+0.19}_{-0.17} \pm 0.10 \text{ pb} \quad (SM : 1.08\text{pb}), \end{aligned}$$

in good agreement with the expected cross sections within the signal definition cuts, reported in the parentheses. The first uncertainty is statistical and the second is systematic. The estimation of the systematic uncertainties is described in the next Section.

7.5 Study of Systematic Errors

The systematic uncertainties are grouped in correlated and uncorrelated sources among the channels. The correlated sources of systematic errors are the background cross sections, the LEP energy and the energy scale of the detector. As they modify the shapes of the investigated distributions, their effect is evaluated performing a new fit to calculate σ_{ZZ} after the quantity under consideration is scaled by a factor listed in Table 7.6. An

Systematic Source	Variation	$\delta\sigma_{ZZ}$ (pb)	$\delta\sigma_{ZZ\rightarrow b\bar{b}X}$ (pb)
Correlated sources			
LEP energy	40 MeV	< 0.01	< 0.01
WW cross section	2%	0.01	< 0.01
Four-jet rate	5%	0.01	0.01
We ν cross section	10%	0.01	< 0.01
Four-fermion cross section	5%	< 0.01	0.01
Energy scale	2%	0.01	0.01
Theory predictions	2%	0.01	< 0.01
Uncorrelated sources			
Jet resolution ($q\bar{q}q'\bar{q}'$)	2%	0.01	< 0.01
Charge multiplicity ($q\bar{q}q'\bar{q}'$)	1%	< 0.01	< 0.01
B-tag ($q\bar{q}q'\bar{q}'$)	see text	0.01	0.01
Bhabha background ($l^+l^-\nu\bar{\nu}$)	see text	0.01	–
Monte Carlo statistics	2%	0.02	0.01
Lepton identification	see text	0.01	0.01
Total		0.04	0.02

Table 7.6: Systematic uncertainties on σ_{ZZ} and $\sigma_{ZZ\rightarrow b\bar{b}X}$.

uncertainty of 2% is attributed to the measured cross section to take into account the difference of the assumed relative weights of the different channels, given by the EXCALIBUR calculation, with respect to those obtained with GRC4F [113] Monte Carlo generator and to parametrise the other uncertainties related to their calculation.

Some sources of systematic uncertainty are uncorrelated among the channels and modify the shapes of some of the discriminating distributions. For the $q\bar{q}q'\bar{q}'$ selection these are the jet resolution, the charged track multiplicity and the b-tag, and their effect is presented in Table 7.6. The jet resolution includes a variation of $\pm 2^\circ$ on the jet direction. A variation of the b-tag discriminant of $\pm 2\%$ models possible systematic effects and includes uncertainties in the Monte Carlo description of b-hadron jets.

Three additional sources of systematic uncertainty, uncorrelated among the channels, are considered: the Monte Carlo statistics of the signal and the background event samples

and the agreement between data and Monte Carlo. The latter comprises normalisation differences as derived from the comparison of data and Monte Carlo samples several times larger than the final ones, obtained by relaxing some selection criteria. It also includes differences in the shape of the distribution of the lepton identification variables around the adopted selection requirements. All these uncertainties, listed in Table 7.7 do not affect the shape of the discriminating distributions and their effect on the total cross section propagates as summarised in Table 7.5. The total systematic uncertainty is the sum in quadrature of all these contributions.

Channel	Systematic Source	Background uncertainty	Signal uncertainty
$q\bar{q}q\bar{q}$	Monte Carlo statistics	0.8%	1.7%
$q\bar{q}\nu\bar{\nu}$	Monte Carlo statistics	4.0%	3.0%
$q\bar{q}l^{+}l^{-}$	Monte Carlo statistics	4.7%	1.7%
	Lepton identification	2.7%	4.1%
$l^{+}l^{-}\nu\bar{\nu}$	Monte Carlo statistics	8.0%	8.0%
	Lepton identification	5.0%	4.0%
$l^{+}l^{-}l^{+}l^{-}$	Monte Carlo statistics	21.4%	2.1%
	Lepton identification	10.1%	4.3%

Table 7.7: Sources of uncorrelated systematic uncertainties.

7.6 Measurement of the $ZZ \rightarrow b\bar{b}X$ Cross Section

The measurement of the b-quark content in ZZ events constitutes a sound test of the detector capability to identify heavy particles decaying in b-quark produced in association with a Z boson. Such a configuration is of paramount importance at LEP as it could occur in the production of the Higgs boson. The production of the minimal or a supersymmetric Higgs boson would manifest via an enhancement of these events and their study complements the dedicated search for such a process.

The investigation of the $ZZ \rightarrow b\bar{b}X$ events proceeds by complementing the analyses of the $q\bar{q}\nu\bar{\nu}$ and $q\bar{q}l^{+}l^{-}$ final states described above with a further variable describing the b-quark content in the event. Three variables are then considered for each final state: M_{5C} for the $q\bar{q}l^{+}l^{-}$ and the neural network output for the $q\bar{q}\nu\bar{\nu}$ analysis together with the b-tag evaluated for each of the two hadronic jets. The combination of each of the sets of these three variables into a single discriminant proceeds as follows. First the variables are mapped to achieve uniform distributions for the background. Then the product of their observed values is calculated event by event. Finally the confidence level is calculated for the product of three uniformly distributed quantities to be less than the observed product. This confidence level is expected to be low for signal and flat for background. The final discriminant is the negative logarithm of this confidence level as shown as an example in Figure 7.18.

The investigation of the $ZZ \rightarrow b\bar{b}q\bar{q}$ ($q = u, d, s, c, b$) events proceeds in the same way as for the $ZZ \rightarrow q\bar{q}q'\bar{q}'$ events. However, the signal definition requires at least a

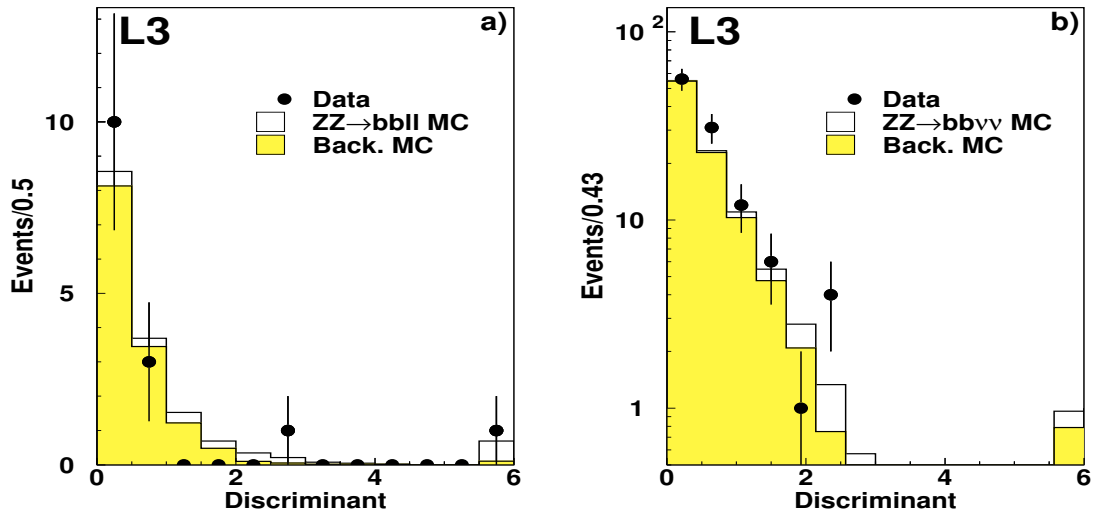


Figure 7.18: The final discriminant distribution for a) the $b\bar{b}l^+l^-$ and b) the $b\bar{b}\nu\bar{\nu}$ selection [112]. The last bin shows the overflows.

Z decaying into a b-quark pair on the generator level. The cross section calculation is performed as above.

The final discriminant distributions for 205 and 207 GeV center-of-mass energies are shown in Figure 7.19. The combined result² for the cross section $\sigma_{ZZ\rightarrow b\bar{b}X}$ is:

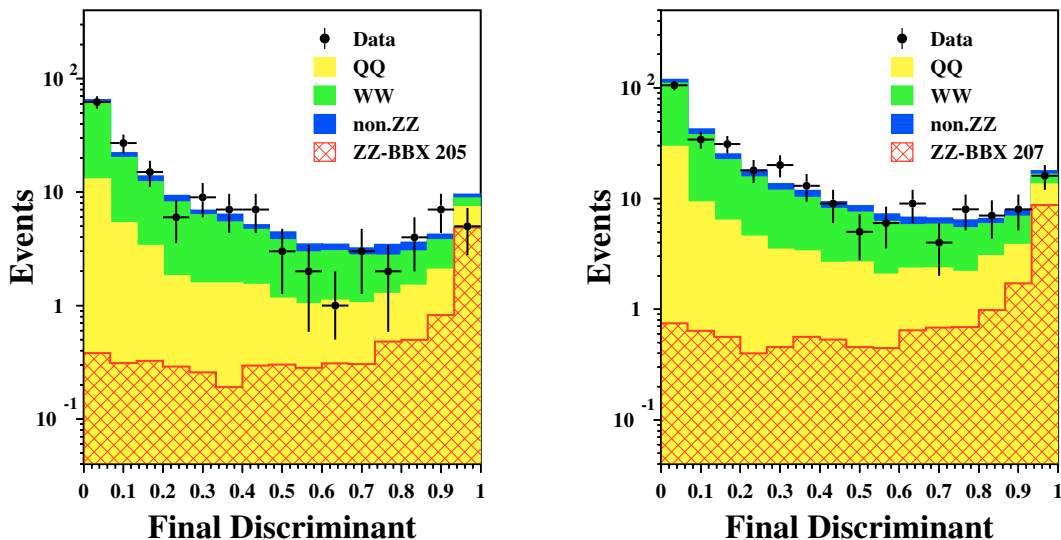


Figure 7.19: The final discriminant distribution for the signal and different background sources for the 205 GeV energy bin (left) and for 207 GeV energy bin (right) for the b-enhanced analysis, with the dedicated b-quark selection, $ZZ \rightarrow b\bar{b}X$.

$$\sigma_{ZZ \rightarrow b\bar{b}X}(206.2\text{GeV}) = 0.23 \pm 0.09 \pm 0.02 \text{ pb.}$$

This result agrees with the Standard Model prediction of 0.30 pb. The first uncertainty is statistical and the second is systematic. In this fit, other ZZ final states are fixed to their Standard Model expectations.

Figure 7.20 compares these measurements and those at lower center-of-mass energies with the Standard Model predictions.

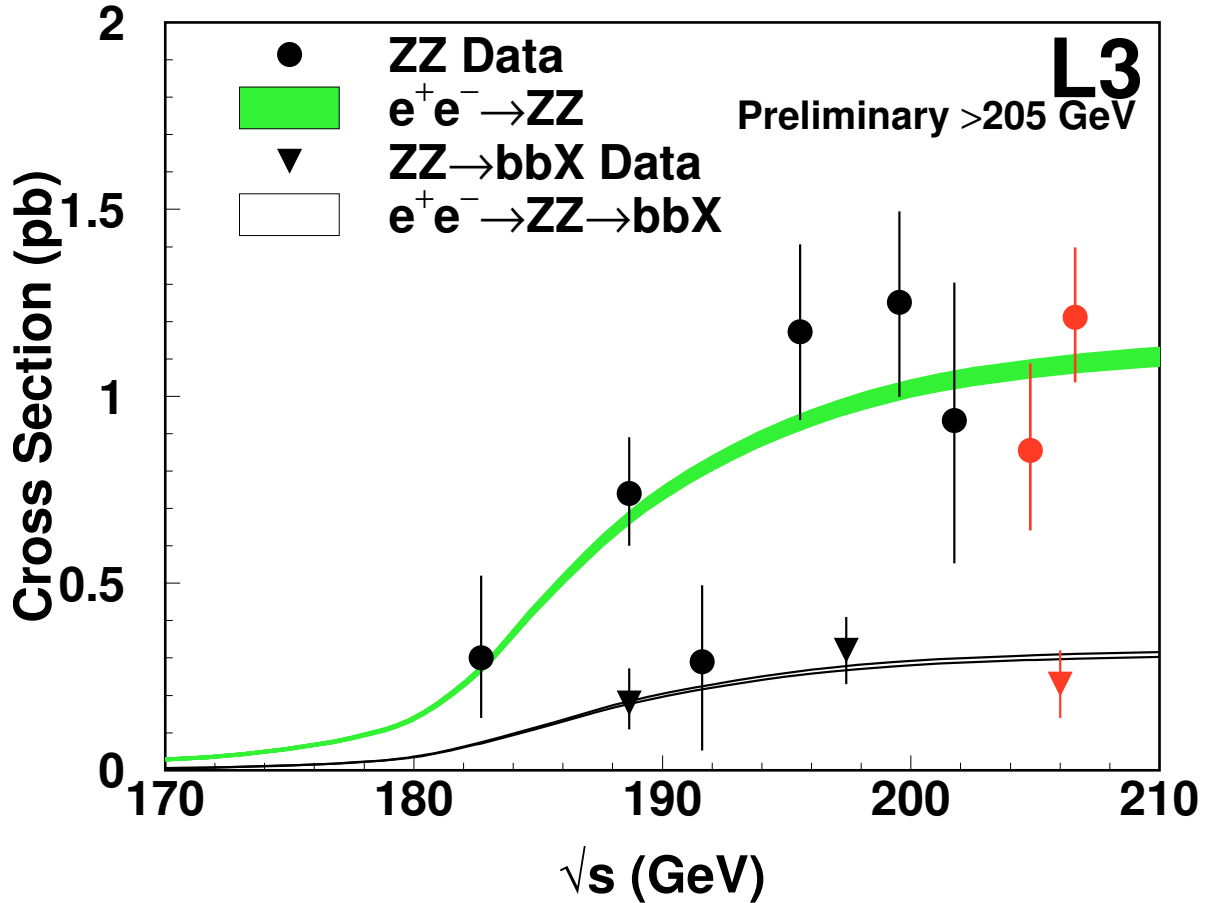


Figure 7.20: Measured values for the $e^+e^- \rightarrow ZZ$ and $e^+e^- \rightarrow b\bar{b}X$ cross sections and the corresponding Standard Model prediction. Signal definition cuts implemented with the EXCALIBUR Monte Carlo are applied and a $\pm 2\%$ uncertainty is associated to the predictions.

7.7 Anomalous Couplings

The effects of anomalous couplings change both the ZZ cross section and the shape of the final discriminant distributions discussed above. In order to calculate the impact of anomalous couplings on the measured distributions in the process $e^+e^- \rightarrow f\bar{f}f'\bar{f}'$,

²Since this process has a relatively low rate due to the small branching fraction $\text{Br}(Z \rightarrow b\bar{b})$ it is investigated in terms of a single luminosity averaged center-of-mass energy, equal to 206.2 GeV.

the EXCALIBUR generator is extended [114]. The matrix elements of the Standard Model are supplemented by an additional term containing anomalous couplings, $M_{AC}(\{p^\nu\}, \lambda, f_i^V)$ [105], where $\{p^\nu\}$ represents the phase space variables and the λ the helicities of initial and final state fermions. Four-fermions Monte Carlo distributions for non-zero anomalous couplings are then obtained by re-weighting each event with the factor

$$W(\{p^\nu\}, f_i^V) \equiv \frac{\frac{1}{4}\sum_\lambda |(M_{4f}(\{p^\nu\}, \lambda) + M_{AC}(\{p^\nu\}, \lambda, f_i^V))|^2}{\frac{1}{4}\sum_\lambda |(M_{4f}(\{p^\nu\}, \lambda)|^2} \quad (7.2)$$

where $M_{4f}(\{p^\nu\}, \lambda)$ is the Standard Model amplitude for the four-fermion final states. An average over initial state and a sum over final state helicities are carried out. Initial state radiation is taken into account by evaluating the event weight at the center-of-mass of the four-fermion system. Figure 7.21 displays the effect of an anomalous value

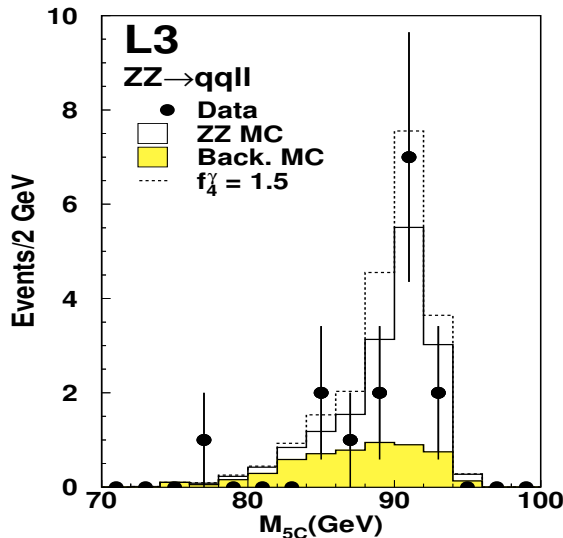


Figure 7.21: Invariant mass after a kinematic fit, M_{5C} , of the lepton pair for the $q\bar{q}l^+l^-$ selected events in the analysis for the $\sqrt{s} = 189$ GeV. The effect of an anomalous $ZZ\gamma$ vertex is also shown for a value of its couplings $f_4^\gamma = 1.5$ [115].

of f_4^γ obtained by re-weighting with this technique the four-fermion Monte Carlo events selected by the $q\bar{q}l^+l^-$ analysis.

Binned maximum likelihood fits to the distributions discussed above are performed allowing each of the anomalous couplings f_i^V to vary, fixing the other three to zero. The results of these fits are comparable with the Standard Model expectation and 95% confidence level limits on these couplings are set [112] as:

$$\begin{aligned} -0.42 &\leq f_4^Z \leq 0.41 \\ -0.46 &\leq f_5^Z \leq 1.21 \\ -0.24 &\leq f_4^\gamma \leq 0.26 \\ -0.48 &\leq f_5^\gamma \leq 0.56 \end{aligned}$$

Those limits include results from the previous analyses at lower center-of-mass energies [116], [117], [118]. These limits are still valid for off-shell ZZ production where additional couplings are possible. The small assymetries in these limits are due to the

interference term between the anomalous couplings diagram and the Standard Model diagrams. Systematic uncertainties on signal and background cross sections are taken into account in the derivation of the limits [119].

7.8 The L3 Combination

This section summarises the combination of published and preliminary results³, based on data collected up to 209 GeV by the L3 experiment on the Z-pair cross section. The detailed breakdown of the systematic errors for the measurements is described in Table 7.8. All these measurements along with the Standard Model predictions are shown in Figure 7.20.

\sqrt{s} (GeV)	σ_{ZZ}	$\Delta\sigma_{ZZ}^{\text{stat}}$	$\Delta\sigma_{ZZ}^{\text{syst(unc)}}$	$\Delta\sigma_{ZZ}^{\text{syst(corr)}}$	$\Delta\sigma_{ZZ}^{\text{syst}}$	$\Delta\sigma_{ZZ}$	$\Delta\sigma_{ZZ}^{\text{stat(exp)}}$
182.7	0.38	$^{+0.16}_{-0.15}$	± 0.05	± 0.01	± 0.05	$^{+0.17}_{-0.15}$	± 0.16
188.6	0.73	$^{+0.15}_{-0.14}$	± 0.03	± 0.02	± 0.04	$^{+0.15}_{-0.14}$	± 0.15
191.6	0.29	± 0.22	± 0.01	± 0.02	± 0.02	± 0.22	± 0.34
195.5	1.18	± 0.24	± 0.06	± 0.07	± 0.09	± 0.26	± 0.22
199.5	1.25	± 0.25	± 0.06	± 0.07	± 0.09	± 0.27	± 0.24
201.6	0.95	± 0.38	± 0.05	± 0.05	± 0.07	± 0.39	± 0.35
204.9	0.84	± 0.22	± 0.05	± 0.05	± 0.07	± 0.23	± 0.23
206.6	1.20	± 0.18	± 0.07	± 0.07	± 0.10	± 0.21	± 0.17

Table 7.8: Z-pair production cross section (in pb) at different energies. The first column contains the LEP center-of-mass energy, the second the measurements and the third the statistical uncertainty. The fourth and the fifth columns list the uncorrelated and correlated components of the systematic errors. The total systematic error is given in the sixth column, the total error in the seventh. The eighth column lists the symmetrised expected statistical error.

7.9 The LEP-wide Combination

This section summarises the combination of published and preliminary results, based on data collected up to 209 GeV by the four LEP Experiments on Z-pair cross section [120], [121], [122], [123].

Results from different experiments are combined by χ^2 minimisation using the Best Linear Unbiased Estimate method described in Ref. [124] and taking into account, when relevant, the correlations between the systematic uncertainties, which arise mainly from

³For the $e^+e^- \rightarrow ZZ \rightarrow q\bar{q}q\bar{q}$ channel the analysis which is developed by the author of this thesis and described in detail in Section 7.3.1 has the best performance among others, but for this combination a different one was taken at the earliest stage of preliminary combination for the 2001 summer conferences. The final combination is foreseen for the year 2002 with this analyses included.

the use of the same Monte Carlo codes to predict background cross sections and to simulate the hadronisation processes.

All numerical results presented in this section are defined as the NC02 [125] ZZ cross section. The combination of results is performed using the symmetrized expected statistical error of each analysis, to avoid biases due to the limited number of events selected. The component of the systematic errors that has been considered as correlated between experiments includes the uncertainty on the background from $q\bar{q}$, WW, Zee and $We\nu$ processes and the uncertainty on the b quark modelling. Summing these contributions together, the common error ranges between 0.01 and 0.07 pb for the various experiments.

The results of the different individual experiments and the LEP averages are summarised for the different center-of-mass energies in Table 7.9

\sqrt{s} (GeV)	ZZ cross section (pb)					$\chi^2/\text{d.o.f.}$
	Aleph	Delphi	L3	Opal	LEP	
182.7	$0.11^{+0.16}_{-0.12}$ *	$0.38 \pm 0.18^*$	$0.31^{+0.17}_{-0.15}$ *	$0.12^{+0.20}_{-0.18}$ *	0.23 ± 0.08	2.28/3
188.6	$0.67^{+0.14}_{-0.13}$ *	$0.60 \pm 0.15^*$	$0.73^{+0.15}_{-0.14}$ *	$0.80^{+0.15}_{-0.14}$ *	0.70 ± 0.18	0.97/3
191.6	$0.53^{+0.34}_{-0.27}$	0.55 ± 0.34	$0.29 \pm 0.22^*$	$1.13^{+0.47}_{-0.41}$	0.60 ± 0.18	2.88/3
195.5	$0.69^{+0.23}_{-0.20}$	1.17 ± 0.29	$1.18 \pm 0.26^*$	$1.19^{+0.28}_{-0.26}$	1.04 ± 0.13	3.23/3
199.5	$0.70^{+0.22}_{-0.20}$	1.08 ± 0.26	$1.25 \pm 0.27^*$	$1.09^{+0.26}_{-0.24}$	1.01 ± 0.13	2.80/3
201.6	$0.70^{+0.33}_{-0.28}$	0.87 ± 0.33	$0.95 \pm 0.39^*$	$0.94^{+0.38}_{-0.33}$	0.86 ± 0.18	0.32/3
204.9	$1.21^{+0.26}_{-0.23}$	1.05 ± 0.26	0.84 ± 0.23	$1.07^{+0.28}_{-0.26}$	1.03 ± 0.13	1.11/3
206.6	$1.01^{+0.19}_{-0.17}$	0.98 ± 0.22	1.20 ± 0.21	$1.07^{+0.22}_{-0.21}$	1.06 ± 0.11	0.76/3

Table 7.9: Z-pair production cross section from the four LEP experiments and combined values for the eight energies between 183 and 207 GeV. All results are preliminary with the exception of those indicated by a “*”. A common systematic error of (0.01-0.07) pb is taken into account in the averaging procedure.

The measurements are shown in Figure 7.22 as a function of the LEP center-of-mass energy, where they are compared to the Standard Model expectations calculated with the ZZTO [126] program with a $\pm 2\%$ uncertainty [126] assigned. The YFSZZ [127] package yields compatible estimations. The data do not show any significant deviation from the theoretical expectations.

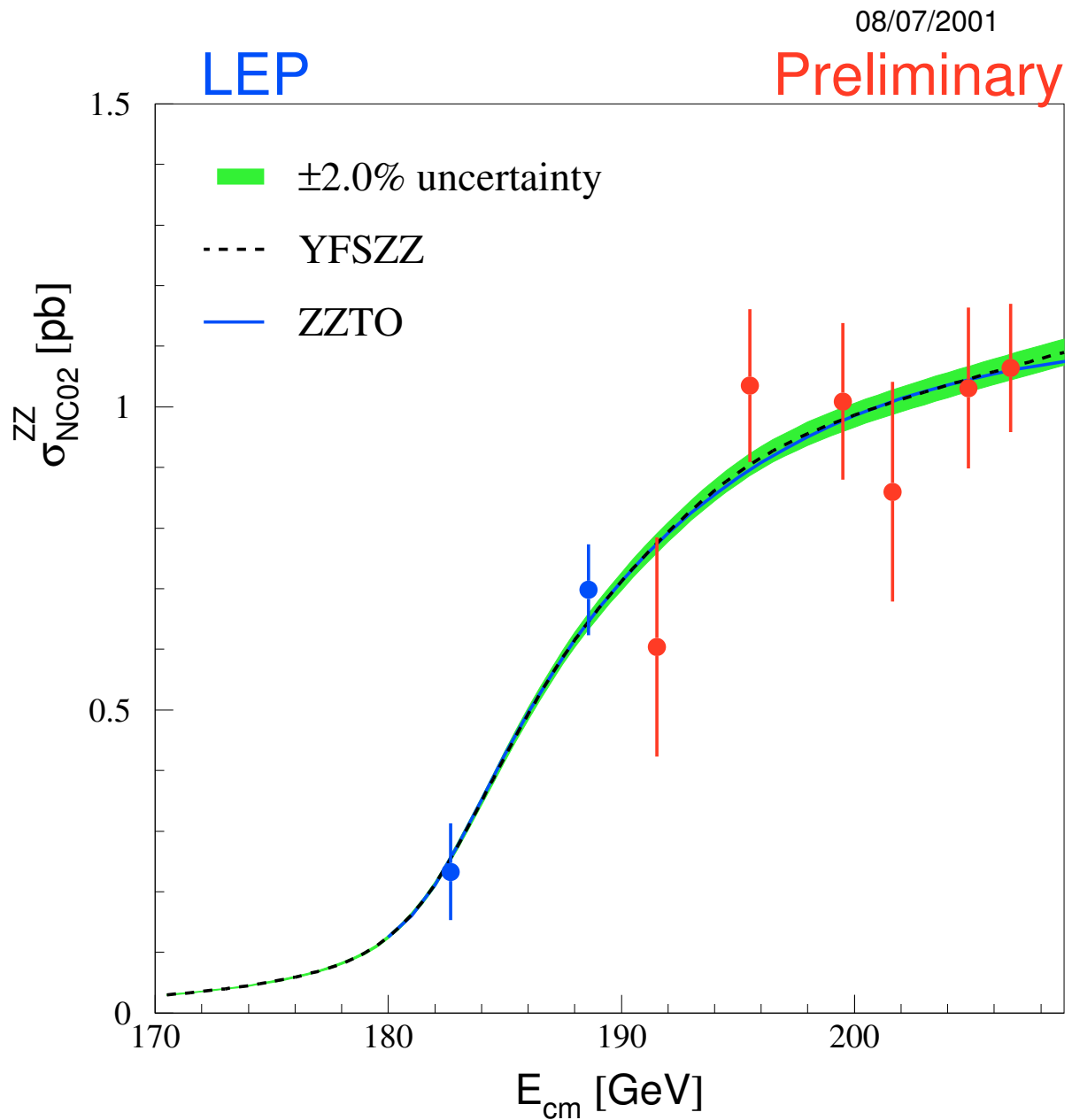


Figure 7.22: Measurements of the Z-pair production cross section, compared to the predictions of YFSZZ and ZZTO. The shaded area represent the $\pm 2\%$ uncertainty on the predictions.

Chapter 8

Conclusions

8.1 Higgs Searches

The Standard Model Higgs boson was searched for in 627 pb⁻¹ of data collected by the L3 detector at the center-of-mass energies $E_{cm} \geq 189$ GeV where ~ 139 pb⁻¹ corresponds to the center-of-mass energies greater than 206 GeV. These data are consistent with the expectations of Standard Model processes and no evidence of a Higgs boson signal is observed. The negative outcome of this search was translated into mass limits.

The SM Higgs boson was searched for in the $Hq\bar{q}$, $H\nu\bar{\nu}$, $H e^+e^-$, $H\mu^+\mu^-$, $H\tau^+\tau^-$ final states with $H \rightarrow b\bar{b}$ decays and the $HZ \rightarrow \tau^+\tau^-q\bar{q}$ channel, where the Higgs boson decays onto $\tau^+\tau^-$. No indication of a Higgs boson was found and a lower mass limit of

$$m_H > 112.0 \text{ GeV}$$

is set at the 95% confidence level. This number is compared to the results of the other LEP collaborations in Table 8.1. The results of the four LEP collaborations were com-

	Expected limit (GeV)	Observed limit (GeV)
ALEPH	114.2	111.5
DELPHI	113.5	114.3
L3	112.4	112.0
OPAL	112.6	109.4
LEP	115.4	114.1

Table 8.1: Expected (median) and observed 95% CL lower bounds on the SM Higgs boson mass, for the individual experiments and for all LEP data combined. Results from DELPHI and OPAL Collaborations are preliminary.

bined and a lower limit of

$$m_H > 114.1 \text{ GeV}$$

is derived at 95% confidence level [100].

8.2 ZZ Production

The pair-production of Z bosons in e^+e^- collisions was studied and the production cross section is measured at center-of-mass energies up to 209 GeV. This measurement is a unique opportunity to cross-check the Higgs analyses. In this thesis, the cross sections for $ZZ \rightarrow q\bar{q}q'\bar{q}'$ at $\sqrt{s} = 205$ GeV and $\sqrt{s} = 207$ GeV were measured to be:

$$\sigma_{ZZ \rightarrow q\bar{q}q'\bar{q}'} = 0.35_{-0.27}^{+0.28} \text{ (stat.) pb at 205 GeV,}$$

$$\sigma_{ZZ \rightarrow q\bar{q}q'\bar{q}'} = 0.53_{-0.14}^{+0.14} \text{ (stat.) pb at 207 GeV,}$$

which is in agreement with the SM expectations of 0.511 pb at 205 GeV and 0.517 pb at 207 GeV. Combining these results with the other channels $ZZ \rightarrow q\bar{q}\nu\bar{\nu}$, $\ell^+\ell^-\nu\bar{\nu}$, $\ell^+\ell^-\ell'^+\ell'^-$ and $ZZ \rightarrow q\bar{q}\ell^+\ell^-$ ($\ell = e, \mu, \tau$), leads to cross sections of:

$$\sigma_{ZZ} = 0.86_{-0.21}^{+0.23} \text{ (stat.)} \pm 0.07 \text{ (syst.) pb at 205 GeV,}$$

$$\sigma_{ZZ} = 1.21_{-0.17}^{+0.19} \text{ (stat.)} \pm 0.10 \text{ (syst.) pb at 207 GeV.}$$

The Standard Model predicts values of 1.07 pb and 1.08 pb in agreement with the measurement. For the combination of the results with the other experiments, the efficiencies are recalculated for the NC02 approximation for double-resonant Z pair production.

The investigation of the $ZZ \rightarrow b\bar{b}X$ events gives us the following result for the $\sigma_{ZZ \rightarrow b\bar{b}X}$:

$$\sigma_{ZZ \rightarrow b\bar{b}X} = 0.23 \pm 0.09 \text{ (stat.)} \pm 0.02 \text{ (syst.) pb at 206.2 GeV,}$$

which is in a good agreement with the Standard Model prediction of 0.30 pb.

The measurement of the cross section for $e^+e^- \rightarrow ZZ$ is used to search for anomalous triple couplings between neutral gauge bosons. Limits on these couplings, forbidden in the Standard Model, are derived at 95% confidence level:

$$\begin{aligned} -0.42 &\leq f_4^Z \leq 0.41 \\ -0.46 &\leq f_5^Z \leq 1.21 \\ -0.24 &\leq f_4^\gamma \leq 0.26 \\ -0.48 &\leq f_5^\gamma \leq 0.56 \end{aligned}$$

No deviation from the Standard Model is found.

8.3 The Phantom of LEP?

The LEP combined results [128] shows a preference for a Higgs boson with a mass of 115.6 GeV. At this mass, the probability for the background to generate the observed effect is 3.4%. Although this is far from evidence for a Higgs boson, theorists often used it as a “working hypothesis” to think about the consequences.

Actually, what would be the impact of a Higgs boson weighting 115 GeV [129]? It would not just be the crowning confirmation of the Standard Model, but would also be evidence for new physics beyond it, at a relatively low scale, potentially accessible to

the LHC. The reason for this is the shape of the effective Higgs potential, determined by the quartic Higgs coupling λ_H . This is subject to renormalization by the top-quark Yukawa coupling λ_t , as well as by the quartic Higgs coupling λ_H itself. With $m_t \sim 175$ GeV and $m_H \sim 115$ GeV, the renormalization by λ_t is stronger. Moreover, it tends to decrease λ_H , eventually turning it negative at a scale $\leq 10^6$ GeV [130]. This causes the effective Higgs potential to become unbounded below, implying that our present electroweak vacuum is unstable - unless some new physics is introduced at an energy below 10^6 GeV.

Could this new physics be a new non-perturbative set of strong interactions, as in technicolour or topcolour models [129]? These generally predict large effective scalar masses, e.g., about 1 TeV in the technicolour case [131]. In order to generate fermion masses, one needs to extend technicolour, and such models predict additional pseudo-scalar bosons weighting ~ 100 GeV. However, these would not be produced at LEP in association with the Z boson [132]. Therefore, technicolour has no obvious candidate for a 115 GeV ‘‘Higgs’’, and the same seems to be true for other strongly-interacting models of electroweak symmetry breaking [133].

In any perturbative framework, one can argue that the new low-energy physics should be bosonic, so that it may help λ_H counterbalance the destabilising effects of λ_t . In MSSM, the task of stabilisation is undertaken by the stop squarks.

In the MSSM the lightest neutral Higgs boson is predicted to weight ≤ 130 GeV. Since its mass is sensitive, via radiative corrections, to sparticle masses, one can try to use the ‘‘measurement’’ $m_H = 115$ GeV to guess how heavy squarks and other sparticles might be. To do this requires some assumption on the nature of the sparticle spectrum. For example, if all the spin-0 sparticles are assumed to be degenerate at some high (GUT) energy scale with a mass m_0 and likewise for the spin-1/2 gauginos with a common mass $m_{1/2}$, one could find that m_H is most sensitive to $m_{1/2}$ [133]. The gluino and squark masses would then be 2 or 3 times heavier: $m_{\tilde{g}} \geq 240$ GeV and $m_{\tilde{q}} \geq 700$ GeV, beyond the reach of the TEVATRON. However, masses up to a factor three above these lower limits are within reach of LHC, which should be able to cover all of the $(m_0, m_{1/2})$ parameter region where the lightest supersymmetric particle is likely to constitute the cold dark matter posited by astrophysicists and cosmologists [133].

8.4 Life After LEP

After the recent upgrade TEVATRON with its CDF and D0 detectors is ready for a data taking with Run2. What is the sensitivity of the TEVATRON experiments to a Higgs weighting 115 GeV? From an estimate [134], shown in Figure 8.1, in order to attain $3(5) \sigma$ they would need ~ 5 (15) fb^{-1} . As for the prospective TEVATRON luminosity, at the moment, 2fb^{-1} is ‘‘promised’’ by 2003. However, a road-map for reaching 15fb^{-1} by 2007 has been proposed. If this is achieved, the TEVATRON may have a chance to find the Higgs boson with $m_H = 115$ GeV.

According to CMS and ATLAS studies, as seen in Figure 8.2, the minimum luminosity required to start seeing a 115 GeV Higgs boson at 5σ is $\sim 10 \text{fb}^{-1}$, which may be achieved after two years of LHC running. Since at most a few weeks of very low

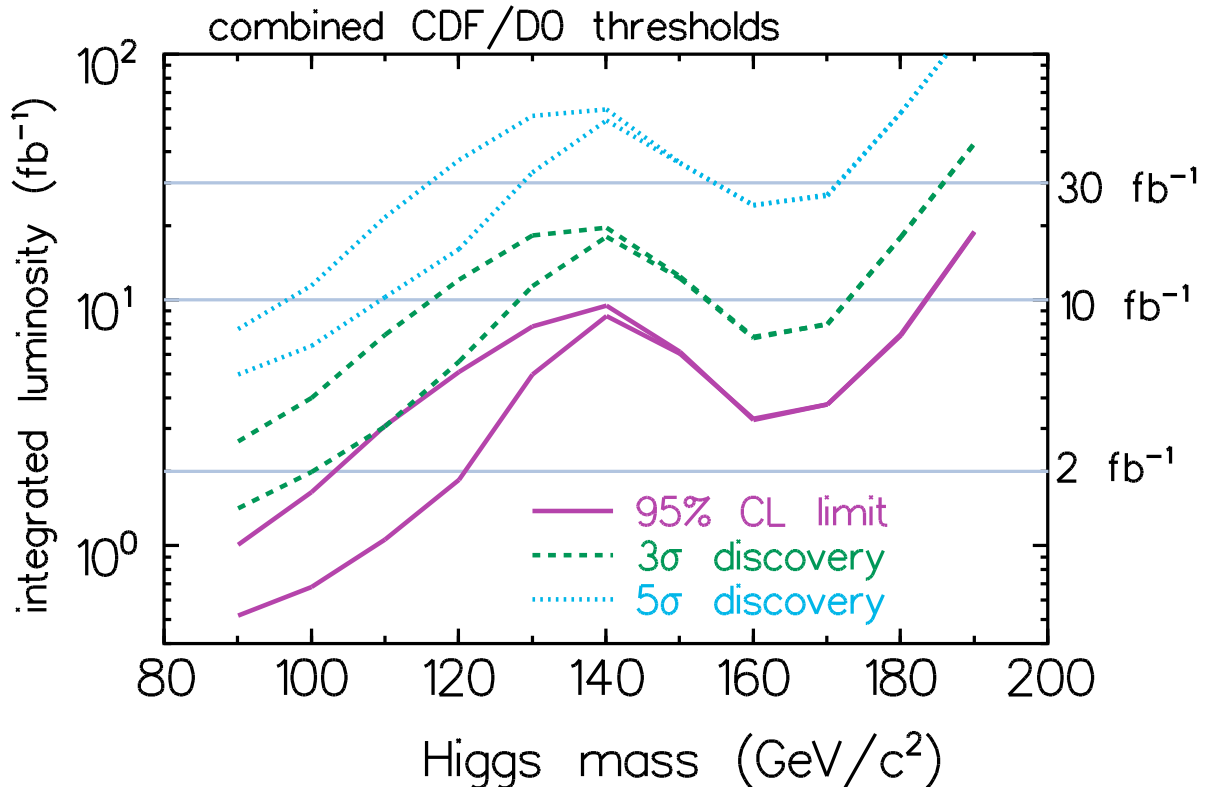


Figure 8.1: The sensitivity of the FNAL TEVATRON experiments to a light Higgs boson, as a function of its mass [134].

luminosity collisions can be envisaged in 2006, and only 1 or 2 fb⁻¹ is anticipated in 2006, this presumably means that the LHC could hope to discover a 115 GeV Higgs boson after the 2007 run.

There is, however, an important proviso. The LEP production mechanism, $e^+e^- \rightarrow ZH$, measures a different coupling - ZZH - from those to which the LHC is sensitive - $t\bar{t}H$ and $\gamma\gamma H$, with the latter being quite model-independent. The $\gamma\gamma H$ coupling is controlled by loop diagrams sensitive to virtual particles and the $t\bar{t}H$ coupling is sensitive to the ratio of VEV's and Higgs mixing in the MSSM. Therefore the information obtained at TEVATRON and the LHC will be complementary to that obtained by LEP, and both sets of information will be helpful in determining whether the candidate Higgs boson has all the expected couplings.

The long-term plans for high-energy physics at all major laboratories around the world (NLC, JLC, TESLA, Muon Collider) depend very much whether or not there is a light Higgs boson. All the indications from LEP precision data are that it must weigh ≤ 200 GeV [136]. A Higgs boson in hand would be worth two in the bush to the NLC, JLC, TESLA and Muon Collider communities, when they approach their funding agencies. For this they may have to wait until 2007. Until then, they and the rest of the particle physics community may be left in suspense while LHC construction will be finished. In the mean time we all support CMS and ATLAS in their definitive search for the Higgs boson.

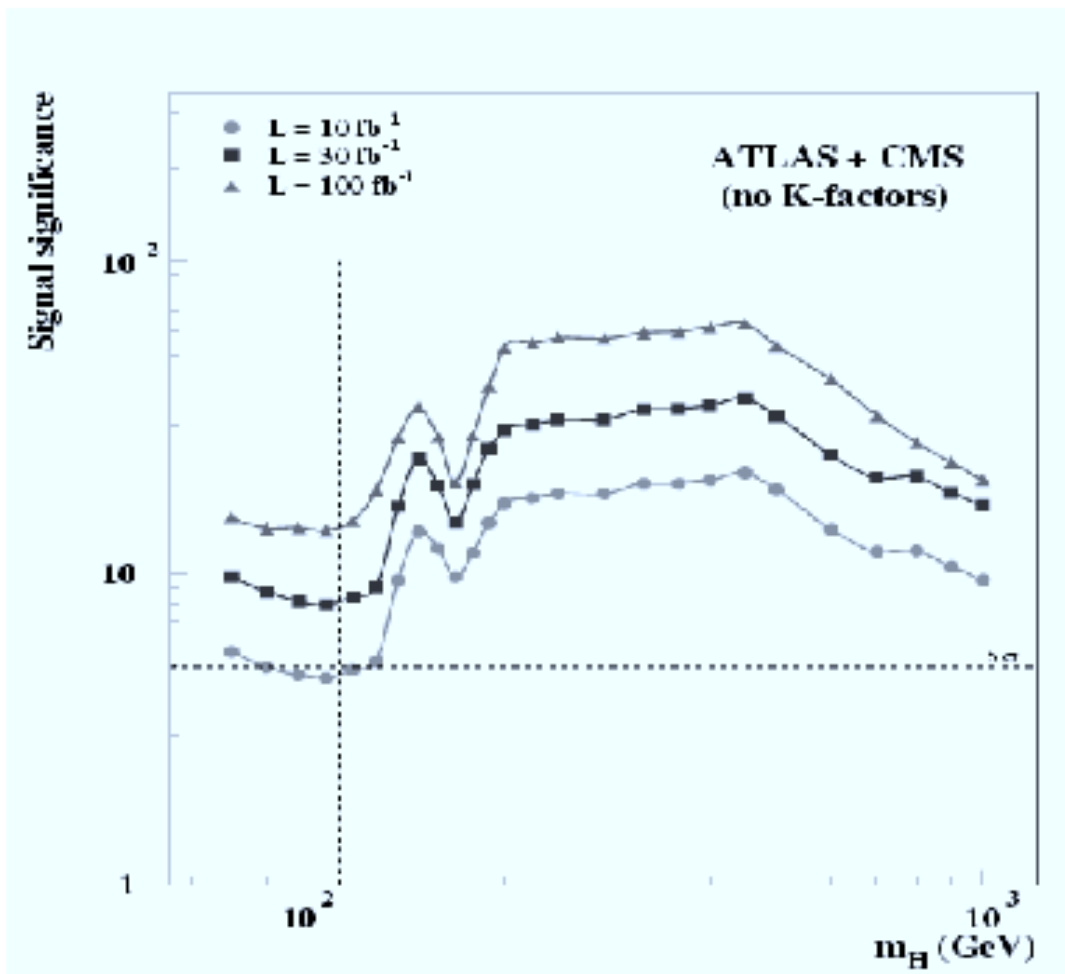


Figure 8.2: The sensitivity of the LHC experiments to a Higgs boson, as a function of its mass, for different accumulated luminosities [135].

Appendix A

Beam Spot Size Determination

The beam spot size and the relative displacement of the beam position from the nominal one are very essential tasks for the primary and secondary vertices determination and for the tagging of b-quarks. This chapter briefly describes the primary vertex position calculation and beam spot size determination technique.

The basic selection, requiring 2 charged tracks in the final state, full energy in the detector and cut on acollinearity to ensure back-to-back topology was performed, selecting Bhabha and dimuon events for the calibration run on the Z-resonance events, collected by L3 detector at year 1999 [137]. Only events from the barrel region of the Central Tracking Chamber were investigated.

The track coordinates $X_i, Y_i (i = 1, 2)$ at the point of closest approach can be parametrised as:

$$\begin{aligned} X_i &= X_r - \delta_i \sin \phi_i \\ Y_i &= Y_r + \delta_i \cos \phi_i, \end{aligned} \tag{A.1}$$

where X_r, Y_r - coordinates of the reference point, ϕ_i - azimuthal angle ϕ of the track i , δ_i - distance of the closest approach (DCA) of the track i .

The primary vertex coordinates X and Y can be calculated in the following way:

$$\begin{aligned} X &= \frac{X_1 + X_2}{2} \\ Y &= \frac{Y_1 + Y_2}{2}. \end{aligned} \tag{A.2}$$

For Z coordinate one obtain:

$$Z = \frac{Z_{IP1} + Z_{IP2}}{2}, \tag{A.3}$$

where Z_{IPi} - track i interception point with the beam axis in SZ plane. The DCA's δ_i of two tracks in a $e^+e^- \rightarrow e^+e^-$ or $e^+e^- \rightarrow \mu^-\mu^+$ event can be parametrised as:

$$\begin{aligned} \delta_1 &= \delta_{r1} + \delta_{BS} \\ \delta_2 &= \delta_{r2} - \delta_{BS} \end{aligned} \tag{A.4}$$

where $\delta_{ri}(i = 1, 2)$ contains the resolution effects and δ_{BS} - the distance between the beam spot (BS) center and the event vertex. From this we can write:

$$\begin{aligned}\delta_1 + \delta_2 &= \delta_{r1} + \delta_{r2} \\ \delta_1 - \delta_2 &= \delta_{r1} - \delta_{r2} + 2\delta_{BS}\end{aligned}\tag{A.5}$$

It follows for the variances:

$$\begin{aligned}\sigma^2(\delta_1 + \delta_2) &= \sigma^2(\delta_{r1}) + \sigma^2(\delta_{r2}) \\ \sigma^2(\delta_1 - \delta_2) &= \sigma^2(\delta_{r1}) + \sigma^2(\delta_{r2}) + 4\sigma^2(\sigma_{BS})\end{aligned}\tag{A.6}$$

The beam spot width $\sigma_{BS} \equiv \sigma^2(\delta_{BS})$ can be then written as:

$$\sigma_{BS}^2 = \frac{\sigma^2(\delta_1 - \delta_2) - \sigma^2(\delta_1 + \delta_2)}{4}\tag{A.7}$$

On the other side, the beam spot width can be expressed in terms of its horizontal and vertical components $\sigma_{BS,x}$ and $\sigma_{BS,y}$:

$$\sigma_{BS}^2(\phi) = \sigma_{BS,x}^2 \sin^2 \phi + \sigma_{BS,y}^2 \cos^2 \phi\tag{A.8}$$

The procedure of the beam spot determination is performed in the following steps:

1. The ϕ -interval $[0; 2\pi]$ is divided in 12 intervals and the variances $\sigma^2(\delta_1 \pm \delta_2)$ are determined for each bin by fitting a single Gaussian to the $\delta_1 \pm \delta_2$ distributions.
2. The beam spot width $\sigma_{BSi}, i = (1, 12)$ is calculated for each ϕ -bin i using the Equation A.7.
3. The vertical and horizontal sizes of the beam spot are determined by fitting the ϕ -dependence of σ_{BS} using the Equation A.8, as shown in Figure A.1

For the center of the beam spot coordinates the following values were derived:

$$\begin{aligned}X &= -0.4878 \pm 0.0012 \text{ mm} \\ Y &= -0.0286 \pm 0.0005 \text{ mm} \\ Z &= -2.95 \pm 0.11 \text{ mm}\end{aligned}\tag{A.9}$$

And for the beam spot sizes:

$$\begin{aligned}\sigma_{BS,x} &= 122 \pm 2 \text{ } \mu\text{m} \\ \sigma_{BS,y} &= 23 \pm 4 \text{ } \mu\text{m}\end{aligned}\tag{A.10}$$

For the year 2000 data the same procedure was performed [138] for the calibration runs at Z-peak and for the high energy data. Table A.1 summarises the values for the beam spot size: The difference in the values of the beam spot size for the calibration runs and the high energy data can be expressed in terms of a synchrotron radiation effects for a different center-of-mass energies.

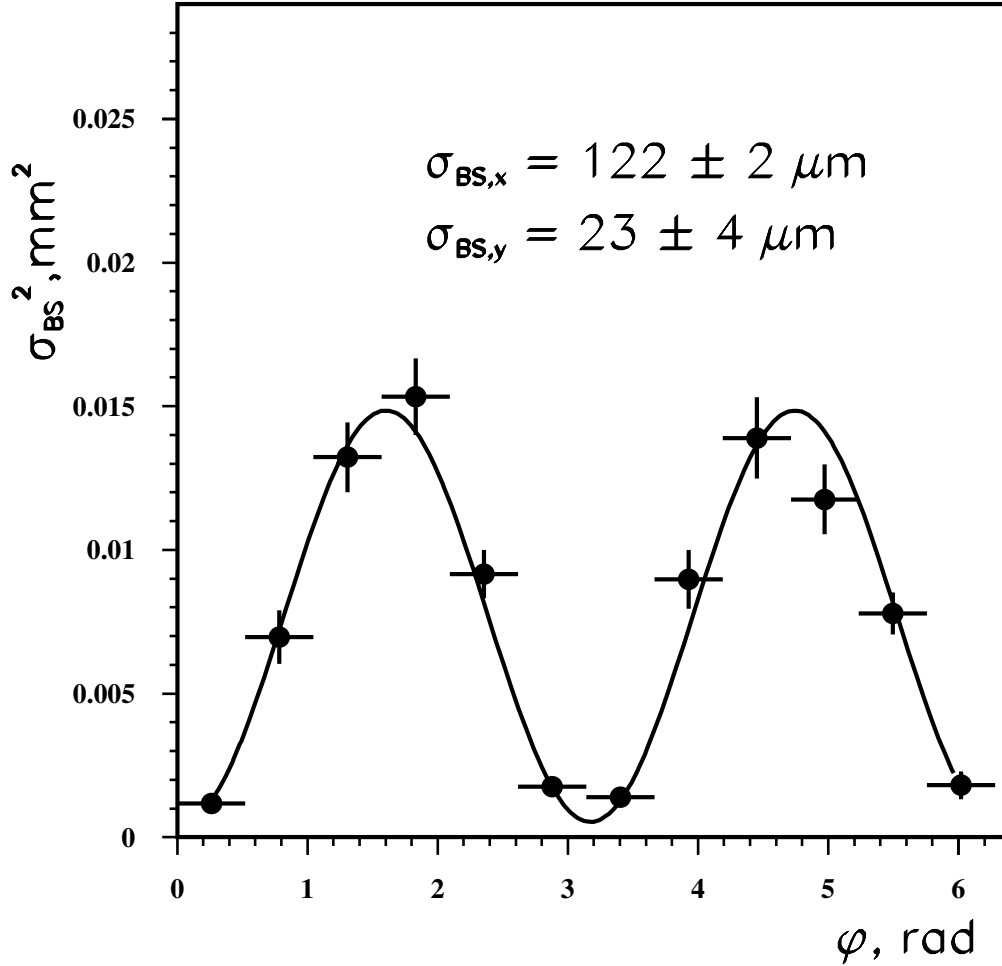


Figure A.1: The beam spot size as the function of polar angle ϕ for the year 1999 Z-peak data. Dots represents the measured values, the solid line is the result of the fit using Equation A.8. e^+e^- and $\mu^+\mu^-$ final states were added together, the barrel region only.

Beam spot size	Z peak	High energy data
$\sigma_{BS,x}$	$113 \pm 2 \mu\text{m}$	$188 \pm 4 \mu\text{m}$
$\sigma_{BS,y}$	$27 \pm 3 \mu\text{m}$	$42 \pm 6 \mu\text{m}$

Table A.1: The results for the beam spot size in terms of $\sigma_{BS,x}$ and $\sigma_{BS,y}$ for the year 2000 data.

Bibliography

- [1] S. Weinberg, *Phys. Rev. Lett.* **19** (1967) 1264.
- [2] S. Glashow, *Nucl. Phys.* **22** (1961) 579; S. Weinberg, *Phys. Rev. Lett.* **19** (1967) 1264; A. Salam, in *Elementary Particle Theory*, ed. N. Svartholm (Almqvist and Wiksells, Stockholm, 1969), p.367.
- [3] D. J. Gross and F. Wilczek, *Phys. Rev. Lett.* **30** (1973) 1343; H.D. Politzer, *Phys. Rev. Lett.* **30** (1973) 1346.
- [4] N. Cabibbo, *Phys. Rev. Lett.* **10** (1963) 531,
M.Kobayashi and K.Maskawa, *Prog. Theo. Phys.* **49** (1973) 652..
- [5] L. Okun, *Phys. Rev. Lett.* **19** (1967) 1264.
- [6] C. Quigg *Gauge Theories of the Strong, Weak, and Electromagnetic Interactions*, Benjamin-Cummings, Reading, M.A., 1983.
- [7] P. W. Higgs, *Phys. Lett.* **12** (1964) 132, *Phys. Rev. Lett.* **13** (1964) 508 and *Phys. Rev.* **145** (1966) 1156;
F. Englert and R. Brout, *Phys. Rev. Lett.* **13** (1964) 321;
G.S. Guralnik *et al*, *Phys. Rev. Lett.* **13** (1964) 585.
- [8] S. Dawson *Introduction to Electroweak Symmetry Breaking*; hep-ph/0091280 v1, 12 Jan 1999.
- [9] T. Appelquist, Lectures given at the 1994 Theoretical Advanced Study Institute, Boulder, CO., May 30 - June 23, 1994.
- [10] P. Ramond, Lectures, given at the 1994 Theoretical Advanced Study Institute, Boulder, CO., May 30 - June 23, 1994.
- [11] K.Wilson, *Phys. Rev.*, **B4** (1971) 3184; K. Wilson and J. Kogut, *Phys. Rep.*, **12** (1974) 75; R. Dashen and H. Neuberger, *Phys. Rev. Lett.*, **50** (1983) 1897; P. Hasefratz and J. Nager, *Z. Phys.*, **C37** (1988); J. Kuti, L. Lin, and Y. Shen, *Phys. Rev. Lett.*, **61** (1988) 678; M. Luscher and P. Weisz, *Phys. Lett.*, **B212** (1988) 472.
- [12] R. Chivukula and E. Simmons, *Phys. Lett.*, **B388** (1996) 788.

- [13] J. Pati and A. Salam, Phys. Rev. **D 10** (1974) 275;
S. Dimopoulos, Nucl. Phys. **B 168** (1980) 69;
C.H. Albright, Phys. Rev. **D 29** (1984) 2595;
B. Schrempp and F. Schrempp, Nucl. Phys. **B 242** (1984) 203;
V.D. Angelopoulos *et al.*, Nucl. Phys. **B 292** (1987) 59..
- [14] M. Quiros, *Perspectives in Higgs physics*, Ed. G. Kane, (World Scientific, Singapore, 1997).
- [15] T. Cheng, E. Eichten and L. Li, Phys. Rev. **D9** (1974) 2259; B. Pendleton and G. Ross, Phys. Lett. **B98** (1981) 291; C. Hill, Phys. Rev. **D24** (1981) 691; J. Bagger, S. Dimopoulos and E. Masso, Nucl. Phys., **B253** (1985) 397; M. Beg, C. Panagiotakopoulos, and A. Sirlin, Phys. Rev. Lett. **52** (1984) 883; M. Duncan, R. Philippe, and M. Sher, Phys. Lett. **B153** (1985) 165; K. Babu and E. Ma, Phys. Rev. Lett. **55** (1985) 3005.
- [16] N. Cabibbo *et al.*, Nucl. Phys. **B158** (1979) 295.
- [17] A. Linde, JETP Lett. **23** (1976) 64; Phys. Lett. **B62** (1976) 435; S. Weinberg, Phys. Rev. Lett. **36** (1976) 294; S. Coleman and E. Weinberg, Phys. Rev. **D7** (1973) 188.
- [18] M. Lindner, M. Sher, and H. Zaglauer, Phys. Lett. **B228** (1989) 139; C. Ford *et al.*, Nucl. Phys. **B395** (1993) 62; M. Sher, Phys. Rep. **179** (1989) 274; F. del Aguila, M. Martinez, M. Quiros, Nucl. Phys. **B381** (1992) 451; J. Casas, J. Espinosa, and M. Quiros, Phys. Lett. **B324** (1995) 171; Phys. Lett. **B382** (1996) 374; J. Espinosa and M. Quiros, Phys. Lett. **B353** (1995) 257.
- [19] The LEP Electroweak Working Group, *A Combination of Preliminary Electroweak Measurements and Constraints on the Standard Model*, CERN-EP/99-15, 1999.
- [20] SLD Collaboration, K. Baird, *Measurements of A_{LR} and A_ℓ from SLD*, Talk Presented at ICHEP 98, Vancouver, B. C., Canada, 23-29 July, 1998.
- [21] UA2 Collaboration, J. Alitti *et al.*, Phys. Lett. **B276** (1992) 354.
- [22] CDF Collaboration, F. Abe *et al.*, Phys. Rev. Lett. **65** (1990) 2243;
CDF Collaboration, F. Abe *et al.*, Phys. Rev. **D43** (1991) 2070;
CDF Collaboration, F. Abe *et al.*, Phys. Rev. Lett. **75** (1995) 11;
CDF Collaboration, F. Abe *et al.*, Phys. Rev. **D52** (1995) 4784;
A. Gordan, Talk Presented at XXXIInd Rencontres de Moriond, Les Arcs, 16-22 March 1997.
- [23] D0 Collaboration, S. Abachi *et al.*, Phys. Rev. Lett. **77** (1996) 3309;
K. Streets, Talk Presented at Hadron Collider Physics 97, Stony Brook.
- [24] CDF Collaboration, W. Yao, *t Mass at CDF*, Talk Presented at ICHEP 98, Vancouver, B. C., Canada, 23-29 July, 1998.

- [25] D0 Collaboration, B. Abbott *et al.*, Phys. Rev. **D58** (1998) 052001.
- [26] CCFR/NuTeV Collaboration, K. McFarland *et al.*, Eur. Phys. J. **C1** (1998) 509; NuTeV Collaboration, K. McFarland, Talk Presented at the XXXIIIth Rencontres de Moriond, Les Arcs, France, 15-21 March, 1998, HEP-EX/9806013.
- [27] Z. Szillasi, *Direct and Indirect SM Higgs Search at LEP*, Talk Presented at the International Europhysics Conference High Energy Physics 99, Tampere, Finland, 15-21 July 1999.
- [28] L3 Collaboration, M. Acciari *et al.*, Phys. Lett. **B461** (1999) 376.
- [29] B. Ioffe and V. Khoze, *Sov. J. Part. Nucl. Phys.* **9** (1978) 50.
- [30] S. Dawson, J.F. Gunion, H.E. Haber and G.L. Kane, *The Physics of the Higgs Bosons: Higgs Hunter's Guide*, Addison Wesley, Menlo Park, 1989.
- [31] S. Dawson and J. Rosner, *Phys. Lett.*, **B148** (1984) 497.
- [32] A. Djouadi, D. Haidt, B. Kniehl, B. Mele, and P. Zerwas, *Proceedings of e+e- collisions at 500 GeV: The Physics Potential*, (Munich-Annecy-Hamburg), ed. P. Zerwas, DESY 92-123A.
- [33] E. Braaten and J. Leveille, *Phys. Rev.*, **D22** (1980) 715; and M. Drees and K. Hikasa, *Phys. Lett.*, **B240** (1990) 455.
- [34] W.-Y. Keung and W. Marciano, Phys. Rev. **D30** (1984) 248.
- [35] A. Vainshtein, M. Voloshin, V. Sakharov, and M. Shifman *Sov. J. Nucl. Phys.* **30** (1979) 711.
- [36] R. Cahn, M. Chanowitz, and N. Fleishon, *Phys. Lett.*, **B82** (1979) 113; G. Gamberini, G. Giudice and G. Ridolfi, *Nucl. Phys.*, **B292** (1987) 237.
- [37] R. Engel, *Z. Phys.* **C 66** (1995) 203;
R. Engel and J. Ranft, *Phys. Rev. D* **54** (1996) 4244.
- [38] S. Jadach, B.F.L. Ward and Z. Was, Preprint CERN-TH/99-235 hep-ph/9912214.
- [39] T. Sjöstrand, CERN-TH 7112/93, CERN (1993), revised August 1995;
T. Sjöstrand, *Comp. Phys. Comm.* **82** (1994) 74.
- [40] M. Skrzypek *et al.*, *Comp. Phys. Comm.* **94** (1996) 216;
M. Skrzypek *et al.*, *Phys. Lett.* **B372** (1996) 289.
- [41] R. Kleiss and R. Pittau, *Comp. Phys. Comm.* **83** (1994) 141;
see also F.A. Berends, R. Kleiss and R. Pittau in "Physics at LEP2", CERN 96-01, Vol. 2, eds. G. Altarelli, T. Sjöstrand and F. Zwirner.
- [42] J. Poole, editor, *Proceedings of the 7th LEP Performance Workshop*, Geneva, Switzerland, 1997, CERN, CERN-SL-97-06-DI.

- [43] G. Altarelli, T. Sjostrand, and F. Zwirner, editors, *Physics at LEP2*, Geneva, Switzerland, 1996, CERN, CERN-96-01.
- [44] The ALEPH Collaboration, Nucl. Instr. Meth. **A 294** (1990) 121.
- [45] The DELPHI Collaboration, Nucl. Instr. Meth. **A 303** (1991) 233.
- [46] L3 Collaboration, B. Adeva *et al.*, Nucl. Instr. Meth. **A289** (1990) 35.
- [47] J.A. Bakken *et al.*, Nucl. Instr. Meth. **A275** (1989) 81.
- [48] O. Adriani *et al.*, Nucl. Instr. Meth. **A302** (1991) 53.
- [49] B. Adeva *et al.*, Nucl. Instr. Meth. **A323** (1992) 109;
S. Lanzano, *et al.*, Nucl. Instr. Meth. **A289** (1990) 335.
- [50] K. Deiters *et al.*, Nucl.Instr.Meth. **A323** (1992) 162.
- [51] M. Chemarin *et al.*, Nucl.Instr.Meth. **A349** (1994) 345.
- [52] B. Acciari *et al.*, Nucl.Instr.Meth. **A351** (1994) 300.
- [53] G. Basti *et al.*, Nucl.Instr.Meth. **A374** (1996) 293.
- [54] I.C. Brock *et al.*, Nucl. Instr. Meth. **A381** (1996) 236.
- [55] U. Uwer, *The L3 Scintillation Counter System: Description and Status*, L3 Internal Note 2003, 1996.
- [56] A. Adam *et al.*, Nucl.Instr.Meth. **A383** (1996) 342.
- [57] The OPAL Collaboration, Nucl. Instr. Meth. **A 305** (1991) 275.
- [58] A. Adam *et al.*, Nucl. Instr. Meth. **A344** (1994) 521.
- [59] The L3 Collaboration, Phys. Rep. **236** (1993).
- [60] I. Brock *et al.*, Nucl. Inst. Meth. **A381** (1996) 236.
- [61] P. Janot, *The HZHA Generator* in G. Altarelli, T. Sjöstrand, F. Zwirner, *Physics at LEP2*, CERN 96-01, 1996, vol. 2, p.309.
- [62] The L3 Detector Simulation is Based on GEANT Version 3.15.
See R. Brun *et al.*, “GEANT 3”, CERN DD/EE/84-1 (Revised), September 1987.
The GHEISHA Program (H. Fesefeldt, RWTH Aachen Report PITHA 85/02 (1985)) is Used to Simulate Hadronic Interactions.
- [63] H. Fesefeldt, RWTH Aachen, Preprint PITHA 85/02 (1985).
- [64] T. Sjöstrand and M. Bengtsson, Comput. Phys. Commun. **43** (1987) 367,
T. Sjöstrand in “Z Physics at LEP 1”, CERN-89-08, ed. G. Altarelli *et al.*, (CERN, Geneva, 1989), vol. 3, p. 143.
For 1990 data we used JETSET 7.2 and for 1991 data we used JETSET 7.3..

- [65] D. Kamrad, Dissertation *Measurement of the Partial Z decay Width into b Quarks with the L3 Detector at LEP*, Humboldt University.
- [66] R.D. Field and R.P. Feynman, Nucl. Phys. **B 136** (1978) 1, and references therein.
- [67] X. Artru and G. Mennessier, Nucl. Phys. **B 70** (1974) 95-115.
- [68] X. Artru, Phys. Rept. **97** (1983) 147.
- [69] R. Odorico, Nucl. Phys. **B 172** (1980) 157.
- [70] G. C. Fox and S. Wolfram, Nucl. Phys. **B 168** (1980) 285.
- [71] R. D. Field and S. Wolfram, Nucl. Phys. **B 213** (1983) 65.
- [72] T. D. Gottschalk, Nucl. Phys. **B 214** (1983) 201.
- [73] T. Sjöstrand, Comp. Phys. Comm. **39** (1986) 347;
T. Sjöstrand and M. Bengtsson, Comp. Phys. Comm. **43** (1987) 367;
T. Sjöstrand, "PHYTHIA 5.6 JETSET 7.3 Physics and Manual", Preprint CERN-TH 6488/92, CERN (1992).
- [74] A. Kunin, M. Maity, G. Majumder, *G-Factors*, L3 note 1840, 1995; S. Banerjee, J. Casaus and S. Sarkar, *Hadron Group G-Factors*, L3 note 1939, 1996.
- [75] S. Bethke *et al.*, Nucl. Phys. **B 370** (1992) 310.
- [76] Serge Likhoded, W. Lohmann, DESY Zeuthen. *The Resolution Functions of Jet Measurements in the L3 Detector*. L3 note 2664. May 14, 2001.
- [77] A. Dominguez, *Search for Neutral Higgs Bosons in e^+e^- Interactions at Center-of-Mass Energies between 130 GeV and 183 GeV*, Ph.D. Thesis, UCSD, 1998, <http://hep.ucsd.edu/thesis/aaron.html>.
- [78] J. Branson, A. Dominguez, I. Fisk and G. Raven, *The UCSD B Tag for 1996*, L3 Internal Note 2108, 1997.
- [79] C. Caso *et al.*, Particle Physics Booklet. Springer, July 1998.
- [80] L. Lönnblad, C. Peterson and T. Rognvaldsson, Nucl. Phys. **B349** (1991) 675;
C. Peterson *et al.*, Comp. Phys. Comm. **81** (1994) 185.
- [81] O. Adriani *et al.*, Phys. Lett. **B307** (1993) 237.
- [82] The L3 Collaboration. (R. Berbeco, M. Felcini, P. Garcia-Abia, A. Holzner, Y. Hu, S. Likhoded, B. Muscar, G. Rahal, A. Raspereza, D. Teyssier, C. Tully, J. Yamamoto). *Search for the Standard Model Higgs Boson with the L3 Experiment at LEP*. L3 note 2688, June 28, 2001.
- [83] L3 Collaboration, *Standard Model Higgs Boson with the L3 Experiment at LEP*, CERN-EP/2001-049, July 10, 2001.

- [84] F. James, CERN Program Library Long Writeup D506 MINUIT, CERN, 1993.
- [85] OPAL Collaboration, K. Ackerstaff *et al.*, Eur. Phys. J. **C1** (1998) 425.
- [86] ZZ Production in 4-Jet Channel, T. Aziz, M. Wadhwa, L3 Note 2481, 1999.
- [87] L3 Collaboration, M. Acciari *et al.*, Phys. Lett. **B 431** (1998) 437.
- [88] L3 Collaboration, M. Acciari *et al.*, Phys. Lett. **B 508** (2001) 225.
- [89] L3 Collaboration, M. Acciari *et al.*, Phys. Lett. **B 495** (2000) 18.
- [90] L3 Collaboration, M. Acciari *et al.*, Phys.Lett. **B411** (1997) 373.
- [91] A. Favara, M. Pieri, *Confidence Level Estimation and Analysis Optimisation*, Preprint DFF-278-4-1997, INFN, 1997.
- [92] L3 Collaboration, M.Acciarri et al., Phys. Lett. **B 495** (2000) 18.
- [93] L3 Collaboration, M.Acciarri et al., Phys. Lett. **B 508** (2001) 225.
- [94] The LEP Energy Working Group Collaboration, A. Blondel *et al.*, *Evaluation of the LEP Centre-of-Mass Energy above the W-pair Production Threshold*, Preprint CERN-EP/98-191, CERN-SL/98-073, CERN 1998, submitted to Eur. Phys. J. C.; The LEP Energy Working Group Collaboration, *Energies for LEP1.5 Run*, Preprint LEP ECAL/97-04, LEP ECAL, 1997; The LEP Energy Working group Collaboration, *Preliminary LEP Energy Calibration for 1997 Data*, Preprint LEP ECAL/98-01, LEP ECAL, 1998; The LEP Energy Working Group Collaboration, *Evaluation of the LEP Centre-of-Mass Energy for Data Taken in 1998*, Preprint LEP ECAL/99-01, LEP ECAL, 1999.
- [95] The ALEPH Collaboration, R. Barate *et al.*, Phys. Lett. **B447** (1999) 336.
- [96] B. A. Kniehl, Phys. Rep. **C240** (1994) 211;
E. Gross, B. A. Kniehl and G. Wolf, Z. Phys. **C63** (1994) 417, *erratum-ibid* **C66** (1995) 321.
- [97] A. Djouadi *et al.*, Z. Phys. **C70** (1996) 427.
- [98] L3 Collaboration, M.Acciarri et al., Phys. Lett. **B 461** (1999) 376.
- [99] The ALEPH, DELPHI, L3 and OPAL Collaborations, the LEP working group for Higgs boson searches, “*Search for the Standard Model Higgs Boson at LEP*”, CERN-EP/2001-055, LHWG Note 2001-05, ALEPH 2001-066 CONF 2001-046, DELPHI 2001-113 CONF 536, L3 Internal Note 2699, OPAL Physics Note PN479, July 11, 2001.
- [100] “*Search for the Standard Model Higgs Boson at LEP*”, ALEPH, DELPHI, L3 and OPAL Collaborations, CERN-EP/2001-055, 11 July, 2001.
- [101] ALEPH Collaboration, R. Barate et al., Phys. Lett. **B 495** (2000) 1.

- [102] OPAL Collaboration, G. Abbiendi et al., Phys. Lett. **B 499** (2001) 38..
- [103] L3 Collab., P.Achard et al., Phys. Lett. **B 517** Issue 3-4, 2001, pp. 319-331.
- [104] ALEPH, DEPLHI, L3 and OPAL Collaborations, The LEP working group for Higgs boson searches, *Searches for Higgs bosons: Preliminary combined results using LEP data collected at energies up to 202 GeV*, CERN-EP/2000-055.
- [105] K. Hagiwara *et al.*, Z. Phys. **C 29** (1985) 115.
- [106] S. Jadach, B.F.L. Ward and Z. Was, Comp. Phys. Comm. **66** (1991) 276.
- [107] S. Jadach *et al.*, Phys. Lett. **B 390** (1997) 298.
- [108] F.A. Berends, P.H. Daverfeldt and R. Kleiss, Nucl. Phys. **B 253** (1985) 441.
- [109] Private communication with Martin Weber, III. Physikalisches Institut, RWTH Aachen.
- [110] The L3 Collaboration. *Z Boson Pair-Production at LEP* L3 note 2696, July 4th, 2001.
- [111] Serge Likhoded, W. Lohmann, DESY Zeuthen. *Observation of Resonant ZZ Production and Measurement of the Cross Section of $e+e- \rightarrow ZZ \rightarrow q\bar{q}q\bar{q}$* . L3 note 2725, December 19, 2001.
- [112] S. Mele, L3 Collaboration, “*Z Boson Pair-Production at LEP*”, L3 Note 2696, 2001.
- [113] J. Fujimoto *et al.*, Comp. Phys. Comm. **100** (1997) 128.
- [114] J. Alcaraz *et al.*, preprint hep-ph/9812435.
- [115] A. Kopp, Dissertation *Search for Higgs Bosons Using the L3 Detector at LEP*, Humboldt University.
- [116] L3 Collab., M.Acciarri *et al.*, Phys. Lett. **B 450** (1999) 281.
- [117] L3 Collab., M.Acciarri *et al.*, Phys. Lett. **B 465** (1999) 363.
- [118] L3 Collab., M.Acciarri *et al.*, Phys. Lett. **B 497** (2001) 23.
- [119] J. Alcaraz *et al.*, “Study of Z Boson Pair Production in $e+e-$ Collisions at LEP at $\sqrt{s} = 189$ GeV”.
- [120] ALEPH Collaboration, ALEPH 2001-013 Conf 2001-010, submitted to the Winter 2001 Conferences.
- [121] DELPHI Collaboration, DELPHI 2001-024 Conf 465, submitted to the Winter 2001 Conferences.

-
- [122] L3 Collaboration, L3 Note 2638, submitted to the Winter 2001 Conferences.
- [123] OPAL Collaboration, OPAL Physics Note PN469, submitted to the Winter 2001 Conferences.
- [124] L. Lyons, D.Gibaut and P.Clifford, Nucl. Instr. Meth. **A270** (1988) 110.
- [125] M.W.Gruenewald, G. Passarino *et al.*, “Four fermion production in electron positron collisions”, Four fermion working group report of the LEP2 Monte Carlo Workshop 1999/2000.
- [126] M.W. Gruenewald *et al.*, Preprint hep-ph/0005309 (2000).
- [127] S. Jadach *et al.*, Phys. Rev. **D56** (1997) 6939.
- [128] The LEP working group for Higgs boson searches, “Search for the Standard Model Higgs Boson at LEP”, LHWG Note/2001-03; CERN-EP/2001-055.
- [129] J. Ellis, “The 115 GeV Higgs Odyssey”, hep-ex/0011086, CERN-TH/2000-307.
- [130] G. Altarelli and G.Isidori, Phys. Lett. **B337** (1994) 141.
- [131] E. Farhi and L.Susskind, Phys. Rept. **74** (1981) 277.
- [132] J. Ellis, M.K. Gaillard, D.V. Nanopoulos and P.Sikivie, Nucl. Phys. **B182**.
- [133] J. Ellis, G. Ganis, D.V. Nanopoulos and K.A. Olive, hep-ph/0009355.
- [134] Tevatron Run II Higgs working Group, hep-ph/0010338.
- [135] ATLAS collaboration, Detector and Physics Performace Technical Design Report, CMS collaboration, Technical Proposal, F.Gianotti.
- [136] LEP Electroweak Working Group, <http://lepewwg.web.cern.ch/LEPEWWG/>.
- [137] Serge Likhoded, the L3 Collaboration, *Beam spot size and vertex position in 1999 data*, L3 Note 2422 av.
- [138] Andre Krueger, the L3 Collaboration, *Beam spot size and Beam position in 2000*, L3 Note 2630, January 17, 2001.

Acknowledgements

First of all, I wish to thank my advisors Wolfgang Lohmann and Thomas Hebbeker for their continuous support and guidance throughout the last three years.

I enjoyed the work in the Higgs group and profited a lot from fruitful discussions with Aaron Dominguez, Ian Fisk, Chris Tully, Pablo Garsia-Abia and Marta Felcini. As a member of L3 Higgs working group I have had a chance to work and to communicate with many talented and interesting young physicists, like Alexei Raspereza, Andre Holzner, Ross Berbeco, Jin Yamamoto, Bryan Musicar and many others. Within the ZZ group I had a pleasure to work with such nice people and scientists, as Salvatore Mele, Juan Alcaraz, Martin Weber, Gagan Bihari Mohanty. Especially I would like to thank Ricardo Vasquez Sierra for his support and those unforgettable social life in Geneva.

I would like to thank all members of the L3 group in Zeuthen and Berlin for providing a very pleasant working atmosphere and a very helpful assistance. I am thankful to Sabine Riemann for her everyday help and a taking care about all the problems I had during these years. My special thank to Ivanka Bozovic-Jelisavcic and to my young German colleagues Michael Unger and Andre Krueger for their openness and friendly attitude.

The analysis presented in this thesis is the result of the combined effort of many people from the L3 Collaboration and, in particular, from other three LEP experiments. These searches and measurements would not have been possible without all those physicists, engineers and technicians who designed, built and maintained the L3 Detector and the LEP collider. I would like to thank all of them for their outstanding work, help and cooperation.

I am grateful to my parents for their permanent support and sharing with me the most difficult and the most glorious moments throughout these years.